

Winter 2006

Robustness and Control of a Magnetically Levitated Transportation System

Grzegorz Oleszczuk
Old Dominion University

Follow this and additional works at: https://digitalcommons.odu.edu/mae_etds

 Part of the [Aerospace Engineering Commons](#), [Electromagnetics and Photonics Commons](#), [Mechanical Engineering Commons](#), and the [Transportation Commons](#)

Recommended Citation

Oleszczuk, Grzegorz. "Robustness and Control of a Magnetically Levitated Transportation System" (2006). Doctor of Philosophy (PhD), dissertation, Aerospace Engineering, Old Dominion University, DOI: 10.25777/sjpr-as69
https://digitalcommons.odu.edu/mae_etds/82

This Dissertation is brought to you for free and open access by the Mechanical & Aerospace Engineering at ODU Digital Commons. It has been accepted for inclusion in Mechanical & Aerospace Engineering Theses & Dissertations by an authorized administrator of ODU Digital Commons. For more information, please contact digitalcommons@odu.edu.

ROBUSTNESS AND CONTROL OF A MAGNETICALLY LEVITATED TRANSPORTATION SYSTEM

by

Grzegorz Oleszczuk

MSc Eng., April 2000, Warsaw University of Technology

A Thesis submitted to the Faculty of
Old Dominion University in Partial Fulfillment of the
Requirement for the Degree of

DOCTOR OF PHILOSOPHY

Aerospace Engineering

OLD DOMINION UNIVERSITY

December 2006

Approved by:

Thomas E. Alberts
(Director)

Colin P. Britcher
(Member)

Jeremiah F. Creedon
(Member)

Oscar R. Gonzalez
(Member)

Brett Newman
(Member)

ABSTRACT

ROBUSTNESS AND CONTROL OF A MAGNETICALLY LEVITATED TRANSPORTATION SYSTEM

Grzegorz Oleszczuk
Old Dominion University, 2006
Director: Thomas E. Alberts

Electromagnetic suspension of Magnetic Levitation Vehicles (Maglev) has been studied for many years as an alternative to wheel-on rail transportation systems. In this work, design and implementation of control systems for a Maglev laboratory experiment and a Maglev vehicle under development at Old Dominion University are described. Both plants are modeled and simulated with consideration of issues associated with system non-linearity, structural flexibility and electromagnetic force modeling. Discussion concerning different control strategies, namely centralized and decentralized approaches are compared and contrasted in this work. Different types of electromagnetic non-linearities are considered and described to establish a convenient method for modeling such a system. It is shown how a Finite Element structural model can be incorporated into the system to obtain transfer function notation. Influence of the dynamic interaction between the Maglev track and the Maglev vehicle is discussed and supported by both analytical results and theoretical examples. Finally, several control laws designed to obtain stable and robust levitation are explored in detail.

ACKNOWLEDGMENTS

I wish to express my gratitude to my advisor, Professor Thomas E. Alberts, for suggesting the subject of this dissertation, for his invaluable support and guidance over the course of this research, and for his patient answering of my many questions. I appreciate the many hours he spent teaching me the practical approach to control design and the art of model simplification of dynamic systems.

I would like to thank Professors Colin Britcher, Jeremiah Creedon, Oscar Gonzales and Brett Newman for their review and constructive comments as readers and as Dissertation Research Committee Members.

My appreciation is extended to the staff of the Aerospace Engineering Department at ODU. I could always rely on their help whenever needed. I also wish to express my thanks to my friends and colleagues for their encouragement, especially Adam Przekop, Jiang Wang, Shen Liu, and Jeremy Roadcap.

I would like to acknowledge that the funding for this effort came from the Federal Railroad Administration grant DTFRDU-03-H-60045 and I thank the ODU Research Foundation for administering the research funding for this project. I'm grateful to Professor Robert L. Ash, the Principal Investigator for this effort.

Finally, I wish to express my thanks to my parents for their unfailing support (sometimes also content-related to my work) and encouragement to seek a higher education. I also thank Kate for her perseverance.

This work is dedicated to the memory of my great-great grandmother Wladyslawie Oleszczuk.

TABLE OF CONTENTS

Abstract	ii
Acknowledgments	iii
Table of Contents	iv
List of Tables	viii
List of Figures	ix
Nomenclature	xv
Chapter 1 Introduction	1
1.1 Magnetism and Maglev Systems	3
1.2 Motivation	8
1.3 Dissertation Statements	10
Chapter 2 Fundamental Modeling and Stability Analysis	11
2.1 Electromagnetic Circuit	11
2.1.1 Electromagnetic Force for Uniform Magnetic Field	12
2.1.2 Electromagnetic Force with Fringing and Lateral Displacement.	14
2.1.3 Coil Dynamics as a Result of Inductance	19
2.1.4 Simplified Electromagnet Model	19
2.2 Linearization	21
2.3 Maglev as a Rigid Mass	22
2.4 Stability of the Rigid Case Under PD Control	24
2.5 Maglev as SISO Flexible System	25
2.6 Collocated Flexible Case Under PD Control	27
2.7 Non-Collocated Flexible Case Under PD Control	28
2.8 Root Locus Analysis of Collocated and Non-Collocated Cases	30
2.9 Non-Collocated Flexible Case Under PD Control with Acceleration Feedback	33
2.10 Maglev as a MIMO Flexible Structure	34
2.11 Centralized vs. Decentralized Control Law for Maglev Application	36
2.12 Centralized vs. Decentralized Control Law with PD Compensation	41
2.13 Flux Feedback	43

2.14 Inverse Electromagnetic Model Calculation	46
2.14.1 Concept of the Inverse Model Calculation	46
2.14.2 Sensitivity of the Inverse Model Calculation	49
2.15 Transfer Function Zeros	52
2.15.1 Zero Movement and its Impact on the Control Design	59
2.16 Summary	61
Chapter 3 Maglev Test Rig Model	62
3.1 Electromagnetic Part of the Test Rig	63
3.2 Current Amplifier Modeling and its Calibration	63
3.3 Effects of Non-linearities on Amplifier Current Following	67
3.3.1 Rate Limit and Amplifier Saturation	67
3.3.2 Effect of Hysteresis	71
3.4 Equations of Motion for Structural Model (rigid)	73
3.5 Equations of Motion for Structural Model (flexible)	76
3.5.1 Levitated System Structural Model	77
3.5.2 Grounded System Structural Model	80
3.5.3 Levitated and Grounded Structural Models Comparison	83
3.6 Equation for the Entire Maglev Test Rig Systems	83
3.6.1. Electromagnet Model Together with Rigid Structural Model	84
3.6.2. Electromagnet Model with Flexible Levitated Structure Model	87
3.6.3 Electromagnet Model Together with Flexible Grounded Structural Model	89
3.7 Model Validation via Experiment	91
3.8 Summary	93
Chapter 4 Test Rig Control Laws	94
4.1 Compensation Based on Gap Feedback	94
4.1.1 Filter Design	98
4.1.1.1 Digital Filter	99

4.1.1.2 Analog Filter	101
4.1.2 Root Locus PD Control Design	102
4.1.2.1 Steady State Error	105
4.1.3 Robustness of the PD Control Design	106
4.2 Sensor Fusion Gap and Acceleration Feedback	110
4.3 Flux Feedback	115
4.3.1 Flux Leakage	119
4.3.2 Flux Feedback Analysis	120
4.4 PD Control with Inverse Calculation	123
4.5 Application and Experiment Results	125
4.5.1 Pure Gap Feedback with PD/PID Compensator	127
4.5.2 PD/PID Compensator based on Gap with Acceleration Feedback	130
4.5.2.1 Steady State Error Tests	133
4.5.3 Compensator with Linearized Calculation (Force Inverse)	134
4.5.4 Compensator with Flux Feedback	136
4.6 Conclusion	140
Chapter 5 ODU Maglev Vehicle Model	143
5.1 Control Current Drive Model (CID)	145
5.2 Coil Dynamics due to Inductance (CID)	147
5.3 Model of the Structural Part of the ODU Maglev System	148
5.4 State Space Format of the Structural Maglev Equations of Motion	154
5.5 Complete Equations of Motion Expression for the ODU Maglev System	159
5.6 Conclusion	164
Chapter 6 ODU Maglev Control	165
6.1 Stability Issues Due to ODU Maglev Structural Flexibility	166
6.2 ODU Maglev Vehicle as MIMO System	169
6.3. PD/PID Compensation	170
6.3.1 Experiment Results	179
6.4. Conclusion	180

Chapter 7 Conclusion	181
References	185
APPENDIX A.1	192
APPENDIX A.2	193
APPENDIX A.3	194
Curriculum Vitae	195

LIST OF TABLES

<i>Table 2.1 Electromagnet parameters</i>	16
<i>Table 2.2 Data used for comparison of collocated and non-collocated Maglev systems</i>	30
<i>Table 2.3 Natural frequencies of the ODU Maglev track idealized model</i>	57
<i>Table 3.1 Electromagnet circuit parameters</i>	64
<i>Table 3.2 Linear tracking amplitudes for various frequencies</i>	68
<i>Table 3.3 Inertia calculation for the Maglev Test Rig</i>	75
<i>Table 3.4 Experiment setup for grounded Test Rig</i>	91
<i>Table 4.1 Minimum requirements for PD compensator</i>	95
<i>Table 4.2 Digital filter comparisons</i>	100
<i>Table 4.3 Test Rig model performance with PD compensator and filters</i>	103
<i>Table 4.4 Leak frequencies comparison</i>	112
<i>Table 4.5 Coefficients for linearized flux expression</i>	119
<i>Table 4.6 Performance of flux feedback control law with PD compensator applied to linear Maglev models</i>	121
<i>Table 4.7 Comparison of tested on actual plant control laws</i>	140
<i>Table 5.1 Notation table for structural ODU Maglev model</i>	151
<i>Table 5.2 First nine natural frequencies for vehicle, obtained from Nastran</i>	153
<i>Table 5.3 Visualization of the first 9 natural frequencies for the Maglev vehicle</i>	153
<i>Table 5.4 Track (first nine) natural frequencies obtained from Nastran software</i>	154
<i>Table 6.1 Maglev poles for the open-loop case and closed-loop cases: center position and quarter position on guideway span</i>	168
<i>Table 6.2 Proposed compensators for the ODU Maglev train</i>	175

LIST OF FIGURES

<i>Figure 1.1 Linear synchronous motors (LSM – top view)</i>	5
<i>Figure 1.2 Electromagnetic suspension (EMS)</i>	6
<i>Figure 1.3 Electrodynamics suspension (EDS)</i>	7
<i>Figure 2.1 U shaped electromagnet with uniform magnetic field</i>	12
<i>Figure 2.2 Magnetic field models for U shaped magnets,</i>	
<i>a) uniform</i>	15
<i>b) with fringing</i>	15
<i>Figure 2.3 Inductance comparison for two different inductance expressions</i>	15
<i>Figure 2.4 Analytical lift force comparison</i>	17
<i>Figure 2.5 Analytical lateral force comparison</i>	18
<i>Figure 2.6 Electromagnet circuit model</i>	20
<i>Figure 2.7 Simple Maglev system</i>	22
<i>Figure 2.8 Block diagram of the 1DOF Maglev rigid system</i>	23
<i>Figure 2.9 Block diagram of the Maglev control loop</i>	24
<i>Figure 2.10 Model of the flexible SISO Maglev</i>	25
<i>Figure 2.11 Collocated system with PD compensator</i>	31
<i>Figure 2.12 Non-Collocated system with PD compensator</i>	32
<i>Figure 2.13 Non-Collocated Maglev system with PD compensator with</i>	
<i>acceleration feedback</i>	34
<i>Figure 2.14 Simple MIMO Maglev model with flexible modes</i>	35
<i>Figure 2.15 Centralized vs. decentralized compensation</i>	37
<i>Figure 2.16 Block diagram of the centralized and decentralized Maglev models</i>	39
<i>Figure 2.17 Decentralized singular value frequency response</i>	40
<i>Figure 2.18 Centralized singular value frequency response</i>	41
<i>Figure 2.19 Decentralized PD control</i>	42
<i>Figure 2.20 Centralized closed-loop root loci with PD compensation</i>	43

<i>Figure 2.21 Schematic of Maglev plant with flux feedback</i>	44
<i>Figure 2.22 Electromagnet Bode plots for different operation points due to Limbirt electromagnet model</i>	47
<i>Figure 2.23 Maglev Test Rig block diagram with inverse calculation block</i>	48
<i>Figure 2.24 Electromagnet Bode plots for a range of operating points with model inversion</i>	48
<i>Figure 2.25 Electromagnet Bode Plots for different operation points with Limbirt partial inverse calculations and electromagnet model</i>	49
<i>Figure 2.26 Maglev system with inverse force calculation</i>	51
<i>Figure 2.27 Maglev vehicle/track interaction modeling</i>	52
<i>Figure 2.28 Simply supported beam under force applied at x_1</i>	55
<i>Figure 2.29 Numerical results of equation (2.146)</i>	56
<i>Figure 2.30 Bode plots for three positions of the vehicle on the rail guideway</i>	58
<i>Figure 2.31 Maglev vehicle above column; PD compensator with notch filter</i>	60
<i>Figure 2.32 Maglev vehicle between columns; PD compensator with notch filter</i>	60
<i>Figure 3.1 The Maglev Test Rig laboratory setup</i>	62
<i>Figure 3.2 Electromagnet block with the current amplifier</i>	65
<i>Figure 3.3 Electromagnet model created in Matlab Simulink</i>	65
<i>Figure 3.4 Electromagnet characteristics for different K_a gains</i>	66
<i>Figure 3.5 Electromagnet model for different gaps at $I_0=30A$ and $K_a=256$</i>	67
<i>Figure 3.6 Amplitude and rate saturation model</i>	68
<i>Figure 3.7 Saturation simulation results for amplitude signal 25 A and frequency 5 and 10 Hz</i>	69
<i>Figure 3.8 Saturation simulation results for amplitude signal 10 A and frequency 10 and 20 Hz</i>	69
<i>Figure 3.9 Simulink model for rate and saturation effect at high frequencies</i>	70
<i>Figure 3.10 Rate limit saturation with high frequency noise</i>	70
<i>Figure 3.11 General example of flux density B vs. field intensity H for different metal materials</i>	71

<i>Figure 3.12 Hysteresis phenomena current vs. gap</i>	72
<i>Figure 3.13 Hysteresis phenomena current vs. lift force</i>	72
<i>Figure 3.14 Simple schematic of the Test Rig</i>	73
<i>Figure 3.15 Top view of the frame inertia components</i>	74
<i>Figure 3.16 Bode plots for the rigid test rig system</i>	76
<i>Figure 3.17 Spring-mass model of the Maglev Test Rig</i>	77
<i>Figure 3.18 Levitated system</i>	78
<i>Figure 3.19 Track mounting</i>	
<i>a) Close-up view of track section mounting</i>	79
<i>b) Modified gap sensing arrangement</i>	79
<i>Figure 3.20 Bode plots for the levitated test rig system modeled</i>	80
<i>Figure 3.21 Grounded system</i>	81
<i>Figure 3.22 Bode plots for the “grounded” Test Rig system</i>	82
<i>Figure 3.23 Bode plot comparison for Test Rig structural models</i>	
<i>a) Non-Collocated case comparison</i>	83
<i>b) Collocated case comparison</i>	83
<i>Figure 3.24 Maglev test rig modeling block diagram</i>	84
<i>Figure 3.25 Pole variation due to non-linearity (rigid model)</i>	86
<i>Figure 3.26 Pole variation due to non-linearity (flexible levitated model)</i>	88
<i>Figure 3.27 Pole variation due to non-linearity (flexible grounded model)</i>	90
<i>Figure 3.28 Experimental and analytical data for three different cases</i>	
<i>gap $z = 0.4$, $z = 0.55$, and $z = 0.7$[in]</i>	92
<i>Figure 4.1 PD compensator via root locus design for the rigid Test Rig model</i>	96
<i>Figure 4.2 Bode plots for PD compensator</i>	97
<i>Figure 4.3 Model block diagram after analog and digital filters were added to plant</i>	98
<i>Figure 4.4 Digital filters comparison</i>	100
<i>Figure 4.5 Analog filter characteristics; Bode plots</i>	101
<i>Figure 4.6 Marked phase delays for the initial compensator design</i>	102
<i>Figure 4.7 Root locus design for system with filters</i>	103
<i>Figure 4.8 Step response for the modeled linear Test Rig system with</i>	

<i>PD controller</i>	104
<i>Figure 4.9 Gap response for modeled non-linear Test Rig systems with PD controller</i>	105
<i>Figure 4.10 Open-loop Bode plots with mass and gap uncertainties</i>	107
<i>Figure 4.11 Robustness of PD compensation</i>	109
<i>Figure 4.12 Step response of Test Rig non-linear simulation</i>	110
<i>Figure 4.13 Simulink model of the acceleration branch in control law</i>	111
<i>Figure 4.14 Washout filter characteristic</i>	112
<i>Figure 4.15 Bode plots of leaky integrators</i>	113
<i>Figure 4.16 Simulink diagram designed to merge components in acceleration stream</i>	114
<i>Figure 4.17 Bode plots of the compensator merged acceleration stream</i>	114
<i>Figure 4.18 Test Rig system with flux feedback</i>	115
<i>Figure 4.19 Flux experiment data</i>	
<i>a) data for gap $z = 0.7$ [in]</i>	117
<i>b) data for gap $z = 0.4$ [in]</i>	117
<i>c) data for gap $z = 0.3$ [in]</i>	118
<i>Figure 4.20 Modeled Test Rig system with and without flux feedback</i>	120
<i>Figure 4.21 Test Rig time response with flux feedback</i>	122
<i>Figure 4.22 Bode plots of the system expressed by equation (4.56)</i>	124
<i>Figure 4.23 PD root locus design for system with inverse calculation</i>	125
<i>Figure 4.24 Scheme of the Test Rig experiment setup</i>	126
<i>Figure 4.25 Gap command for Test Rig experiment</i>	127
<i>Figure 4.26 Simulink diagram of the gap feedback control law</i>	128
<i>Figure 4.27 Gap response with PD compensator – pure gap feedback</i>	
<i>a) full time 60 [sec] range</i>	129
<i>b) 1[ms] time range</i>	129
<i>Figure 4.28 Noisy current command signal</i>	129
<i>Figure 4.29 Simulink diagram of the mix gap and acceleration feedback</i>	

control law	130
Figure 4.30 Gap response with PD compensator – gap and acceleration feedback 1 [ms] time range	131
Figure 4.31 Current command signal (gap and acceleration feedback)	132
Figure 4.32 0.8 [Hz] fluctuation in gap response	132
Figure 4.33 Test Rig response without current offset and without integrator	133
Figure 4.34 Test Rig response with integrator when acceleration feedback is used	134
Figure 4.35 Model of the force inverse calculation	135
Figure 4.36 Test Rig response with force inversion	135
Figure 4.37 Test Rig response with force inversion and integrator $K_I=3000$	136
Figure 4.38 Simulink diagram of the mixed gap and acceleration feedback control law with flux feedback	137
Figure 4.39 Gap response system with PD compensation and flux feedback	138
Figure 4.40 Gap response system with PID compensation and flux feedback	138
Figure 4.41 Gap response system with PID compensation and flux feedback and additional load	139
Figure 5.1 ODU Maglev system	
a) Maglev vehicle	144
b) Vehicle on the track	144
c) Layout of the lift magnets	144
Figure 5.2 Electromagnets mounts	
a) LIM magnet	144
b) Coil assembly to the hockey stick	144
Figure 5.3 Scheme of the CID	145
Figure 5.4 Simplified model of CID	146
Figure 5.5 Model of CID for non-linear simulation	146
Figure 5.6 CIDs frequency responses obtained from experiment	147

<i>Figure 5.7 Schematic model of the ODU Maglev system</i>	148
<i>Figure 5.8 Bode plots for levitation DOF -case when vehicle is in the middle of the track span (center between pillars)</i>	158
<i>Figure 5.9 Bode plots for levitation DOF - case when vehicle is close to pillar (approximately one quarter length of the track span)</i>	158
<i>Figure 5.10 Scheme of the complete ODU Maglev model</i>	160
<i>Figure 5.11 Bode plots for the ODU Maglev system</i>	
<i>a) Vehicle above concrete pillar</i>	163
<i>b) Vehicle in the middle of track span</i>	163
<i>Figure 6.1 Maglev poles before and after closing feedback loop</i>	167
<i>Figure 6.2 Original structural ODU Maglev system and after reduction (example for magnet B only)</i>	171
<i>Figure 6.3 Reduced model of the ODU Maglev system (vehicle at center position on the guideway 12 magnets transfer functions)</i>	171
<i>Figure 6.4 Reduced model of the ODU Maglev system (vehicle at quarter position on the guideway 12 magnets transfer functions)</i>	172
<i>Figure 6.5 Impact of the cross product matrix on the Maglev transfer functions</i>	173
<i>Figure 6.6 Root locus and Bode design (example for magnet A at $gap = 0.4$ [in])</i>	174
<i>Figure 6.7 Compensator Bode plots</i>	175
<i>Figure 6.8 Step response of the linear ODU Maglev train (magnet A)</i>	176
<i>Figure 6.9 Full Maglev model simulation results gap vs. time</i>	177
<i>Figure 6.10 Simulink non-linear model of the ODU Maglev Plant</i>	178
<i>Figure 6.11 Gap response of the actual ODU Maglev vehicle</i>	179

NOMENCLATURE

α	- vector of ODU Maglev rigid body center of mass displacements
α	- pole due to current feedback
Σ	- Test Rig pivot degree-of-freedom
γ	- threshold for the optimal solution
ε	- induced voltage in the coil
ε_H	- epsilon (small number ≈ 0)
ϕ	- ODU Maglev vehicle roll angle
ψ	- ODU Maglev vehicle yaw angle
ζ_{vi}	- ODU vehicle damping components
ζ_{Ti}	- ODU track damping components
θ	- ODU Maglev vehicle pitch angle
Φ	- flux
Φ_{LP}	- poles flux losses
Φ_{LY}	- yoke flux losses
Φ	- mode shape matrix
Φ_V	- vehicle mode shape matrix
Φ_T	- track mode shape matrix
A_i	- skew symmetric position operator matrix (for a single magnet)
A_V	- vehicle stiffness matrix
A_T	- track stiffness matrix
μ_0	- air permeability ($\mu_0 = 4 \cdot \pi \cdot 10^{-7} \left[N / A^2 \right]$)
μ_1 and μ_2	- electromagnet core permeability (upper and lower piece)
ω_{vi}	- vehicle natural frequencies ($i=1..9$)
ω_{Ti}	- track natural frequencies ($i=1..9$)
a	- filters brake frequency
A	- state space matrix A

A_R	- sub-matrix (rigid) of the state space matrix A
\tilde{A}	- state space matrix A for full Maglev model (with CID and electromagnet)
A'_{K_i}	- sub-matrix (due to electromagnet) of the state space matrix \tilde{A}
A'_R	- sub-matrix (rigid) of the state space matrix \tilde{A}
A_V	- sub-matrix (vehicle flexibility) of the state space matrix A
A_T	- sub-matrix (track flexibility) of the state space matrix A
A_{CL}	- closed loop matrix A
A_{CID}	- sub-matrix (CID) of the state space matrix A
b	- filters brake frequency
B	- electromagnetic field
B	- state space matrix B
\tilde{B}	- state space matrix B for full Maglev model (with CID and electromagnet)
c	- filters brake frequency
c_1	- modeled Test Rig damping
c_2	- modeled Test Rig damping
c_3	- modeled Test Rig damping
C	- state space matrix C
C_D	- generalized damping matrix
$Comp_i$	- compensator designed for ODU Maglev vehicle ($i=1..4$)
C_R	- state space matrix corresponds to a velocity states
\tilde{C}	- state space matrix C for full Maglev model (with CID and electromagnet)
$C(s)$	- compensator transfer function
d	- depth of the electromagnet
d	- vector of disturbances signal
D	- state space matrix D
\tilde{D}	- state space matrix D for full Maglev model (with CID and electromagnet)

D_D	- generalized damping matrix
D_V	- vehicle damping matrix
D_T	- track damping matrix
E_{cov}	- signal error covariance
e_i	- Test Rig frame dimensions
e_{ss}	- steady state error
F	- generalized force input matrix
f_i	- magnetic force component
F_{LEV}	- levitation electromagnetic force
F_{LAT}	- lateral electromagnetic force
g	- gravity
$G_{ec}(s)$	- electromagnetic circuit transfer function
$G_{wash}(s)$	- wash filter transfer function
$G_{Leak}(z)$	- leaky integrator transfer function
$G_{LP}(z)$	- generalized low pass filter transfer function
$g_m(z)$	- merging filter transfer function
$G(s)$	- maglev model transfer function
$G_{openloop}(s)$	- maglev open-loop transfer function
$G_{closedloop}(s)$	- maglev closed-loop transfer function
H	- input matrix for measurement noise
$H_B(s)$	- Butterworth filter transfer function
$H_{Ch2}(s)$	- Chebyshev filter type II transfer function
h_m	- the pole electromagnet pole height
$H_N(s)$	- Notch filter transfer function
I	- current
I^{Cmd}	- current command
I_0	- current reference value
I^{OFF}	- currentoffset

J	- Test Rig model main body inertia
\bar{J}	- Test Rig model inertia
J_i	- test rig frame components inertia
J_{frame}	- test rig frame inertia
J_V	- matrix of the vehicle inertia
K	- generalized stiffness matrix
k_1	- modeled Test Rig stiffness
k_2	- modeled Test Rig stiffness
k_3	- modeled Test Rig stiffness
K_a	- amplifier feedback gain
k_{BI}	- flux density linearized coefficient i.r.t current
k_{BZ}	- flux density linearized coefficient i.r.t current
K_D	- derivative gain
K_I	- integrator gain
k_I	- levitation force linearized coefficient i.r.t current
K_P	- proportional gain
k_Φ	- flux feedback gain
$k_{\Phi I}$	- flux linearized coefficient i.r.t current
$k_{\Phi Z}$	- flux linearized coefficient i.r.t current
k_Z	- levitation force linearized coefficient i.r.t gap
L	- inductance
l_1, l_2	- length of the upper and lower electromagnet parts
m_1	- Test Rig track weight
m_2	- Test Rig track holder weight
m_2'	- Test Rig track holder weight (when inertia the frame counts)
m_{Cbeam}	- mass of C beam (Test Rig frame component)
m_{Cbeams}	- mass of C beams (Test Rig frame components)
m_{frame}	- mass of the Test Rig frames

M	- Test Rig rear mass
\overline{M}	- Test Rig model mass
M_V	- matrix of the vehicle weight
$M_{Weights}$	- applied load to the Test Rig
N	- turns of wire to create an electromagnet
N_f	- number of flexible modes
N_F	- order of the filter
R	- coil resistance
R_f	- skew symmetric position operator matrix (for a entire system)
S	- pole cross section area ($S = wd$)
V_{source}	- voltage applied to electromagnet circuit
w	- width of the electromagnet pole
x	- propulsive displacement
q_T	- track modal vector
q_V	- vehicle modal vector
y	- lateral gap (lateral displacement)
z	- vertical gap (levitation displacement)
z^{Cmd}	- gap command
z_0	- gap reference value

1. INTRODUCTION

Electromagnetism is one among many phenomena that researchers have focused on in response to society's desire to explore alternative transportation systems. One result is an approach in which an electromagnetic "cushion" replaces conventional suspension systems. Systems incorporating electromagnetic suspension are commonly referred to as Maglev (Magnetic Levitation) systems. Maglev systems are very different in nature compared to wheel suspended vehicles and exhibit behaviors that make them far more difficult to control [1]. Issues related to modeling non-linearities, uncertainties, etc. present many obstacles to designing an appropriate control law capable of achieving stable levitation and good performance. One characteristic that makes Maglev systems such as the ones considered herein more difficult to analyze and control compared to other systems is inherent instability. Moreover, very often there is a need to accomplish stable and robust levitation performance while keeping project budgets at a low level. Reducing the cost of Maglev systems is critical to the realization of their widespread implementation around the world. This dissertation explores levitation control related issues associated with characteristics typical to low cost maglev system designs. A particular focus is the interaction of levitation controllers with the characteristically flexible structures often associated with low cost guideway design. In this dissertation a generalized approach is taken: starting from Maglev modeling, through control design,

and finally control system testing. Guidelines are established which suggest favorable approaches for magnetic suspension for low cost Maglev systems.

Maglev system behavior can be characterized by experimental data or computer simulation. The application of new mathematical tools to numerical models offers the tremendous advantage of testing controllers without any impact on the real plant. Simulation studies are used in this work. In actual practice though, there are very few processes that can be modeled exactly. It is not unusual for the characteristics of a system's model to differ from the real plant behavior, which of course, is not desirable. Therefore an experimental validation is required and is presented in this work as well.

In this work a few concepts for Maglev plant modeling are introduced. As may be expected, a magnetically suspended system must be modeled to account for a variety of different external circumstances. The Maglev models shown in Chapters 3 and 5 were constructed to address possible applications of the Maglev system at Old Dominion University.

There are many available control strategies including some well known classical linear design approaches such as frequency domain design, [2]-[4] time-domain design and root-locus design [5][3]. There are methods that utilize optimization, such as the LQR approach [6]-[8] or H_∞ and μ synthesis [9]-[14]. Non-linear control design approaches [15]-[19] like back-stepping, sliding mode control [20], neural networks [21][22], genetic algorithms, and fuzzy-logic [23] controllers. All the above mentioned control strategies are applicable depending on external factors, desired properties, and different system behavior. In this dissertation several of them are presented and compared.

Generally speaking, a system is said to be robust [12] if it is capable of operating successfully in a wide range of conditions, and fails gracefully when outside of that range. This clearly desirable condition is reached not only through thoughtful controller design, but also with a firm understanding of the range of possible controllers that can provide acceptable stability and performance. Thus, in this dissertation for dealing with complex phenomena such as Maglev systems, robust performance is investigated. The robustness will be evaluated based on comparison of different control laws and model setups and their responses.

1.1 Magnetism and Maglev Systems

Magnetic phenomena have been observed since the time of the ancients [1i]¹. The first scientific study of magnets is attributed to the English physician William Gilbert, who in 1600 discovered that the Earth itself is a magnet. In 1785 the subject was taken up again, first by the Frenchman Charles Coulomb followed by Poisson, Oersted, Ampere, Henry, Faraday, Weber, and Gauss. Maxwell in his synthesis of electromagnetic theory in 1875, made major contributions to develop this field of research [24].

The first recorded vehicle to employ a magnetically levitated suspension was the “floating train” developed by Girard in 1864 and shown at the 1869 World Fair in Paris [25]. In the early 1960s, physicists at universities throughout North America, the United Kingdom, Germany and Japan began conducting Maglev transportation research. Today, electromagnetic suspension is a potential candidate in the search for alternatives to conventional means of ground transportation.

General Advantages of Magnetic Suspension include:

- High peak speed and high acceleration/braking enable average speeds three to four times the national highway speed limit of 60 m.p.h and because they may be more accessible for passengers, they offer the potential for lower door-to-door trip time than air travel for trips under about 400 miles.
- A Maglev vehicle floats along a guideway and there is no contact between the vehicle and the track. There is no need for moving parts that would wear out. Thus, in theory, the train and the track would require little or no maintenance.
- Maglev trains consume less energy compared to conventional rolling stock, due to the lack of frictional forces. Maglev vehicles need no petroleum based fuels to operate, due to the fact that such trains use repulsion and attraction of magnets and no natural resources beyond those needed to generate electric power required to drive electromagnets.

¹ When the numerical reference is followed by “i”, it means that it is a internet website reference.

- The noise level is significantly lower in Maglev compared to conventional vehicles. The only inherent noise is due to air friction, making the Maglev the quietest mass transportation system.
- Maglev systems generally use elevated guideways which provide a small disruptive footprint.

General disadvantages include the following:

- The preliminary costs of building the guideways used for Maglevs are bound to be more expensive than conventional steel railways especially in the case where the entire track has to be equipped with repulsive electromagnets.
- High-speed wheeled trains can be designed to run on a high-speed track line, and also on conventional railways for low-speed use.

Among many countries which are developing Maglev systems (China, Germany, Great Britain, Korea, United States, Japan) the leading production-ready systems developed in Japan and Germany can be used to illustrate the two main categories of Maglev. Two very different approaches to the Maglev problem have evolved [2i][3i][6i]. The two basic sub-categories are:

- Electromagnetic Suspension (EMS)
- Electrodynamic Suspension (EDS)

The German Maglev system (known as Transrapid [8][26][4i]) and HSST (Japan) [27][28][29][30][31][3i] trains are examples of the EMS approach, employing so called “attractive” levitation. The chief differences between these two EMS systems are the solutions incorporated to propel the vehicle.

- Transrapid uses a linear synchronous motor (LSM)
- HSST uses a linear induction motor (LIM)

Both EDS and EMS systems can employ either LSM (*Figure 1.1*) or LIM to propel the vehicle forward.

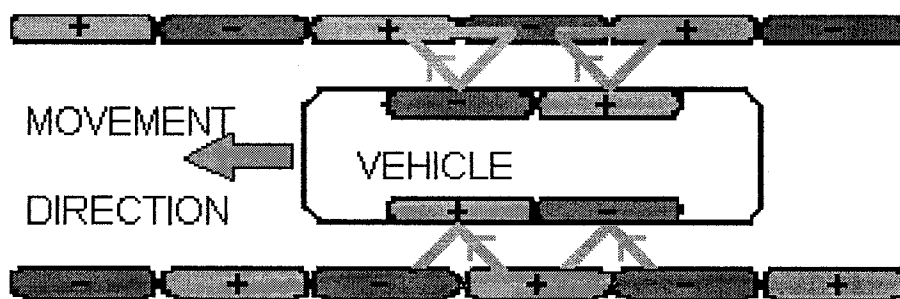


Figure 1.1 Linear synchronous motors (LSM – top view)

The LSM propulsion system, sometimes referred to as “long stator” propulsion is very much like a normal synchronous electrical motor, laid out flat along the entire length of a guideway. Using a separate set of magnetic coils inlaid in the track (not the same coils employed for EDS levitation), a carefully controlled alternating current creates a traveling magnetic wave along the track that is synchronized with the desired motion of the Maglev vehicle. This traveling magnetic wave interacts with either a separate set of on-board electromagnets (EMS vehicles) or with the same super-conducting magnetic coils utilized for levitation (EDS vehicles.) The magnetic wave is configured to create a dynamic sequence of north and south poles, which repel the vehicle away from the “back” of the track and attract it forward. This alternating magnetic field essentially travels with the Maglev train, allowing the train to accelerate quickly to high velocities. Braking is achieved by reversing the current.

“Short-stator” propulsion systems typically use a linear induction motor onboard the vehicle and a passive guideway. The “short-stator” propulsion system reduces guideway costs, but the LIM is heavy and reduces vehicle payload capacity. An unequivocal answer to the question of which approach is more effective in practical applications is currently unknown.

Attractive levitation (EMS) is considered to be a simpler concept than the EDS system. In the EMS approach, the bottom of the Maglev train has appendages (referred to here as “hockey sticks”) that wrap around a ferromagnetic (steel) track. Powerful electromagnets attached to the hockey sticks, as shown in Figure 1.2, are attracted upwards to the underside of the steel guideway, lifting up the entire train. Since the attractive force increases as the distance between magnet and the track decreases, the

EMS system is inherently unstable and requires feedback control to maintain a proper gap between the magnets and steel. The control system regulates electric current flowing through the electromagnets to maintain a fixed gap between the magnets and the track. Guidance magnets stabilize the vehicle laterally, keeping it centered on the guideway. In some applications active stabilization is included for lateral positioning. However, there have been several EMS vehicles, in which passive control realized by the levitation electromagnets is sufficient for keeping the vehicle in the centerline position with respect to the guideway [8][29] (the effectiveness of this approach can be evaluated from static analysis). For a schematic of an EMS Maglev design, *see Figure 1.2.*

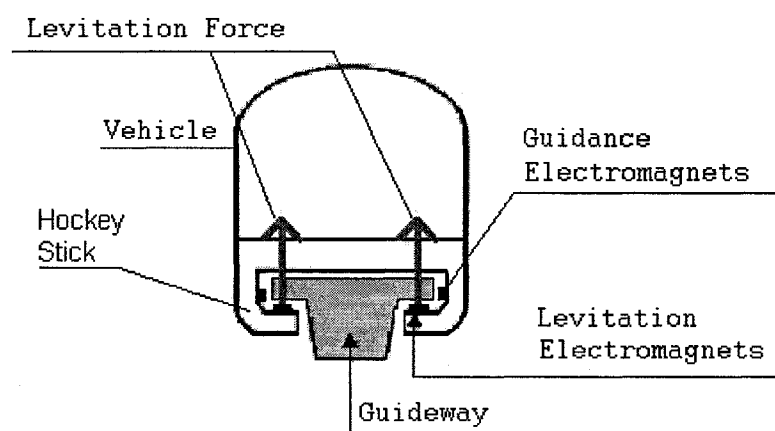


Figure 1.2 Electromagnetic suspension (EMS)

Among the distinct advantages of the EMS system is the use of conventional electromagnets rather than the high-tech super-conducting magnets employed by EDS systems. EMS levitation consumes less energy than EDS systems. Additionally, in contrast to EDS, the EMS Maglev trains can levitate at zero speed, which is a useful feature for loading and unloading passengers. The EMS approach, however, is afflicted with some significant obstacles. As already noted a major disadvantage of EMS systems is that they are inherently unstable systems. The gap between the track and the vehicle generally has to be in a range between 0.01 – 1 inches. Unfortunately, in general the size of the gap cannot be increased without incurring unacceptable increases in power

consumption. For this reason, EMS guideways often require a relatively high degree of precision in construction, which greatly increases their cost [32].

EDS levitation is contingent upon train movement. To levitate, an EDS train must reach a critical speed, typically of approximately 60 m.p.h, for example by rolling on rubber wheels. Once the critical speed is achieved the changes in flux induces currents in track mounted coils, creating magnetic forces. The Electrodynamics Suspension (EDS) which has been tested in Japan's Yamanashi Line, is a "repulsive" levitation system (*Figure 1.3*). In EDS systems, the repulsive forces between super-conducting electromagnets mounted on the undercarriage of the vehicle and aluminum plates fixed to the guideway are used to levitate the vehicle.

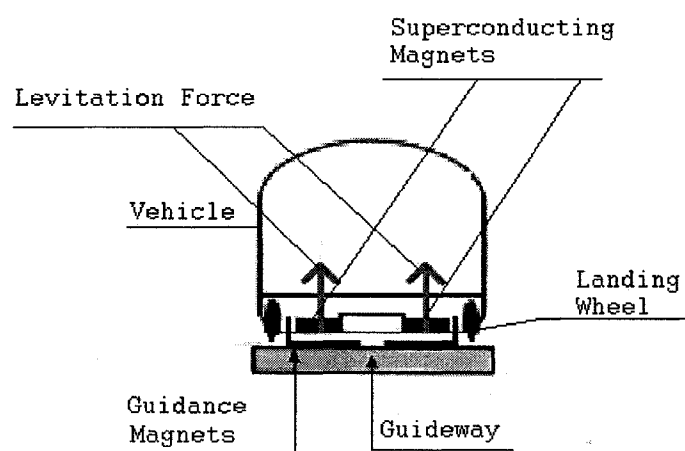


Figure 1.3 Electrodynamics suspension (EDS)

As previously mentioned with regard to the EDS system, these same on-board magnets and levitation coils provide lateral guidance to the vehicle. When a Maglev vehicle containing the super-conducting magnets displaces laterally, the magnetic field running through the loops changes, inducing current in the loops. The magnetic fields produced by this induced current are different from the magnetic fields that allow the train to levitate. Instead, the levitation coils on the sidewall that the train is approaching exert a repulsive force and the coils on the other sidewall exert an attractive force. Thus, the moving Maglev train stays centered in the guideway. Moreover, EDS configurations are inherently stable.

However, the EDS approach suffers from its own afflictions. Super-conducting magnets require elaborate and expensive cooling systems, since super-conductors function only at very low temperatures. Furthermore, EDS trains must be shielded with heavy iron to protect the vehicle passengers from the high-powered electromagnetic field generated by these magnets. Finally, EDS vehicles must be equipped with wheels or other forms of support for takeoff and landing because the EDS will not levitate at speeds below approximately 60 m.p.h.

Nevertheless, some experts consider EDS systems to be the most promising approach to problem of achieving high speed Maglev transportation, for example the EDS Yamanashi system holds the current (year 2006) world speed record. Recent research in super-conducting materials offers the potential for further upgrading and developing repulsive Maglev systems. The acceptable air gap for an EDS system is generally much larger than that necessary for EMS systems. This large levitation height requires less precision in guideway construction, which in turn allows such vehicles to operate in severe climates.

The system envisioned for implementation at Old Dominion University (ODU) is an EMS design. This design choice was a result of the presumed lower cost of an EMS design and the fact that vehicle can levitate at low speed in this design approach. For these reasons this dissertation will only consider design approaches for EMS systems.

1.2 Motivation

“We may perhaps learn to deprive large masses of their gravity and give them absolute levity, for the sake of easy transport.”

-Benjamin Franklin

Like many other projects, this dissertation subject was motivated by a real need. Old Dominion University is doubly involved in a Magnetic Levitation Transportation System project, as both a host and more recently as a participant in the research. The

electromagnetic suspension system at ODU was designed to be a low cost project with respect to existing Maglev systems across the world.

The outstanding issue during the implementation of the Old Dominion University Maglev turned out to be levitation stability. Levitating the vehicle above the track while maintaining the constant gap necessary for operation was not achieved in the initial effort. An appropriate model of the track and vehicle with correctly assumed uncertainties is required to enable analytical calculations in support of successful application of control laws with stable characteristics. The problem associated with the interaction between the vehicle and the guideway is important not only from the standpoint of stability, but also for economic reasons. The cost of the guideway structure is expected to be roughly 60-80% of the initial capital required for a Maglev project [32]. An optimal guideway design is essential for a high speed Maglev system with good ride quality. As the speed of the vehicle increases to 200-400 m.p.h, or when the track becomes lighter to reduce its cost, the dynamic interaction between the vehicle and the guideway plays a dominant role in establishing vehicle suspension requirements and specifications for a magnetic suspension system. The related issue of the Maglev system flexibility, which is evaluated in this dissertation, involves the interaction of the Maglev vehicle with the guideway. This interaction changes with the vehicle position on elevated guideways.

This overall situation led to the decision to develop appropriate system models and to investigate a range of controller designs with the goal of determining which design would be best able to stabilize the system and make it more robust.

Magnetic suspension is an emerging technology [4i],[5i],[6i], with overwhelming benefits applicable not only to the transportation industry but also to several other industries and research areas including:

- Wind tunnel magnetic suspension and balance systems [13][33],
- Micro gravity and vibration isolation systems, [8i]
- Magnetic bearings [33][34][35],
- Space applications, [36][8i][7i]
- Biomedical applications,[10i]
- Magnetic weapon applications,[7i][9i]

After carefully considering the statements above, it was decided to participate in the Maglev stability investigation process by taking this subject as a dissertation research topic.

1.3 Dissertation Statements

In this dissertation, an investigation is carried out to evaluate and compare different control strategies applied to EMS based Maglev systems such as the ODU Maglev vehicle. For these situations, both experimental results and simulation (supported by analytical calculation) are presented.

The investigation identifies the causes of the stability problems previously encountered in applications at ODU and provides an analytical basis for possible solutions. Different compensators are applied and compared regarding robustness and performance. A theme explored in this dissertation is a comparison between decentralized control strategies and centralized control laws. Another theme explored is the flexibility of the vehicle and of the track, and what impact this has on the Maglev system's stability. The final consideration is an investigation of several different feedback and compensator combinations in an effort to optimize performance in the Maglev application.

Modeling procedures are presented for complex multivariable systems based on finite element data. Analytical transformation from finite element output data to state space and transfer function form is shown in this work. A model of the U-shaped electromagnet (used on the ODU Maglev vehicle) and the electromagnetic force it produces are calculated. Two different current amplifiers driving these electromagnets are modeled and their characteristics validated via experiment.

In this dissertation, example simulations for each approach are presented and comparisons between some of the different control approaches listed above are shown to illustrate the nature of the problems. Each solution approach considered is introduced as a basic model and progresses toward a more complex system. Several possible solutions are expounded upon. Some proposed compensators are tested experimentally on the one-degree of freedom ODU Maglev test-rig. The most conservative approach is tested on the ODU Maglev vehicle.

2. FUNDAMENTAL MODELING AND STABILITY ANALYSIS

In this chapter simple models of Maglev systems are developed. First, to provide a base for the more detailed modeling efforts in Chapter 3, electromagnetic modeling of Maglev systems is reviewed. The interaction of the electromagnetic actuators with structural models of progressively increasing complexity is considered. Then stability of simple PD controllers is evaluated with regard to these models. The results suggest basic guiding principles for Maglev controller design.

2.1 Electromagnetic Circuit

In the literature [25][26][37][38][39][40] at least two forms of the magnetic force expressions can be found. These equations differ somewhat due to the associated approximations. In this work, these two magnetic force expressions are referred to as Limbert's [37][38] approach and Davey's [26][40] approach, after the authors of the citations where the expressions appear. In this chapter both formulations will be reviewed and compared.

2.1.1 Electromagnetic Force for Uniform Magnetic Field

Consider two U-shaped pieces of iron as illustrated in *Figure 2.1*. Let each pole have uniform cross sectional area S , and mean lengths l_1 and l_2 , corresponding to the upper piece (track) and lower piece (magnet) respectively. These two sections are separated by a small gap of thickness z . The lower section is wound with N turns of wire to create an electromagnet. The current I flows in the coil. The permeabilities of the upper and lower parts are assumed constants, μ_1 and μ_2 . In this case the total uniform flux density in the cross section of the circuit of *Figure 2.1* is given by [24]:

$$\Phi = \frac{NI}{\frac{l_1}{\mu_1 S} + \frac{l_2}{\mu_2 S} + \frac{2z}{\mu_0 S}} \quad (2.1)$$

where $S = wd$.

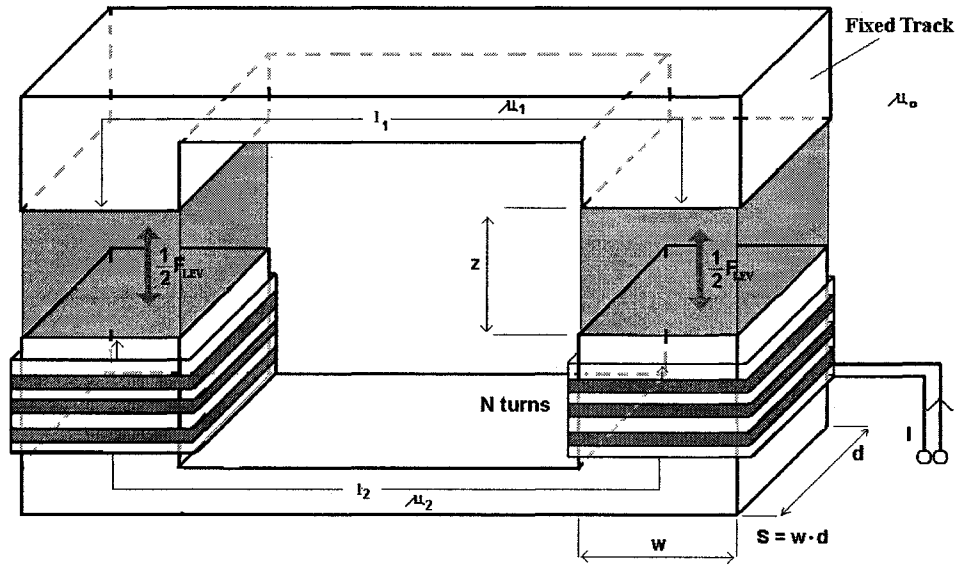


Figure 2.1 U shaped electromagnet with uniform magnetic field

The inductance of the coil under the given condition is

$$L = \frac{N\Phi}{I} = \frac{SN^2}{\frac{l_1}{\mu_1} + \frac{l_2}{\mu_2} + \frac{2z}{\mu_0}} \quad (2.2)$$

since the flux density Φ links N turns. If the lower U-section is displaced by an amount Δz in the time interval Δt , then, assuming constant current, the flux density Φ changes. According to Faraday's law this results in an induced voltage ε in the coil, where:

$$\varepsilon = -N \frac{d\Phi}{dt} \bigg|_{I=const.} = -I \frac{dL}{dt}. \quad (2.3)$$

In order to keep the current I constant, a voltage ε must be applied to electromagnet. This applied voltage does the following work [41]

$$dW_1 = -\varepsilon I dt = I^2 dL \quad (2.4)$$

in the time interval dt . During the displacement Δz , the energy in the magnetic field in one electromagnet pole changes by an amount:

$$dW_m = I^2 \frac{dL}{2} \quad (2.5)$$

If the field exerts a force F_{LEV} on the lower U-section, a force $-F_{LEV}$ must be applied in order to increase the air gap by an amount dz . During the displacement the work done is expressed as:

$$dW = -F_{LEV} dz \quad (2.6)$$

Equating the work done on the system to the change in field energy, the following equation can be obtained:

$$dW_m = dW + dW_1 \Rightarrow -F_{LEV} dz + I^2 dL = \frac{1}{2} I^2 dL \quad (2.7)$$

and hence

$$F_{LEV} = \frac{1}{2} I^2 \frac{dL}{dz}. \quad (2.8)$$

For ferrous materials, the permeability μ typically exceeds $500 \cdot \mu_0$, thus it can be assumed that $\mu_1 \gg \mu_0$ and $\mu_2 \gg \mu_0 \Rightarrow \frac{l_1}{\mu_1} \rightarrow 0$, and also $\frac{l_2}{\mu_2} \rightarrow 0$ compared to

$\frac{2z}{\mu_0}$. Thus (2.2) becomes:

$$L = \frac{N\Phi}{I} \cong \frac{SN^2}{\frac{2z}{\mu_0}} \quad (2.9)$$

Further,

$$\frac{dL}{dz} \cong -\frac{\mu_0 S N^2}{2z^2} \quad (2.10)$$

Now, by substituting (2.11) into (2.9), equation (2.9) can be simplified into the following form:

$$F_{LEV} \cong -\frac{\mu_o N^2 I^2 S}{4z^2}. \quad (2.11)$$

Equation 2.12 expresses the magnetic levitation force as a function of two variables, gap z and current I . The negative sign in (2.11) indicates that the force is attractive under the given conditions.

$$B = \mu_o H = \frac{\mu_o NI}{2z} \quad (2.12)$$

The electromagnetic field density expressed by (2.12) is a linear function of gap to current ratio, as opposed to the quadratic proportion in (2.11).

$$\Phi = BS \quad (2.13)$$

Thus, the levitation force between an electromagnet and the track based on (2.1), (2.19) and (2.13) can be given as follows:

$$F_{LEV} = -\frac{\Phi^2}{\mu_o S} \quad (2.14)$$

This modified form of the equation (2.11) can be useful in the case when flux is used for feedback. In equation (2.12), significant simplification was achieved by assuming uniform electromagnetic flux density B in the air gap between the U-shaped sections. The effects of fringing and lateral displacement will be explored in the next section.

2.1.2 Electromagnetic Force with Fringing and Lateral Displacement

In real systems, additional electromagnetic flux fringing fields occur around electromagnet poles [26][37][39][40][41][42] as illustrated in *Figure 2.2*.

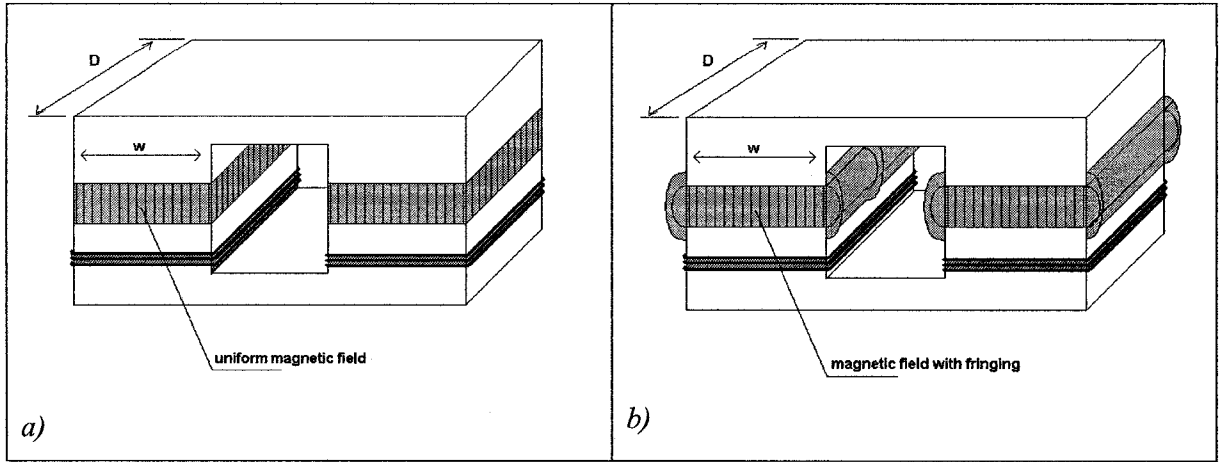


Figure 2.2 Magnetic field models for U shaped magnets, a) uniform, b) with fringing

Accounting for lateral displacement, the inductance expression for the U-shaped magnet can be variously expressed [26][38][43][44][45] as:

$$L_{Davey}(z, y) = \frac{1}{2} \mu_0 d N^2 \left[\frac{w - y}{z} + \frac{4}{\pi} \cdot \ln \left(1 + \frac{\pi y}{4z} \right) \right] \quad (2.15)$$

$$L_{Limbert}(z, y) = \frac{1}{2} \mu_0 d N^2 \frac{\left[-\pi w - 2z \ln \left(\frac{1}{z} \right) + 2ya \tan \left(\frac{y}{z} \right) - z \ln \left(\frac{z^2 + y^2}{z^2} \right) \right]}{z \cdot \pi} \quad (2.16)$$

The first expression, due to Davey, is simplified through the exclusion of fringing effects. The second expression, due to Limbert, includes an approximate expression for the fringing field.

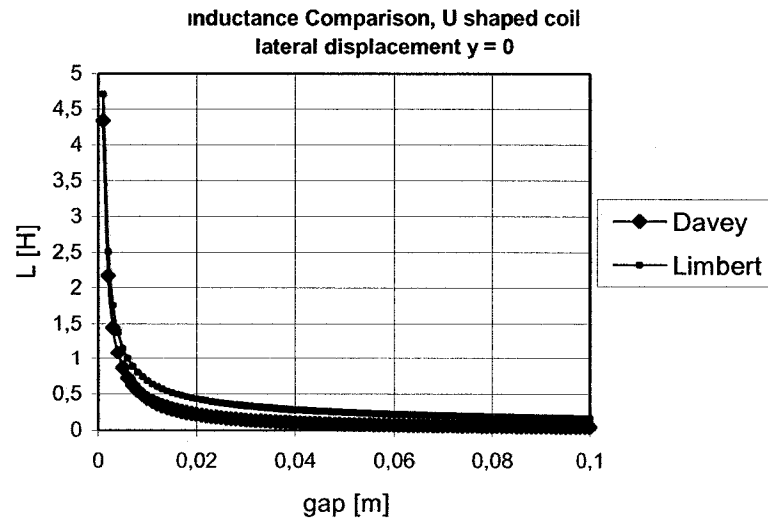


Figure 2.3 Inductance comparison for two different inductance expressions

In these expressions, μ_0, d, N, w are as used in the previous text: respectively permeability, coil length, number of turns, and width of the coil. To obtain analytical curves shown in *Figure 2.3*, the following parameters were used:

VARIABLE	VALUE
Permeability μ_0	$4\pi \cdot 10^{-7}$ N/A
Coil width w	2.007 in.
Coil depth d	15 in.
Number of coil turns N	2·(298)
Lateral displacement y	0 in.

Table 2.1 Electromagnet parameters

Based on the Limbert expression for the inductance L (2.16) and with an assumed gap of $z = 0.4$ [in], which is the nominal stable operating position for the Maglev test-rig and ODU Maglev vehicle, the levitation force and guidance (lateral) force can be evaluated using (2.9) [26][39][40][46] as:

$$F_{LEV} = \frac{1}{2} \frac{\partial}{\partial z} [L(z, y)] I^2 \quad (2.17)$$

$$F_{LAT} = \frac{1}{2} \frac{\partial}{\partial x} [L(z, y)] I^2 \quad (2.18)$$

After substitution of equations (2.15) and (2.16) into (2.17) and (2.18), final levitation and lateral force expressions, respectively due to Davey and Limbert approaches, become:

$$F_{LEV \text{ Davey}} = \frac{1}{4} \mu_0 d N^2 I^2 \left[-\frac{w-y}{z^2} - \frac{4y}{4z^2 + \pi zy} \right] \quad (2.19)$$

$$F_{LAT \text{ Davey}} = \frac{1}{4} \mu_0 d N^2 I^2 \left[-\frac{1}{z} + \frac{4}{4z + \pi y} \right] \quad (2.20)$$

$$F_{LEV \text{ Limbert}} = \frac{1}{4} \frac{\mu_0 N^2 I^2 dw}{z^2} \left\{ 1 + \frac{2z}{\pi w} \left[1 - \frac{y}{z} a \tan\left(\frac{y}{z}\right) \right] \right\} \quad (2.21)$$

$$F_{LAT\ Limbert} = \frac{\mu_0 N^2 I^2 d}{2\pi z} a \tan\left(\frac{y}{z}\right) \quad (2.22)$$

It can be observed that both levitation force expressions (2.19) and (2.21) reduce to equation (2.11), by neglecting lateral displacement y for Davey's case (2.19), or by neglecting lateral displacement y and fringing field factor $\left(\frac{2z}{\pi w}\right)$ in the Limbert force expression (2.21). It is clear that these two methods of computation give substantially different results in the region of interest.

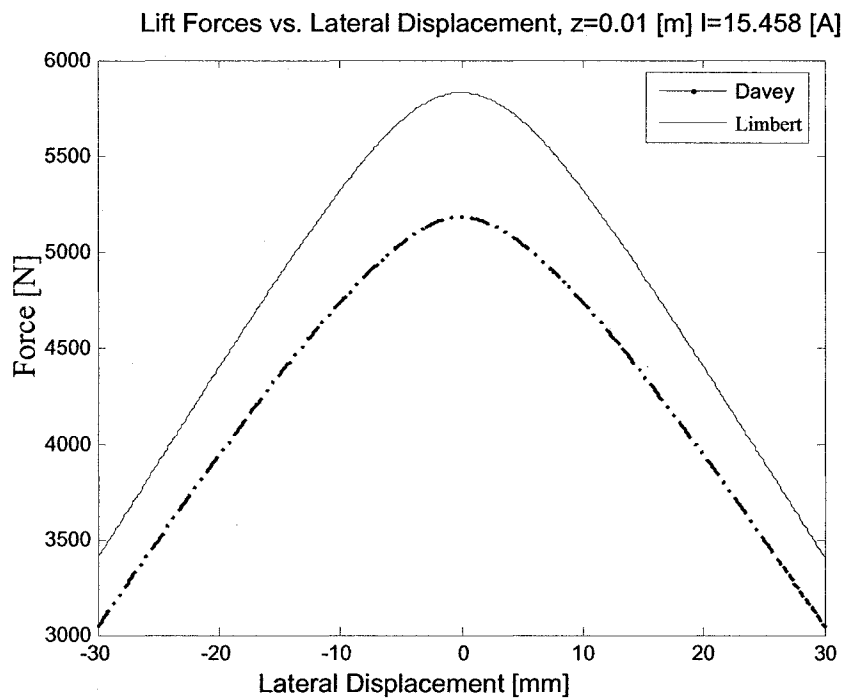


Figure 2.4 Analytical lift force comparison

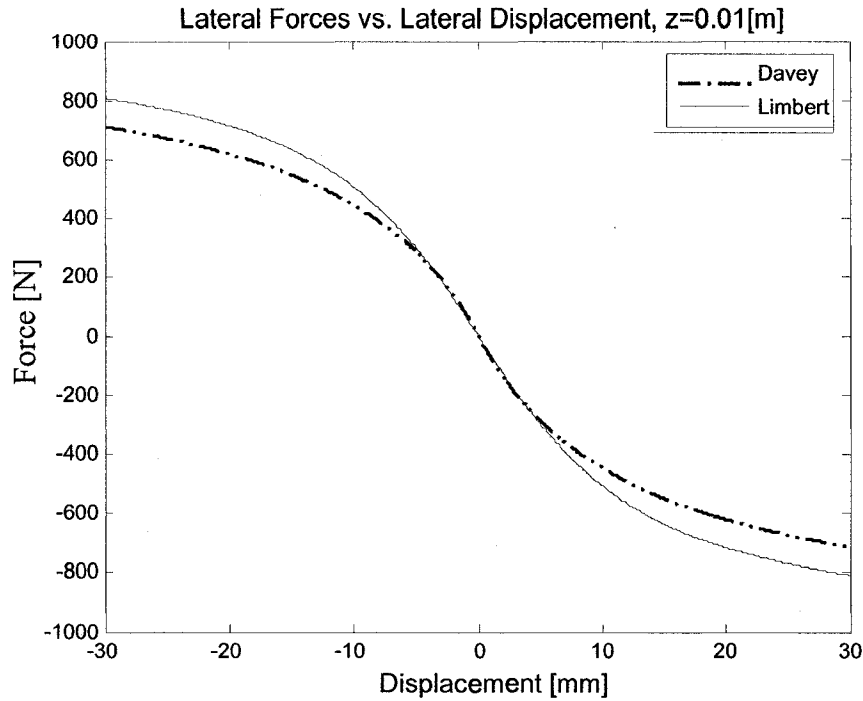


Figure 2.5 Analytical lateral force comparison

Evaluation of the lateral force as a result of lateral offset did not show significant variation as can be seen in *Figure 2.5*. Both methods match better than they do for the levitation force expressions *Figure 2.4*. As is illustrated, only for large gaps (greater than 1 [in.]) where the error of 50 [N] in the range of span of 2000 [N] ($\sim 4\%$) is the difference visible. For operational conditions (gap around 0.4 in.) the curves for lateral force nearly match.

Due to its dependence on geometry (*Figure 2.3*) coil inductance has significant influence not only on the levitation force but also has an impact on the system dynamic behavior, determining the limiting rate of current variation. These issues will be explored in the following chapters.

Since the discrepancy between levitation force expressions was around 12% (see *Figure 2.4*), an electromagnet was tested experimentally and based on these results Limbert force form was chosen.

2.1.3 Coil Dynamics as a Result of Inductance

Dynamic behavior of the electromagnet can be expressed using Maxwell's law of electromagnetism along with Faraday's self-inductance equation. Considering the magnet as a single conducting circuit around which a current I is flowing, a magnetic field B is generated which gives rise to a magnetic flux Φ linking the circuit. We expect the flux to be directly proportional to the current I (eq. 2.1) with inductance L as a proportional coefficient. The inductance of a circuit is measured in units of Henrys, which is a purely geometric quantity, depending only on the shape of the circuit and number of turns in the circuit (eq. 2.13, 2.14).

If the current flowing around the circuit changes by an amount ΔI in a small time interval Δt , then the magnetic flux linking the circuit changes by an amount

$$\Delta\Phi = \frac{L}{N} \cdot \Delta I \quad (2.23)$$

in the same time interval. According to Faraday's law (2.3) together with (2.18), the electromotive force (emf) voltage on the coil can be written:

$$V_{emf} = N \frac{d\Phi}{dt} = \frac{d(LI)}{dt} = L(z, y) \frac{dI}{dt} + I \frac{dL}{dt} \quad (2.24)$$

The emf generated around the circuit due to the current is a function of current rate and inductance. Because of the existing resistance R in the circuit, (2.19) becomes:

$$V_{source} - IR = L(z, y) \frac{dI}{dt} + I \frac{dL}{dt}, \quad (2.25)$$

Then applying (2.9)

$$V_{source} - IR = \frac{\mu_0 S N^2}{2z} \frac{dI}{dt} - \frac{\mu_0 S N^2 I}{2z^2} \frac{dz}{dt} \quad (2.26)$$

Equation (2.26) can be used to simplify the linearization procedure. It leads to the same linearization coefficients for current and force expressions (see section 2.2).

2.1.4 Simplified Electromagnet Model

In actual applications, a current amplifier is required. To drive the current to the coil, modern current amplifiers are generally switching devices; however, in the interest

of simplicity, the current amplifier is modeled as a constant gain K_a with a current feedback loop using feedback gain. With these assumptions the current in the electromagnet is related to a current commanded as shown in *Figure 2.6*.

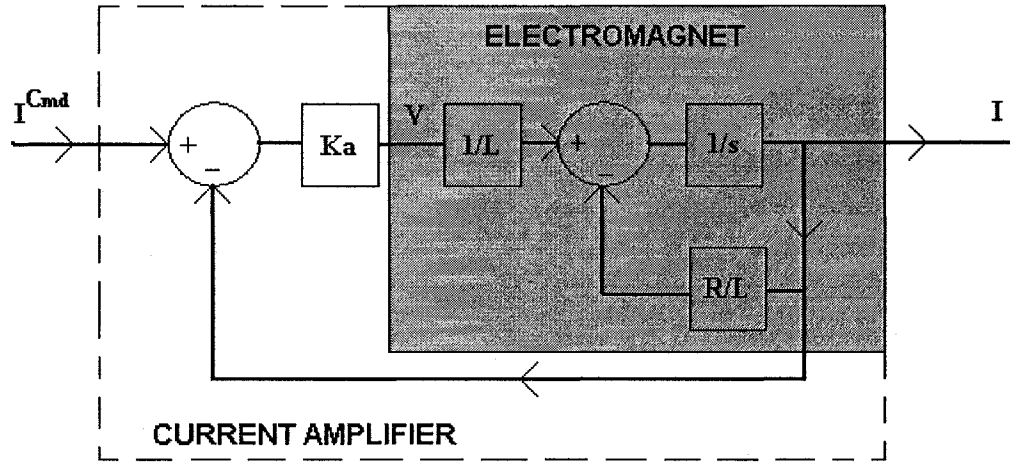


Figure 2.6 Electromagnet circuit model

Based on this model, the governing equation of the electromagnet circuit can be expressed as:

$$\frac{dI}{dt} = \frac{I^{Cmd} K_a - I(K_a + R)}{L(z, y)} \quad (2.27)$$

where K_a is the amplifier feedback gain.

Assuming that inductance L is constant, the following transfer function relating the current command to the current response can be obtained from (2.21):

$$G_{ec}(s) = \frac{\frac{K_a}{L}}{s + \frac{K_a + R}{L}} \quad (2.28)$$

This transfer function (2.22) represents the Maglev actuator, a combination of the amplifier with the coil inductance. It is important to note that the combination of the amplifier feedback gain K_a and coil resistance R introduces a left half plane pole. Thus large values of K_a move the amplifier pole toward the more stable region.

In actuality, the response current slew rate is also limited as a result of coil inductance. The current slew rate $\frac{dI}{dt}$ is limited, above and below, as follows:

$$\left. \frac{dI}{dt} \right|_{\max} = \frac{V_{\text{source}}}{L} \quad (2.29)$$

$$\left. \frac{dI}{dt} \right|_{\min} = \frac{-V_{\text{source}}}{L} \quad (2.30)$$

These limits cause saturation in the current signal, the effect of which is explored later sections.

2.2 Linearization

Because of the non-linearities in equations (2.16) and (2.17) linearization is required to obtain a state space system model. Assuming small deviations from a nominal operating condition, linearized models can be appropriate. Thus, for further analysis, equation (2.17) will be linearized with respect to reference values for gap z_0 and current I_0 , using the first derivative components from the Taylor series expansion [47]:

$$F_{LEV} \cong F_{LEV} \Big|_{I_0}^{z_0} \frac{\partial F_{LEV}}{\partial z} \Big|_{I_0}^{z_0} (z - z_0) + \frac{\partial F_{LEV}}{\partial I} \Big|_{I_0}^{z_0} (I - I_0) \quad (2.31)$$

where

$$\frac{\partial F_{LEV}}{\partial z} = \frac{1}{2} \frac{\mu_0 N^2 d w I_0^2}{z_0^3} \left(1 + 2 \frac{z_0}{\pi w} \right) - \frac{\mu_0 N^2 d I_0^2}{2 \pi z_0^2} = k_z \quad (2.32)$$

$$\frac{\partial F_{LEV}}{\partial I} = -\frac{1}{2} \frac{\mu_0 N^2 d w I_0}{z_0^2} \left(1 + 2 \frac{z_0}{\pi w} \right) = -k_i \quad (2.33)$$

According to equations (2.24) the linearized form of levitation force is:

$$F_{LEV} = k_z z - k_i I \quad (2.34)$$

Linearization of (2.26) can be carried out in the similar way [25][48][49], if L refers to inductance linearized around the operation point, z_0 .

$$L \Big|_{z=z_0, y=y_0=0} = \frac{\mu_0 S N^2}{2 z_0} \quad (2.35)$$

$$V - IR = \frac{\mu_0 S N^2}{2 z_0} \frac{dI}{dt} - \frac{\mu_0 S N^2 I_0}{2 z_0^2} \frac{dz}{dt} \quad (2.36)$$

by utilizing (2.32)(2.33) equation (2.36) can be expressed as:

$$\frac{dI}{dt} = \frac{k_z}{k_i} \frac{dz}{dt} - \frac{IR - V}{L} \quad (2.37)$$

After the current amplifier is incorporated in the electromagnet circuit equation (2.28) becomes

$$\frac{dI}{dt} = \frac{k_z}{k_i} \frac{dz}{dt} + \frac{I^{Cmd} K_a - I(K_a + R)}{L} \quad (2.38)$$

Note that the equations above differ from these presented in [25][49]. This difference results from the inclination of the current amplifier model which is not present in the reference sources.

2.3 Maglev as a Rigid Mass

Consider a simple one-degree-of-freedom rigid model of the Maglev system (*Figure 2.7*).

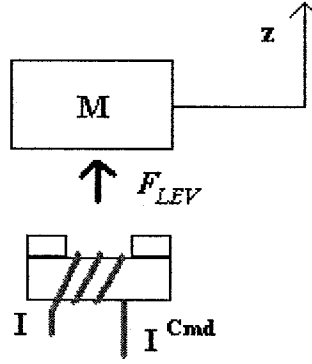


Figure 2.7 Simple Maglev system

Equations of motion for the system shown above based on (2.34) and (2.37) become:

$$\frac{d^2 z}{dt^2} = \frac{k_z}{M} z - \frac{k_i}{M} I \quad (2.39)$$

$$\frac{dI}{dt} = \frac{k_z}{k_i} \frac{dz}{dt} + \frac{I^{Cmd} K_a - I(K_a + R)}{L(z, y)} \quad (2.40)$$

In standard state-space form

$$\begin{aligned} \dot{\vec{x}} &= A \cdot \vec{x} + B \cdot \vec{u} \\ \vec{y} &= C \cdot \vec{x} + D \cdot \vec{u} \end{aligned} \quad (2.41)$$

the equations of motion for the rigid system are expressed as:

$$\begin{bmatrix} \dot{z} \\ \ddot{z} \\ \dot{I} \end{bmatrix} = \begin{bmatrix} 0 & 1 & 0 \\ \frac{k_z}{M} & 0 & -\frac{k_i}{M} \\ 0 & \frac{k_z}{k_i} & -\frac{(K_a + R)}{L} \end{bmatrix} \begin{bmatrix} z \\ \dot{z} \\ I \end{bmatrix} + \begin{bmatrix} 0 \\ 0 \\ \frac{K_a}{L} \end{bmatrix} I^{Cmd}$$

$$[z] = \begin{bmatrix} 1 & 0 & 0 \end{bmatrix} \begin{bmatrix} z \\ \dot{z} \\ I \end{bmatrix}; \quad (2.42)$$

The basic schematic of the system (2.42) is shown in Figure 2.8. [25][49]

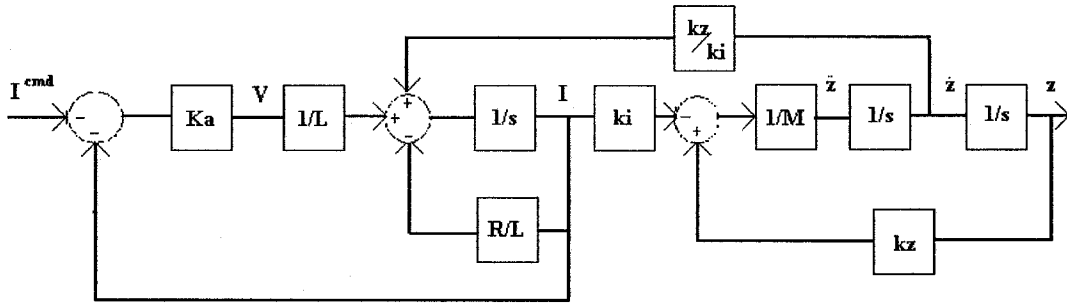


Figure 2.8 Block diagram of a 1DOF Maglev rigid system

Then based on (2.42) the transfer function can be calculated:

$$G_{rigid}(s) = \frac{-K_x}{(s-p)(s+p)(s+\alpha)} = \frac{-K_x}{(s^2 - p^2)(s+\alpha)} \quad (2.43)$$

where

$$K_x = K_a \frac{k_i}{L} \quad (2.44)$$

$$\alpha = \frac{K_a + R}{L} \quad (2.45)$$

$$p \cong \sqrt{\frac{k_z}{M}} \quad (2.46)$$

The system has three real poles. One is positive, which is indicative of the inherent instability of the attractive types of Maglev systems. The pole α is associated with current feedback (2.28). The pair $\pm p$ represents the rigid body motion of the structural model. The value of p can vary significantly with gap and current as shown in (2.46).

2.4 Stability of the Rigid Case Under PD Control

Since the rigid model of the Maglev system (2.43) has a positive pole, feedback compensation is required to render the closed-loop system stable [25][50][51].

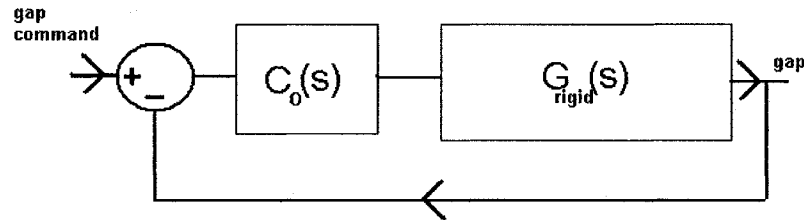


Figure 2.9 Block diagram of the Maglev control loop

Here a PD compensator is considered in the form:

$$C_o(s) = K_p + K_D s \quad (2.47)$$

The closed-loop transfer function is:

$$G^{CL}(s) = \frac{C_o(s)G(s)}{1 + C_o(s)G(s)} \quad (2.48)$$

Substituting (2.43) and (2.47) into (2.48)

$$G_{rigid}^{CL}(s) = \frac{-K_x(K_p + K_D s)}{s^3 + s^2 \alpha - s(p^2 + K_x K_D) - (p^2 \alpha + K_x K_p)} \quad (2.49)$$

The sufficient conditions for the stability of this system are determined using the Routh criterion [3].

$$K_D < \frac{-p^2}{K_x} \quad (2.50)$$

$$K_P < \frac{-p^2 \alpha}{K_x} \quad (2.51)$$

$$K_P > K_D \alpha \quad (2.52)$$

As can be seen the compensator gains must be negative for stability, which is to say that positive feedback is necessary.

2.5 Maglev as SISO Flexible System

As a first step toward evaluation of the impact of structural flexibility on control of a Maglev system, a single flexible mode of the vehicle is introduced through the modification of (2.39) [52][53][54]. The new structure is shown in the *Figure 2.10*.

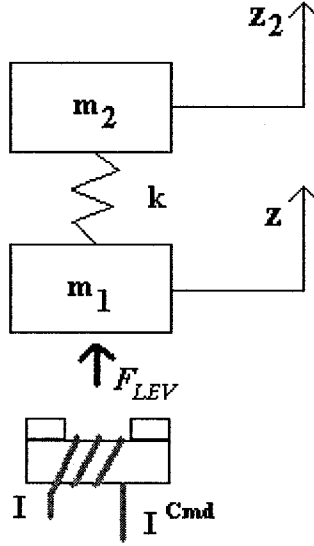


Figure 2.10 Model of the flexible SISO Maglev

In this system $m_1 + m_2 = M$ still represents the overall weight of the Maglev vehicle. The actuator model equation remains the same. The spring constant k represents the flexibility of the vehicle. The displacement resulting from structural flexibility is denoted by z_2 , while the electromagnetic air gap is denoted by z . The new equations of motion become:

$$\frac{d^2 z}{dt^2} = \frac{k_z - k}{m_1} z + \frac{k}{m_1} z_2 - \frac{k_i}{m_1} I \quad (2.53)$$

$$\frac{d^2 z_2}{dt^2} = \frac{k}{m_2} z - \frac{k}{m_2} z_2 \quad (2.54)$$

$$\frac{dI}{dt} = \frac{I^{Cmd} K_a}{L} - I\alpha \quad (2.55)$$

Similar to the notation of the rigid case, the following notation is introduced:

$$\omega_1^2 = \frac{k}{m_1} \quad (2.56)$$

$$\omega_2^2 = \frac{k}{m_2} \quad (2.57)$$

$$p_z^2 = \frac{k_z}{m_1} \quad (2.58)$$

The state space form of (2.39) is:

$$\begin{bmatrix} \dot{z} \\ \dot{z}_2 \\ \ddot{z} \\ \ddot{z}_2 \\ \dot{I} \end{bmatrix} = \begin{bmatrix} 0 & 0 & 1 & 0 & 0 \\ 0 & 0 & 0 & 1 & 0 \\ p_z^2 - \omega_1^2 & \omega_1^2 & 0 & 0 & -K_x \frac{L}{K_a} \\ \omega_2^2 & -\omega_2^2 & 0 & 0 & 0 \\ 0 & 0 & 0 & 0 & -\alpha \end{bmatrix} \begin{bmatrix} z \\ z_2 \\ \dot{z} \\ \dot{z}_2 \\ I \end{bmatrix} + \begin{bmatrix} 0 \\ 0 \\ 0 \\ 0 \\ \frac{K_a}{L} \end{bmatrix} I^{Cmd} \quad (2.59)$$

The C matrix (2.42) of the state-space representation (2.59) depends on the sensor locations. When the actuator and sensor pairs are located together, the pair is said to be collocated. With regard to the present system, the collocated case has C matrix (2.60):

$$C_c = [1 \ 0 \ 0 \ 0 \ 0] \quad (2.60)$$

The so-called non-collocated² case has:

$$C_n = [0 \ 1 \ 0 \ 0 \ 0] \quad (2.61)$$

The D matrix is zero for either case. Applying the standard transformation from state-space to transfer function form, the open loop transfer functions for collocated and non-collocated plants are [52][54]:

$$G_c(s) = \frac{-K_x(s^2 + \omega_2^2)}{s^5 + s^4\alpha + s^3(\omega_1^2 + \omega_2^2 - p_z^2) + s^2\alpha(\omega_1^2 + \omega_2^2 - p_z^2) - sp_z^2\omega_2^2 - p_z^2\omega_2^2\alpha} \quad (2.62)$$

$$G_n(s) = \frac{-K_x\omega_2^2}{s^5 + s^4\alpha + s^3(\omega_1^2 + \omega_2^2 - p_z^2) + s^2\alpha(\omega_1^2 + \omega_2^2 - p_z^2) - sp_z^2\omega_2^2 - p_z^2\omega_2^2\alpha} \quad (2.63)$$

As in the rigid case, it is observed from inspection of the transfer functions that Maglev systems can be characterized as unstable and non-minimum phase. For the non-collocated case there are no zeros, which makes the system more difficult to stabilize because relative degree for collocated system is lower than for the non-collocated analogue.

² Since the system considered has only 2 masses, this is an extreme example of non-collocation. Actual system with approximate collocation may be more forgiving

2.6 Collocated Flexible Case Under PD Control

A procedure similar to that applied to the rigid model can now be used to evaluate the flexible Maglev models expressed by (2.59). It can be shown that a collocated system's closed-loop transfer function has the form:

$$G_c^{CL}(s) = \frac{K_x (s^2 + \omega_2^2) (K_P + K_D s)}{\left[s^5 + s^4 \alpha + s^3 (\omega_1^2 + \omega_2^2 - p_z^2 - K_x K_D) + s^2 \alpha (\omega_1^2 + \omega_2^2 - p_z^2 - \frac{K_x K_P}{\alpha}) + \dots \right.} \quad (2.64)$$

$$\left. \dots + s(-\omega_2^2 p_z^2 - K_x K_D \omega_2^2) - K_x K_P \omega_2^2 - p_z^2 \omega_2^2 \alpha \right]$$

Routh array analysis yields the following conditions for closed loop stability:

$$K_D < \frac{-p_z^2}{K_x} \quad (2.65)$$

$$K_D < \frac{(-p_z^2 + \omega_1^2 + \omega_2^2)}{K_x} \quad (2.66)$$

$$K_P < \frac{-p_z^2 \alpha}{K_x} \quad (2.67)$$

$$K_P < \alpha \frac{(-p_z^2 + \omega_1^2 + \omega_2^2)}{K_x} \quad (2.68)$$

$$K_P > K_D \alpha \quad (2.69)$$

$$K_P < \alpha \frac{(-p_z^2 + \omega_1^2)}{K_x} \quad (2.70)$$

From the above conditions, as in the rigid body case, two important conclusions can be drawn:

1. Positive feedback is required (negative compensation gain).
2. A control law such as (2.47) that can stabilize the rigid maglev system also stabilizes the collocated flexible system over a limited range of gains using PD control.

The second observation can be demonstrated using the expressions (2.65) in combination with the condition:

$$p^2 < p_z^2 \quad (2.71)$$

Equation (2.71) holds due to (2.46) with assumption that $M > m_l$ and since (2.58) is valid.

Thus K_p :

$$K_p < \frac{-p^2 \alpha}{K_x} < \frac{-p_z^2 \alpha}{K_x} \quad (2.72)$$

where

$$\frac{-p_z^2 \alpha}{K_x} < \alpha \frac{(-p_z^2 + \omega_1^2)}{K_x} < \alpha \frac{(-p_z^2 + \omega_1^2 + \omega_2^2)}{K_x} \quad (2.73)$$

and for K_D :

$$K_D < \frac{-p^2}{K_x} < \frac{-p_z^2}{K_x} \quad (2.74)$$

where

$$\frac{-p_z^2}{K_x} < \frac{(-p_z^2 + \omega_1^2 + \omega_2^2)}{K_x} \quad (2.75)$$

Therefore, the region of stability is bounded by $K_p < \frac{-p_z^2 \alpha}{K_x}$ and $K_D < \frac{-p_z^2}{K_x}$,

which can be evaluated for a rigid system. Conditions obtained for flexible cases are always within this range. A compensator capable of stabilizing the flexible case will also stabilize the rigid case. When a flexible system is collocated, a compensator designed to stabilize its rigid analogue, will not necessarily stabilize the flexible system. Further, the compensator has more restricted gain limits.

2.7 Non-Collocated Flexible Case Under PD Control

Consider the case of non-collocated actuator and sensors represented equations (2.59) and (2.61) with compensator (2.47). The closed loop transfer function for such a system is as follows:

$$G_n^{CL}(s) = \frac{K_x \omega_2^2 (K_P + K_D s)}{\left[s^5 + s^4 \alpha + s^3 (\omega_1^2 + \omega_2^2 - p_z^2) + s^2 \alpha (\omega_1^2 + \omega_2^2 - p_z^2) + \dots \right.} \quad (2.76)$$

$$\left. \dots + s(-\omega_2^2 p_z^2 - K_x K_D \omega_2^2) - K_x K_P \omega_2^2 - p_z^2 \omega_2^2 \alpha \right]$$

Considering the denominator of (2.76), it is noted that in contrast to the collocated case, only the zero degree and first degree terms are influenced by the controller. Moreover, in contrast to the collocated case, a necessary condition for stability is that:

$$\omega_1^2 + \omega_2^2 > p_z^2 \quad \Rightarrow \quad k \left(1 + \frac{m_1}{m_2} \right) > k_z \quad (2.77)$$

which is usually the case in practice. The s^3 term in the first column of the Routh table is zero, indicating that the system may be marginally stable at best under PD control³. Interestingly, the remaining terms indicate that the requirements for marginal stability are the same as the stability requirements for the collocated case:

$$K_D < \frac{-p_z^2}{K_x} \quad (2.78)$$

$$K_P < \frac{-p_z^2 \alpha}{K_x} \quad (2.79)$$

$$K_P > K_D \alpha \quad (2.80)$$

Thus, in this case a compensator (2.47) is not capable of stabilizing a flexible model (2.76).

³ Not necessarily the case in actual system with non-zero damping and with approximate collocation

2.8 Root Locus Analysis of Collocated and Non-Collocated Cases

As an example for root locus evaluation, consider the following parameters:

VARIABLE	VALUE
Vehicle weight m_2	1000 lbf
Mass ratio r	0.15
Suspension weight m_1	$r \cdot m_2$
Coil resistance R	1.83 Ω
Coil inductance L	0.68 H
Current I_0	35 A
Gap z_0	0.4 in
Current feedback gain K_a	256
Heave frequency	10 Hz

Table 2.2 Data used for comparison of collocated and non-collocated Maglev systems

In the first figure, a PD controller with coefficients K_p and K_D is used as shown in *Figure 2.11*. The bounding gain values for stability are used to determine the initial compensator zero location. The arrows in *Figure 2.11* show the tendency of the complex closed-loop poles' movement as the PD compensator zero is moved closer to the origin. As can be observed, the collocated system exhibits stability for all gains beyond the critical values.

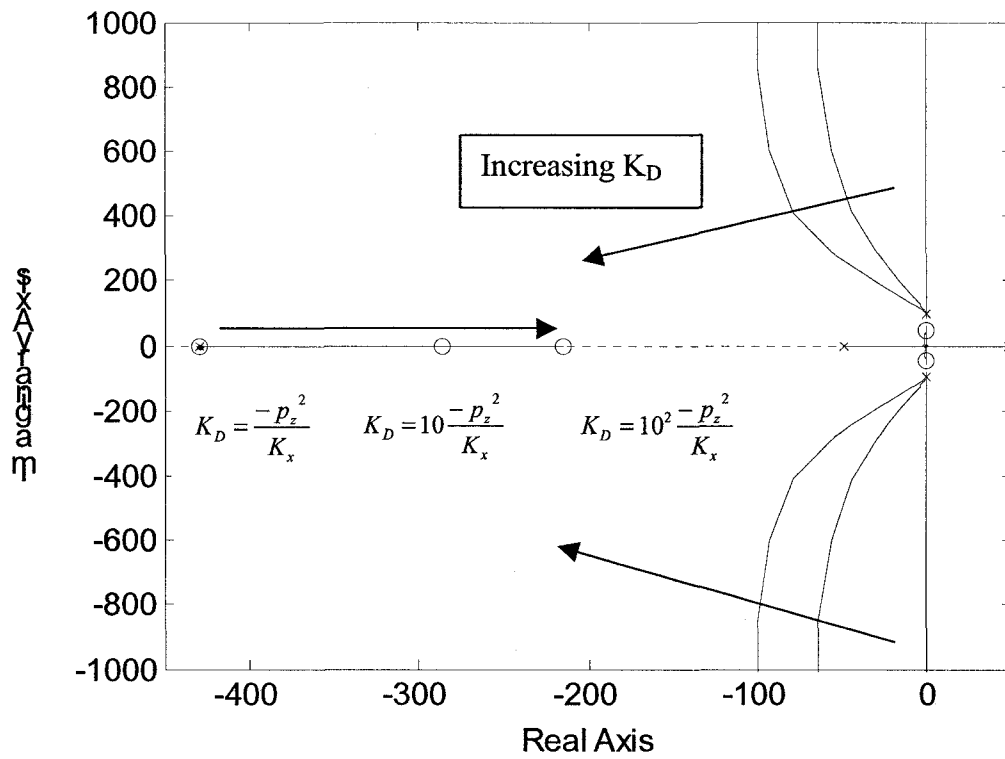


Figure 2.11 Collocated system with PD compensator

For the non-collocated case, which is marginally stable in the bounding case, some of the poles tend to move toward the unstable right half of s-plane as the compensator zero moves in either direction (see Figure 2.12).

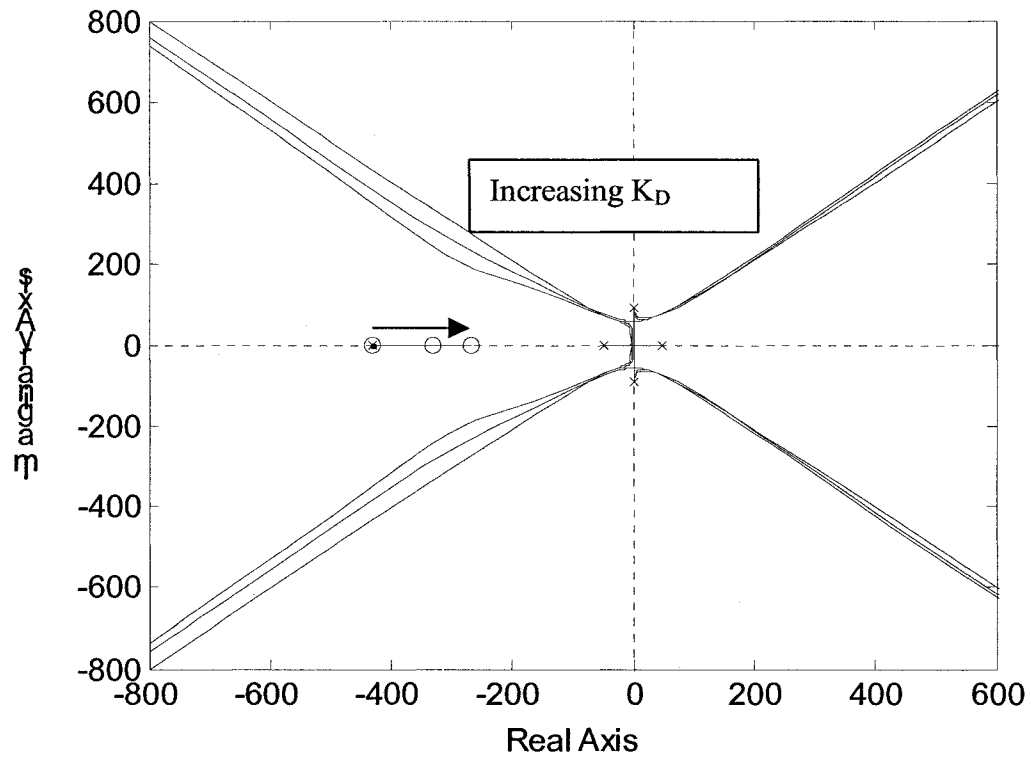


Figure 2.12 Non-Collocated system with PD compensator

As shown by the Routh analysis, this non-collocated Maglev system cannot be successfully stabilized with PD controller.

2.9 Non-Collocated Flexible Case Under PD Control with Acceleration Feedback

The marginal stability of the non-collocated case under PD control can be resolved by adding acceleration feedback, which results in the following compensator:

$$C_o(s) = K_p + K_D s + K_A s^2 \quad (2.81)$$

The closed-loop transfer function now becomes:

$$G_n^{CL}(s) = \frac{K_x \omega_2^2 (K_p + K_D s + K_A s^2)}{\left[s^5 + s^4 \alpha + s^3 (\omega_1^2 + \omega_2^2 - p_z^2) + s^2 (\omega_2^2 K_x K_A + \alpha \omega_1^2 + \alpha \omega_2^2 - \alpha p_z^2) \dots \right.} \quad (2.82)$$

$$\left. \dots + s(-\omega_2^2 p_z^2 - K_x K_D \omega_2^2) - K_x K_p \omega_2^2 - p_z^2 \omega_2^2 \alpha \right]$$

As can be seen, the numerator remains the same as well as all the coefficients in the denominator, with the single exception of the constant due to acceleration in the s^2 term. Routh analysis shows that the stability conditions are as follows:

$$\omega_1^2 + \omega_2^2 > p_z^2 \quad (2.83)$$

$$K_p > K_D \alpha \quad (2.84)$$

$$K_D < \frac{-p_z^2}{K_x} \quad (2.85)$$

$$K_p < \frac{-p_z^2 \alpha}{K_x} \quad (2.86)$$

$$K_p < K_D \alpha + \frac{K_A (\omega_1^2 \alpha + \omega_2^2 \alpha - p_z^2 \alpha - \omega_2^2 K_x K_A)}{\alpha} \quad (2.87)$$

$$K_D > \frac{K_p}{\alpha} + \frac{K_A (p_z^2 \alpha + \omega_2^2 K_x K_A - \omega_1^2 \alpha - \omega_2^2 \alpha)}{\alpha^2} \quad (2.88)$$

$$K_A < \frac{\alpha (-p_z^2 + \omega_1^2 + \omega_2^2)}{K_x \omega_2^2} \quad (2.89)$$

$$K_A > 0 \quad (2.90)$$

A root locus with such a compensator is shown in the figure below.

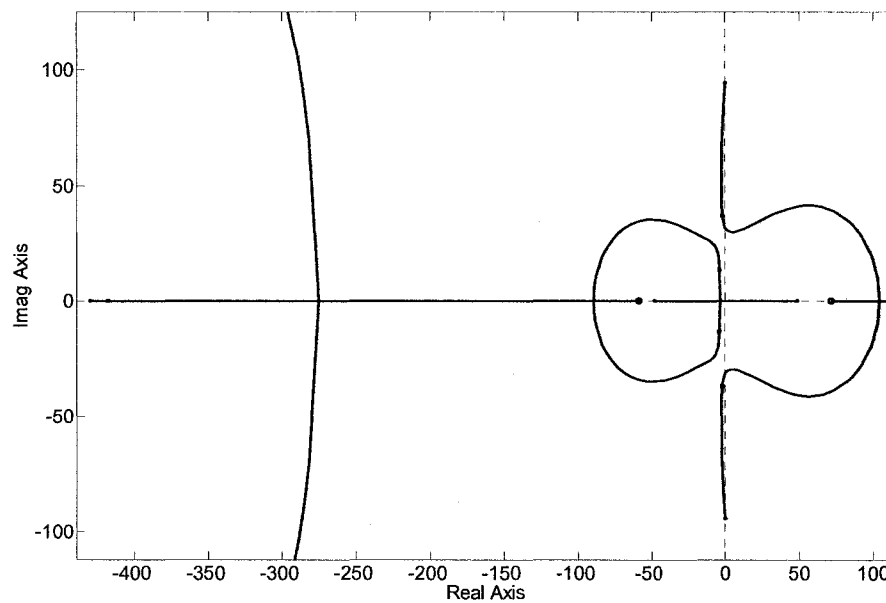


Figure 2.13 Non-Collocated Maglev system with PD compensator with acceleration feedback

As can be seen in this example, an acceleration feedback approach can provide a stable response. The result was not achievable without acceleration feedback. Collocation of system has significant impact on stability therefore during system design the goal of keeping collocation between sensor and actuators are important.

2.10 Maglev as a MIMO Flexible Structure

It has been shown that a SISO Maglev systems can be stabilized in spite of inherent electromagnet instability and flexible modes. For the collocated system, a simple PD control law can provide guaranteed stability if the gain limitations indicated by Routh analysis are not violated. In this section, similar calculations will be carried out for a MIMO system. It was shown (2.43) that the electromagnet introduces instability that can be readily compensated. Therefore for simplicity, the electromagnetic actuator models are excluded from this analysis.

By analogy to the models presented in the previous sections, a simple MIMO Maglev structure can be introduced (*Figure 2.14*):

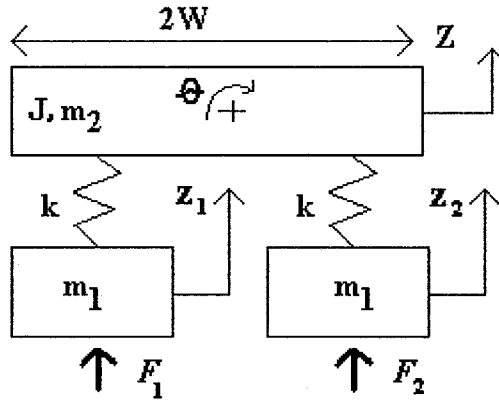


Figure 2.14 Simple MIMO Maglev model with flexible modes

In this simplified system, the large mass, m_2 , can be thought of as representing the passenger cabin, while the small masses, m_1 , represent the magnets. This system has the following equations of motion:

$$\begin{aligned}
 \frac{d^2 z}{dt^2} &= -\frac{2k}{m_2} z + \frac{k}{m_2} z_1 + \frac{k}{m_2} z_2 \\
 \frac{d^2 \theta}{dt^2} &= -\frac{2kW^2}{J} \theta + \frac{kW}{J} z_1 - \frac{kW}{J} z_2 \\
 \frac{d^2 z_1}{dt^2} &= \frac{k}{m_1} z + \frac{kW}{m_1} \theta - \frac{k}{m_1} z_1 + \frac{F_1}{m_1} \\
 \frac{d^2 z_2}{dt^2} &= \frac{k}{m_1} z - \frac{kW}{m_1} \theta - \frac{k}{m_1} z_2 + \frac{F_2}{m_1}
 \end{aligned} \tag{2.91}$$

The new variables $2W$ and J represent width and inertia of the Maglev passenger cabin, respectively. The state space equations can be written as:

$$\begin{bmatrix} \dot{Z} \\ \dot{\theta} \\ \dot{z}_1 \\ \dot{z}_2 \\ \ddot{Z} \\ \ddot{\theta} \\ \ddot{z}_1 \\ \ddot{z}_2 \end{bmatrix} = \begin{bmatrix} 0 & 0 & 0 & 0 & 1 & 0 & 0 & 0 \\ 0 & 0 & 0 & 0 & 0 & 1 & 0 & 0 \\ 0 & 0 & 0 & 0 & 0 & 0 & 1 & 0 \\ 0 & 0 & 0 & 0 & 0 & 0 & 0 & 1 \\ -\Omega^2 & 0 & \frac{\Omega^2}{2} & \frac{\Omega^2}{2} & 0 & 0 & 0 & 0 \\ 0 & -\kappa^2 & \frac{\kappa^2}{2W} & -\frac{\kappa^2}{2W} & 0 & 0 & 0 & 0 \\ \omega^2 & W\omega^2 & -\omega^2 & 0 & 0 & 0 & 0 & 0 \\ \omega^2 & -W\omega^2 & 0 & -\omega^2 & 0 & 0 & 0 & 0 \end{bmatrix} \begin{bmatrix} Z \\ \theta \\ z_1 \\ z_2 \\ \dot{Z} \\ \dot{\theta} \\ \dot{z}_1 \\ \dot{z}_2 \end{bmatrix} + \begin{bmatrix} 0 & 0 \\ 0 & 0 \\ 0 & 0 \\ 0 & 0 \\ 0 & 0 \\ \frac{1}{m_1} & 0 \\ 0 & \frac{1}{m_1} \end{bmatrix} \begin{bmatrix} F_1 \\ F_2 \end{bmatrix} \quad (2.92)$$

where

$$\Omega^2 = 2k / m_2 \quad (2.93)$$

$$\kappa^2 = 2kW^2 / J \quad (2.94)$$

$$\omega^2 = k / m_1. \quad (2.95)$$

The non-zero Eigenvalues of this system are:

$$\pm j\sqrt{\omega^2 + \kappa^2} \quad (2.96)$$

$$\pm j\sqrt{\omega^2 + \Omega^2} \quad (2.97)$$

Note that Ω represents the passenger cabin heave mode frequency when the magnets are held still. Similarly, κ represents the roll mode frequency with the magnets fixed, and ω represents the magnet vibration frequency with the passenger cabin fixed. These frequencies emerge as zero frequencies in the various transfer functions that follow.

The MIMO system presented above will be used to study of the stability of centralized and decentralized controllers on Maglev system approaches.

2.11 Centralized vs. Decentralized Control Law for Maglev Application

Decentralized control implies that each actuator's control input is based strictly upon local sensor measurements. On the other hands a centralized approach means that each actuator is controlled based on feedback variables from a combination of sensors,

possibly other than the local ones. Decentralized control is generally simpler, cheaper for implementation, and typically easier to achieve guaranteed stability, while centralized laws are more complex, but can potentially achieve a greater range of specific loop transfer characteristics [55][56][57][55][56][57][58] [59][60]. In *Figure 2.15* a basic schematic comparison of these two approaches is shown.

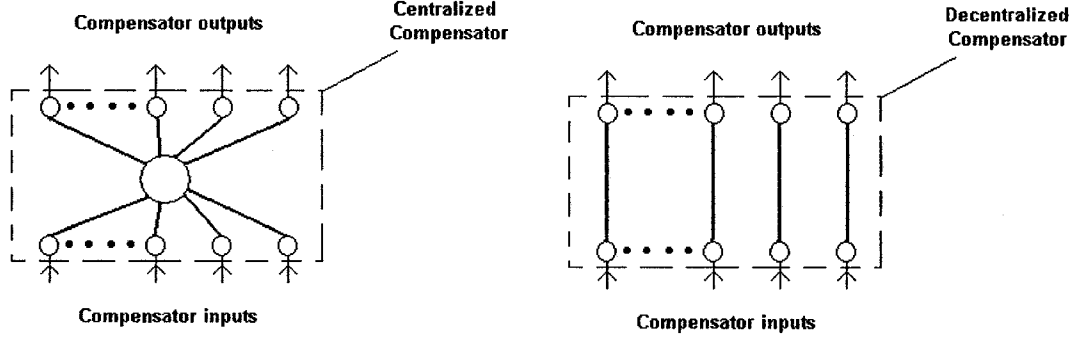


Figure 2.15 Centralized vs. decentralized compensation

Here the application of a decentralized [55][60][61] approach to the MIMO system is considered. The transfer function G_D represents the relationships between outputs z_1, z_2 and inputs F_1, F_2 . Thus the C matrix of the state-space model (2.92) is:

$$C_D = \begin{bmatrix} 0 & 0 & 1 & 0 & 0 & 0 & 0 & 0 \\ 0 & 0 & 0 & 1 & 0 & 0 & 0 & 0 \end{bmatrix} \quad (2.98)$$

The decentralized Maglev model has transfer function:

$$G_D = C_D (sI - A)^{-1} B = \begin{bmatrix} g_{d11} & g_{d12} \\ g_{d21} & g_{d22} \end{bmatrix} \quad (2.99)$$

where the A and B matrices are taken from (2.55).

$$g_{d11} = g_{d22} = \frac{2s^4 + s^2(2\Omega^2 + 2\kappa^2 + 2\omega^2) + \omega^2\kappa^2 + 2\kappa^2\Omega^2 + \omega^2\Omega^2}{s^2 2m \left[s^4 + s^2(2\Omega^2 + \kappa^2 + \omega^2) + \omega^2\kappa^2 + \kappa^2\Omega^2 + \omega^2\Omega^2 + \omega^4 \right]} \quad (2.100)$$

$$g_{d12} = g_{d21} = \frac{-\omega^2(\kappa^2 - \Omega^2)}{s^2 2m \left[s^4 + s^2(2\Omega^2 + \kappa^2 + \omega^2) + \omega^2\kappa^2 + \kappa^2\Omega^2 + \omega^2\Omega^2 + \omega^4 \right]} \quad (2.101)$$

It can be shown that for the decentralized system (2.99) the eigenvalues are as shown in (2.96) and (2.97).

Considering the centralized case [49][59], the outputs are θ , Z and the inputs remain F_1 , F_2 . The variables Z and θ may not be conveniently measured directly; however, in practice they are sometimes inferred from gap measurements. In other words, one might evaluate Z based on following relation:

$$Z = \frac{z_1 + z_2}{2} \quad (2.102)$$

Similarly θ could be approximated as:

$$\theta = \frac{z_1 - z_2}{2W} \quad (2.103)$$

Now the C matrix for centralized control would be:

$$C_c = \left[\begin{array}{cc|c|cccc} 0 & 0 & P & 0 & 0 & 0 & 0 \\ 0 & 0 & & 0 & 0 & 0 & 0 \end{array} \right], \quad (2.104)$$

where

$$P = \begin{bmatrix} 0.5 & 0.5 \\ \frac{1}{2W} & \frac{-1}{2W} \end{bmatrix} \quad (2.105)$$

Note that the transformation P in C_c implies that the system (2.92) has been assumed to be very rigid, which may not necessarily be valid. Also, in order to compare the centralized and decentralized approaches, it is necessary to transform the centralized controller outputs θ^{Cmd} , Z^{Cmd} back to decentralized form, F_1 and F_2 . For this purpose the transformation H is introduced:

$$H = \begin{bmatrix} 0.5 & \frac{1}{2W} \\ 0.5 & \frac{-1}{2W} \end{bmatrix} \quad (2.106)$$

In the *Figure 2.16*, the transformations between the centralized and decentralized systems are illustrated.

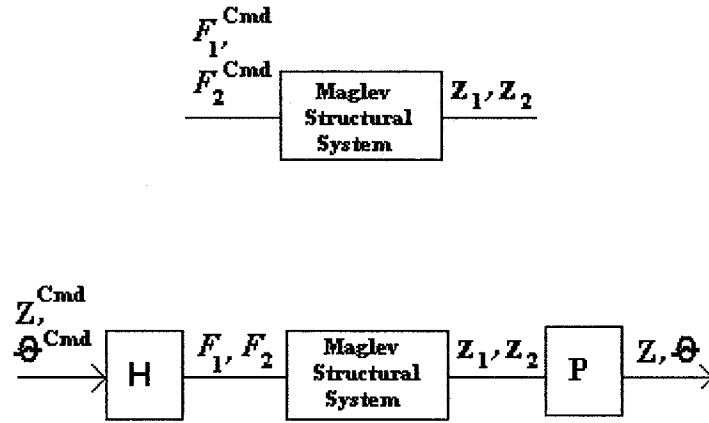


Figure 2.16 Block diagram of the centralized and decentralized Maglev models

Based on these transformations, the centralized Maglev transfer function has the following decoupled form:

$$G_C = HG_D P = \begin{bmatrix} \frac{s^2 + \Omega^2}{s^2 2m_1 (s^2 + \omega^2 + \Omega^2)} & 0 \\ 0 & \frac{s^2 + \kappa^2}{s^2 2m_1 W^2 (s^2 + \kappa^2 + \omega^2)} \end{bmatrix} = \begin{bmatrix} g_{c11} & 0 \\ 0 & g_{c22} \end{bmatrix} \quad (2.107)$$

The decoupled heave-mode transfer function is thus denoted as g_{c11} and the roll-mode transfer function is g_{c22} . It is a simple matter to show that this system reduces to the rigid system model by letting stiffness k go to infinity:

$$\lim_{\substack{\Omega \rightarrow \infty \\ \kappa \rightarrow \infty}} G_C = \begin{bmatrix} \frac{1}{\bar{M}s^2} & 0 \\ 0 & \frac{1}{\bar{J}s^2} \end{bmatrix}, \quad (2.108)$$

where

$$\bar{M} = m_2 + 2m_1 \quad (2.109)$$

$$\bar{J} = J + 2m_1 W^2 \quad (2.110)$$

Referring again to (2.92) the system with finite stiffness, it can be noted that in contrast to the decentralized case, the centralized system's transfer functions have fewer poles. In g_{c11} the poles at $\pm j\sqrt{\omega^2 + \kappa^2}$ have been cancelled, and in g_{c22} the poles at

$\pm j\sqrt{\omega^2 + \Omega^2}$ have been cancelled. This is an indication that the centralized system will have uncontrollable modes.

Comparing singular value plots for these two systems it is possible to make an additional observation. Singular value frequency response plots were obtained based on the data from *Table 2.2*. The main body's inertia (2.110) was based on the calculation for a long slender bar $J = \frac{1}{12}m_2(2W)^2$, where the length $W = 5$. As can be seen in *Figures 2.17* and *2.18*, the variation in the bounds of the gain is much greater in the centralized case.

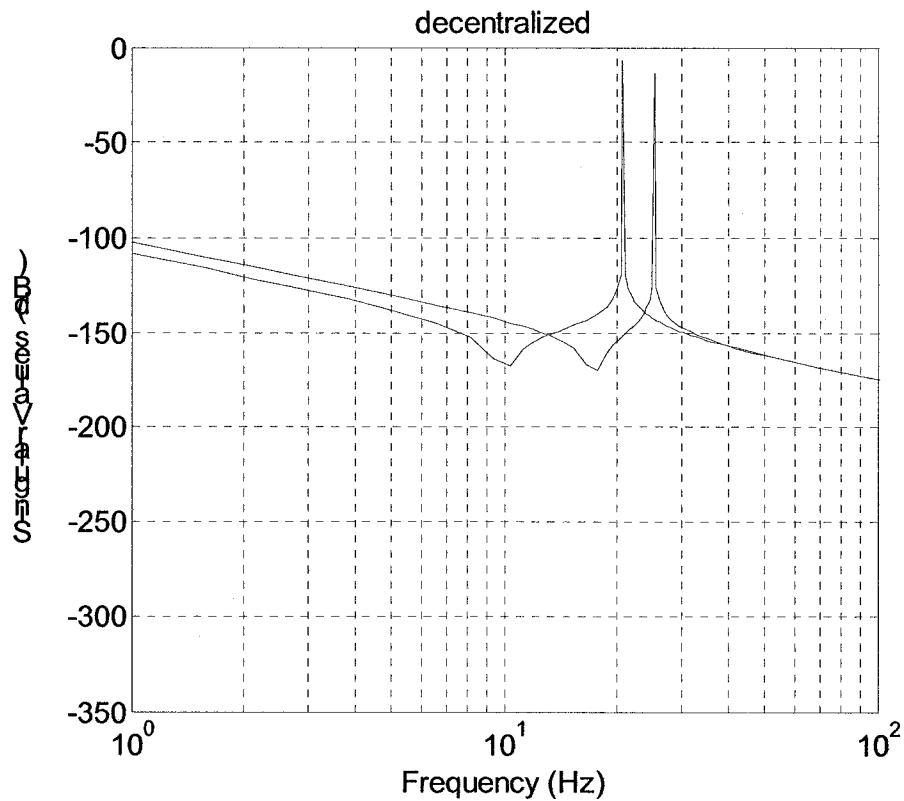


Figure 2.17 Decentralized singular value frequency response

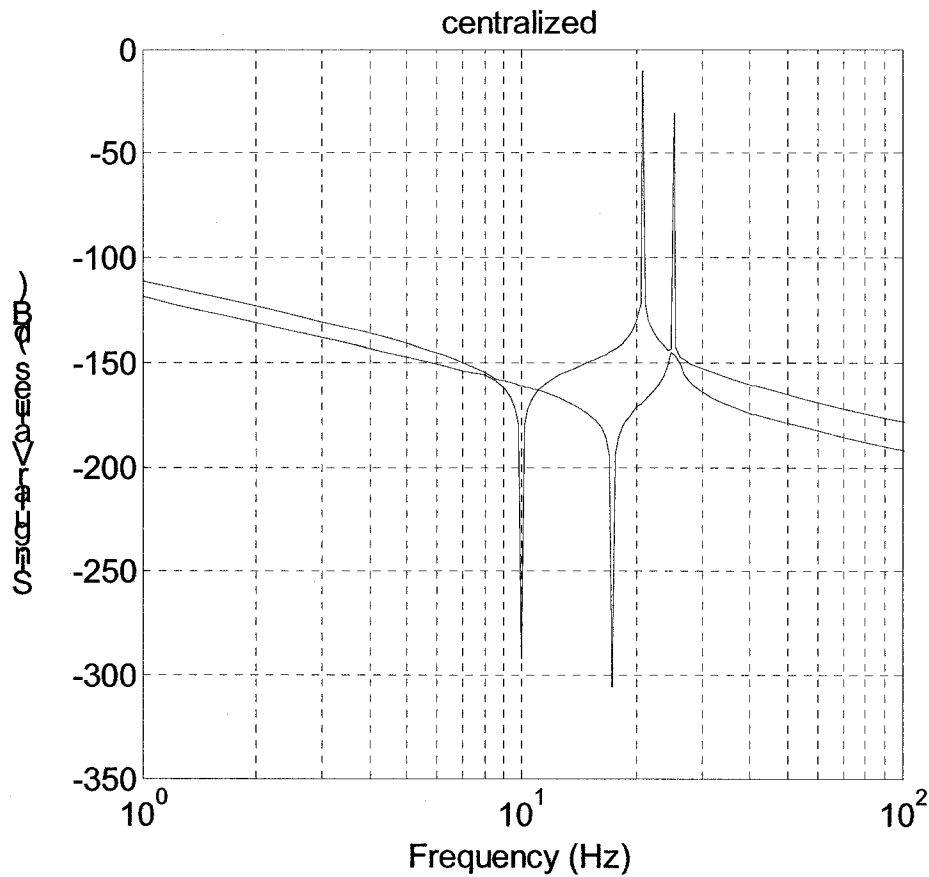


Figure 2.18 Centralized singular value frequency response

The difference observed is associated with the choice of different variables for control versus the measured data.

2.12 Centralized vs. Decentralized Control Law with PD Compensation

The centralized and decentralized examples are 2-input, 2-output systems. For purposes of comparing these systems, diagonal PD compensators can be applied. Note that for the decentralized case, the compensators can be identical. Thus for the decentralized case, the compensator has the form:

$$C_{oD} = \begin{bmatrix} K_P + K_D s & 0 \\ 0 & K_P + K_D s \end{bmatrix} \quad (2.111)$$

For the centralized approach different compensators would most likely be used for heave and roll. Thus, the compensator for the centralized case has the form:

$$C_{oc} = \begin{bmatrix} K_{pz} + K_{Dz}s & 0 \\ 0 & K_{pr} + K_{Dr}s \end{bmatrix} \quad (2.112)$$

Based on the characteristic equations of (2.99) and (2.107) it can be shown that both the centralized and decentralized systems can be stabilized with compensators (2.111) and (2.112) respectively. It can be seen on the root locus plots below that for the decentralized case increased damping can be achieved for all modes. However, it is noted that for the centralized case, the PD controller cannot influence certain frequencies. The root locus plots for centralized case illustrate the pole/zero cancellations discussed above (see Figure 2.20). These cancellations, marked by arrows, correspond to modes that are unreachable by the controller.

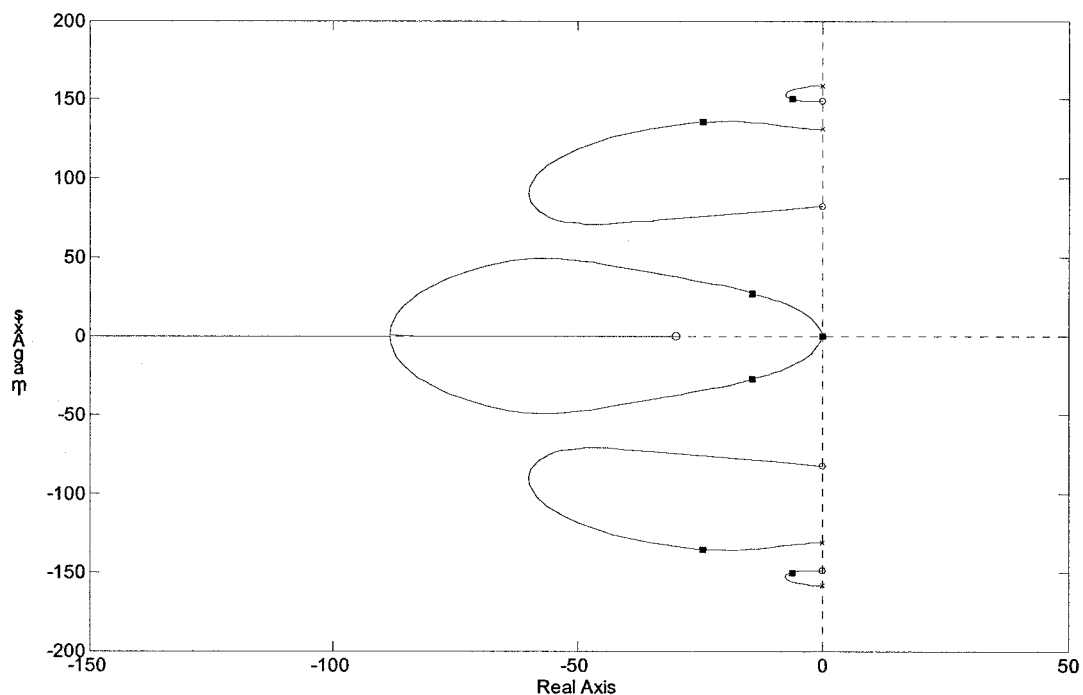
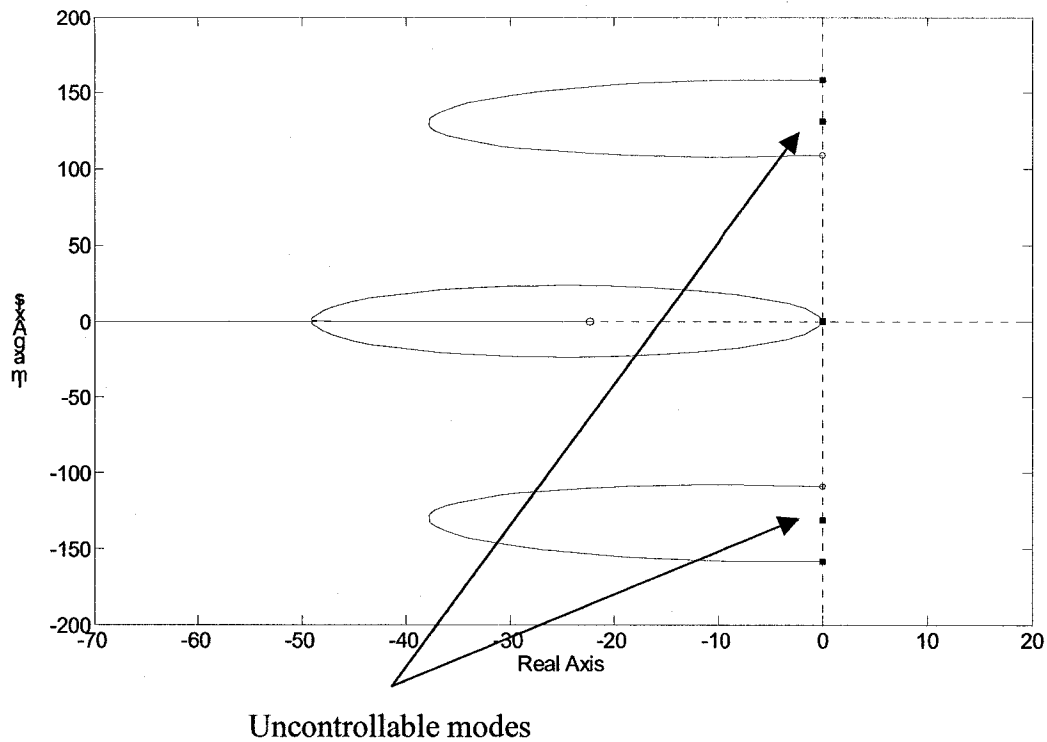


Figure 2.19 Decentralized PD control



Uncontrollable modes
 Figure 2.20 Centralized closed-loop root loci with PD compensation (for levitation, angular degree of freedom, and arrows mark uncontrollable modes)

The analysis above is based on an idealized case where real-world influences such as actuator dynamics discrete time implementation are not accounted for. Such influences may tend to destabilize the marginally stable modes. Based on these results, the centralized control approach presented is not recommended for systems with significant flexibility.

2.13 Flux Feedback

A well-known way to improve the stability of Maglev systems is to utilize magnetic flux as a control feedback measurement [49][62][63][64]. The objective of air gap flux feedback is to reduce the influence of the coefficients k_z and k_i (2.32) and (2.33). There is a significant variation of these values with changes in operation point. However, since according to (2.12) and (2.12), the flux linkage between the coil and the track is linearly proportional to the magnet excitation current and inversely proportion to the air gap, the perturbation of force with respect to flux variations about an operating point Φ_0 ,

is less than the its perturbation with respect to gap and current about their respective operating points, z_0 and I_0 . The linearization of the flux expression (2.13) can be written as:

$$\Delta\Phi = k_{\phi i} I - k_{\phi z} z \quad (2.113)$$

where $k_{\phi i}$, $k_{\phi z}$ are new linearization coefficients which can be evaluated empirically, based experimental results or estimated based on force expressions.

A diagram for magnet control with flux feedback is given in *Figure 2.21*.

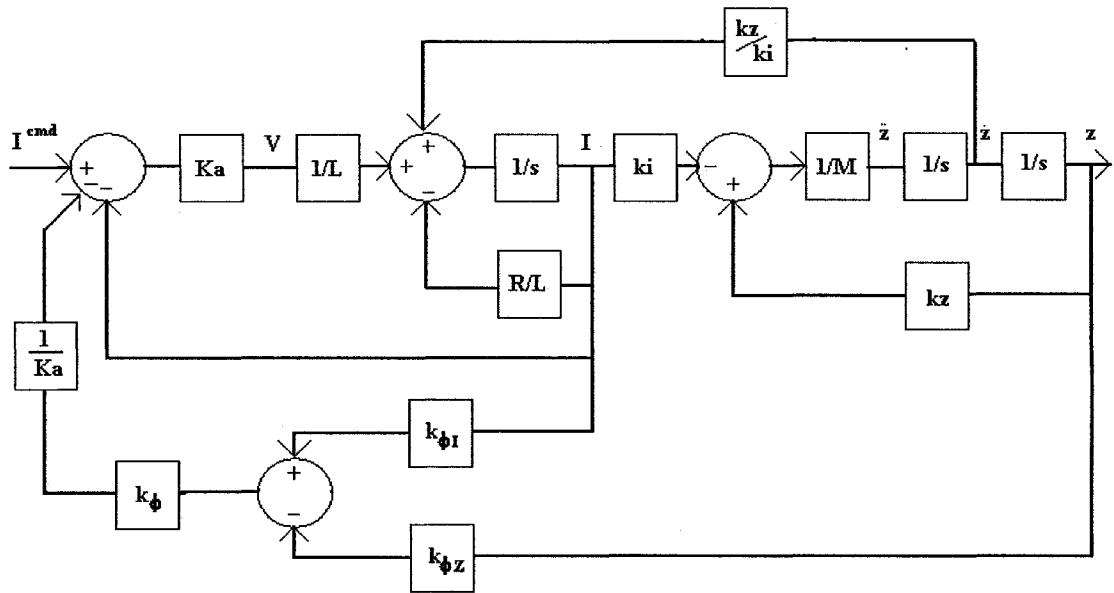


Figure 2.21 Schematic of Maglev plant with flux feedback

Based on this scheme, the state space model of the test rig rigid system from (2.42) becomes:

$$\begin{bmatrix} \dot{z} \\ \ddot{z} \\ \dot{I} \end{bmatrix} = \begin{bmatrix} 0 & 1 & 0 \\ \frac{k_z}{M} & 0 & -\frac{k_i}{M} \\ \frac{k_\Phi \cdot k_{zFlux}}{L} & \frac{k_z}{k_i} & -\frac{(k_\Phi \cdot k_{iFlux} + K_a + R)}{L} \end{bmatrix} \begin{bmatrix} z \\ \dot{z} \\ I \end{bmatrix} + \begin{bmatrix} 0 \\ 0 \\ \frac{K_a}{L} \end{bmatrix} I^{Cmd};$$

$$[z] = [1 \quad 0 \quad 0] \begin{bmatrix} z \\ \dot{z} \\ I \end{bmatrix} \quad (2.114)$$

which gives

$$\hat{G}_{rigid}^{Flux}(s) = \frac{-K_a k_i}{s^3 ML + s^2 M(k_\Phi k_{iFlux} + K_a + R) + k_\Phi(k_i k_{zFlux} - k_z k_{iFlux}) - k_z(K_a + R)} \quad (2.115)$$

If the gain of flux feedback is adjusted in such a way that:

$$k_\Phi(k_i k_{zFlux} - k_z k_{iFlux}) = k_z(K_a + R) \quad (2.116)$$

then $\hat{G}_{rigid}^{Flux}(s)$ is reduced to the following form:

$$G_{rigid}^{Flux}(s) = \frac{-K_a k_i}{s^3 ML + s^2 M(K_a + R + k_\Phi k_{iFlux})} \quad (2.117)$$

As it can be seen by comparing equations (2.43) and (2.117), the main advantage of flux feedback is that the unstable pole in (2.43) has been eliminated. Note that the new system has two poles at the origin in place of p_1 and p_2 . Also, the poles are independent of k_z rendering the new system less sensitive to variations in the operating gap. In the overall control scheme, the flux control loop is an inner loop, and the position feedback is retained as an outer loop. In this arrangement, the flux measurement improves stability while gap feedback is responsible for establishing the prescribed performance, and also contributes to noise rejection.

2.14 Inverse Electromagnetic Model Calculation

As a result of the non-linearity of force with respect to gap and current, the linearized levitation force model is highly sensitive to variations in the operating point. As a result, the effective open-loop gain of the electromagnetic suspension varies substantially with operating conditions. In the previous section it was illustrated that the introduction of flux feedback improves upon this situation. As an alternate approach to this issue, McLagan and Vidyasagar [15][49] discuss the use of a model inversion approach to linearize the electromagnetic model of a magnetic suspension system.

2.14.1 Concept of the Inverse Model Calculation

Considering that the main non-linearities are those of the electromagnet model, as opposed to the structural model, the gain variation problem can be studied through consideration of the current amplifier device together with an electromagnet. In general the amplifier is driven by the current command value, which comes from the compensator.

The problem of non-linear variation of gain with respect to operating condition is clearly visible in *Figure 2.22*. This figure was obtained by normalizing the electromagnet equation together with the levitation force expression (2.21) and (2.26) about several different gaps. It can be seen that gap variation in the range of 0.1 [in.] to 0.8 [in.] results in a 20 [dB] variation in gain. This is primarily due to the appearance of the quadratic term I^2/z^2 in the force expression.

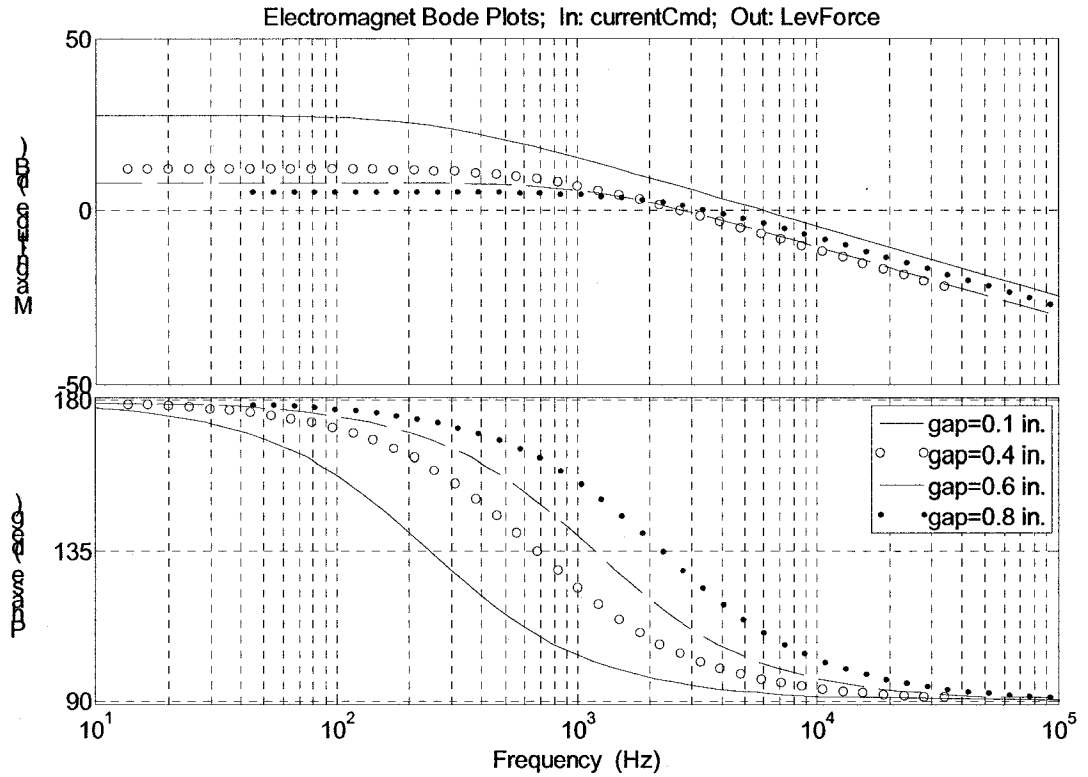


Figure 2.22 Electromagnet Bode plots for different operation points due to Limbert electromagnet model

The resulting wide variations in gain result in poor robustness. A model inversion approach can help avoid this. The idea is to linearize the electromagnetic model by commanding force, and using a calculation based on (2.21) to determine the corresponding current. Equation (2.118) presents such a calculation based on the Limbert force expression and Figure 2.22 is a block diagram of this approach.

$$I^{Cmd} = \sqrt{\frac{4 \cdot F_{LEV}^{Cmd} \cdot z^2}{\mu_0 \cdot N^2 \cdot d \cdot w \cdot \left(1 + \frac{2 \cdot z}{\pi \cdot w} \cdot \left[1 - \frac{y}{z} \cdot a \tan\left(\frac{y}{z}\right) \right] \right)}} \quad (2.118)$$

A block diagram illustrating this scheme is presented in the Figure 2.23

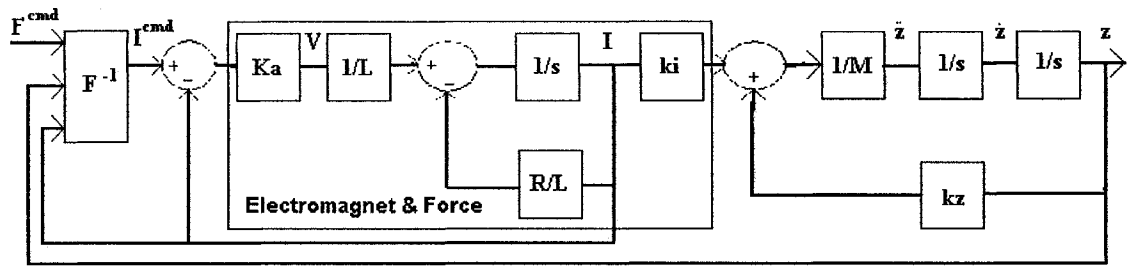


Figure 2.23 Maglev Test Rig block diagram with inverse calculation block

Linearization of the model relating F^{Cmd} to F_{LEV} , as expressed by (2.21) and (2.118), leads to the following Bode plots (see Figure 2.24).

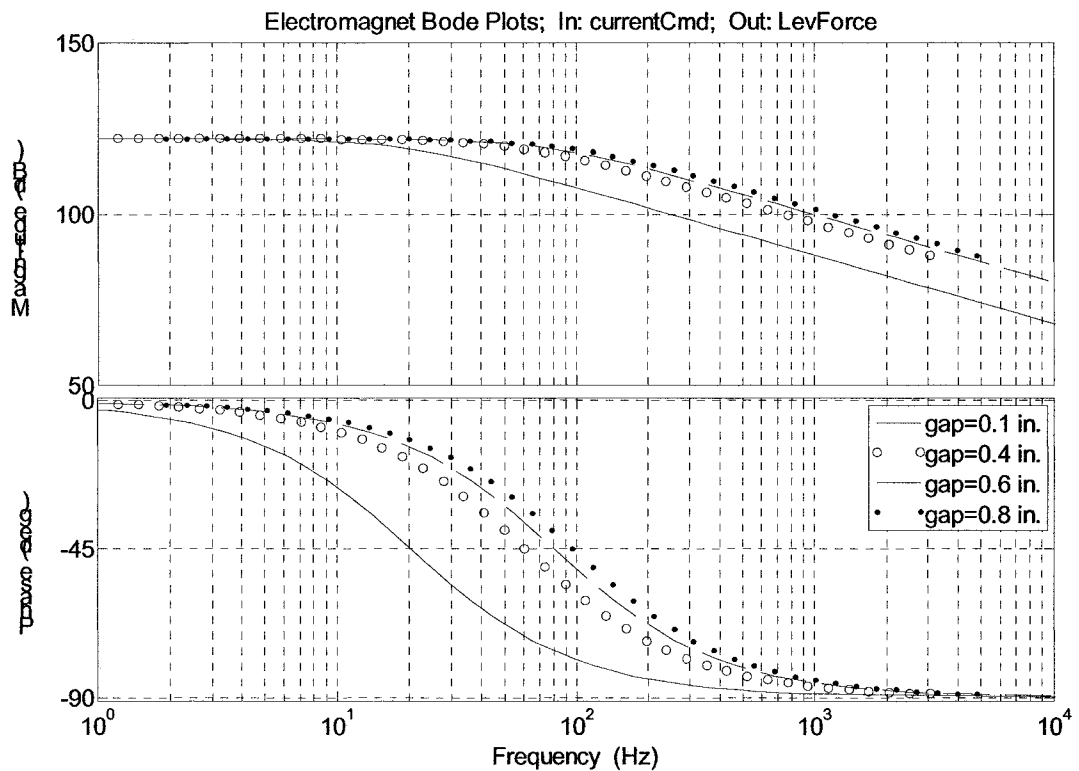


Figure 2.24 Electromagnet Bode plots for a range of operating points with model inversion

As can be seen, the low frequency gain variation has vanished, thus the controller doesn't have to work with such a wide range of possible gains. The model inversion calculation can be simplified by using the force expression derived for a uniform magnetic field (2.12).

:

$$I^{Cmd} = \sqrt{\frac{4F_{LEV}^{Cmd} z^2}{\mu_0 N^2 dw}} \quad (2.119)$$

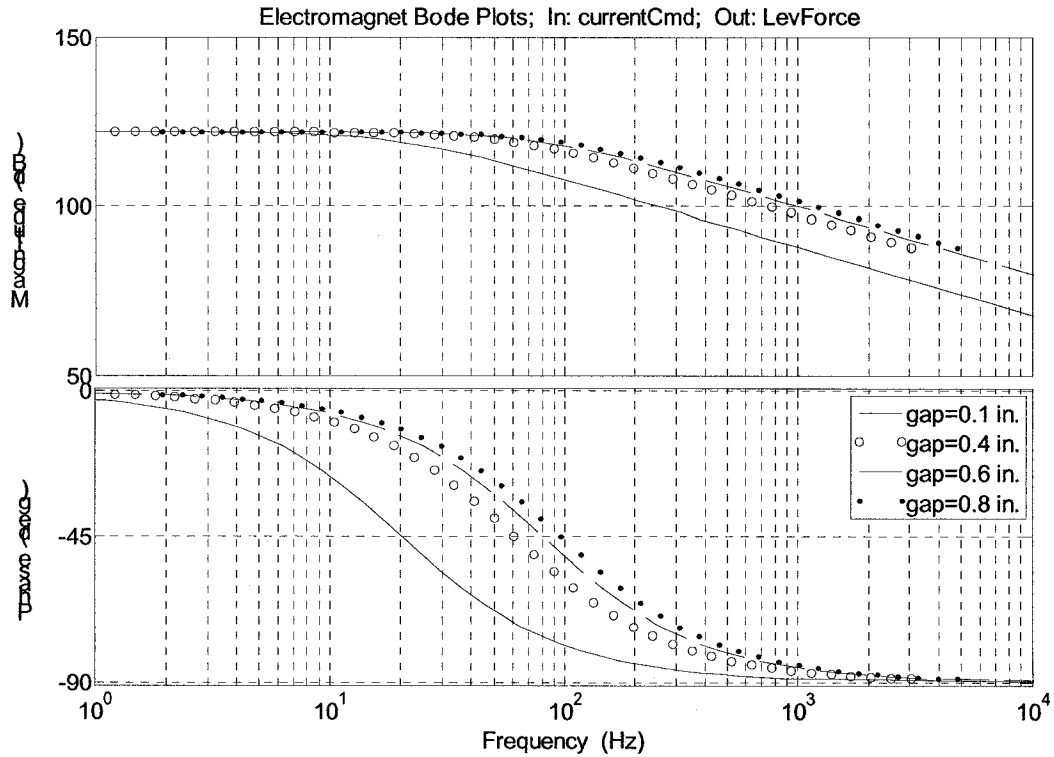


Figure 2.25 Electromagnet Bode plots for different operation points with Limbert partial inverse calculations and Limbert electromagnet model

Figure 2.25 shows results based on the simplified inversion (2.119). In this case, a very small variation in gains is observed, but it is clearly a substantial improvement over the 20 [dB] variation predicted without the model inversion. Note that this approach would not account for lateral motion though.

2.14.2 Sensitivity of the Inverse Model Calculation

To investigate the robustness of the inversion-based approach, one can apply a linearization of the force expression as was shown in (2.34). Thus, the expression for commanded force has the following form:

$$F^{Cmd} = k_{zForce} z - k_{iForce} I \quad (2.120)$$

where k_{zForce} , k_{iForce} are respectively gap and current linearization coefficients. Assuming a rigid system (2.42) and incorporating the electromagnet model, the current equation becomes:

$$\frac{dI}{dt} = \frac{k_{zForce}K_a}{k_{iForce}L} - \frac{(K_a + R)}{L}I - \frac{K_a}{k_{iForce}L}F^{Cmd} \quad (2.121)$$

The linearized equations of motion are thus:

$$\begin{bmatrix} \dot{z} \\ \ddot{z} \\ \dot{I} \end{bmatrix} = \begin{bmatrix} 0 & 1 & 0 \\ \frac{k_z}{M} & 0 & -\frac{k_i}{M} \\ \frac{K_a k_{zForce}}{k_{iForce}L} & \frac{k_z}{k_i} & -\frac{(K_a + R)}{L} \end{bmatrix} \begin{bmatrix} z \\ \dot{z} \\ I \end{bmatrix} + \begin{bmatrix} 0 \\ 0 \\ -\frac{K_a}{k_{iForce}L} \end{bmatrix} F^{Cmd}$$

$$[z] = \begin{bmatrix} 1 & 0 & 0 \end{bmatrix} \begin{bmatrix} z \\ \dot{z} \\ I \end{bmatrix} \quad (2.122)$$

The corresponding transfer function has the form:

$$G_{rigid}^i(s) = \frac{\frac{k_i K_a}{L}}{s^3 M k_{iForce} + s^2 k_{iForce} M \left(\frac{K_a + R}{L} \right) - s k_{iForce} k_z - R k_z k_{iForce} \dots \dots - K_a (k_{iForce} k_z + k_i k_{zForce})} \quad (2.123)$$

where the superscript i on G_{rigid}^i indicates inverse.

The main reason for using the inverse calculation is to account for non-linearities. The non-linearities are represented by k_z and k_i . To evaluate the best-case scenario, assume that there is an ideal inversion. Thus:

$$k_{zForce} = k_z \quad (2.124)$$

$$k_{iForce} = k_i \quad (2.125)$$

Then the transfer function from force command to gap transforms into:

$$G_{rigid}^{ii}(s) = \frac{K_a/L}{s^3 M + s^2 M \left(\frac{K_a + R}{L} \right) - s k_z - \frac{R k_z}{L}} \quad (2.126)$$

where upper script *ii* denotes ideal inverse. Comparing (2.126) with (2.43) introduced in the earlier section, it can be noted that the coefficients of the characteristic equation are different. The k_i terms have been cancelled out and the zero degree polynomial coefficient was reduced.

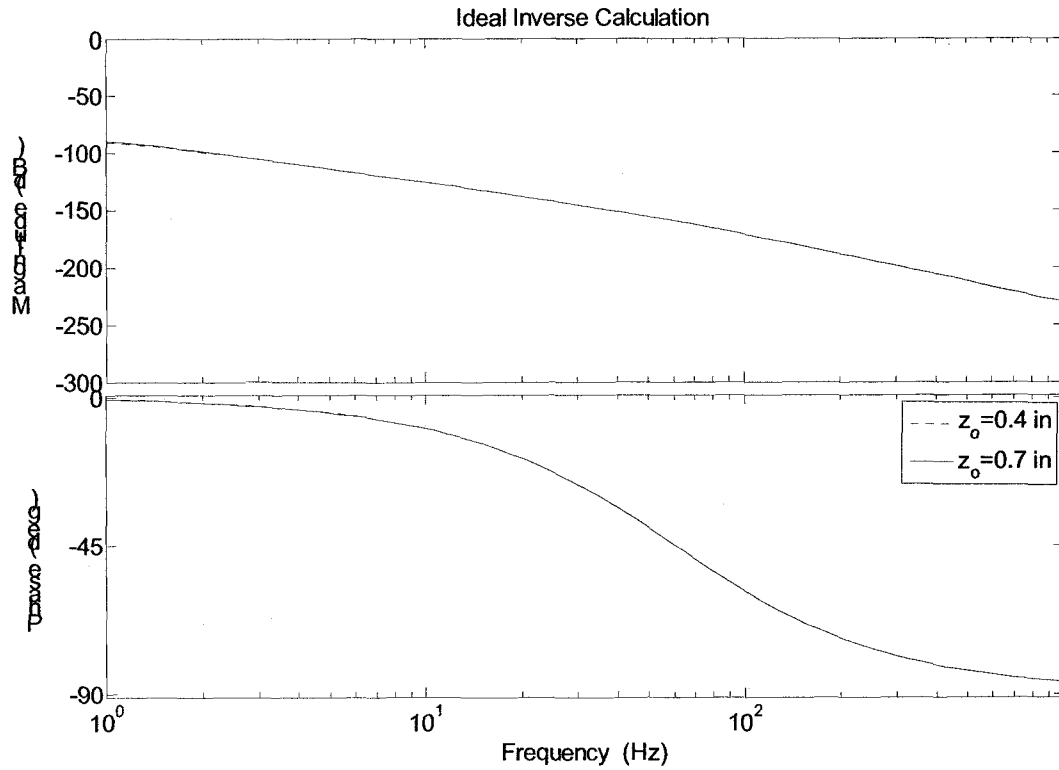


Figure 2.26 Maglev system with inverse force calculation

In this system the zero degree denominator term has been reduced from (2.123) to (2.126). Based on consideration of the Routh Hurwitz criterion for this system and knowing that $\frac{R k_z}{L} \ll \frac{R \cdot k_z + k_z K_a}{L}$, it can be concluded that the open loop system with force inversion is less sensitive to linearization around different operation points.

2.15 Transfer Function Zeros

In Chapter 1 it was pointed out that the transfer functions relating current to gap vary with respect to position along the guideway. Here, this phenomenon will be explored based on a simple beam (guideway) and point mass (vehicle) model.

The literature contains many investigations [32][59][68][69][70][71][72][73] of the relation between coupled vehicle/guideway systems. In this work transcendental transfer functions were used to study the impact of the track dynamics on overall system stability.

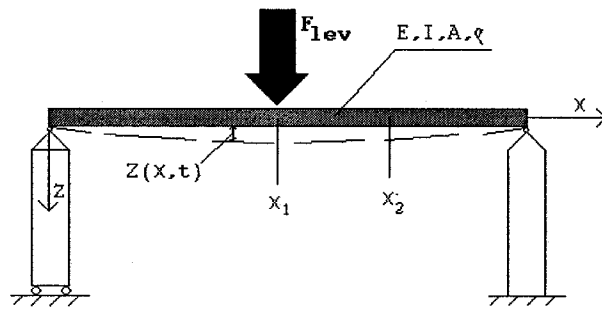


Figure 2.27 Maglev vehicle/track interaction modeling

Consider the following partial differential equation that describes the elastic deflection of a simply supported beam [74][75], meant to represent the guideway shown in Figure 2.27):

$$-\frac{\partial^2}{\partial z^2} \left[EI_b \frac{\partial^2 z(x, t)}{\partial z^2} \right] + f(y, t) = \rho A_b \frac{\partial^2 z(x, t)}{\partial t^2}, \quad (2.127)$$

where the variables $E, I_b, f(x, t), \rho, A_b$ represent the Young's Modulus, moment of area, external force per unit length, cross section area, and the density of the beam respectively. For a simply supported beam, the boundary conditions can be written as follows:

$$\begin{aligned}
z(0,t) &= 0; \\
z(L,t) &= 0; \\
EI \frac{\partial^2 z(0,t)}{\partial y^2} &= 0; \\
EI \frac{\partial^2 z(L,t)}{\partial y^2} &= 0;
\end{aligned} \tag{2.128}$$

Applying the Laplace transform, letting

$$\beta = \frac{-\rho A s^2}{EI} \tag{2.129}$$

and after some simplification [54][76], (2.127) becomes:

$$Z^{IV}(x,s) - \beta^4 Z(x,s) = F(x,s) \tag{2.130}$$

with boundary conditions:

$$Z(0,s) = 0, \quad Z(L,s) = 0, \quad Z''(0,s) = 0, \quad Z''(L,s) = 0; \tag{2.131}$$

Rewriting the above formula in the state space form

$$\begin{bmatrix} Z'(x,s) \\ Z''(x,s) \\ Z'''(x,s) \\ Z^{IV}(x,s) \end{bmatrix} = \begin{bmatrix} 0 & 1 & 0 & 0 \\ 0 & 0 & 1 & 0 \\ 0 & 0 & 0 & 1 \\ \beta^4 & 0 & 0 & 0 \end{bmatrix} \begin{bmatrix} Z(x,s) \\ Z'(x,s) \\ Z''(x,s) \\ Z'''(x,s) \end{bmatrix} + \begin{bmatrix} 0 \\ 0 \\ 0 \\ 1 \end{bmatrix} F(y,s) \tag{2.132}$$

where state space vector is:

$$S(x,s) = [Z(x,s) \quad Z'(x,s) \quad Z''(x,s) \quad Z'''(x,s)]^T \tag{2.133}$$

To obtain a compact form of (2.132), define:

$$A = \begin{bmatrix} 0 & 1 & 0 & 0 \\ 0 & 0 & 1 & 0 \\ 0 & 0 & 0 & 1 \\ \beta^4 & 0 & 0 & 0 \end{bmatrix}; \quad B = \begin{bmatrix} 0 \\ 0 \\ 0 \\ 1 \end{bmatrix} \tag{2.134}$$

and noting that

$$F(x,s) = \delta(x - x_0)F(s) \tag{2.135}$$

equation (2.132) becomes:

$$S'(x,s) = AS(x,s) + BF(s) \tag{2.136}$$

At this point by using the general form of the solution from modern control theory (2.136) becomes:

$$\begin{aligned}
S(x,s) &= e^{A \cdot L} S(0,s) + \int_0^L e^{A(l-x)} B \delta(x-x_1) F(s) dx = \\
&= e^{A \cdot L} S(0,s) + e^{A(l-x_1)} B F(s)
\end{aligned} \tag{2.137}$$

Knowing the boundary conditions for $S(y=0,s)$ and $S(y=L,s)$ the general expression for $S(y,s)$ can be found as following:

$$S(x,s) = \begin{cases} e^{A \cdot x} S(0,s) & \text{for } 0 \leq x \leq x_1 \\ e^{A \cdot x} S(0,s) + e^{A(x-x_1)} B F(s) & \text{for } x_1 \leq x \leq L \end{cases} \tag{2.138}$$

The matrix exponential function $e^{A \cdot x}$ corresponding to (2.138) can be expressed using the inverse Laplace transform of the matrix $(sI - A)^{-1}$;

$$e^{A \cdot x} = \begin{bmatrix} f'''(x) & f''(x) & f'(x) & f(x) \\ \beta^4 f(x) & f'''(x) & f''(x) & f'(x) \\ \beta^4 f'(x) & \beta^4 f(x) & f'''(x) & f''(x) \\ \beta^4 f''(x) & \beta^4 f'(x) & \beta^4 f(x) & f'''(x) \end{bmatrix}; \tag{2.139}$$

where: $f(x) = \frac{[\sinh(\beta x) - \sin(\beta x)]}{2\beta^3}$.

Thus, for a simply supported beam the transfer function between the displacement at position x_2 and a point force at x_1 (see Figure 2.26) can be written as follows [55][58]:

$$\begin{aligned}
G_T(s) = \frac{Z(x_2,s)}{F(s)} &= \frac{\sinh(\beta L) \sin(\beta x_1) \sin(\beta(L-x_2)) \dots}{2\beta^3 EI \sin(\beta L) \sinh(\beta L)} \\
&\dots - \sin(\beta L) \sinh(\beta x_1) \sinh(\beta(L-x_2))
\end{aligned} \tag{2.140}$$

where subscript T denotes track.

Note that to transform the transcendental [74] transfer function into a ratio of polynomials in the Laplace operator s , $G_T(s)$ can be converted by using power series expansion in terms of β and then β^4 is replaced by $\frac{-\rho A s^2}{EI}$ using (2.129). Finally, after these operations, a closed form can be achieved:

$$G_T(s) = \frac{N_T(s)}{D_T(s)} \tag{2.141}$$

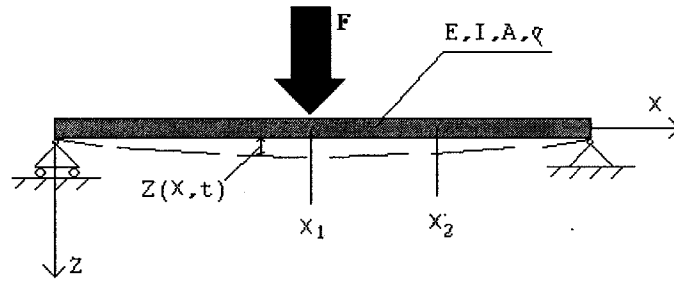


Figure 2.28 Simply supported beam under force applied at x_1

If the measurement and the applied force are collocated, then $x_2 = x_1 = x$. Also for simplification one can define a dimensionless complex number related to the Laplace variable s in the following form:

$$\lambda = \beta L \quad (2.142)$$

Therefore expression (2.140) can be simplified to:

$$G_T(s) = \frac{\sinh(\lambda) \sin\left(\frac{\lambda}{L}x\right) \sin\left(\frac{\lambda}{L}(L-x)\right) - \sin(\lambda) \sinh\left(\frac{\lambda}{L}x\right) \sinh\left(\frac{\lambda}{L}(L-x)\right)}{2\left(\frac{\lambda}{L}\right)^3 EI \sin(\lambda) \sinh(\lambda)} \quad (2.143)$$

The Taylor Power Series for the numerator can be expressed as:

$$N_T(\lambda) = \sum_{n=0}^{\infty} \frac{\lambda^n}{n!} \frac{d^n N_T}{d\lambda^n}(0) \quad (2.144)$$

It can be shown that $\frac{d^i N_T}{d\lambda^i}(0) = 0$ for $i = 1, 2, 3, 4$. Thus, after the 5th differentiation and

substitution of the values from Table 2.3 polynomial (2.144) can be factored as:

$$N_T(\lambda, x) = (-7.8 \cdot 10^{-3} x^3 + 1.4 \cdot 10^{-4} x^4 + 0.1 x^2) \prod_{i=0}^{\infty} \left(1 - \frac{\lambda^4}{\lambda_i^4}\right) \quad (2.145)$$

where λ_i is the i^{th} root of the numerator equation (2.145) obtained numerically by utilizing the Newton-Raphson method.

$$\sinh(\lambda) \sin\left(\frac{\lambda}{L}x\right) \sin\left(\frac{\lambda}{L}(L-x)\right) - \sin(\lambda) \sinh\left(\frac{\lambda}{L}x\right) \sinh\left(\frac{\lambda}{L}(L-x)\right) = 0 \quad (2.146)$$

Values of λ_i as a function of y are illustrated in *Figure 2.29*.

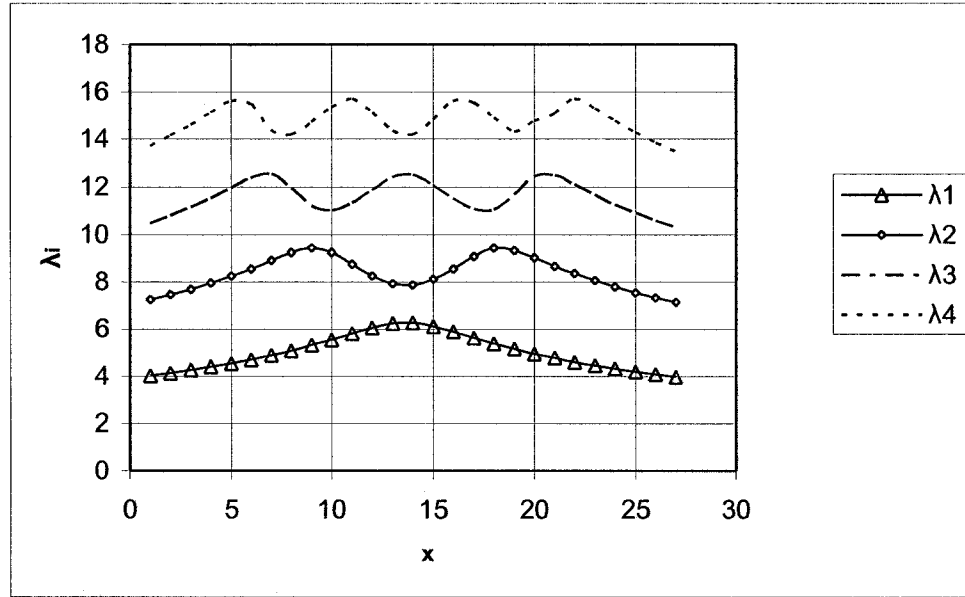


Figure 2.29 Numerical results of equation (2.146)

As a result of expressions (2.146) and (2.142) vibration frequencies Ω_i are defined as:

$$\Omega_i = \sqrt{\frac{EI}{\rho L^4}} \lambda_i, \quad i=1,2,3,4 \quad (2.147)$$

In this particular case it has been assumed that a model based on the first four modes provides results with sufficient accuracy. Now the numerator of (2.145) becomes:

$$\begin{aligned} N_T(\lambda, x) = & \left(-7.8 \cdot 10^{-3} x^3 + 1.4 \cdot 10^{-4} x^4 + 0.1 x^2 \right) \left\{ \left(\frac{1}{\Omega_1^2 \Omega_2^2 \Omega_3^2 \Omega_4^2} \right) s^8 + \dots \right. \\ & + \left(\frac{\frac{1}{\Omega_2^2} + \frac{1}{\Omega_1^2}}{\Omega_3^2} + \frac{1}{\Omega_1^2 + \Omega_2^2} + \frac{1}{\Omega_1^2 \Omega_2^2 \Omega_3^2} \right) s^6 + \left(\frac{\frac{1}{\Omega_3^2} + \frac{1}{\Omega_2^2} + \frac{1}{\Omega_1^2}}{\Omega_4^2} + \frac{\frac{1}{\Omega_2^2} + \frac{1}{\Omega_1^2}}{\Omega_3^2} + \frac{1}{\Omega_1^2 \Omega_2^2} \right) s^4 + \dots \\ & \left. + \left(\frac{1}{\Omega_4^2} + \frac{1}{\Omega_3^2} + \frac{1}{\Omega_2^2} + \frac{1}{\Omega_1^2} \right) s^2 + 1 \right\} \end{aligned} \quad (2.148)$$

A similar procedure can be applied to obtain a denominator expression of (2.141).

$$D_T(\lambda) = 2 \left(\frac{\lambda}{L} \right)^3 EI \sin(\lambda) \sinh(\lambda) \quad (2.149)$$

Further, by analogy to the procedure used to obtain the numerator, equation (2.148) becomes:

$$D_T(\lambda) = \left(240E \frac{I}{L^3} \right) \prod_{i=0}^{\infty} \left(1 - \frac{\lambda^4}{\lambda_{Di}^4} \right) \quad (2.150)$$

where λ_{Di} are given by

$$D_T(\lambda) = 0 \quad (2.151)$$

Thus by using an numerical approach and solving equation (2.151) for the first 4 modes, and by knowing that:

$$\omega_i = \sqrt{\frac{EI}{\rho L^4}} \lambda_i \quad (2.152)$$

the following natural frequencies can be obtained:

Natural vibration frequencies	Values [rad/s]
ω_1	1.0060
ω_2	4.0240
ω_3	9.0540
ω_4	16.0960

Table 2.3 Natural frequencies of the ODU Maglev track idealized model

Finally combining (2.150) and (2.152), an expression for the denominator of the transcendental transfer function (2.149) can be presented:

$$D_T(s) = 16713002.8 \cdot \left[\left(1 + \frac{s^2}{\omega_1^2} \right) \left(1 + \frac{s^2}{\omega_2^2} \right) \left(1 + \frac{s^2}{\omega_3^2} \right) \left(1 + \frac{s^2}{\omega_4^2} \right) \right] = \quad (2.153)$$

$$= 46.88s^8 + 16782.83s^6 + 126931.83s^4 + 17366828.01s^2 + 16713002.81$$

which yields:

$$\begin{aligned}
G_T(s) = \frac{Z(x_2, s)}{F(s)} = & \left(-7.8 \cdot 10^{-3} x^3 + 1.4 \cdot 10^{-4} x^4 + 0.1 x^2 \right) \left\{ \left(\frac{1}{\Omega_1^2 \cdot \Omega_2^2 \cdot \Omega_3^2 \cdot \Omega_4^2} \right) s^8 + \dots \right. \\
& + \left(\frac{\frac{1}{\Omega_2^2} + \frac{1}{\Omega_1^2}}{\Omega_3^2} + \frac{1}{\Omega_1^2 + \Omega_2^2} + \frac{1}{\Omega_1^2 \cdot \Omega_2^2 \cdot \Omega_3^2} \right) s^6 + \left(\frac{\frac{1}{\Omega_3^2} + \frac{1}{\Omega_2^2} + \frac{1}{\Omega_1^2}}{\Omega_4^2} + \frac{\frac{1}{\Omega_2^2} + \frac{1}{\Omega_1^2}}{\Omega_3^2} + \frac{1}{\Omega_1^2 \Omega_2^2} \right) s^4 + \dots \\
& \left. \left(\frac{1}{\Omega_4^2} + \frac{1}{\Omega_3^2} + \frac{1}{\Omega_2^2} + \frac{1}{\Omega_1^2} \right) \cdot s^2 + 1 \right\} / (46.8s^8 + 16782.8s^6 + 126931.8s^4 + 17366828.0s^2 + 16713002.8)
\end{aligned}
\tag{2.154}$$

Bode plots of the above transfer function (2.154) for three different cases when the vehicle is on the track at: $x = 254$ [in], $x \cong \frac{L}{4} = 1778$, [in], $x \cong \frac{L}{2} = 3302$ [in], are shown in the *Figure 2.30*.

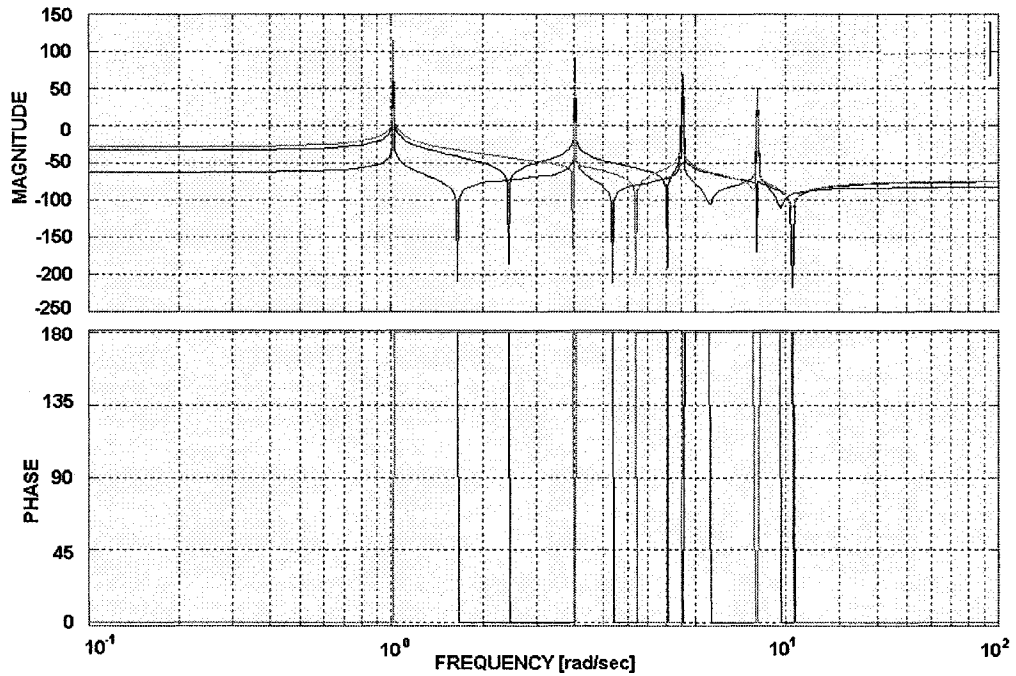


Figure 2.30 Bode plots for three positions of the vehicle on the rail guideway

This figure illustrates that the transfer function zeros exhibit considerable variation as the vehicle moves along the guideway. The implications of this variation are explored next.

2.15.1 Zero Movement and its Impact on the Control Design

Transmission zero variation in the Maglev transfer function can have significant impact on closed-loop stability. To illustrate this, consider a simple Maglev transfer function where only the first guideway bending mode is included. According to (2.62), the transfer function can be written as:

$$G(s) = \frac{K_x(s + \delta b)(s + \delta \bar{b})}{(s - p_1)(s + p_2)(s + p_3)(s + a)(s + \bar{a})} \quad (2.155)$$

where a, \bar{a} and b, \bar{b} are conjugate imaginary poles and zeros associated with guideway flexibility. It is well known that if the actuators and sensors are collocated, then $|a| > |b|$ and $|\bar{a}| > |\bar{b}|$. In (2.155), the variable δ represents zero variation due to vehicle position change. Thus, for the Maglev vehicle $\delta = 1$ when vehicle is above the column, while $\delta > 1$ when vehicle approaches a center position between two pillars.

Assume that, in addition to a classical PD compensator (2.47), a Notch filter is used to alleviate the impact of the mode at frequency a .

$$G_N(s) = \frac{(s + a + \varepsilon_1)(s + \bar{a} + \bar{\varepsilon}_1)}{(s^2 + 2\omega\zeta s + \omega^2)} \quad (2.156)$$

This implies that open loop transfer function has following form:

$$G_{OL}(s) = \frac{(K_p + K_D s)K_x(s + \delta b)(s + \delta \bar{b})(s + a + \varepsilon_1)(s + \bar{a} + \bar{\varepsilon}_1)}{(s - p_1)(s + p_2)(s + p_3)(s + \delta \cdot a)(s + \delta \cdot \bar{a})(s^2 + 2\omega\zeta s + \omega^2)} \quad (2.157)$$

Because of the existence of $\varepsilon_1, \bar{\varepsilon}_1$ and δ terms a and \bar{a} cannot be eliminated [3]. Furthermore, the open loop expression (2.155) with compensator (2.47) together with (2.156) and following conditions:

$$a + \varepsilon_1 < \delta a, \quad (2.158)$$

$$\bar{a} + \varepsilon_2 < \delta \bar{a}, \quad (2.159)$$

makes changes in the poles and zeros order.

As can be seen (2.157), the system's performance was degraded where the order of poles and zeros is distorted. This situation is illustrated in *Figures 2.32 and 2.33* below.

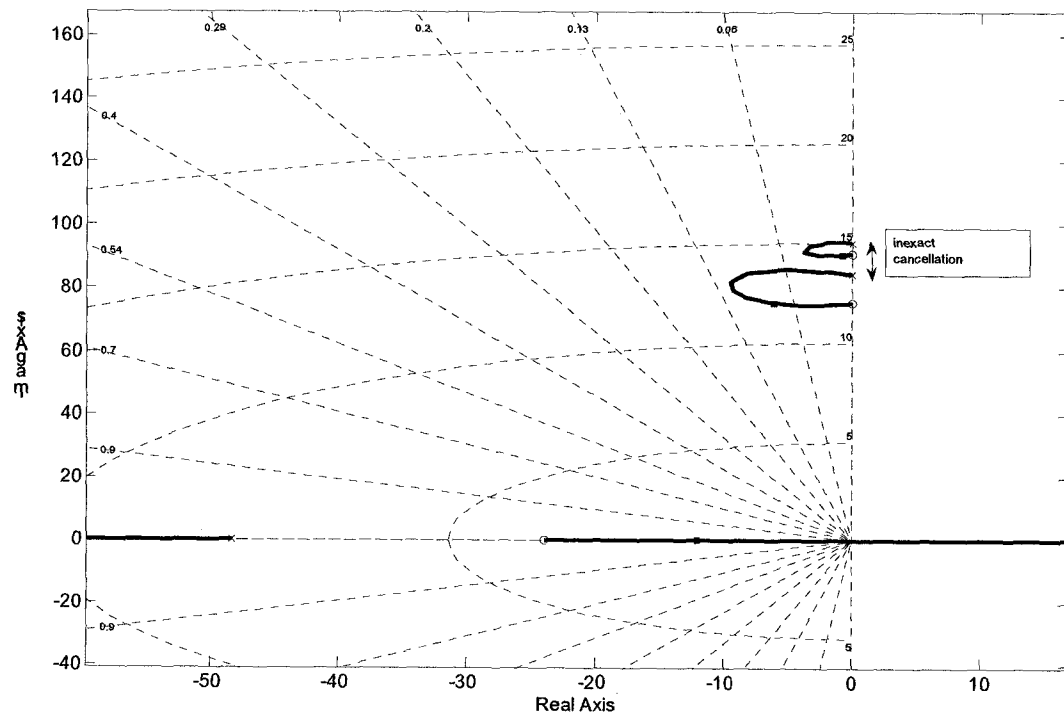


Figure 2.31 Maglev vehicle above column; PD compensator with notch filter

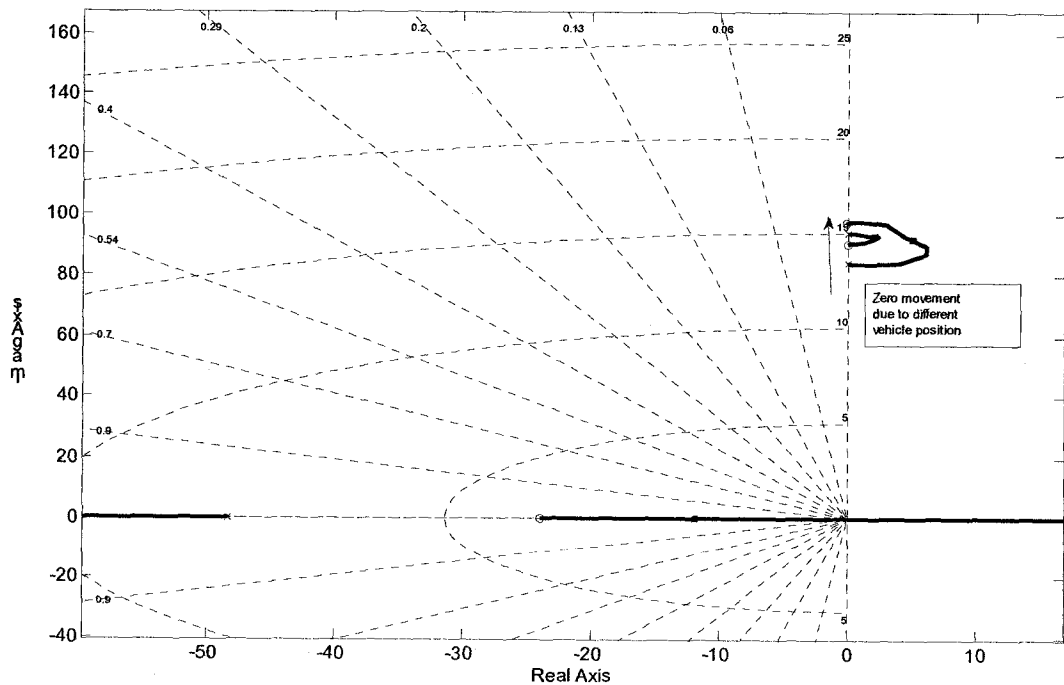


Figure 2.32 Maglev vehicle between columns; PD compensator with notch filter

In the example shown in the above figures it is clear that change of zero frequency from i.e.: 8 [Hz] into 11 [Hz] while Notch filter remains the same makes system unstable.

2.16 Summary

In this chapter a few simple concepts related to the Maglev controller design were introduced.

First, expressions for levitation force were developed as functions of gap and flux for use with feedback control laws that used gap and flux sensors respectively. Consideration of fringing effects led to significant changes in the levitation force, thus fringing should be included in designing a successful control system. An example model of a current amplifier and an electromagnet illustrated existence of a stable pole which should be considered in controller design.

Second, it was shown that as long as a flexible system is collocated, a compensator designed to stabilize its rigid analogue, will not necessarily stabilize the flexible system, further, the compensator has more restricted gain limits.

Third, based on basic models, some advantages of using a decentralized control approach were presented. It was demonstrated that centralized control with PD compensation exhibits lack of authority for control of some flexible modes.

Fourth, it was found that using flux feedback in the Maglev control system provides more robustness meaning smaller variation in Bode plot gains for different operation conditions. Thus flux feedback de-attenuates the impact of the nonlinearities. The use of inverse force calculation for feedback linearization provides similar benefits.

Finally the dynamics of the Maglev's position on the track and its interaction with the guideway was evaluated. It is shown that as a result of variations in positions the system transfer function zeros vary, and this makes robust control design more difficult.

In the next chapters most of the issues taken up in this section will be further investigated for specific examples.

3. MAGLEV TEST RIG MODEL

A laboratory built, Maglev Test Rig was created to enable the design and investigation of different control laws in a realistic environment. The use of the Test Rig designed to emulate actual vehicle characteristics, provided the ability to evaluate the performance of designs and to identify designs that could possibly be used with the real full-scale ODU Maglev vehicle. This simplified version of a full-scale EMS system is shown in *Figure 3.1*.

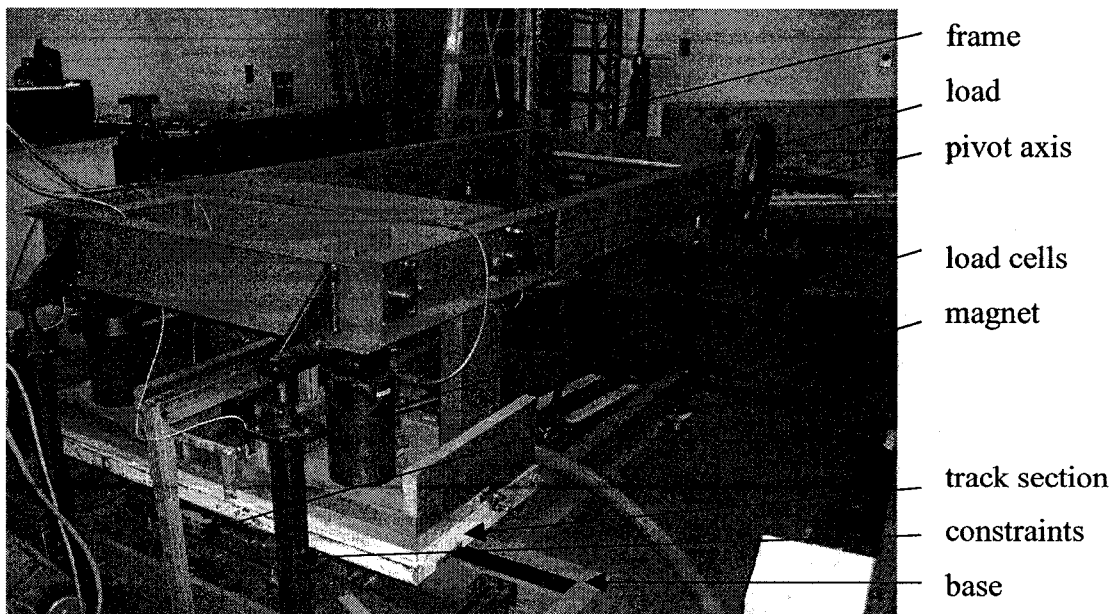


Figure 3.1 The Maglev Test Rig laboratory setup

In this chapter a model of the Maglev Test Rig system will be developed. As discussed in Chapter 1, EMS Maglev systems use electromagnets to attract the vehicle towards the track. In the Test Rig one electromagnet is fixed to the base of the Test Rig. A short length of track connected to load cells is suspended above the magnet via a hinged steel frame in a four-bar linkage arrangement. Weights attached to the opposite end of the hinged frame represent the load of the vehicle. When the electromagnets are activated, the track section is pulled down, thus levitating the load. To avoid a situation where the track hits electromagnet, two adjustable motion constraints were attached to the Test Rig base. The electromagnet and the track section are components from the original ODU maglev system. The frame bar linkage and weights were chosen so that the magnet would be reacting to a load similar to that which one magnet would encounter in the actual vehicle.

3.1 Electromagnetic Part of the Test Rig

In Chapter 2 it was noted that the Maglev system can be considered as divided into two subsystems: electromagnetic and structural. Here, the electromagnetic part of the Test Rig was described.

A high voltage source is required to drive the electromagnet. A laboratory DC power supply for the Test Rig was provided by a Clinton 3-Phase SCR controlled rectifier capable of producing up to 400 Volts DC with a maximum current output of up to 300 [Amps]. To drive the current to the coil, a Pulse Width Modulated (PMW) Advanced Motion Controls model 100A40K servo amplifier was used. The amplifier has a maximum intermittent output current of 100 [Amps], and a rated continuous current of 50 [Amps].

3.2 Current Amplifier Modeling and its Calibration

In this section, the modeling and calibration of the PWM 100A40K current amplifier is discussed. The current circuit specifications are shown in *Table 3.1*.

VARIABLE	VALUE
Voltage	400 V
Coil resistance	1.83 Ω
Inductance	0.68 H
Maximum current	50+ A
Nominal current at 0.4 inch gap	25 A

Table 3.1 Electromagnet circuit parameters

Initially, as a result of the electromagnet's large inductance, the amplifier provided poor current tracking response using the factory settings. Increasing the current feedback gain by a factor of 4.7 from the factory settings was found to give acceptable current tracking.

To validate the simplified representation of the PWM amplifier, a model of the combined electromagnet amplifier system was built. This model was created using Matlab[®] software and Simulink[®] toolbox. Block schemes of this model are shown in *Figure 3.2*. The amplifier is modeled as a constant gain with a current feedback loop. The current feedback gain, K_a , was introduced in the previous chapter.

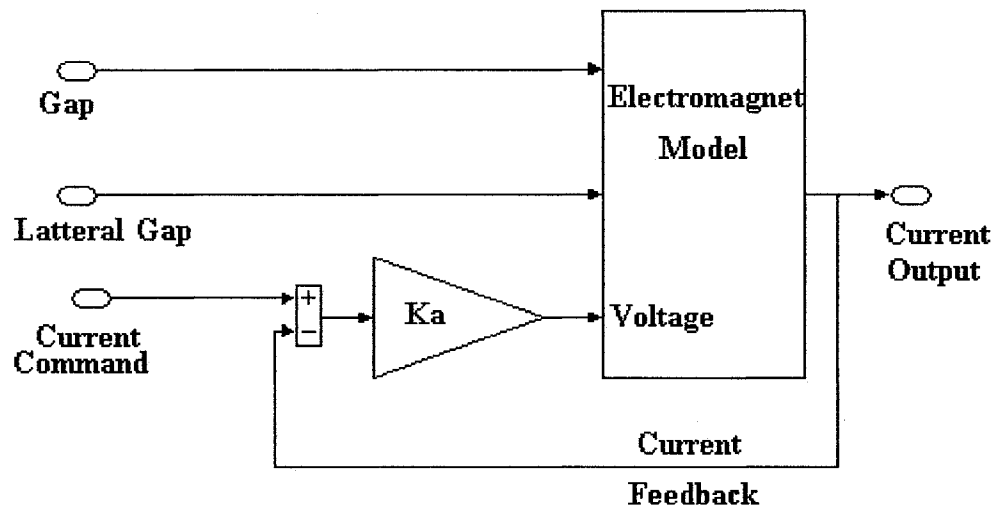


Figure 3.2 Electromagnet block with the current amplifier

In Figure 3.2 a general view of the combined current amplifier and electromagnet is presented. The electromagnet details inside the block labeled Electromagnet Model are shown below in Figure 3.3. The slew rate and current limiter are included to account for nonlinearities.

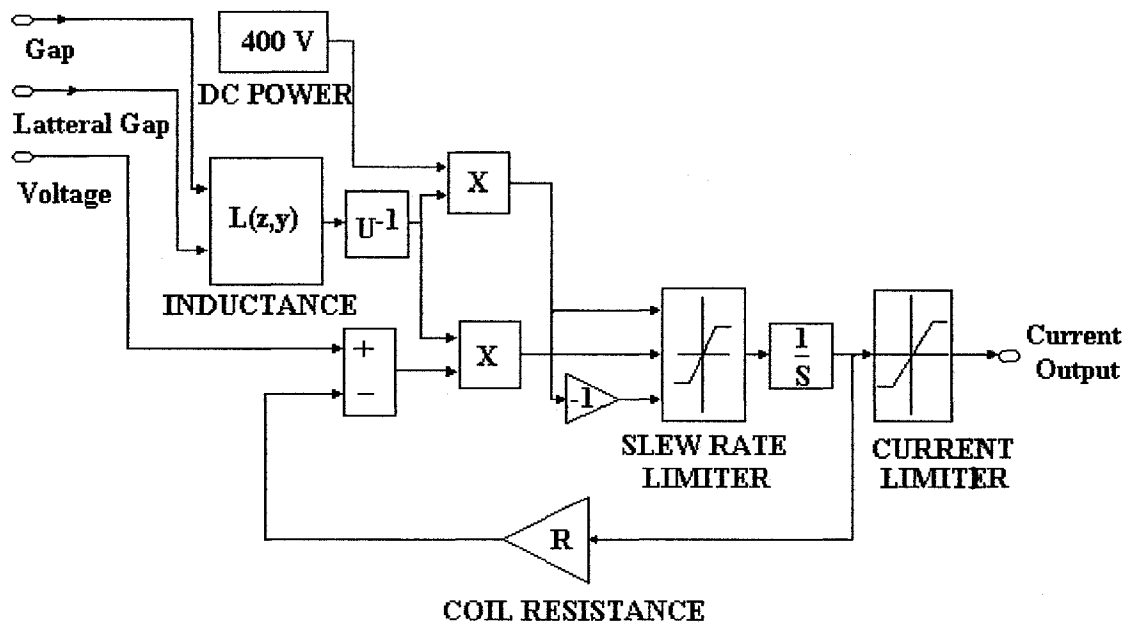


Figure 3.3 Electromagnet model created in Matlab® Simulink®

Experimental results indicated that, increasing the current feedback resistor from the factory setting 100 [k Ω] to 470 [k Ω], the value of K_a in the amplifier model was increased to approximately 256 (from the initial value of 56).

Figure 3.4 showed that by increasing current feedback gain inductance pole migrates to higher frequencies. A similar phenomenon can be observed when the gap is increased (Figure 3.5). From the perspective of stability, it is not desirable to have this pole near the origin. For larger gaps the inductance pole approaches high frequencies on the order of ~ 100 [Hz] (gap $z_0 = 0.9$ [in], current reference $I_0 = 30$ [Amps], $K_a = 256$). For small gaps its value is around ~ 20 [Hz] (gap $z_0 = 0.1$ [in], current reference $I_0 = 30$ [Amps], $K_a = 265$). For a resistance of 470 [k Ω], resulting K_a of 256 the inductance pole was judged to be at a high enough frequency for both small and large gaps.

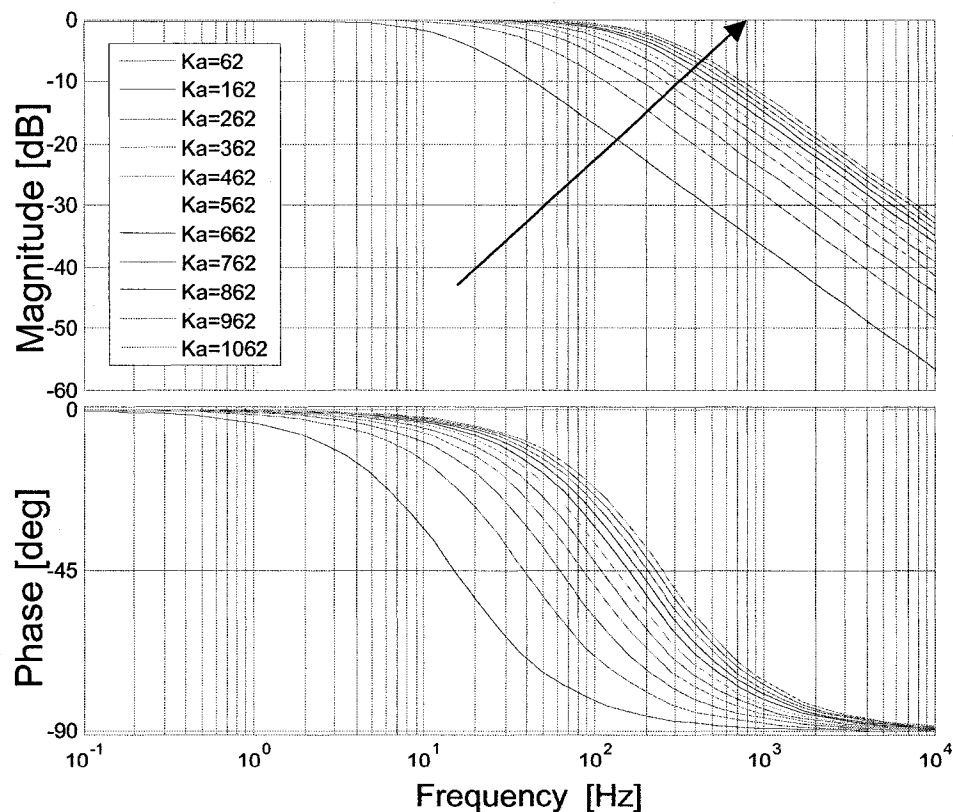


Figure 3.4 Electromagnet characteristics for different K_a gains (arrow indicates increasing K_a)

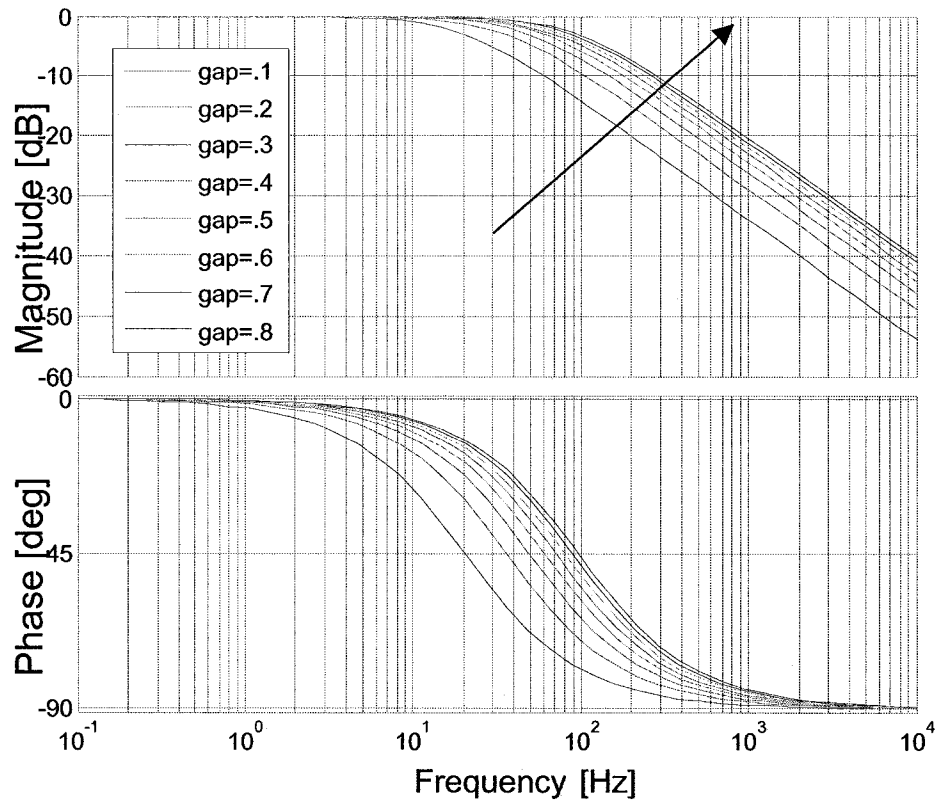


Figure 3.5 Electromagnet model for different gaps at $I_0=30A$ and $K_a=256$ (arrow indicates increasing gaps)

3.3 Effects of Non-linearities on Amplifier Current Following

3.3.1 Rate Limit and Amplifier Saturation

Here the combined effects of rate limit and amplitude saturation in the amplifier/magnet coil sub-system of the Maglev Test Rig are discussed. Primary emphasis is on rate limit saturation, which is a influential factor in tracking the current.

For a given gap, and assuming the magnet inductance L , the maximum current slew rate is determined by (2.29) and (2.30) to be:

$$\left. \frac{di}{dt} \right|_{\max} = \frac{V_{\max}}{L} = 667 \quad [\text{A/sec}] \quad (3.1)$$

:

Consider a sinusoidal current command at a given radian frequency, ω , and zero-to-peak amplitude, A_m .

$$I^{Cmd} = A_m \sin \omega t \quad (3.2)$$

This command has a maximum slope of $A_m \omega$. For a given frequency ω , the maximum amplitude that can be tracked linearly is governed by the slew rate limit of 667 [A/sec], according to:

$$A_{\max}(\omega) = 667 / \omega \quad (3.3)$$

The maximum linear tracking amplitudes for various frequencies are tabulated below (Table 3.2).

$f = 2\pi\omega$ (Hz)	5	10	20	40	70	100
A_{\max} (A)	21.23	10.62	5.31	2.65	1.52	1.06

Table 3.2 Linear tracking amplitudes for various frequencies

To compare the effects of amplitude and rate saturation, the following simple Simulink® simulation was prepared (Figure 3.6).

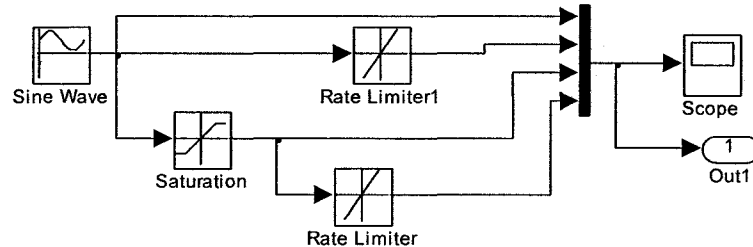


Figure 3.6 Amplitude and rate saturation model

Figures 3.7 and 3.8 present results obtained using this simulation at various representative frequencies and amplitudes to illustrate the separate and combined effects of rate and amplitude saturation shown in Table 3.2. It can be seen that for a 25 [A] (measured current command) expressed by (3.2) the response is good, but as the frequency increases the rate saturation reduces the amplitude of the response signal and tends to change its shape toward that of a triangle wave. This could be very undesirable in some cases. The sharp peaks in the output signal may inadvertently excite high frequency dynamics. Moreover, the resulting triangle wave is phase shifted with respect to the command signal, and in the limit this phase shift approaches $\pi/2$ radians.

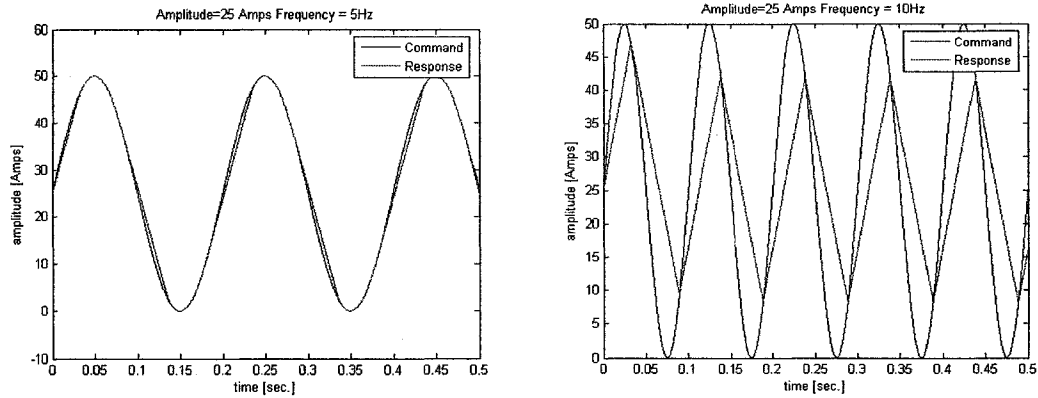


Figure 3.7 Saturation simulation results for amplitude signal 25 [A] and frequency 5 and 10 [Hz]

As the command amplitude decreases the same phenomena occurs but at a higher frequency.

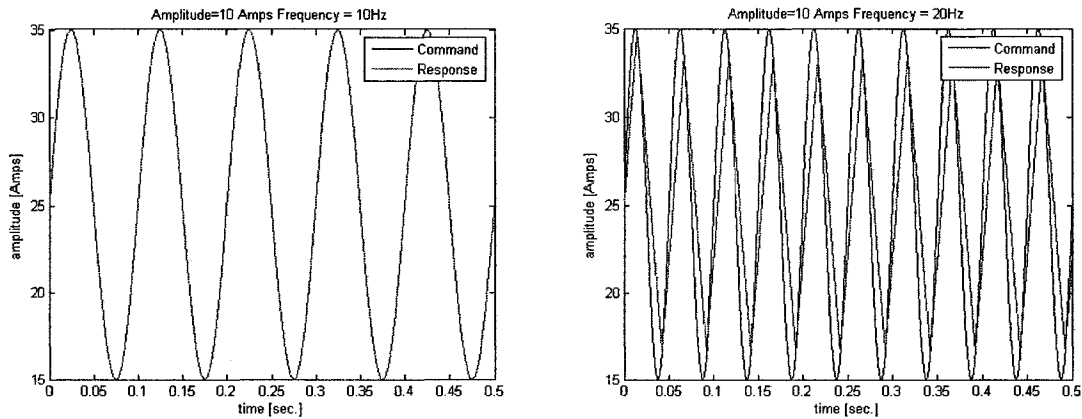


Figure 3.8 Saturation simulation results for signal amplitude 10 [A] and frequency 10 and 20 [Hz]

The net result of the amplitude reduction and phase shift is similar to a low pass filter with an amplitude-dependent break frequency.

For real systems, accurate tracking of the desired signal is not the only issue. In many applications signal noise appears to have significant impact on the system response. To evaluate the effect of saturation on a desired command signal carrying an additive higher frequency noise signal, the simulation from the Figure 3.6 was modified as follows.

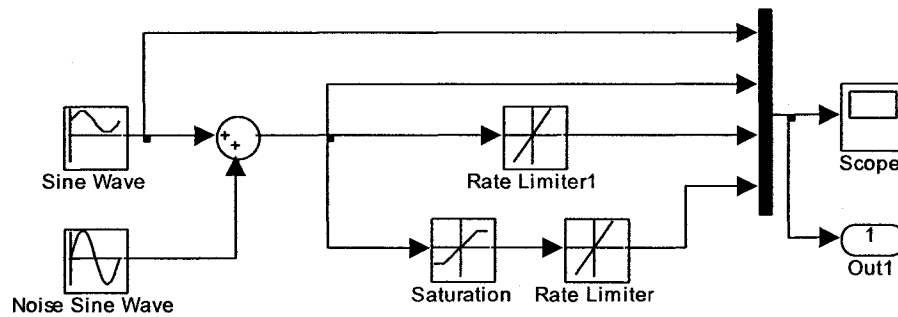


Figure 3.9 Simulink® model for rate and saturation effect at high frequencies

The following Figure 3.10 shows the impact of rate and amplitude saturation on a 2 [Hz] command signal (desired) tainted with a 100 [Hz] spurious sinusoid of equal amplitude. Noise signal parameters are picked up based on experimental data. It is noted that the rate limiter serves the desirable function of selectively attenuating the response to the spurious 100 [Hz] signal, without attenuating the command signal.

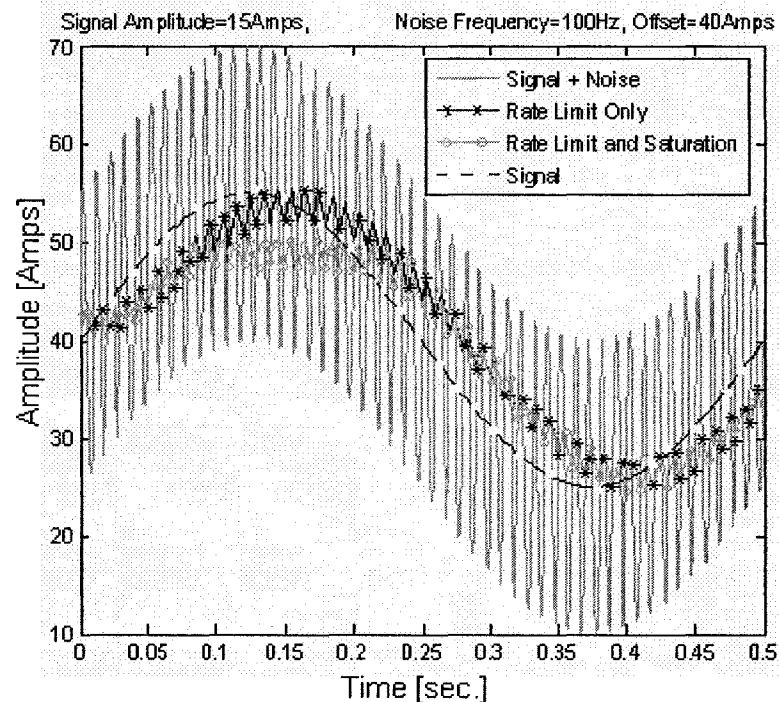


Figure 3.10 Rate limit saturation with high frequency noise

On the other hand, the cost of this amplitude reduction is significant phase shifting of the overall output signal. This generally has a destabilizing effect on feedback control systems.

3.3.2 Effect of Hysteresis

The hysteresis can be explained based on the non-linear properties of magnetic materials (*Figure 3.11*).

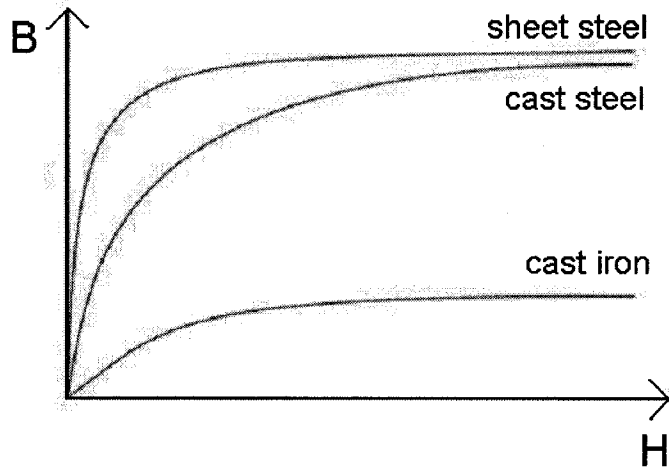


Figure 3.11 General example of flux density B vs. field intensity H for different metal materials

The relationship of field intensity H (which is part of force expression) to flux density B is graphed in a form called the normal magnetization curve. In practice it is possible to apply so much magnetic field using current to a ferromagnetic material that no more flux can be sustained. This condition is known as magnetic saturation. When the retentivity of a ferromagnetic substance interferes with its re-magnetization in the opposite direction, a hysteresis occurs for flux density. As shown in equations (2.13) and (2.14) this hysteresis can be mapped from the electromagnetic field B into a lift force (*Figure 3.13*). In such a situation, ion for electromagnetic force computed based on the analytical express can differ from its real measured value.

Actual force and gap characteristics are compared in *Figure 3.12* and *Figure 3.13*. During the experiment used to obtain the data in *Figures 3.14* and *Figure 3.13* 4 cycles of increasing and decreasing current were repeated. In the worst case, the difference due to the hysteresis effect reaches a value of uncertainty around 0.017 [in.] in the gap measurements and 800 [lbf] for the resulting force.

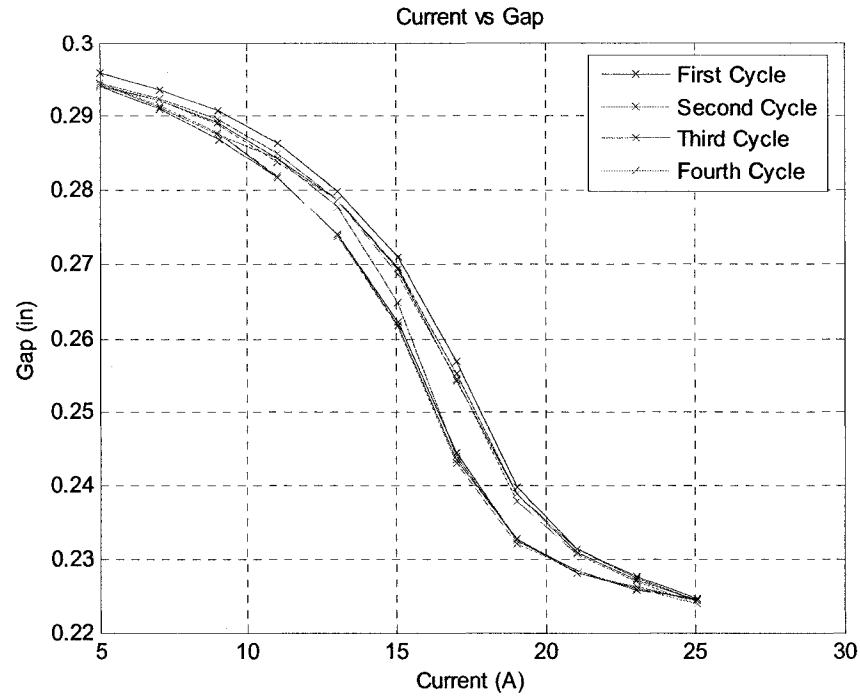


Figure 3.12 Hysteresis phenomena current vs. gap

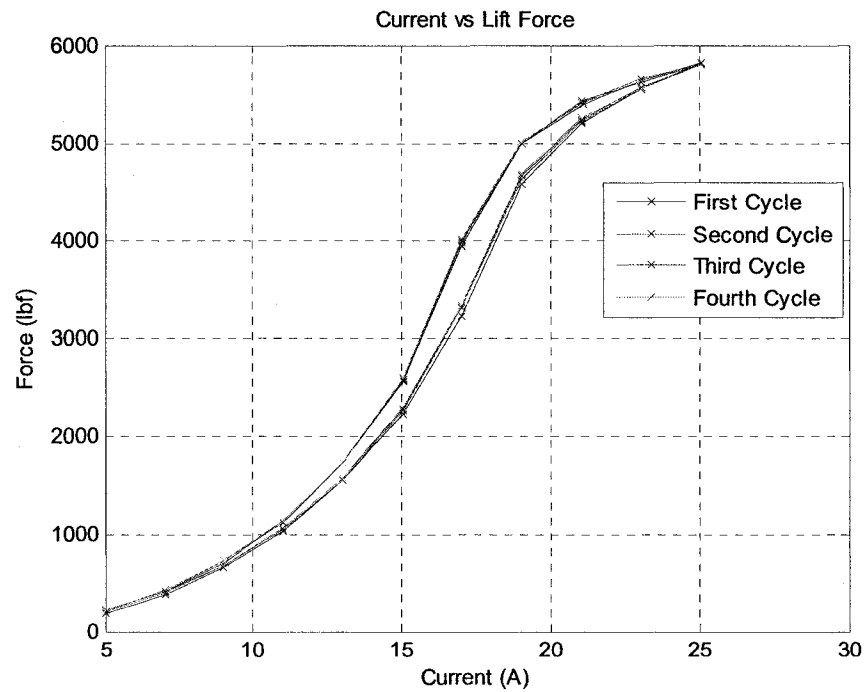


Figure 3.13 Hysteresis phenomena current vs. lift force

In summary, it is obvious that under certain conditions, current slew rate limit and the electromagnet hysteresis could have significant impact on system stability. This is the

In equations (3.4) values e_i represent distances, shown in the *Figure 3.14*, between the geometrical center of the Test Rig frame and the location where steel linkage are attached to the four-bar frame. Values M , $M_{weights}$, m_1 , m_2 , m_{frame} , m represent respectively: total mass hinged on the rear side of the frame, weights used as an applied load, mass of the track, mass of the track holder and load cell, mass of the Test Rig frame, and total mass hinged on the front side of the frame. The value of $M_{weights}$ can be varied to simulate variations in passenger loading on the real Maglev vehicle (40 [lbs] up to 320 [lbs]). A value of 40 [lbs] on the Test Rig represents the empty ODU vehicle while 260 [lbs] attached to the Test Rig frame represents 120 passengers (170 [lbs] each) onboard on the vehicle. Also, to be more conservative for design testing a weight of 320 [lbs] was sometimes used (fully loaded case).

Values x_{cm_f} and x_{cm} define respectively, the dimensions between the geometrical center of the frame and center mass of the frame, and the distances between the geometrical center of the frame and center mass of the entire system. Gravitational acceleration is defined as g and the gap between the track and the electromagnet as z .

To calculate mass and inertia values for the Test Rig, the frame structure was divided into elements. Expressions used for all inertia value calculations are shown in the *Table 3.3*. In cases where the moment of the inertia is not about the center of mass of the considered element, then Steiner's law is applied.

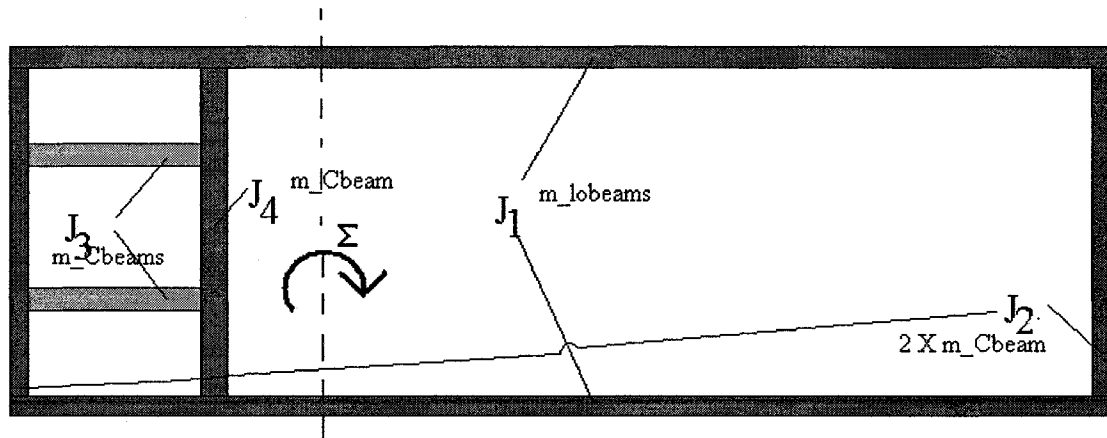


Figure 3.15 Top view of the frame inertia components

INERTIA DESCRIPTION	EXPRESSION
Mass center of the frame	$x_{cm_f} = \frac{\sum_i e_i \cdot m_i}{m_{frame}} = \frac{m_{_Cbeam} \cdot e_3 + m_{_Cbeams} \cdot e_2 + m \cdot e_1}{m_{_Cbeam} s + m_{_Cbeam}}$
Inertia of the long C beams	$J_1 = (1/3) \cdot m_{_lobeams} \cdot (2 \cdot e_0)^2 + m_{_lobeams} \cdot (e_4)^2$
Inertia of the C beams (border ones - 2 pieces):	$J_2 = m_{_Cbeam} \cdot (e_0 - e_4)^2 + m_{_Cbeam} \cdot (e_0 + e_4)^2$
Inertia of the C beams (small ones inside frame - 2 pieces):	$J_3 = m_{_Cbeams} \cdot (e_2 - e_4)^2$
Inertia of the C beam inside frame:	$J_4 = m_{_Cbeam} \cdot (e_3 - e_4)^2$
Total Test Rig frame inertia	$J_{frame} = J_1 + J_2 + J_3 + J_4$
Inertia due to load mass at the rear side of the frame	$J = J_{frame} + (M + M_{weights}) \cdot (e_1 + e_4)^2 + m \cdot (e_1 - e_4)^2$

Table 3.3 Inertia calculation for the Maglev Test Rig

Assuming small variations in angular rotation Σ , it is convenient to express equation (3.4) in terms of gap z as follows:

$$\frac{J}{e_5} \ddot{z} = F_{LEV} e_5 - m e_5 g + m_{frame} g (e_4 - x_{cm_f}) + (M + M_{Weights}) g e_6 \quad (3.5)$$

For control design, it is desirable to represent the equation of motion (3.5) in state space form. The following states are assumed: $\vec{x} = \begin{bmatrix} z \\ \dot{z} \end{bmatrix}$. Then (3.5) can be written as:

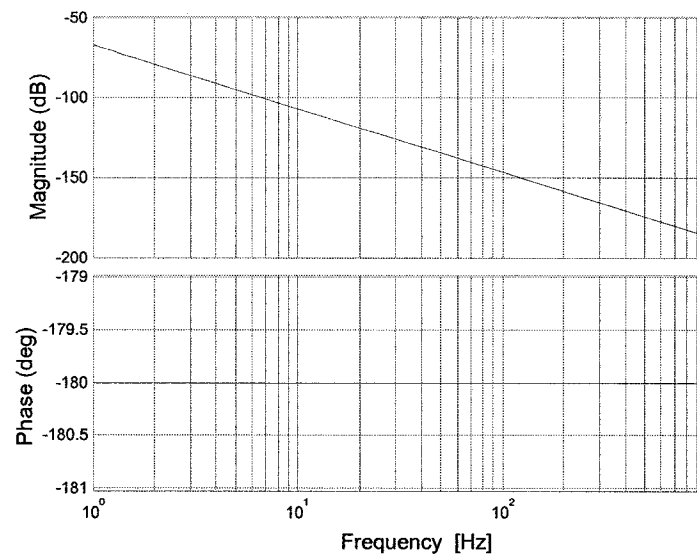
$$\dot{\vec{x}} = \begin{bmatrix} \dot{z} \\ \ddot{z} \end{bmatrix} = \begin{bmatrix} 0 & 1 \\ 0 & 0 \end{bmatrix} \begin{bmatrix} z \\ \dot{z} \end{bmatrix} + \begin{bmatrix} 0 & 0 \\ \frac{e_5^2}{J} & -\frac{e_5^2}{J} \end{bmatrix} \begin{bmatrix} 0 \\ \frac{(e_4 - x_{cm_f}) e_5}{J} \end{bmatrix} + \begin{bmatrix} 0 \\ \frac{e_5 e_6}{J} \end{bmatrix} \begin{bmatrix} F_{LEV} \\ mg \\ m_{frame} g \\ (M + M_{Weights}) g \end{bmatrix} \quad (3.6)$$

Choosing gap as the output variable leads to:

$$\vec{y} = [z] = \begin{bmatrix} 1 & 0 \end{bmatrix} \begin{bmatrix} z \\ \dot{z} \end{bmatrix} \quad (3.7)$$

Figure 3.16 illustrates the Bode plots for the rigid Maglev Test Rig system.

Rigid structural model of the Maglev test rig

*Figure 3.16 Bode plots for the rigid Test Rig system*

It can be seen that the above Bode plot represents a system similar to that introduced in Chapter 2, corresponding to a single rigid mass in space.

In this section a very basic structural model of the Maglev Test Rig was developed. Because of its simplicity, it was intended to be a useful a reference example for the more complex systems that are to follow.

3.5 Equations of Motion for Structural Model (flexible)

In sub-chapter 3.4 a Maglev Test Rig was assumed and modeled as a rigid structure. This is not entirely accurate for this effort. In fact, the Test Rig was designed to have structural flexibility representative of the ODU Maglev vehicle. During laboratory testing, the investigated system exhibited elastic behavior. In this section, flexibility of the Test Rig are discussed and modeled.

In the interest of obtaining a simple model to characterize this flexibility, a system (illustrated in *Figure 3.14*) can be idealized as the lumped spring-mass model shown in *Figure 3.17*.

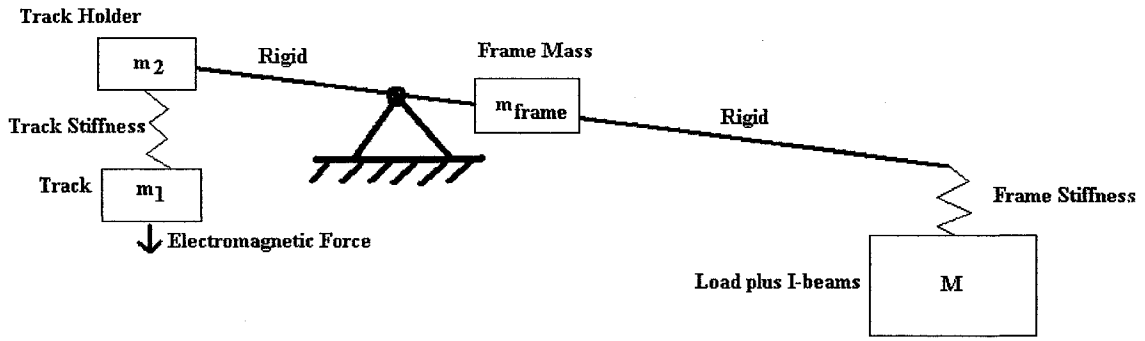


Figure 3.17 Spring-mass model of the Maglev Test Rig

It is noted that the system dynamics undergo a transition at the instant of levitation. Thus, it is necessary to model the system separately in the levitated and grounded states.

3.5.1 Levitated System Structural Model

First, consider the case when the system is levitated as idealized in Figure 3.18. Mass M represents the actual load hinged on the rear side of the frame, mass m_2' represents the mass of the track holder and the effective mass representing the inertia of the frame, therefore:

$$m_2' = m_2 + m_{frame} \cdot \left(\frac{e_4 - x_{cm_f}}{e_5} \right) \quad (3.8)$$

By measuring a deflection of one end of the Test Rig frame for known applied forces, values for k_1 and k_2 have been estimated to be:

$$k_1 = 1.1300e5 \text{ [lbf/in}^2\text{]} - \text{stiffness between track and track holder} \quad (3.9)$$

$$k_2 = 1.2126e5 \text{ [lbf/in}^2\text{]} - \text{stiffness of the frame} \quad (3.10)$$

$$k_3 = 2.5140e5 \text{ [lbf/in}^2\text{]} - \text{stiffness between mass M and ground} \quad (3.11)$$

Structural damping of 2%, has been incorporated into the model.

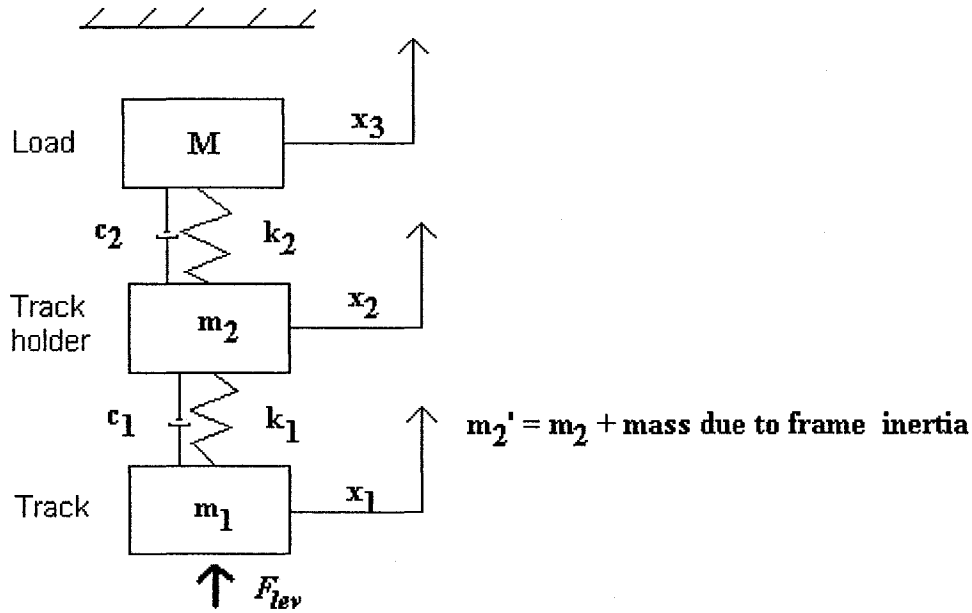


Figure 3.18 Levitated system

Thus, equations of motion of the Maglev system of Figure 3.18 can be expressed as:

$$\begin{bmatrix} \dot{x}_1 \\ \dot{x}_2 \\ \dot{x}_3 \\ \ddot{x}_1 \\ \ddot{x}_2 \\ \ddot{x}_3 \end{bmatrix} = \begin{bmatrix} 0 & 0 & 0 & 1 & 0 & 0 \\ 0 & 0 & 0 & 0 & 1 & 0 \\ 0 & 0 & 0 & 0 & 0 & 1 \\ -\frac{k_1}{m_1} & \frac{k_1}{m_1} & 0 & -\frac{c_1}{m_1} & \frac{c_1}{m_1} & 0 \\ \frac{k_1}{m_2'} & -\frac{(k_1 + k_2)}{m_2'} & \frac{k_2}{m_2'} & \frac{c_1}{m_2'} & -\frac{(c_1 + c_2)}{m_2'} & \frac{c_2}{m_2'} \\ 0 & \frac{k_2}{M} & -\frac{k_2}{M} & 0 & \frac{c_2}{M} & -\frac{c_2}{M} \end{bmatrix} \begin{bmatrix} x_1 \\ x_2 \\ x_3 \\ \dot{x}_1 \\ \dot{x}_2 \\ \dot{x}_3 \end{bmatrix} + \frac{1}{m_1} \begin{bmatrix} 0 \\ 0 \\ 0 \\ 1 \\ 0 \\ 0 \end{bmatrix} [F_{LEV}] \quad (3.12)$$

The above equations define a flexible structural model in a very convenient notation for further analysis of systems with collocated actuator and sensors. In the Test Rig setups the track section is attached to the track holder (see Figure 3.1 and Figure 3.19a), gap sensor is above the track holder. Thus, to be able to directly measure the actual gap between track and magnet a sensor target plate is built into the system, as shown in Figure 3.19b. In the results discussed herein, the case of measuring track motion directly is referred to as the collocated case. The non-collocated case represents the arrangement in which track holder position is actually measured.

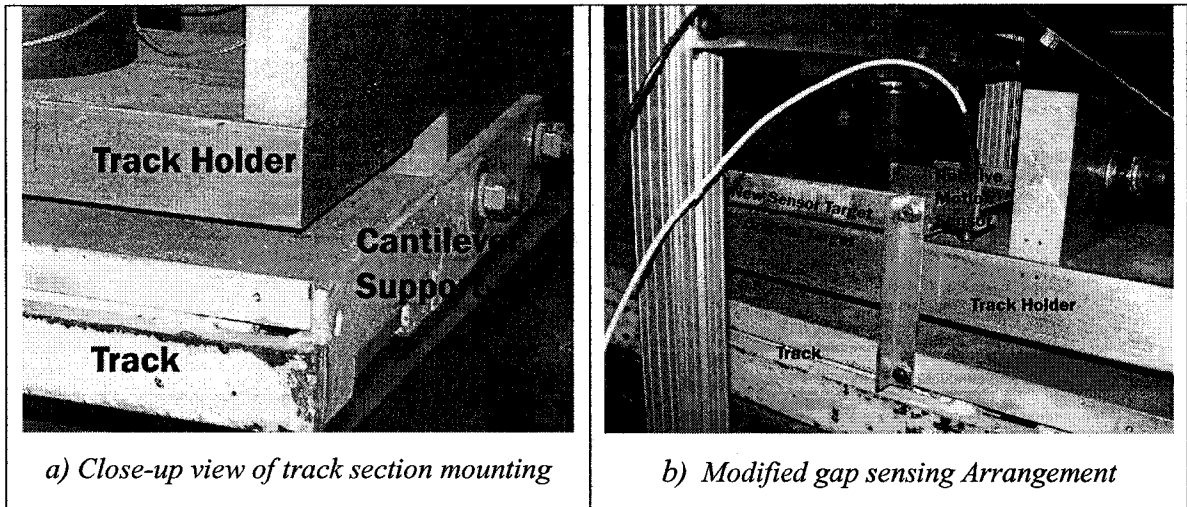


Figure 3.19 Track mounting

In order to consider and compare both cases, two different output equations are used:

$$\bar{y}_{collocated} = [x_1] = \begin{bmatrix} 1 & 0 & 0 & 0 & 0 & 0 \end{bmatrix} \begin{bmatrix} x_1 \\ x_2 \\ x_3 \\ \dot{x}_1 \\ \dot{x}_2 \\ \dot{x}_3 \end{bmatrix}; \quad (3.13)$$

$$\bar{y}_{non-collocated} = [x_2] = \begin{bmatrix} 0 & 1 & 0 & 0 & 0 & 0 \end{bmatrix} \begin{bmatrix} x_1 \\ x_2 \\ x_3 \\ \dot{x}_1 \\ \dot{x}_2 \\ \dot{x}_3 \end{bmatrix} \quad (3.14)$$

Figure 3.20 compares the Bode plots for the levitated collocated and non-collocated systems.

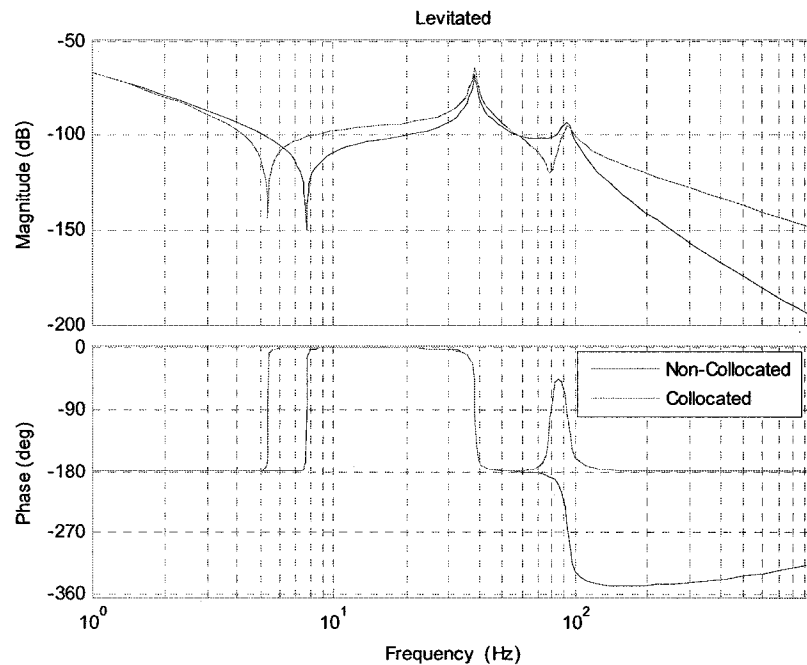


Figure 3.20 Bode plots for the levitated Test Rig system modeled

In the above figure, a lack of zero for the non-collocated case is clearly visible. This makes the system difficult to stabilize (as discussed in Chapter 2).

As was shown in this subsection, system flexibility can be modeled in a very simple and convenient way. This sprung-mass approach makes the system of interest easy for further analysis.

3.5.2 Grounded System Structural Model

Before the Maglev Test Rig achieves stable levitation and its gap between track and electromagnet will be set to its operational value, the system starts with the load resting on supports. This is referred to here as a grounded condition (see *Figure 3.14*). Using a variation of the levitated system model, the grounded Maglev Test Rig can be represented. The idealized schematic of this case is shown in *Figure 3.21*.

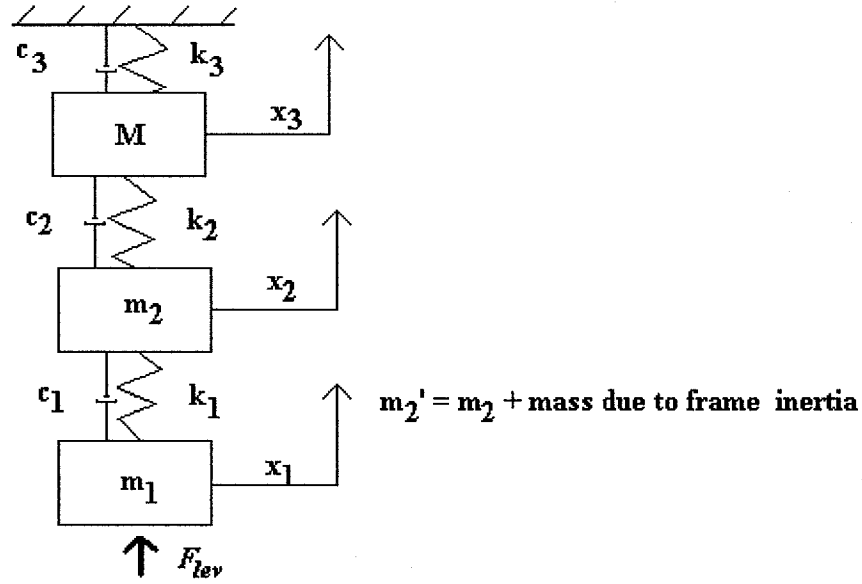


Figure 3.21 Grounded system

Figure 3.22 compares the Bode plots for the grounded collocated and non-collocated systems. The main difference between these two models is modeling the ground effect and interaction between frame supports and frame presented as k_3 and c_3 .

Equations of motion for system in the Figure 3.21 are following:

$$\begin{bmatrix} \dot{x}_1 \\ \dot{x}_2 \\ \dot{x}_3 \\ \ddot{x}_1 \\ \ddot{x}_2 \\ \ddot{x}_3 \end{bmatrix} = \begin{bmatrix} 0 & 0 & 0 & 1 & 0 & 0 \\ 0 & 0 & 0 & 0 & 1 & 0 \\ 0 & 0 & 0 & 0 & 0 & 1 \\ -\frac{k_1}{m_1} & \frac{k_1}{m_1} & 0 & -\frac{c_1}{m_1} & \frac{c_1}{m_1} & 0 \\ \frac{k_1}{m_2'} & -\frac{(k_1+k_2)}{m_2'} & \frac{k_2}{m_2'} & \frac{c_1}{m_2'} & -\frac{(c_1+c_2)}{m_2'} & \frac{c_2}{m_2'} \\ 0 & \frac{k_2}{M} & -\frac{(k_2+k_3)}{M} & 0 & \frac{c_2}{M} & -\frac{(c_2+c_3)}{M} \end{bmatrix} \begin{bmatrix} x_1 \\ x_2 \\ x_3 \\ \dot{x}_1 \\ \dot{x}_2 \\ \dot{x}_3 \end{bmatrix} + \dots$$

$$\dots + \begin{bmatrix} 0 \\ 0 \\ 0 \\ 1 \\ 0 \\ 0 \end{bmatrix} \frac{1}{m_1} [F_{LEV}] \quad (3.15)$$

As was done for the levitated case, the grounded case is studied for both possible situations. Collocated and non-collocated systems are shown (3.16 and 3.17).

$$\bar{y}_{collocated} = [x_1] = \begin{bmatrix} 1 & 0 & 0 & 0 & 0 & 0 \end{bmatrix} \begin{bmatrix} x_1 \\ x_2 \\ x_3 \\ \dot{x}_1 \\ \dot{x}_2 \\ \dot{x}_3 \end{bmatrix} \quad (3.16)$$

$$\bar{y}_{non-collocated} = [x_2] = \begin{bmatrix} 0 & 1 & 0 & 0 & 0 & 0 \end{bmatrix} \begin{bmatrix} x_1 \\ x_2 \\ x_3 \\ \dot{x}_1 \\ \dot{x}_2 \\ \dot{x}_3 \end{bmatrix} \quad (3.17)$$

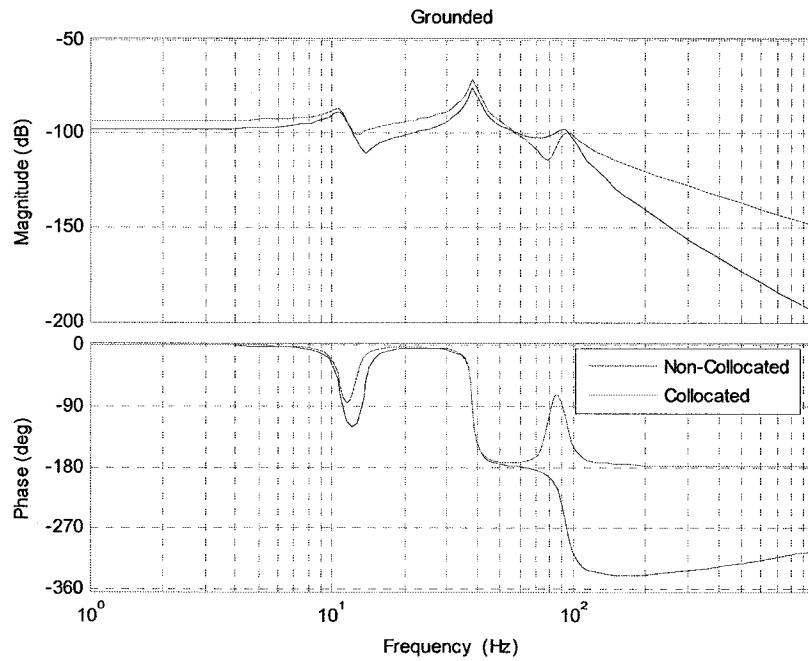


Figure 3.22 Bode plots for the “grounded” Test Rig system

According to Figure 3.20, it can be concluded that despite different system setups, sensor collocation has significant impact on stability.

3.5.3 Levitated and Grounded Structural Models Comparison

Here a comparison between different forms of the Maglev the Test Rig model is shown and briefly discussed. In *Figures 3.23 a* and *b* the grounded and levitated lumped-parameter models are compared with the rigid model obtained in Chapter 3.4.

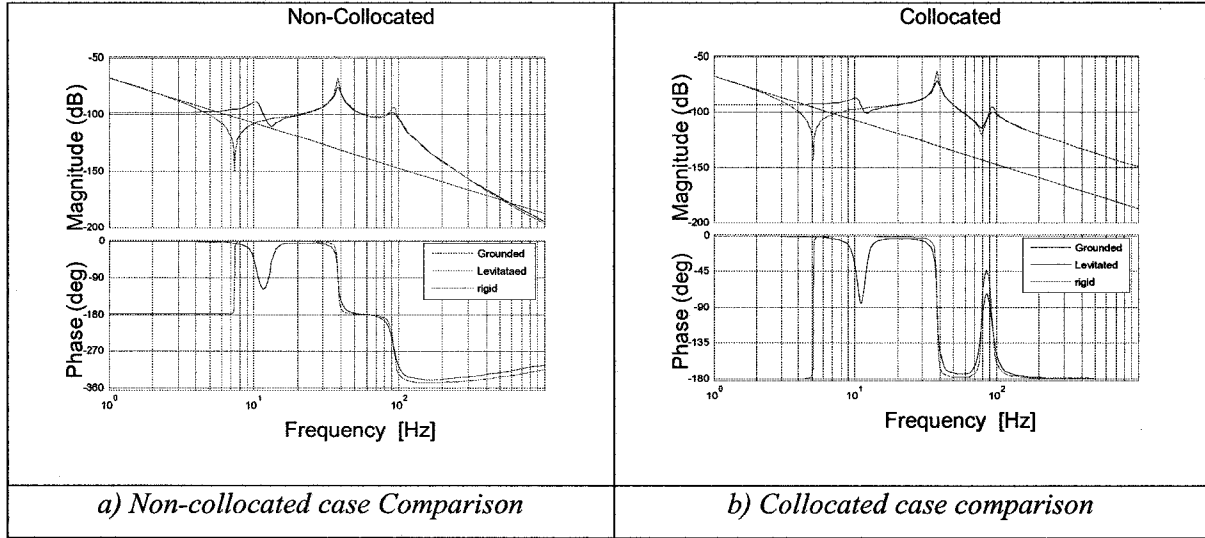


Figure 3.23 Bode plot comparison for Test Rig structural models

From the above figures it can be observed that:

- A simple rigid system and the flexible models, have matching dc gains and the slope of both bode curves is the same at low frequencies.
- An additional pair of zeros (at ~ 6.5 [Hz] or ~ 9 [Hz]) appears in levitated system. For the grounded case pole-zero combination occurs at 11 [Hz], which is a ground interaction effect. These zeros in both cases are due to stiffness k_3 .
- The low frequency poles in the grounded cases come from the rigid body poles. These observations show that the dynamic character of the system undergoes a significant change once levitation occurs.

3.6 Equation for the Entire Maglev Test Rig System

In this section the electromagnetic and structural models are combined. The expression (2.21) for the electromagnetic force is employed throughout. This choice was

based on experimental validation (see Chapter 2). Lateral displacement will be assumed to be zero ($y = 0$).

The equations introduced in the previous chapter can be combined in the order shown in the block diagram in *Figure 3.24* below.

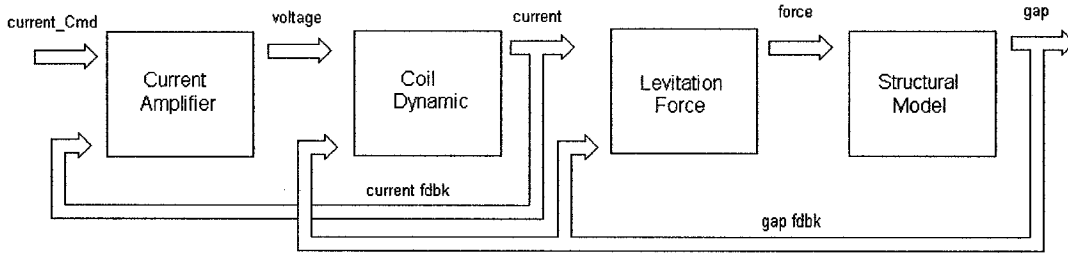


Figure 3.24 Maglev Test Rig modeling block diagram

This section compares different types of structural models. The equations of motion for three different systems are now explored.

3.6.1. Electromagnet Model Together with Rigid Structural Model

The Test Rig model equations introduced in subchapter 3.2 can be merged with the electromagnet equation from Chapter 2. Thus, combining (3.4) and (2.40) the following equations can be obtained:

$$\ddot{z} = F_{LEV} \frac{e_5^2}{J} - m \frac{e_5^2}{J} g + m_{frame} g \frac{(e_4 - x_{CM})e_5}{J} + (M + M_{Weights}) g \frac{e_5 e_6}{J} \quad (3.18)$$

$$\frac{dI}{dt} = \frac{I^{Cmd} K_a - I(K_a + R)}{L(z, y)} \quad (3.19)$$

where:

$$F_{LEV} = -\frac{1}{4} \frac{\mu_0 N^2 I^2 dw}{z^2} \left\{ 1 + \frac{2z}{\pi w} \left[1 - \frac{y}{z} a \tan\left(\frac{y}{z}\right) \right] \right\} \quad (3.20)$$

Equation (3.20) is to be linearized with respect to gap z_0 and current I_0 , by using first derivative components from the Taylor expansion expressed by k_z and k_i coefficients derived in (2.32) and (2.33). Based on (3.18) and (3.19) the state space equations for the rigid and collocated system can be obtained:

$$\begin{aligned} \begin{bmatrix} \dot{z} \\ \ddot{z} \\ \dot{I} \end{bmatrix} &= \begin{bmatrix} 0 & 1 & 0 \\ \frac{k_z}{J} & 0 & -\frac{k_i}{J} \\ 0 & 0 & -\frac{(K_a + R)}{L} \end{bmatrix} \begin{bmatrix} z \\ \dot{z} \\ I \end{bmatrix} + \dots \\ &+ \begin{bmatrix} 0 & 0 & 0 & 0 \\ 0 & -\frac{e_5^2}{J} & \frac{(e_4 - x_{cm_f}) \cdot e_5}{J} & \frac{e_5 \cdot e_6}{J} \\ \frac{K_a}{L} & 0 & 0 & 0 \end{bmatrix} \begin{bmatrix} I^{Cmd} \\ mg \\ m_{frame}g \\ (M + M_{Weights})g \end{bmatrix} \\ [z] &= [1 \quad 0 \quad 0] \begin{bmatrix} z \\ \dot{z} \\ I \end{bmatrix}; \end{aligned} \quad (3.21)$$

In the above equations (3.21), inputs mg , $m_{frame}g$ and $(M+M_{weights})g$ represent gravity loads applied to the Test Rig. They are not used for control design, but are useful for the purpose of simulation. One can note that these equations (3.21) in transfer function form (3.22) are similar to the transfer function obtained in Chapter 2 (2.43).

$$G(s) = \frac{-\frac{K_a k_i}{L}}{s^3 + s^2 \left(\frac{K_a + R}{L} \right) - s k_z - \frac{k_z K_a + R k_z}{L}} = -\frac{K_x}{(s - p_1)(s + p_2)(s + \alpha)} \quad (3.22)$$

As was previously mentioned, excluding the current feedback pole α , two electromagnetic poles p_1 and p_2 exist. Both (2.43) and (3.22) are one-degree-of-freedom systems, but with a different state variable. Therefore, comparing (3.22) to its analogue (2.43) it can be noted that the original is scaled due to the inertia value J , and the second by the mass M . This factor does not have an impact on the general form of transfer function (3.14). This observation illustrates that poles p_1 and p_2 are characteristic for

Maglev systems and they are associated with the original rigid body poles. They acknowledge inherent instability of Maglev systems and their non-linear behavior. The positions of these two poles vary significantly as a function of gap. This situation is illustrated in *Figure 3.25*.

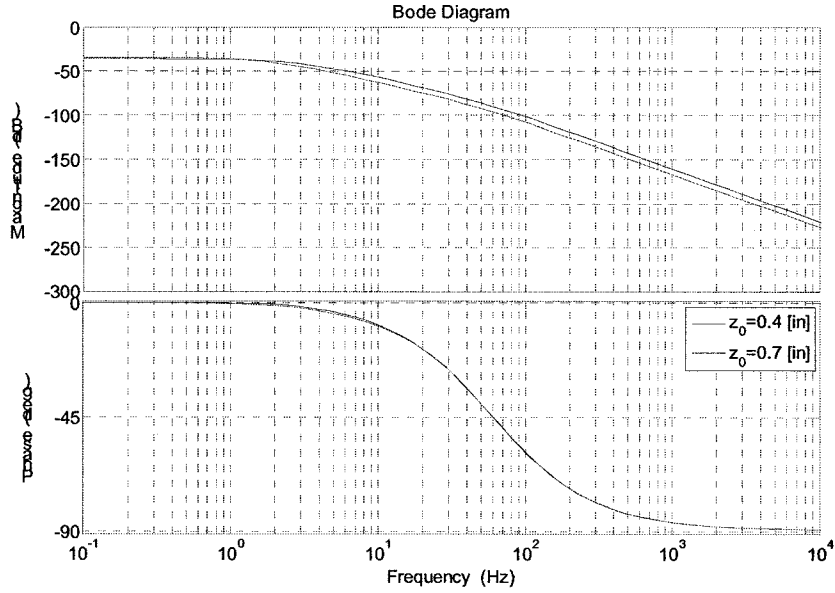


Figure 3.25 Pole variation due to non-linearity (rigid model)

The transfer function for the rigid Test Rig Maglev system at gap $z_0 = 0.4$ [in] has following form:

$$G_{rigid}^{gap=0.4}(s) = \frac{-2230.8}{(s - 28.7)(s + 29.8)(s + 375)} \quad (3.23)$$

while at gap $z_0 = 0.7$ [in.]:

$$G_{rigid}^{gap=0.7}(s) = \frac{-1082.07}{(s - 17.1)(s + 16.5)(s + 377)} \quad (3.24)$$

As it can be seen, poles p_1 and p_2 in (3.24) change their frequency from ~ 2.5 [Hz] to ~ 4.5 [Hz] which is not desirable. Similar features will be shown for the flexible Test Rig models.

3.6.2 Electromagnet Model with Flexible Levitated Structural Model

In this section, a structural levitated model of the Test Rig Maglev system is merged with an electromagnet model. After combining equations (3.12) and (3.19), the following system state space representation can be derived:

$$\begin{aligned}
 \begin{bmatrix} \dot{x}_1 \\ \dot{x}_2 \\ \dot{x}_3 \\ \ddot{x}_1 \\ \ddot{x}_2 \\ \ddot{x}_3 \\ \dot{I} \end{bmatrix} &= \begin{bmatrix} 0 & 0 & 0 & 1 & 0 & 0 & 0 \\ 0 & 0 & 0 & 0 & 1 & 0 & 0 \\ 0 & 0 & 0 & 0 & 0 & 1 & 0 \\ -\frac{k_1 + k_z}{m_1} & \frac{k_1}{m_1} & 0 & -\frac{c_1}{m_1} & \frac{c_1}{m_1} & 0 & -\frac{k_i}{m_1} \\ \frac{k_1}{m_2} & -\frac{(k_1 + k_2)}{m_2} & \frac{k_2}{m_2} & \frac{c_1}{m_2} & -\frac{(c_1 + c_2)}{m_2} & \frac{c_2}{m_2} & 0 \\ \frac{k_2}{M} & -\frac{k_2}{M} & 0 & \frac{c_2}{M} & -\frac{c_2}{M} & 0 & 0 \\ 0 & 0 & 0 & 0 & 0 & 0 & -\frac{(K_a + R)}{L} \end{bmatrix} \dots \\
 \dots \begin{bmatrix} x_1 \\ x_2 \\ x_3 \\ \dot{x}_1 \\ \dot{x}_2 \\ \dot{x}_3 \\ I \end{bmatrix} &+ \begin{bmatrix} 0 & 0 & 0 & 0 \\ 0 & 0 & 0 & 0 \\ 0 & 0 & 0 & 0 \\ 0 & -\frac{e_5^2}{J} & \frac{(e_4 - x_{cm-f})e_5}{J} & \frac{e_5 e_6}{J} \\ 0 & 0 & 0 & 0 \\ 0 & 0 & 0 & 0 \\ \frac{K_a}{L} & 0 & 0 & 0 \end{bmatrix} \begin{bmatrix} I^{Cmd} \\ mg \\ m_{frame}g \\ (M + M_{Weights})g \end{bmatrix} \quad (3.25)
 \end{aligned}$$

Figure 3.26 illustrates the variation of pole locations due to non-linearity for the flexible, levitated case.

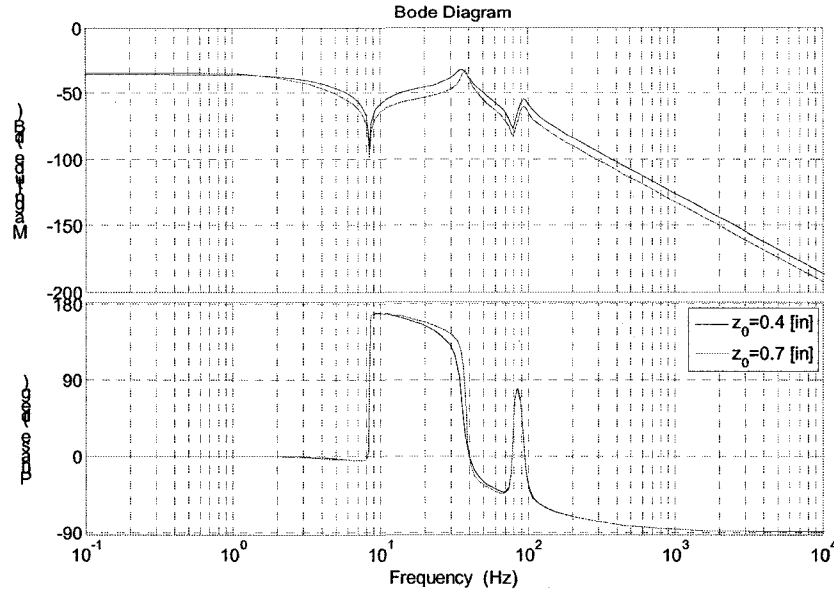


Figure 3.26 Pole variation due to non-linearity (flexible levitated model)

The transfer function for the flexible levitated Maglev system at gap $z = 0.4$ [in.] is:

$$G_{levitated}^{gap=0.4}(s) = \frac{-121517.6(s^2 + 0.31s + 2796)(s^2 + 26.89s + 2.47e^5)}{(s - 28.04)(s + 31.1)(s + 376.6)(s^2 + 16.65s + 5.68e^4)(s^2 + 46.9s + 3.39e^5)} \quad (3.26)$$

The transfer function for the rigid Maglev system at gap $z = 0.7$ [in.] is:

$$G_{levitated}^{gap=0.7}(s) = \frac{-58866.21(s^2 + 0.31s + 2797)(s^2 + 27.95s + 2.47e^5)}{(s - 17.8)(s + 17.1)(s + 372)(s^2 + 15.3s + 5.63e^4)(s^2 + 47.1s + 3.37e^5)} \quad (3.27)$$

In equations (3.16), the electromagnetic poles' migration is shown (at gap 0.7 [in] 2.7 [Hz] vs. 4.4 [Hz] for system linearized around gap 0.4 [in]). It is similar to what was shown in a previous section. Additional flexible modes corresponding to the structural modes show up as predicted in (2.59) and (3.12).

3.6.3 Electromagnet Model Together with Flexible Grounded Structural Model

Finally, assume that the electromagnet is activated while the Maglev Test Rig is on the ground. After combining equations (3.15) and (3.19), the following system state space representation can be derived:

$$\begin{aligned}
 \begin{bmatrix} \dot{x}_1 \\ \dot{x}_2 \\ \dot{x}_3 \\ \ddot{x}_1 \\ \ddot{x}_2 \\ \ddot{x}_3 \\ \dot{I} \end{bmatrix} &= \begin{bmatrix} 0 & 0 & 0 & 1 & 0 & 0 & 0 \\ 0 & 0 & 0 & 0 & 1 & 0 & 0 \\ 0 & 0 & 0 & 0 & 0 & 1 & 0 \\ -\frac{k_1+k_z}{m_1} & \frac{k_1}{m_1} & 0 & -\frac{c_1}{m_1} & \frac{c_1}{m_1} & 0 & -\frac{k_i}{m_1} \\ \frac{k_1}{m_2'} & -\frac{(k_1+k_2)}{m_2'} & \frac{k_2}{m_2'} & \frac{c_1}{m_2'} & -\frac{(c_1+c_2)}{m_2'} & \frac{c_2}{m_2'} & 0 \\ 0 & \frac{k_2}{M} & -\frac{(k_1+k_2)}{M} & 0 & \frac{c_2}{M} & -\frac{(c_2+c_3)}{M} & 0 \\ 0 & 0 & 0 & \frac{k_z}{k_i} & 0 & 0 & -\frac{(K_a+R)}{L} \end{bmatrix} \dots \\
 \dots \begin{bmatrix} x_1 \\ x_2 \\ x_3 \\ \dot{x}_1 \\ \dot{x}_2 \\ \dot{x}_3 \\ I \end{bmatrix} &+ \begin{bmatrix} 0 & 0 & 0 & 0 \\ 0 & 0 & 0 & 0 \\ 0 & 0 & 0 & 0 \\ 0 & -\frac{e_3^2}{J} & \frac{(e_4-x_{cm=f})e_5}{J} & \frac{e_5e_6}{J} \\ 0 & 0 & 0 & 0 \\ 0 & 0 & 0 & 0 \\ \frac{K_a}{L} & 0 & 0 & 0 \end{bmatrix} \begin{bmatrix} I^{Cmd} \\ mg \\ m_{frame}g \\ (M+M_{Weights})g \end{bmatrix} \quad (3.28)
 \end{aligned}$$

Figure 3.27 illustrates the variation of pole locations due to non-linearity for the flexible, grounded case.

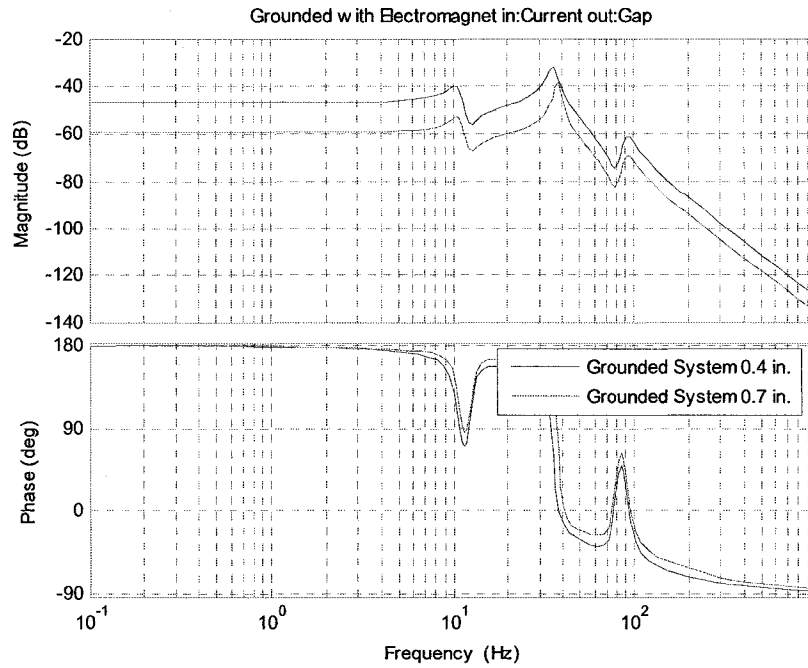


Figure 3.27 Pole variation due to non-linearity (flexible grounded model)

The transfer Function for the flexible, levitated Maglev system at gap $z = 0.4$ [in.] is:

$$G_{grounded}^{gap=0.4}(s) = \frac{-83077.3(s^2 + 9.82s + 6025)(s^2 + 56.68s + 2.45e^5)}{(s + 364)(s^2 + 9.6s + 4443)(s^2 + 22.16s + 4.99e^4)(s^2 + 80.17s + 3.36e^5)} \quad (3.29)$$

The transfer Function for the rigid Maglev system at gap $z = 0.7$ [in.] is:

$$G_{grounded}^{gap=0.7}(s) = \frac{-38647.23(s^2 + 9.82s + 6025)(s^2 + 56.68s + 2.45e^5)}{(s + 380)(s^2 + 9.29s + 4705)(s^2 + 14.52s + 5.59e^4)(s^2 + 78.81s + 3.39e^5)} \quad (3.30)$$

Because system (3.28) does not levitate there are no unstable poles. Flexible modes and their frequencies are clearly visible and match those occurring in the levitated system.

The conclusions made in section 3.5.3 hold.

To summarize section 3.6, it can be said that electromagnetic dynamics have an enormous impact on the structural systems introduced in section 3.5. The system's dynamics vary significantly with gap.

3.7 Model Validation via Experiment

In this subchapter, the results of experiments to validate the models created in 3.6 are presented and discussed. Because of the inherent instability of the uncontrolled, levitated Maglev system, only results with the Test Rig resting on the ground are used. Tests were carried out with the rig “nearly levitated” (rear mass M was primarily supported by the rubber pads). It was assumed that this represented the grounded condition (3.28).

Validation tests for the model of the entire system (3.28), (comprised of the combined electromagnetic and structural components), were performed using a HP Dynamic Signal Analyzer 3562A. Input signals were used (see *Table 3.4*) for several different operational conditions.

Signal Setup	GAP
Sine sweep $I = 10 \pm 1$ Amp	Gap = 0.4 in.
Sine sweep $I = 20 \pm 1$ Amp	Gap = 0.55 in.
Sine sweep $I = 25 \pm 1$ Amp	Gap = 0.7 in.

Table 3.4 Experimental setup for grounded Test Rig

Results obtained from these tests (after curve fitting) are presented in *Figure 3.28*.

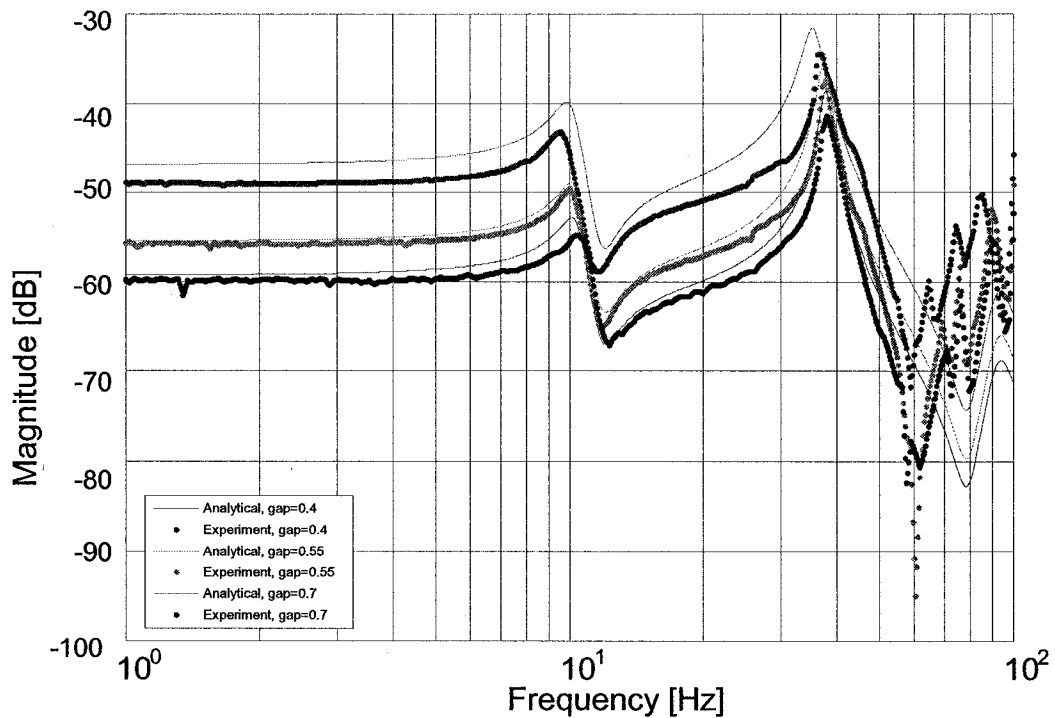


Figure 3.28 Experimental and analytical data for three different cases gap $z = 0.4$, $z = 0.55$, and $z = 0.7$ [in]

Two main points can be noted from Figure 3.28. First, the models generally have good agreement with the experimental results for each gap. A small difference in dc gain (~ 2 dB) between experiment data and model curves for the same gap=0.4 [in.] can be noted. It is believed that this difference is due to increasing influence of non-linearities and fringing flux losses as gap decreases. Second, the steady-state gain varies significantly as a function of gap. This is a resultant of the system being linearized around different operating points. The significance of these observations is that the dynamic character of the system goes through significant change once levitation occurs. In theory, a prospective controller has to work with a wide range of plant gains. This implies a large gain margin will be required for the closed loop system.

3.8 Summary

In this chapter a model of a laboratory Maglev Test Rig was presented. This Test Rig was designed to provide a realistic testing environment for control system design. Different setups and different possible structural flexibility and Test Rig configurations such as grounded and levitated were investigated. The impact of non-collocation in sensor measurements was shown. The Test Rig Maglev model was validated via experiment, confirming the accuracy of the analytical approach. This model will be exploited in the following chapter for control design.

4. TEST RIG CONTROL LAWS

In this chapter control laws are designed for the Test Rig system presented in the previous section. For a complex system it is reasonable to begin with simple control laws such as proportional plus derivative gain feedback, before attempting more advanced designs. In this chapter several different approaches will be discussed. These approaches are basic PD compensators, PID, gap and acceleration feedback, inverse dynamic calculation and finally, flux feedback.

4.1 Compensation Based on Gap Feedback

The advantage of a PD/PID controller with gap feedback approach is two-fold. First, simple control laws provide a baseline for performance comparisons with high order compensators discussed later in this work. Second, comparing experimental and simulated response can test the accuracy of the dynamic model. Discrepancies (such as non-linearity or sensor/actuator modeling) between the model and the physical system can be identified.

Consider first a rigid model of the Test Rig system (3.22):

$$G(s) = \frac{-K_x}{(s - p_1)(s + p_2)(s + \alpha)} = \frac{-2231}{(s - 28.52)(s + 29.09)(s + 375.9)} \quad (4.1)$$

The open loop poles (4.1) suggest that at least one negatively defined zero with appropriate gain is needed for levitation if the system is to be stabilized (see Chapter 2). Thus, the compensator takes the following form:

$$C(s) = -K_p - K_D s \quad (4.2)$$

As shown in Chapter 2 stability can always be achieved with PD control using K_D and K_p greater than some critical value depending on the load applied to the Test Rig [1][25][38][50][51][63][77]. This can be explained by considering the active control law as an equivalent mechanical spring and dashpot placed between the electromagnet and the track. The dashpot will always provide damping to the system modes, i.e., will always remove energy from their motion, thus insuring stability.

A rough approximation for a desired K_p and K_D can be obtained by checking the coefficients of the closed loop characteristic polynomial; as was evaluated in (2.50-2.52), thus:

$$K_p < -132 \quad (4.3)$$

$$K_D < -0.35 \quad (4.4)$$

Equations (4.3)(4.4) can be modified depending on desired damping and performance. In Table 4.1, compensator conditions for different model setups are presented.

Different Test Rig rigid plants	K_p	K_d
Linearized at gap = 0.4 [in.]	-132.2	-0.35
Linearized at gap = 0.7 [in.]	-89.3	-0.23

Table 4.1 Minimum requirements for PD compensator

Below (Figure 4.1), a simple compensator is shown where the damping requirement for the Test Rig system was assumed to be less than 0.707 and its time response less than 1 second. As a starting point, the system was considered without an applied load, and linearized around a gap $z_0 = 0.4$ [in.].

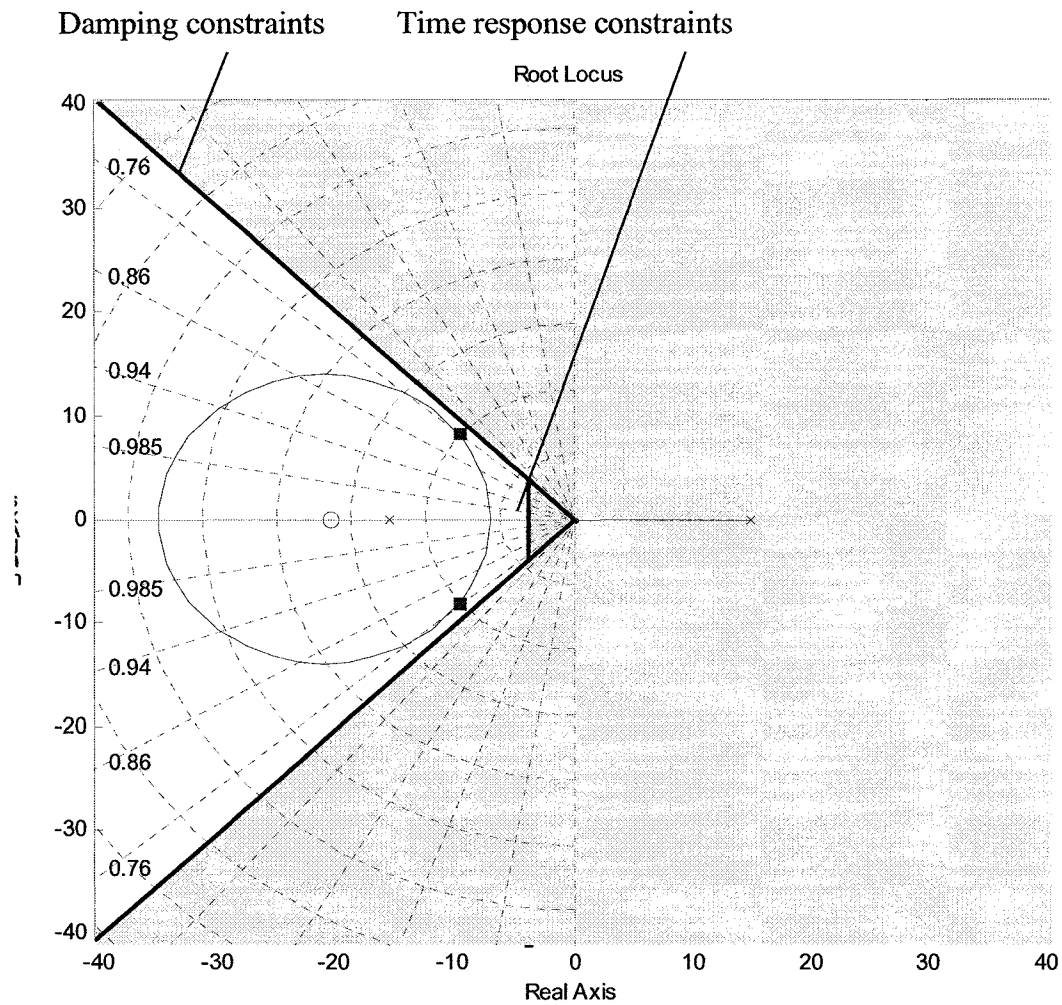


Figure 4.1 PD compensator via root locus design for the rigid test-rig model

Based on the design illustrated in *Figure 4.1*, the following values were obtained:

$$K_p = -170 \quad (4.5)$$

and

$$K_d = -6.3 \quad (4.6)$$

Bode plots of the proposed compensator are shown in *Figure 4.2*.

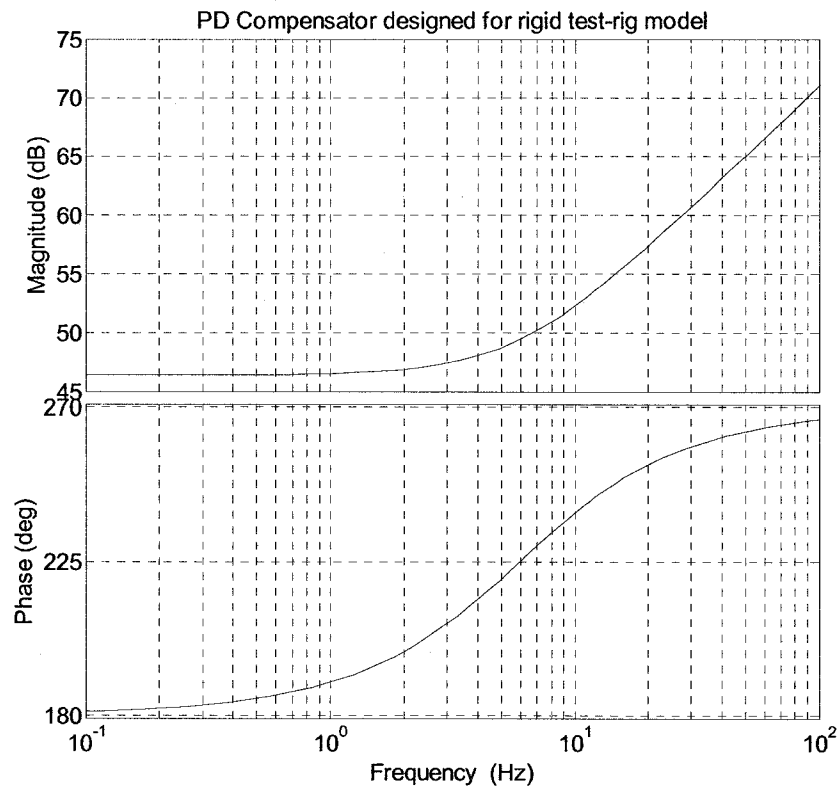


Figure 4.2 Bode plots for PD compensator

In the theory for all rigid test-rig models, the proposed controller in the form of (4.2) provides stable response. As shown later, on the actual plant this simple PD compensator did not work correctly since:

- 1) Existing flexible modes required the compensator design procedure to be based on the full structural model.
- 2) Some high frequency limitation for the derivative part in the PD compensator is required.

All of these aspects are discussed in the following sub-chapters.

4.1.1 Filter Design

Through experimentation, it became evident that the impact of noise on the Maglev system performance was so significant that it would be impossible to achieve a suitable response without appropriate filtering. In this subsection, various filters used in experimentation are described [78][79] and compared.

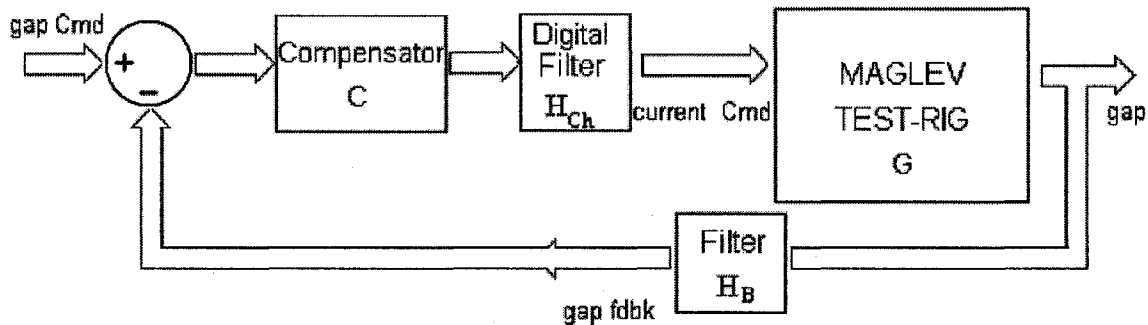


Figure 4.3 Model block diagram after analog and digital filters were added to plant (H_{Ch} - Chebyshev filter, H_B - Butterworth filter)

Consider the PD compensator expressed by (4.2) and the open-loop transfer function

$$G_{openloop}(s) = H_{Ch}(s)C(s)G(s) \quad (4.7)$$

where $G(s)$ is the transfer function of the modeled system. The input is the current command and output is the unfiltered gap signal. The $G(s)$ can have different forms depending on whether:

- The model includes flexible modes or not (3.21) or (3.25), (3.28)
- The model can be linearized around different operating points
- The model can be considered as grounded (3.25) or levitated (3.28)

While all of these cases were investigated, only those that are required for illustration purposes are shown.

A closed loop transfer function can be obtained:

$$G_{ClosedLoop} = \frac{G_{openloop}(s)}{1 + H_B(s)G_{openloop}(s)} \quad (4.8)$$

where $H_B(s)$ is the Butterworth filter transfer function.

The practical disadvantage of the PD controller (*Figure 4.2*) is that the differentiator portion is a high-pass filter which usually magnifies any high frequency noise that is carried by the input signal.

4.1.1.1 Digital Filter

The filters discussed here were designed to achieve less than 0.5 dB pass band ripple; the minimum order of the filter was assumed to be $N_F = 3$. Among many filters investigated the following was chosen for digital filtering use:

1) The type II Chebyshev filter where phase delay at 100 [Hz] is around 16.3° and roll-off at 1250 [Hz] is 15.6 dB. Its transfer function is expressed as follows:

$$H_{Ch}(s) = \frac{0.001 \cdot s^3 + 71.5 \cdot s^2 + 1.67 \cdot 10^6 \cdot s + 8.89 \cdot 10^{10}}{s^3 + 8906 \cdot s^2 + 3.96 \cdot 10^7 \cdot s + 8.89 \cdot 10^{10}} \quad (4.9)$$

2) If the controlled process contains one or more pairs of complex-conjugate poles that are very close to imaginary axis of the s-plane, these complex poles usually cause the closed loop system to be lightly damped or unstable. In this case it was found that the effective approach was to modify the zeros of the Chebyshev type II filter to form an Notch characteristic while retaining Chebyshev type II pole pattern. This provides low pass filtering while keeping the phase delay in reasonable range (*4.10*):

$$H_N(s) = \frac{3107.2(s^2 + 559.6s + 9.193 \cdot 10^5)}{(s + 1223)(s^2 + 2080s + 2.336 \cdot 10^6)} \quad (4.10)$$

A notch filter attenuates the impact of the mode at frequency a (see equation 2.156). The parameters in the denominator describe desired performance.

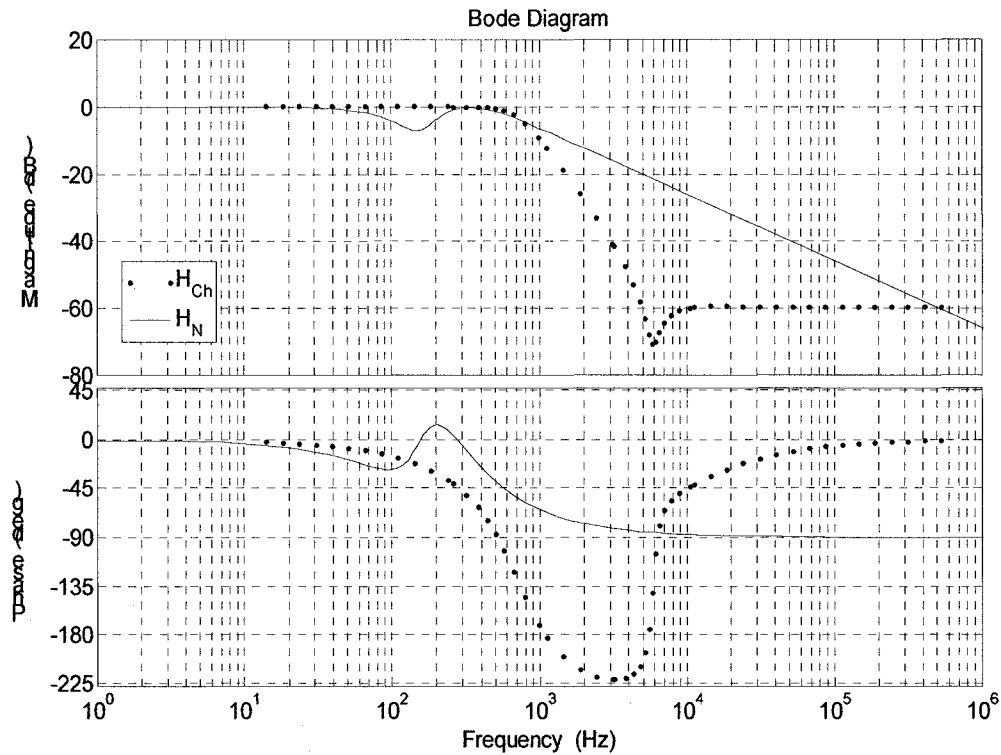


Figure 4.4 Digital filters comparison

The advantages and disadvantages of notch filters were discussed in Chapter 2 where it was pointed out that because of the migration of plant transfer function zeros it is not the best solution for a moving Maglev vehicle. However for the test-rig application, a notch filter can be sufficient.

Property	Chebyshev II	Notch
Phase at 100[Hz]	-15.3	-24.1
dB at 1250[Hz]	-14.6	-8.4
# of Poles	3	3

Table 4.2 Digital filter comparisons

Therefore Chebyshev or Notch (see Table 4.2) should be used interchangeably depending on the application case.

4.1.1.2 Analog Filter

The test-rig application uses 12-bit A/D hardware with a sample rate of 20 [kHz]. A 12-bit A/D converter has 72dB of dynamic range. Accordingly, it is generally desired to have 72dB of attenuation at the Nyquist frequency, 10 [kHz], to avoid aliasing.

Anti-aliasing was achieved by introducing a second filter. It is an analog device, Wavetec model 842. It was set up to be an 8th order Butterworth filter with a cutoff frequency at 4000 [Hz].

$$H_B(s) = \frac{1.59 \cdot 10^{35}}{(s^2 + 4.9 \cdot 10^4 s + 6.3 \cdot 10^8)(s^2 + 4.2 \cdot 10^4 s + 6.3 \cdot 10^8)} \cdots \frac{1}{(s^2 + 2.8 \cdot 10^4 s + 6.3 \cdot 10^8)(s^2 + 9806 s + 6.3 \cdot 10^8)} \quad (4.11)$$

This filter introduces 7.7° phase delay at 100 [Hz], which has to be considered in the design process. Characteristics of this filter are presented in *Figure 4.5* below.

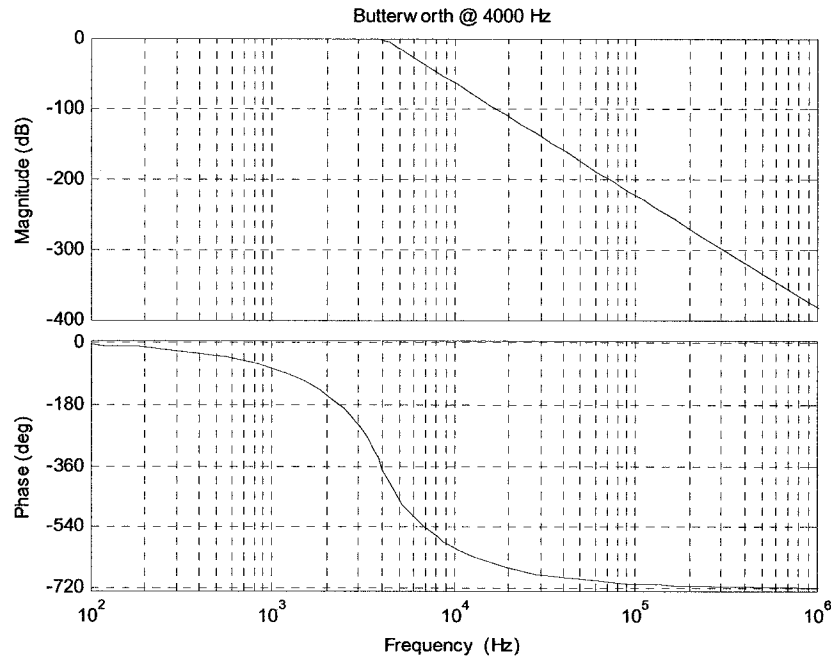


Figure 4.5 Analog filter characteristics; Bode plots

4.1.2 Root Locus PD Control Design

In this section, the Evans root locus design approach is used. The basic properties and systematic construction of the root loci were first presented by W.R. Evans. For plotting the root loci accurately the Matlab[®] root locus tool in the Control System Toolbox[®] was used. Magnitude and phase characteristics can be obtained by applying this tool to the open loop system modeled in (3.25). Through root locus design, the performance of the system can be analyzed and different compensators' parameters can be chosen accordingly.

As a starting point for design and tuning of the compensator $C(s)$, let $G(s)$ be a transfer function of the flexible levitated plant linearized at $gap = 0.4$ [in.], and the current reference value $I_{ref} = 25$ [A]. The current reference can be easily evaluated for a given gap and applied load as shown (2.118). According to frequency plots in *Figure 4.6* a phase margin begins to degrade ~ 7 [deg], due to the first pole at around 5 [Hz]. This value can vary and will be higher when the gap decreases. Furthermore, phase is lower than -180 [deg] in the range of frequency between 40 [Hz] and 80 [Hz] (~ 35 [deg]). For frequencies higher than 70 [Hz], the system phase margin becomes negative for frequencies (~ 45 [deg] up to 90 [deg]), see *Figure 4.6* below.

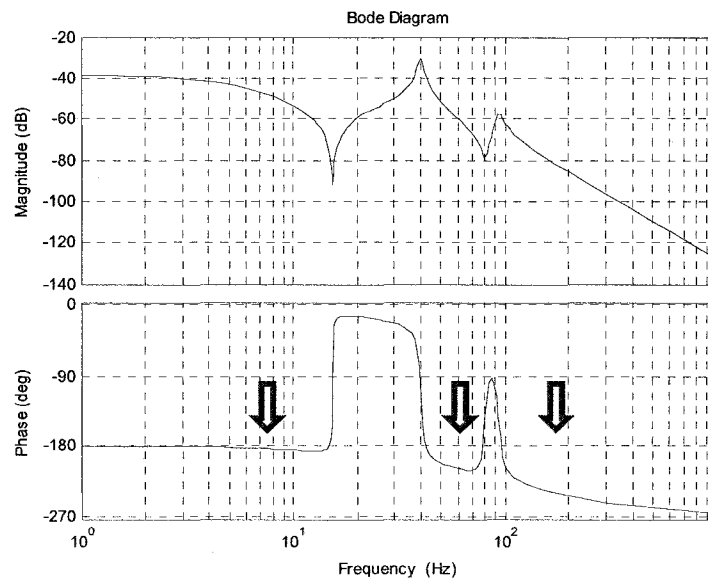


Figure 4.6 Marked phase delays for the initial compensator design

The compensator

$$C(s) = -185 - 2.2s, \quad (4.12)$$

provides stable results for all different test-rig setups for both analytical and experimental tests.

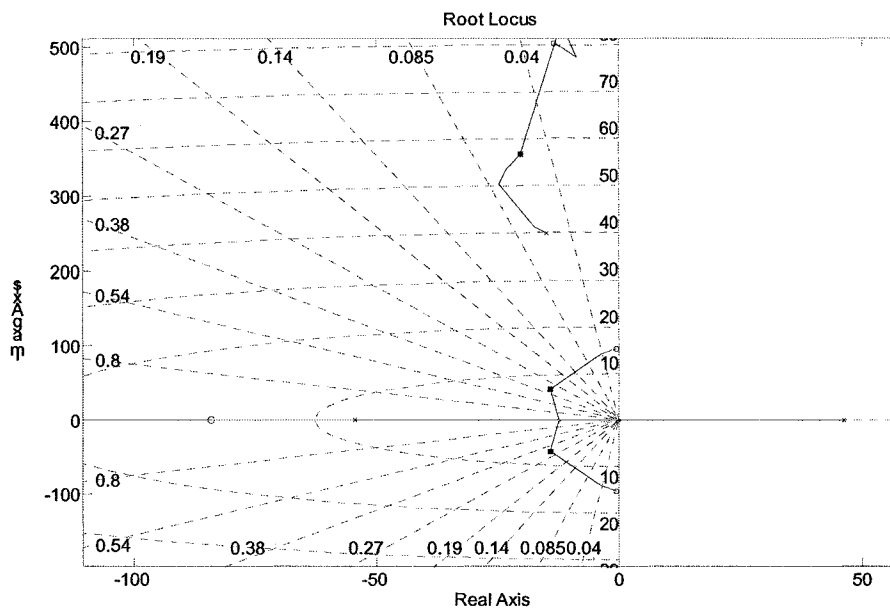


Figure 4.7 Root locus design for modeled system with filters

Performance characteristics for different system models with the same compensator (4.12) and the same filters (4.9) (4.10) are tabulated below (Table 4.3).

Property	Gain Margin [dB]	Phase Margin [deg]	Time response [sec.]
Gap $z = 0.4$ in.	4.7	10.4	0.4
Gap $z = 0.7$ in.	9.3	11.8	0.6

Table 4.3 Test-rig model performance with PD compensator and filters

Step response result of system linearized around operating gap 0.4 [in.] is presented in Figure 4.8.

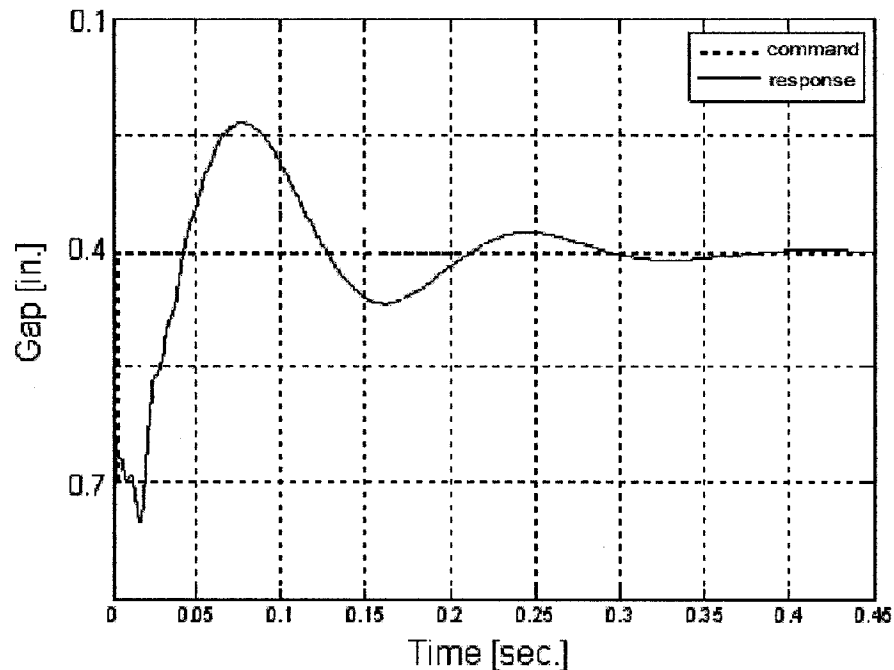


Figure 4.8 Step response for the modeled linear Test Rig system with PD controller

As shown in the above figure, a stable response was obtained for modeled test-rig case with this compensator (4.12). The Maglev Test Rig model linearized around an operating gap of 0.4 [in.] provided fast response 0.4 [sec.] but at the same time relatively high overshoot. Also it has to be pointed out that no compensator was found which would work for both Maglev Test Rig systems with and without a large applied load ($M_{weights}$). In Figure 4.9 a gap response was shown for a non-linear model simulation without applied load. It can be seen that stable result was obtained; however, the steady state error is significant.

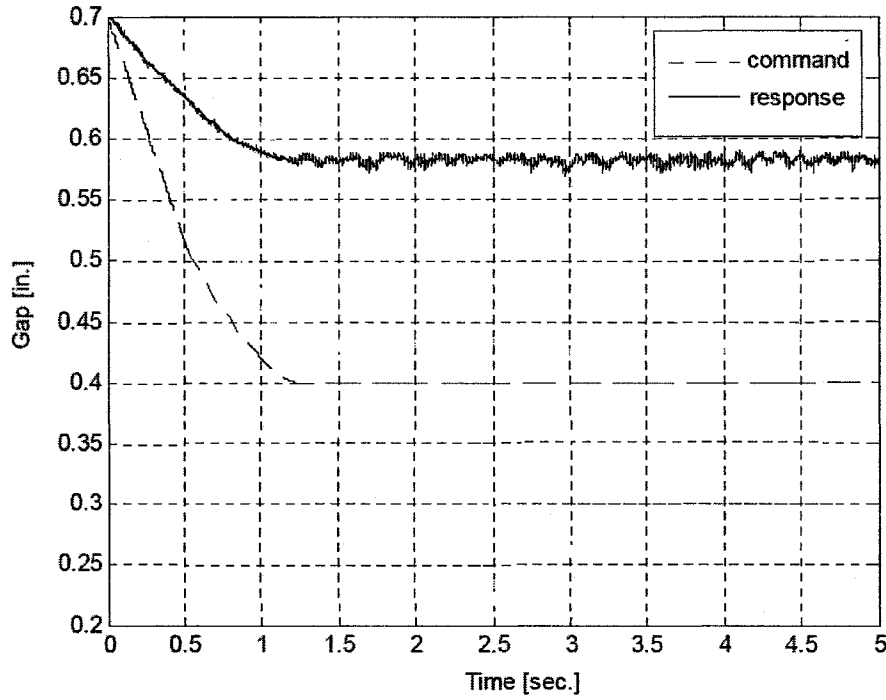


Figure 4.9 Gap response for modeled non-linear Test Rig systems with PD controller

4.1.2.1 Steady State Error

It is seen in Figure 4.9 that response has steady-state error as was expected for PD compensation. For a step command (0.4 [in.]) steady state-error is caused by gravity, and due to Simulink® simulation $e_{ss} = 0.162$ [in.] when the gap command $z^{Cmd} = 0.4$ [in.].

Steady state errors can be reduced by either the incorporation of an integrator into the control law, or by adding a constant current offset I^{OFF} to the compensator output signal. The second method can be illustrated; based on equation (4.13), where measured gap z can be expressed as:

$$z = \frac{G_{openloop} (I^{OFF} + z^{Cmd} C)}{1 + z^{Cmd} H_B G_{openloop}} \quad (4.13)$$

Knowing that steady state error is expressed by:

$$e_{ss} = z^{Cmd} - z, \quad (4.14)$$

the following expression for e_{ss} can be obtained:

$$e_{ss} = z^{Cmd} - \frac{G_{openloop} (I^{OFF} + z^{Cmd} C)}{1 + z^{Cmd} H_B G_{openloop}} \quad (4.15)$$

Thus, by increasing the current offset I^{OFF} for a constant gap command z^{Cmd} , the value of the e_{ss} decreases.

For suppressing e_{ss} and to avoid destabilizing effects it may be preferable to use a current offset instead of an integrator. Both solutions will be discussed and evaluated experimentally in the following subchapters.

4.1.3 Robustness of the PD Control Design

In this subchapter, robustness of the solution proposed in 4.1.2 is discussed. To investigate robustness of the controller, an additive plant uncertainty can be defined as [43]:

$$G_{openloop}^{Real}(s) = G_{openloop}^{modeled}(s) + \Delta G_{openloop}(s), \quad (4.16)$$

$$\Delta G_{openloop}(s) = \begin{bmatrix} \Delta m & 0 \\ 0 & \Delta gap \end{bmatrix} \quad (4.17)$$

Here, Δm represents mass uncertainty with possible variation in the range of 50% of its nominal value (weight hung on the rear side of the test-rig frame). Further Δgap represents gap variation in the range 0.1 to 0.7 [in]. This is approximately 40% of the fluctuation around nominal and desired gap 0.4 [in.]. *Figure 4.10* presents how the open loop transfer function varies in this range of uncertainty.

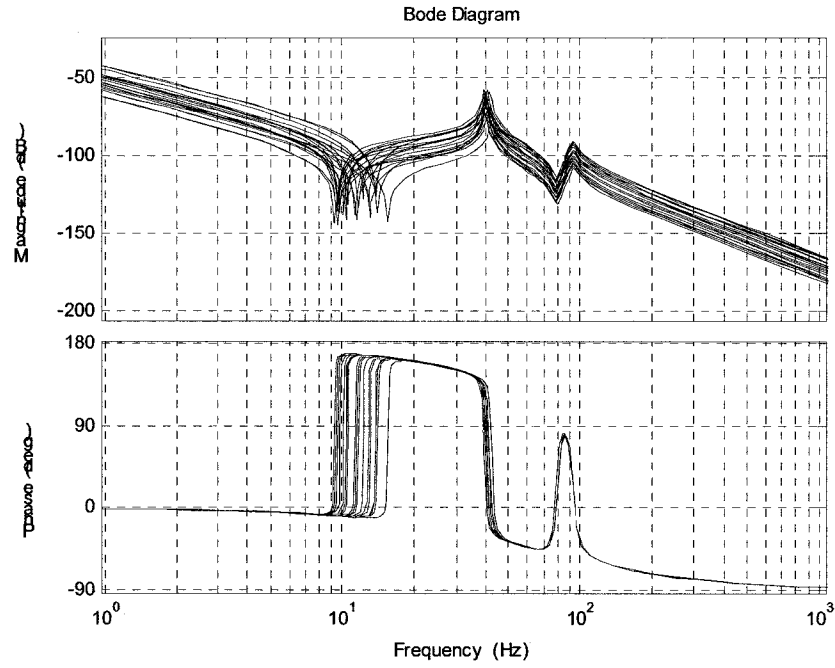


Figure 4.10 Open-loop Bode plots with mass and gap uncertainties

Based on uncertainty models, some evaluation of the stability regions can be determined using stability sigma calculations. These calculations are valid for both MIMO and SISO systems.

Since an open loop system with additive error has the form (4.16) with (4.17), a closed loop plant with unity feedback gain is [43]:

$$G_{closedloop}^{Real}(s) = G_{closedloop}^{mod\,eled}(s) + \Delta G_{closedloop}(s) \quad (4.18)$$

From Nyquist theory it is known that:

$$\det \left[I + G_{openloop}^{Real}(s)C(s) \right] \neq 0 \quad (4.19)$$

$$\Rightarrow \det \left[I + \left(G_{openloop}^{mod\,eled}(s) + \Delta G_{openloop}(s) \right) C(s) \right] \neq 0 \quad (4.20)$$

$$\Rightarrow \underline{\sigma} \left[I + \left(G_{openloop}^{mod\,eled}(s) + \Delta G_{openloop}(s) \right) C(s) \right] > 0 \quad (4.21)$$

$$\Rightarrow 0 < \underline{\sigma} \left[I + C(s)G_{openloop}^{mod\,eled}(s) + \Delta G_{openloop}(s)C(s) \right] \quad (4.22)$$

$$\Rightarrow 0 < \underline{\sigma} \left[\left\{ I + \Delta G_{openloop}(s) \cdot C(s) \cdot (I + G_{openloop}(s) \cdot C(s))^{-1} \right\} \cdot (I + \Delta G_{openloop}(s) \cdot C(s)) \right] \quad (4.23)$$

Assuming a conservative solution:

$$\Rightarrow 0 < \underline{\sigma} \left[I + \Delta G_{openloop}(s) \cdot C(s) \cdot (I + G_{openloop}(s) \cdot C(s))^{-1} \right] \cdot \underline{\sigma} [I + G_{openloop}(s) \cdot C(s)] \quad (4.24)$$

Knowing that the nominal system is stable with $C(s)$ from (4.12), it follows:

$$\underline{\sigma} \left[I + G_{openloop}(s) C(s) \right] > 0 \quad (4.25)$$

Since both sides of (4.24) can be divided by LHS of (4.25)

$$\Rightarrow 0 < \underline{\sigma} [I + \Delta G_{openloop}(s) \cdot C(s) \cdot (I + G_{openloop}(s) \cdot C(s))^{-1}] \quad (4.26)$$

$$\Rightarrow 0 < \underline{\sigma} [I] - \overline{\sigma} \left[\Delta G_{openloop}(s) \cdot C(s) (I + G_{openloop}(s) C(s))^{-1} \right] \quad (4.27)$$

since

$$\underline{\sigma} [I] = 1 \quad (4.28)$$

equation (4.27) becomes:

$$\overline{\sigma} \left[\Delta G_{openloop}(s) \cdot C(s) \cdot (I + G_{openloop}(s) C(s))^{-1} \right] < 1 \quad (4.29)$$

From singular value properties:

$$\overline{\sigma} \left[(I + G_{openloop}(s) C(s))^{-1} \right] = \frac{1}{\underline{\sigma} \left[I + G_{openloop}(s) C(s) \right]} \quad (4.30)$$

Thus, (3.35) can be expressed as follows:

$$\overline{\sigma} [\Delta G_{openloop}(s) C(s)] < \underline{\sigma} [I + G_{openloop}(s) C(s)] \quad (4.31)$$

The solution of (4.31) can be shown graphically assuming a compensator in the form of (4.12) with system uncertainty (4.17). As it can be observed (Figure 4.11), equation (4.31) is valid in nearly the entire frequency range. Only for frequencies between 0.2 [Hz] to 1 [Hz] (highlighted by a rectangle) did the test fail to validate. Due to the conservativeness with which the equations (4.24)-(4.31) were derived, an unequivocal conclusion cannot be made. But at least a range of frequency where potential problems can occur can be distinguished.

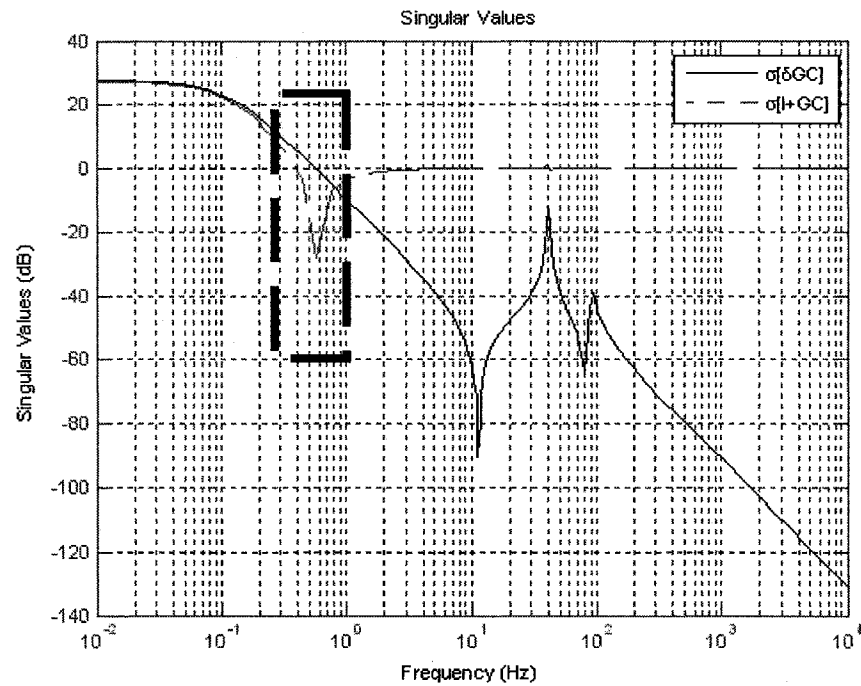


Figure 4.11 Robustness of PD compensation

However as it will be shown, some experimental results on the actual Test Rig plant exhibited small vibration in gap response with frequency around 0.8 [Hz] (see Figure 4.32). According to analysis this is caused by electromagnetic field stiffness and its associated poles at low frequencies (see equations (3.23) and (3.24)).

The solution presented in the Figure 4.11 above was validated via non-linear simulation (Figure 4.12) and by experiment. It is found that the system's simulated response does not contain low frequency fluctuations observed in gap measurements.

Because of the steady-state error which was not eliminated by PD compensation, it was required to incorporate for a non-linear simulation a current offset value equal to 15 [A]. Also it was necessary to command a lower gap 0.35 [in.] instead of 0.4 [in.] to get a desire gap (see Figure 4.12).

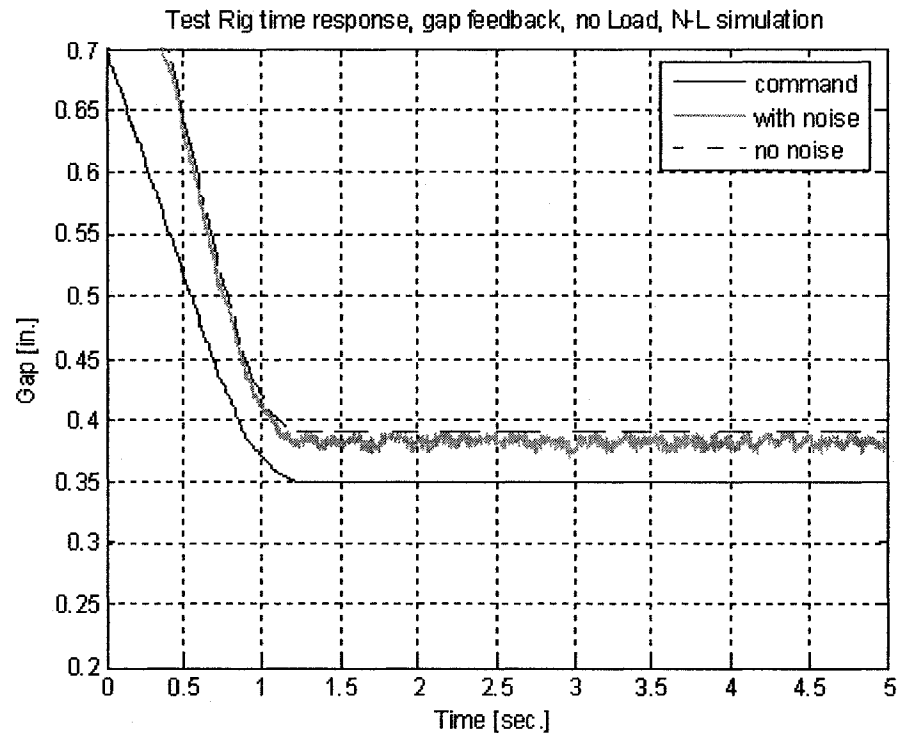


Figure 4.12 Step response of Test Rig non-linear simulation

To summarize this section, it can be said that proposed compensator (4.12) can be successfully applied to the Test Rig system. However the actual plant response with this controller will be shown in following subchapters.

4.2 Sensor Fusion, Gap and Acceleration Feedback

In section 4.1 all compensators presented were designed based on gap feedback only. In Maglev applications, the high frequency noise content of measured gap data hampers the computation of its discrete derivative for feedback control, and indeed renders it useless if the noise is of high enough amplitude. The addition of low pass filters to the gap signal reduces stability margins if the passband is low, or leads to derivatives with noise associated with filter response to quantization if the passband is high. To avoid amplification of noise due to the derivative, it is convenient to incorporate acceleration measurement feedback. Using the integral of measured acceleration seems attractive because it eliminates the need for derivatives; however accelerometer integrators are

subject to low frequency drift. To work around these problems in practice one could resort to a washout filter [80] on the acceleration signal and a leaky integrator to compute an approximate derivative. For systems where the derivative term serves to stabilize low frequency dynamics, these strategies will reduce the stabilizing influence of the derivative term. The goal of this section is to investigate an approach to merge discretely differentiated gap data with discretely integrated accelerometer data, in such a way that the merged result approximates a derivative.

Laboratory experience shows that the following arrangement serves to minimize the low frequency drift of the acceleration data and its integral.

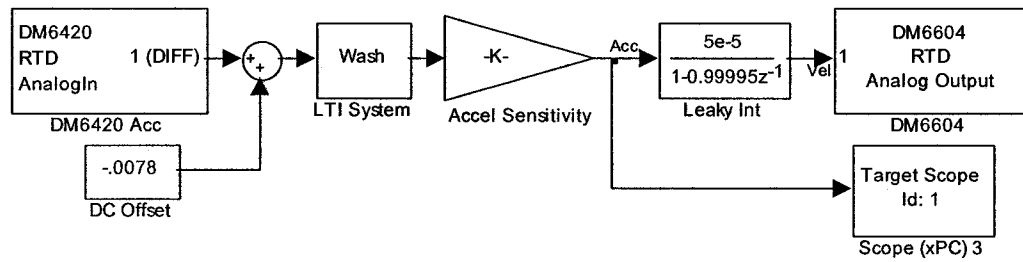


Figure 4.13 Simulink[®] model of the acceleration branch in control law

The raw data is adjusted for DC offset, passed through a washout filter, and finally integrated using a leaky integrator. In continuous time, the washout filter has the form:

$$G_{wash}(s) = \frac{s}{s + a} \quad (4.32)$$

The discrete-time zero order hold equivalent of the washout filter implemented with sample period T is:

$$G_{wash}(z) = \frac{z - 1}{z - e^{-aT}} \quad (4.33)$$

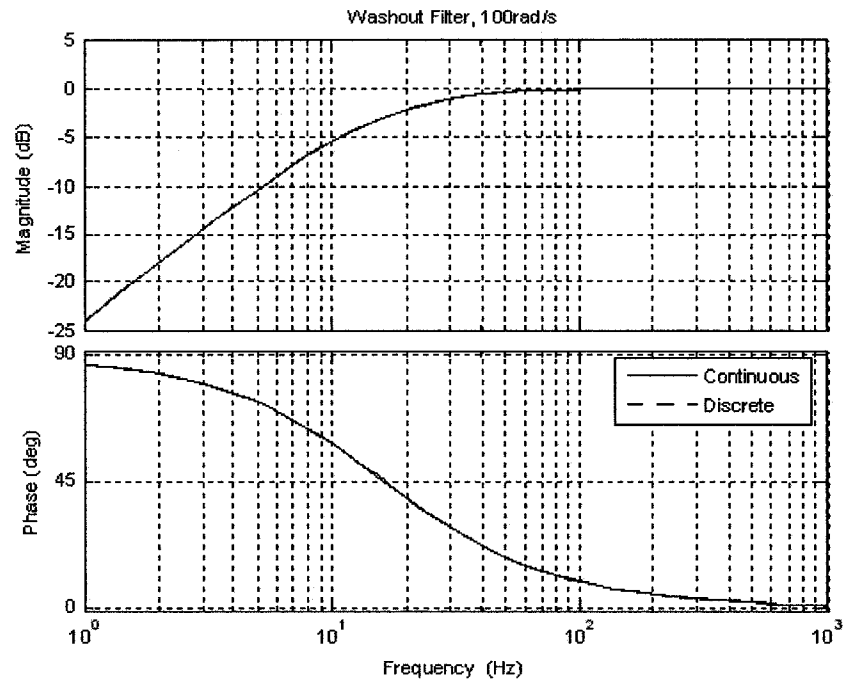


Figure 4.14 Washout filter characteristic

The washout filter Bode plot for $a=100$ [rad/sec]=15.91 [Hz] and $T=5\times 10^{-5}$ (20 [kHz] sample rate) above illustrates (Figure 4.14) that this is a highpass filter. A leaky integrator is usually specified in discrete form as:

$$G_{Leak}(z) = \frac{Tz}{z - e^{-bT}} \quad (4.34)$$

where b can be thought of as the “leak” frequency in radians/second. The Table 4.4 below compares the values of e^{-bT} for various leak frequencies, b , with $T=5\times 10^{-5}$. Note that an ideal discrete integrator is a special case of the washout filter with $e^{-bT} = 1$.

b (rad/sec)	0	0.2	2.0	20.0	200
e^{-bT}	1	0.99999	0.99990	0.99900	0.99000

Table 4.4 Leak frequencies comparison

The Figure 4.15 compares Bode plots of leaky integrators with a range of leak frequencies, using $T = 5 \times 10^{-5}$. Note that in each case the slope of the magnitude plot passes through the 1 rad/second line at 0 dB gain, thus the leaky integrator is seen to approximate an ideal integrator for frequencies greater than b by approximately 1 decade.

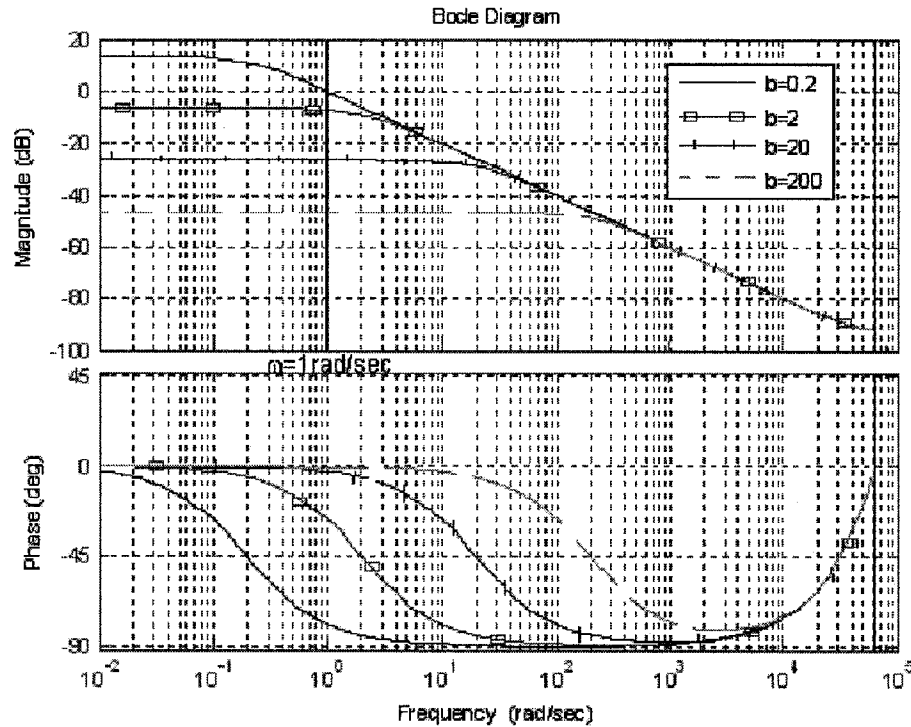


Figure 4.15 Bode plots of leaky integrators

The gap signal can be lowpass filtered using a single pole unity gain system of the form:

$$G_{LP}(s) = \frac{c}{s + c} \quad (4.35)$$

The discrete-time zero order hold equivalent of the lowpass filter implemented with sample period T is:

$$G_{LP}(z) = \frac{(1 - e^{-cT}) \cdot z}{z - e^{-cT}} \quad (4.36)$$

Figure 4.16 below shows a Simulink[®] diagram designed to merge the washed-out and leaky integrated acceleration signal with the lowpass filtered discrete derivative of gap.

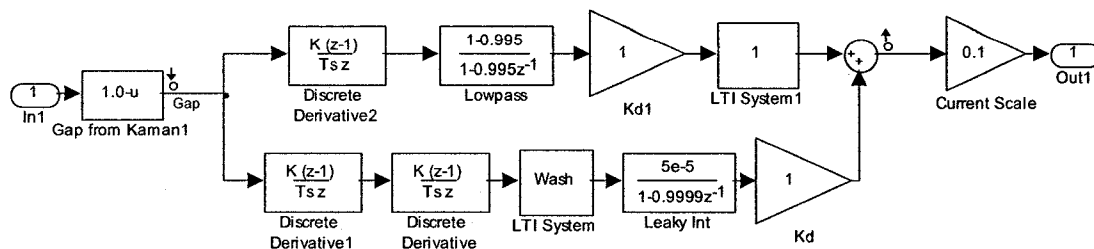


Figure 4.16 Simulink[®] diagram designed to merge components in acceleration stream

Equating the washout frequency a to the break frequency c of the lowpass filter, results in a system with Bode plot that approximates an ideal derivative. The x -axis is radians/second to facilitate the confirmation that the magnitude passes through the 0 dB point at 1 [rad/sec] as an ideal derivative would.

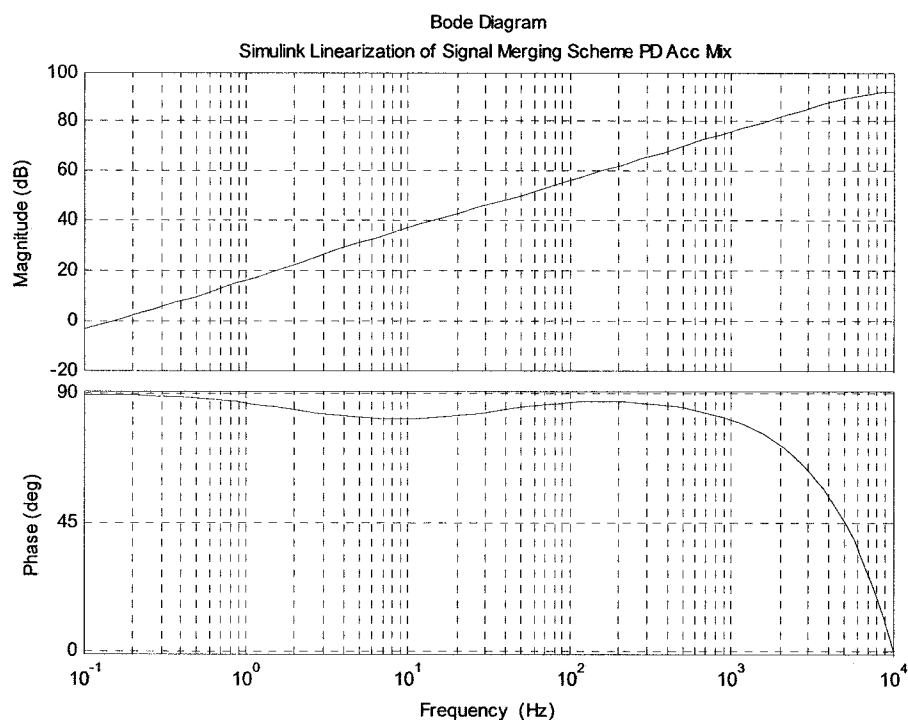


Figure 4.17 Bode plots of the compensator merged acceleration stream

Note that the dip in phase is apparently due to the Simulink[®] linearization, since a linear analysis does not exhibit this property.

The method shown above illustrates how additional sources of measurement data (in this example acceleration measurements) can be utilized during compensator application. It was shown that in the control law the problem with a discrete derivative term arises; however it can be relatively easy rectified.

4.3 Flux Feedback

Consider system (3.22) but assuming that a measurement of flux density B , obtained via a sensor placed in the magnet, is available. It is more convenient for modeling to use the air gap flux Φ instead of its density B . The relation between these two variables is following:

$$B = \frac{\Phi}{wd} \text{ [Tesla]} \quad (4.37)$$

When air gap flux is linearized as a function of gap z and current I [47], [63] it becomes:

$$\Phi = k_{\Phi I} I + k_{\Phi Z} z \quad (4.38)$$

where

$$k_{\Phi Z} = \left. \frac{\partial \Phi}{\partial z} \right|_{I_0}^{z_0} (< 0), \quad k_{\Phi I} = \left. \frac{\partial \Phi}{\partial I} \right|_{I_0}^{z_0} I (> 0) \quad (4.39)$$

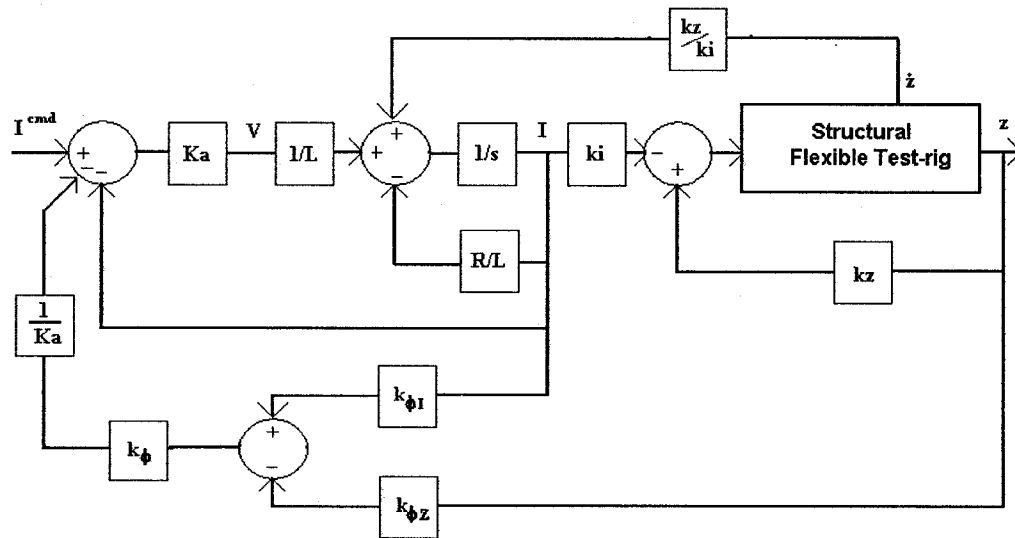


Figure 4.18 Test Rig system with flux feedback

A control scheme with flux measurement can be illustrated by a block diagram in *Figure 2.18* introduced in Chapter 2. According to this scheme and equation (2.38) which represents the current state, a new form of equation (2.38) with flux feedback becomes:

$$\frac{dI}{dt} = \frac{k_z}{k_i} \dot{z} + \frac{k_\Phi k_{\Phi Z}}{L} z - \left(\frac{K_a + R + k_\Phi k_{\Phi I}}{L} \right) I + \frac{K_a}{L} I^{Cmd} \quad (4.40)$$

Thus, the state-space matrices of the system (3.25) can be expressed by:

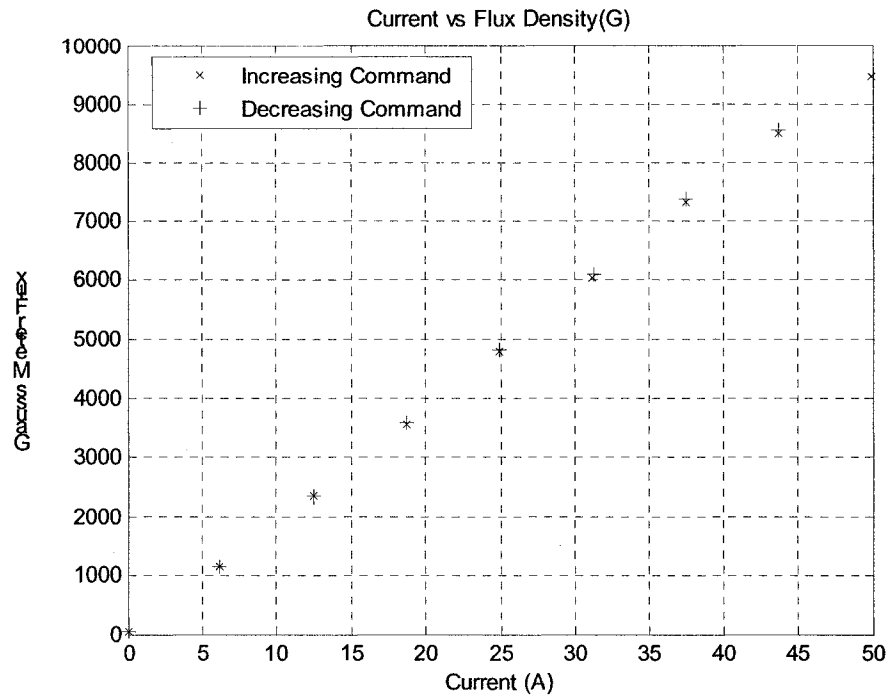
$$A^F = \begin{bmatrix} 0 & 0 & 0 & 1 & 0 & 0 & 0 \\ 0 & 0 & 0 & 0 & 1 & 0 & 0 \\ 0 & 0 & 0 & 0 & 0 & 1 & 0 \\ \frac{k_z - k_1}{m_1} & \frac{k_1}{m_1} & 0 & -\frac{c_1}{m_1} & \frac{c_1}{m_1} & 0 & -\frac{k_i}{m_1} \\ \frac{k_1}{m_2} & -\frac{(k_1 + k_2)}{m_2} & \frac{k_2}{m_2} & \frac{c_1}{m_2} & -\frac{(c_1 + c_2)}{m_2} & \frac{c_2}{m_2} & 0 \\ 0 & \frac{k_2}{m_3} & -\frac{k_2}{m_3} & 0 & \frac{c_2}{m_3} & -\frac{c_2}{m_3} & 0 \\ \frac{k_\Phi k_{\Phi Z}}{L} & 0 & 0 & \frac{k_z}{k_i} & 0 & 0 & -\left(\frac{K_a + R + k_\Phi k_{\Phi I}}{L} \right) \end{bmatrix}$$

$$B^F = B = \begin{bmatrix} 0 \\ 0 \\ 0 \\ 0 \\ 0 \\ 0 \\ \frac{K_a}{L} \end{bmatrix} \quad C^F = C = [1 \ 0 \ 0 \ 0 \ 0 \ 0 \ 0] \quad (4.41)$$

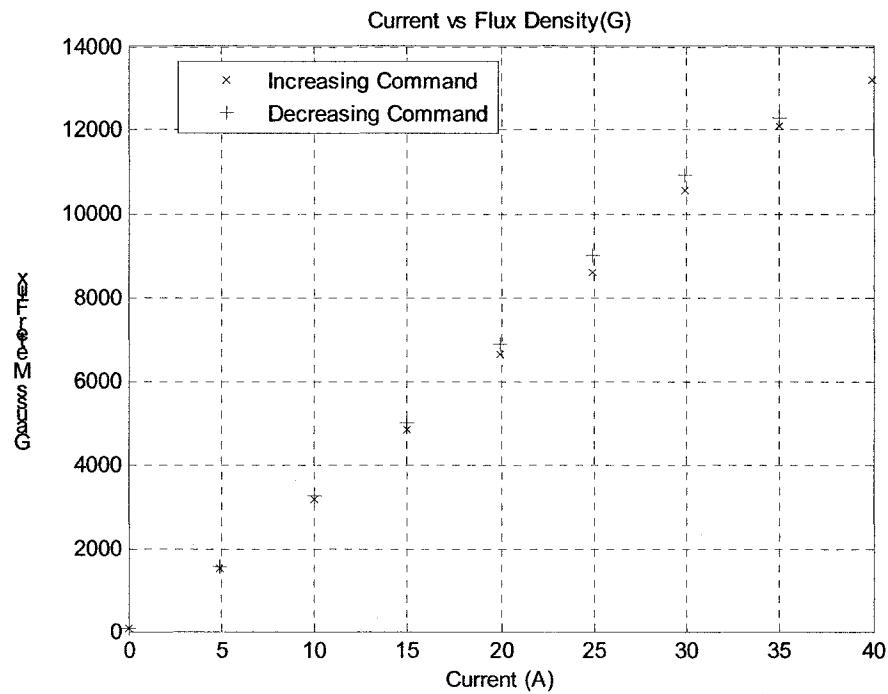
By investigating the characteristic equation of (A^F, B^F, C^F) , it can be noted [25],[63] that flux feedback can make the system conditionally stable without gap feedback, only if:

$$k_\Phi = \frac{k_z (R + K_a)}{(k_{\Phi Z} k_i - k_{\Phi I} k_z)} \quad (4.42)$$

In the above equation all coefficients apart from $k_{\Phi Z}$ and $k_{\Phi I}$ are known. The values of $k_{\Phi Z}$ and $k_{\Phi I}$ can be based on experimental data (*Figures 4.19 a, b, c*).

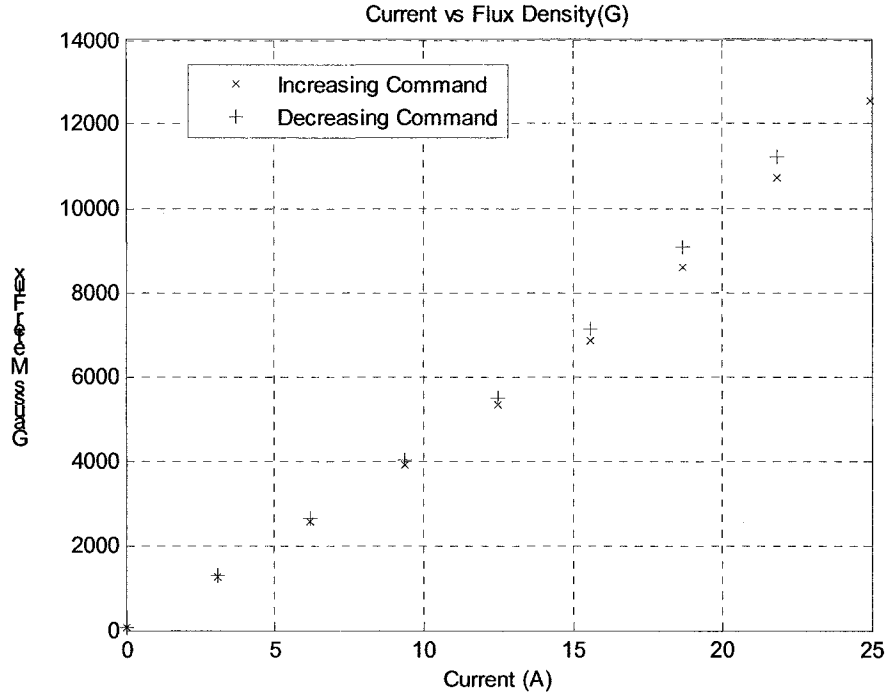


a) data for gap $z = 0.7$ [in]



b) data for gap $z = 0.4$ [in]

Figure 4.19 Flux experimental data



c) data for gap $z = 0.3$ [in]
Figure 4.19 Flux experimental data

Knowing that $\Phi = Bwd$, first one can calculate k_{BI} based on the flux density curve obtained at gap $z_0 = 0.4$ [in] around operation current $I_0 = 25$ [A] (+/- 5 [A]).

$$k_{BI} = \frac{\Delta B}{\Delta I} = \frac{B(30) - B(20)}{30 - 20} = \frac{10500 - 6800}{30 - 20} = 370 \quad [\text{Gauss/A}] \quad (4.43)$$

To convert the flux density units from Gauss to Tesla (SI system) let apply : 1 [Tesla] = 10^4 [Gauss], which gives:

$$k_{BI} = 370 \cdot 10^{-4} = 0.037 \quad [\text{Tesla / A}] \quad (4.44)$$

Thus,

$$k_{\Phi I} = k_{BI} wd = 7.1895 \cdot 10^{-4} \quad [\text{Webers / A}] \quad (4.45)$$

Second, calculate k_{BZ} based on B curves obtained at current $I_0 = 25$ [A] around operation gaps $z = \left\{ 0.3, 0.4, 0.7 \right\}$ [in.].

$$k_{BZ} = -\frac{\Delta B}{\Delta z} = -\frac{B(0.017) - B(0.007)}{0.017 - 0.007} = -\frac{4800 - 12400}{0.017 - 0.007} = 8 \cdot 10^5 \quad [\text{Gauss / m}] \quad (4.46)$$

After conversion into SI units system it becomes

$$k_{BZ} = 8 \cdot 10^5 \cdot 10^{-4} = 80 \text{ [Tesla / m]} \quad (4.47)$$

Thus,

$$k_{\Phi Z} = k_{BZ} w d = 1.55 \text{ [Webers / m]}. \quad (4.48)$$

Substituting expressions (4.50) and (4.51) into (4.49)

$$k_{\Phi} = 1.95 \cdot 10^5 \text{ [A / Webers]} \quad (4.49)$$

Where k_{Φ} is the gain for flux feedback loop.

4.3.1 Flux Leakage

Values (4.51) and (4.52) can be obtained analytically from linearized expression (2.13).

$$k_{\Phi Z} = \left. \frac{\partial \Phi}{\partial z} \right|_{I_0} = - \frac{\mu_o N I_0 S}{2 z_0^2} \quad (4.50)$$

$$k_{\Phi I} = \left. \frac{\partial \Phi}{\partial I} \right|_{I_0} = \frac{\mu_o N S}{2 z_0} \quad (4.51)$$

The difference between these two sets of numbers (4.48)(4.45) vs. (4.50)(4.51) is shown in the below Table 4.5.

Linearized coefficients for flux. ($I_0 = 25 \text{ [A]}$, $z_0 = 0.4 \text{ [in]}$)	Analytical	Experimental	Flux Error [Webers]	Total Flux Losses [Webers]
$k_{\Phi Z}$	1.82	1.55	$\Delta k_{\Phi Z} z_0 = 0.0027$	$\Phi_{Loss} = 0.0052$
$k_{\Phi I}$	$7.28 \cdot 10^4$	$7.18 \cdot 10^4$	$\Delta k_{\Phi I} I_0 = 0.0025$	

Table 4.5 Coefficients for linearized flux expression

These discrepancies may be due to unmodelled [38] flux leakage and flux fringing. Assuming a uniform field between the magnets poles, the pole leakage can be defined as:

$$\Phi_{LP} = - \frac{\mu_o N I_0 d h_m}{2 z_0^2} = 0.0027, \quad (4.52)$$

where h_m is the electromagnet pole height.

Also for the lower part of the electromagnet, the core leakage flux can be modeled as a semicircular shape, called the yoke leakage, expressed as follows:

$$\Phi_{LY} = -\frac{\mu_o N I_0 d}{\pi} = 0.0023 \quad (4.53)$$

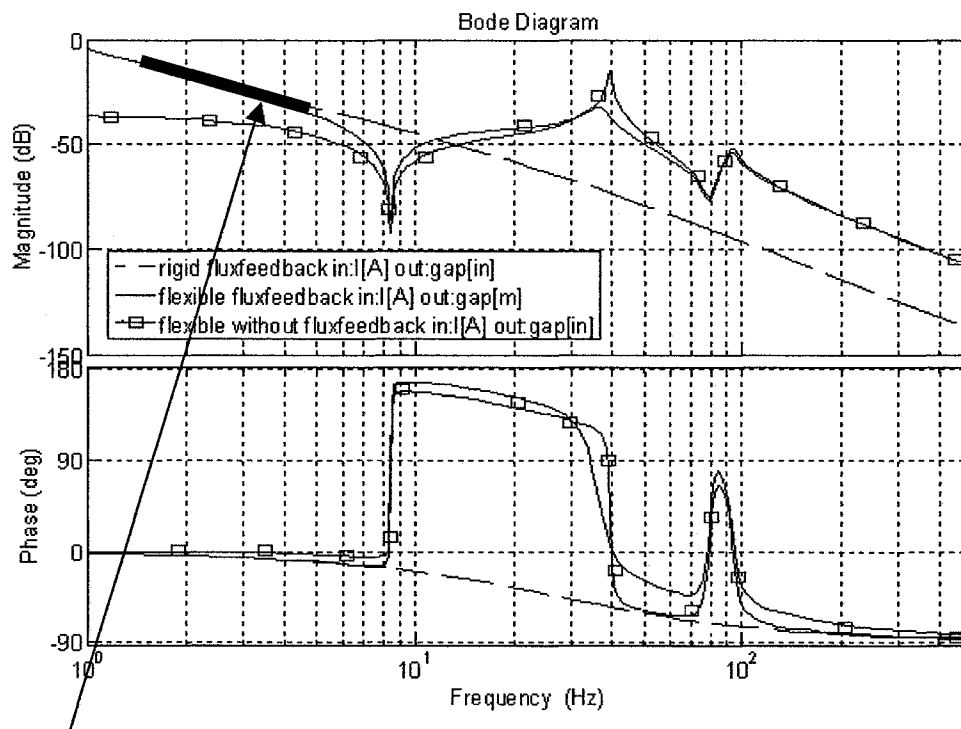
Thus total flux leakage is equal

$$\Phi_{LY} + \Phi_{LP} = 0.0051 \text{ [Webers]} \quad (4.54)$$

which is almost exactly the flux error indicated in *Table 4.5*.

4.3.2 Flux Feedback Analysis

With the value of k_ϕ from (4.52) the open loop Bode plots are illustrated in *Figure 4.20*.



Nonlinearities are linearized

Figure 4.20 Modeled Test Rig system with and without flux feedback

Based on the magnitude plot one can say that the Test Rig system behaves like a system without unstable poles. Using $k_\phi = 1.95 \cdot 10^5$ the transfer function for flexible test-rig system with the flux feedback loop is presented below.

$$G(s) = -\frac{121517.6165(s^2 + 0.318s + 2796)(s^2 + 26.89s + 2.473 \cdot 10^5)}{s^2(s + 174.8)(s^2 + 5.485s + 6.054 \cdot 10^4)(s^2 + 44.82s + 3.398 \cdot 10^5)} \quad (4.55)$$

The advantage of using flux feedback is clearly evident in that the real valued poles linearizing the unstable and have moved to the origin. Both the rigid and flexible Maglev systems illustrated in *Figure 4.20* reveal constant slope 40dB/decade at low frequency.

However there are known practical problems [25] associated with the Hall plates used to effect a flux feedback sensor. Hall sensors are fragile and hence they need to be protected. In this particular application they were put in composite “envelopes” inside a slot in the electromagnet core. These devices are also sensitive to temperature (the sensor used in this application can operate only in the range between -40 [°C] to 100 [°C]), which is not desirable especially when the magnet is driven by high current for long period of time.

One can apply a root locus method in the compensator design for the system with flux feedback as was performed for gap feedback. In this case also, a PD compensator was designed (*Table 4.6*), which provided a stable model response with sufficient performance. In the tables and figure below (*Figure 4.21*) performance of the designed compensators is shown.

Compensator $C(s) = -280-2.2s$	Gap = 0.4 [in.]		Gap = 0.7 [in.]	
	Gain Margin [dB]	Phase Margin [deg]	Gain Margin [dB]	Phase Margin [deg]
no load	7.13	32.5	2.1	9.5
with load	16.9	24.6	11.8	35.0

Table 4.6 Performance of flux feedback control law with PD compensator applied to linear Maglev models

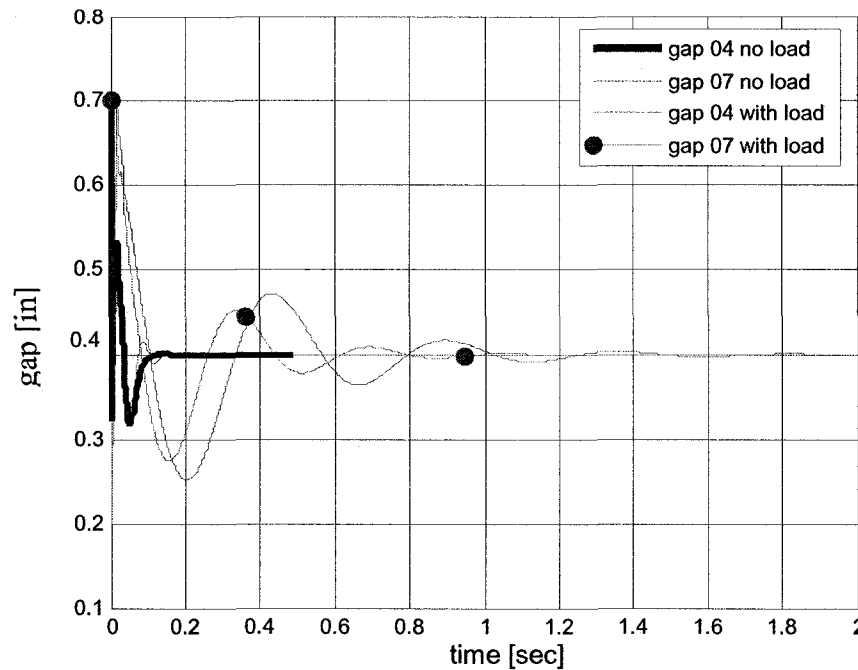


Figure 4.21 Test Rig time response with flux feedback

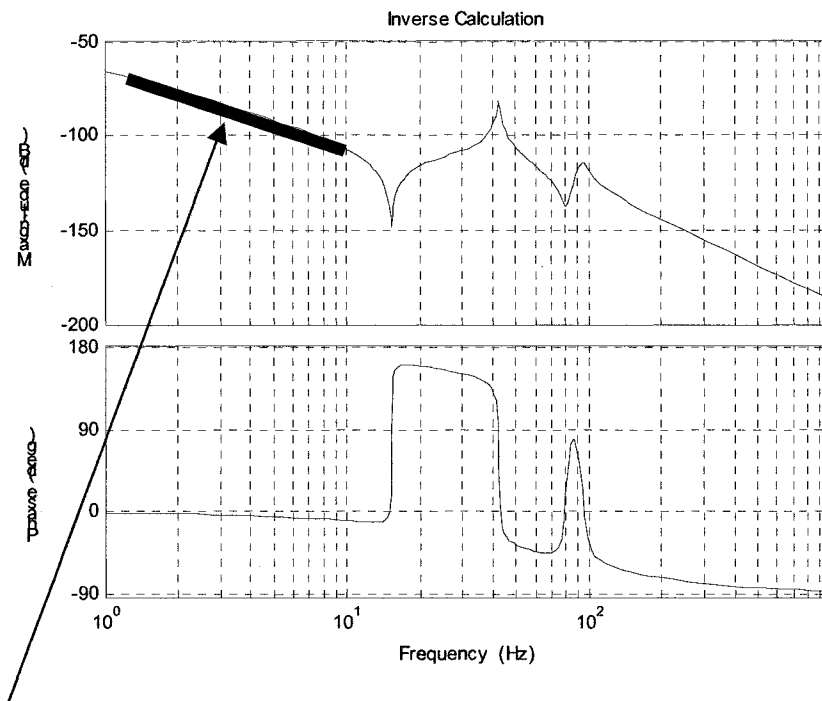
In these tests two modeled test-rig system were investigated, one with extra load applied $M_{weights} = 320$ [lbs] (see Figure 3.14) and a second without additional mass $M_{weights} = 40$ [lbs].

Observing the above figures it can be noted that system without applied load tracks the gap command faster and with smaller overshoot. This situation can be easily explained by mass inertia, which is much higher when $M_{weights}$ acts on the test-rig frame. It is worth noting that for loaded system with flux feedback, a stable response exists, while for pure gap feedback a compensator setup which could guarantee stable response for both plants (with and without applied load) was not found. Also for the system without additional mass on the rear side of the Test Rig frame the settling time appears to be worse in the gap feedback case (Figure 4.8 - 0.4 seconds), comparing to 0.2 second for the modeled flux feedback incorporated into system (Figure 4.21). These notes clearly indicate that the flux feedback is desirable to improve system robustness.

4.4 PD Control with Inverse Calculation

As was mentioned in section 2.14 non-linearity of the Maglev systems equations can be neutralized by applying inverse force calculations into the control law (see *Figure 2.23*). In this section a model of the system with inverse force calculations is developed and a compensator design is presented. Based on equations of motion (3.25) and levitation force characteristics from (2.120) a new flexible test-rig model can be derived.

$$\begin{aligned}
 \begin{bmatrix} \dot{x}_1 \\ \dot{x}_2 \\ \dot{x}_3 \\ \ddot{x}_1 \\ \ddot{x}_2 \\ \ddot{x}_3 \\ \dot{I} \end{bmatrix} &= \begin{bmatrix} 0 & 0 & 0 & 1 & 0 & 0 & 0 \\ 0 & 0 & 0 & 0 & 1 & 0 & 0 \\ 0 & 0 & 0 & 0 & 0 & 1 & 0 \\ -\frac{(k_1+k_z)}{m_1} & \frac{k_1}{m_1} & 0 & -\frac{c_1}{m_1} & \frac{c_1}{m_1} & 0 & -\frac{k_i}{m_1} \\ \frac{k_1}{m_2} & -\frac{(k_1+k_z)}{m_2} & \frac{k_2}{m_2} & \frac{c_1}{m_2} & -\frac{(c_1+c_2)}{m_2} & \frac{c_2}{m_2} & 0 \\ \frac{k_1}{m_2} & -\frac{(k_1+k_z)}{m_2} & \frac{k_2}{m_2} & \frac{c_1}{m_2} & -\frac{(c_1+c_2)}{m_2} & \frac{c_2}{m_2} & 0 \\ 0 & \frac{k_2}{M} & -\frac{k_2}{M} & 0 & \frac{c_2}{M} & -\frac{c_2}{M} & 0 \\ \frac{K_a k_z}{k_i L} & 0 & 0 & \frac{k_z}{k_i} & 0 & 0 & -\frac{(K_a + R)}{L} \end{bmatrix} \begin{bmatrix} x_1 \\ x_2 \\ x_3 \\ \dot{x}_1 \\ \dot{x}_2 \\ \dot{x}_3 \\ I \end{bmatrix} + \\
 &\quad \dots + \begin{bmatrix} 0 \\ 0 \\ 0 \\ 0 \\ 0 \\ 0 \\ \frac{K_a}{Lk_{iz}} \end{bmatrix} [I^{Cmd}] \quad (4.56)
 \end{aligned}$$



Nonlinearities are linearized (2 real poles have migrated to $s=0$)

Figure 4.22 Bode plots of the system expressed by equation (4.56)

As can be seen (Figure 4.22) the two real poles p_1 and p_2 which were unstable for (3.26) for the system expressed by equation (4.56) have moved to the origin and are similar to rigid body poles. This makes the system easier to stabilize. The inverse force calculation idea is very similar to flux feedback approach shown in section 4.3.2. In the both cases an inner control loop attempts to linearize the system first and then, an outer loop stabilizes the plant.

An example of compensator root locus design is shown in Figure 4.23 where system poles for PD compensation remain in the stable region for all compensator gains (black squares on the loci curves).

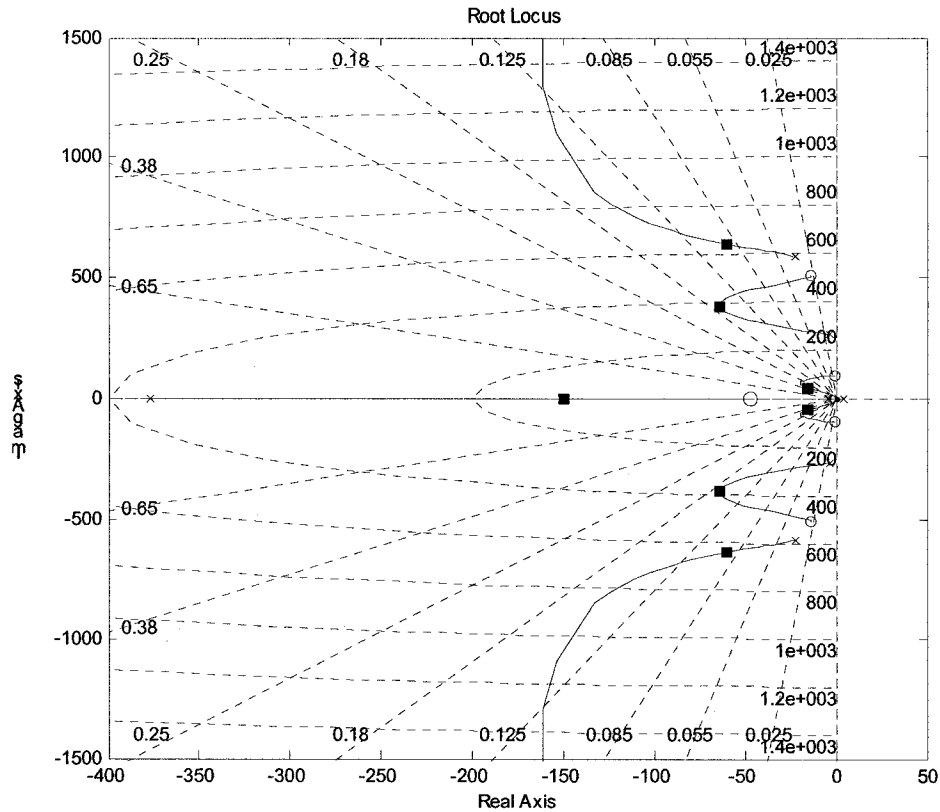


Figure 4.23 PD root locus design for system with inverse calculation

The compensator $C(s) = -10400 - 220s$ provides the best performance among these which were tested. Moreover; systems with inverse calculations as an integral part, tolerate variation in compensator coefficients up to $\pm 50\%$ of their nominal values. Experimental results are presented in section 4.5.

4.5 Application and Experiment Results

In the earlier sections control laws for the Test Rig system modeled in Chapter 3 were designed. To validate all these proposed controllers, experiments were carried out at the ODU laboratory facility (see Figure 3.1). In this section the hardware setup of the experiment will be discussed and results presented.

For control law application the Matlab[®] tool called xPcTarget was utilized. The advantage of using xPcTarget is flexibility in the control design. A prospective compensator can be changed very easily in Matlab[®] Simulink[®] software on the host computer, then compiled and sent to the target machine. In this particular test configuration a desktop PC computer was used as a host. A PC104 single based computer with Intel[®] 468 series processor was used as a target. Communication between these two devices was established via Ethernet. The RTD[®] PC104 computer was equipped with data acquisition card. Sampling time for PC104 was set to 20 [kHz].

Scheme of the Test Rig setup is shown in the *Figure 4.24*.

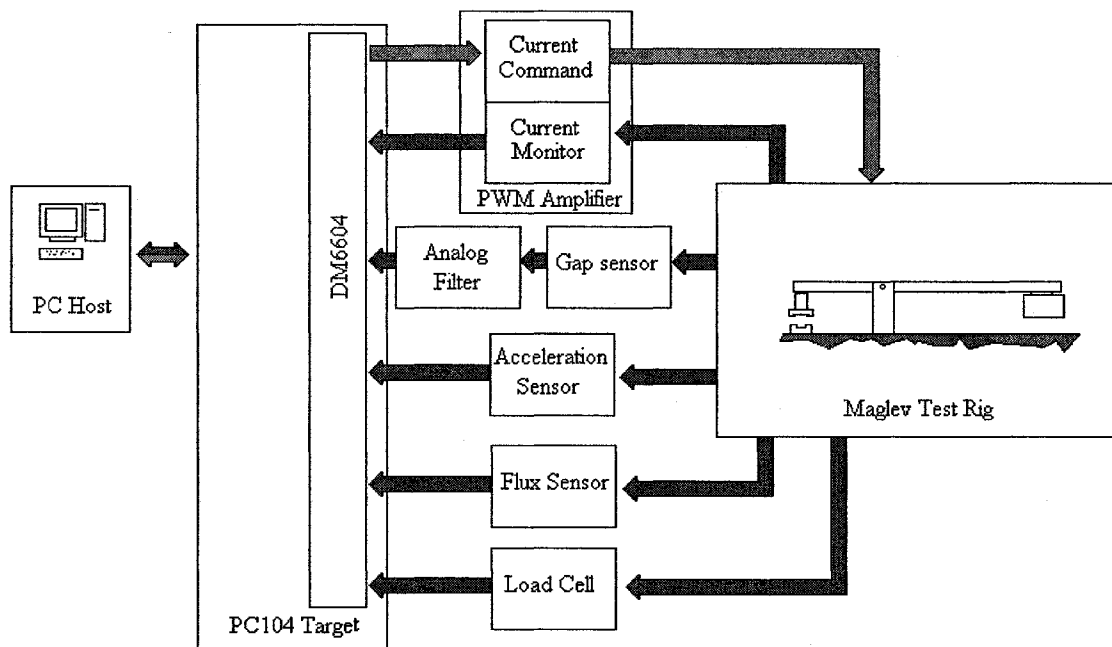


Figure 4.24 Schematic of the Test Rig experiment setup

The PWM amplifier, Clinton power supply, electromagnet and analog filter used in these experiments were already introduced in Chapter 3. A Kaman model 12CU eddy current type gap sensor was used. For acceleration measurement a PCB 302A sensor was used, while to measure flux a BH-202 Hall sensor was adopted. Additionally for magnetic force monitoring two load cells were built into the system, Omegadyne[®], model

LCHD-10K, measuring range 0-10000 lbs. All reading data was converted by National Instrument data acquisition card to monitor and plot results in Matlab®.

The duration of each test was 60 seconds. The gap command was a ramp function with negative slope starting from gap 0.7 [in]. (initial value of gap). The final desired gap was value of 0.4 [in.] achieved after 7 seconds.

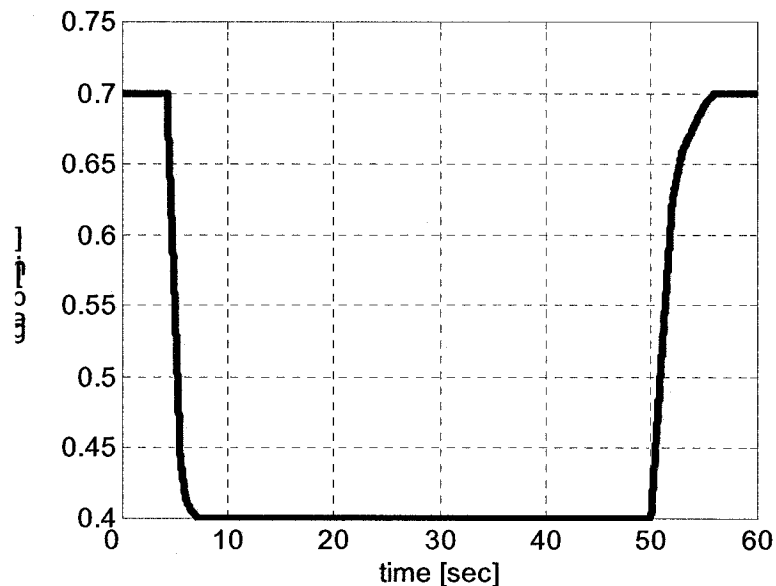


Figure 4.25 Gap command for the Test Rig experiment

After 50 seconds another ramp function was activated to smoothly decrease the command value back to its initial 0.7 [in].

4.5.1 Pure Gap Feedback with PD/PID Compensator

In the first test, gap feedback control laws were investigated. The best performance in this case was achieved with a PD compensator and a 3 pole Chebyshev type II digital filter. The Simulink® diagram for this configuration in xPTarget software is shown in the below *Figure 4.26*.

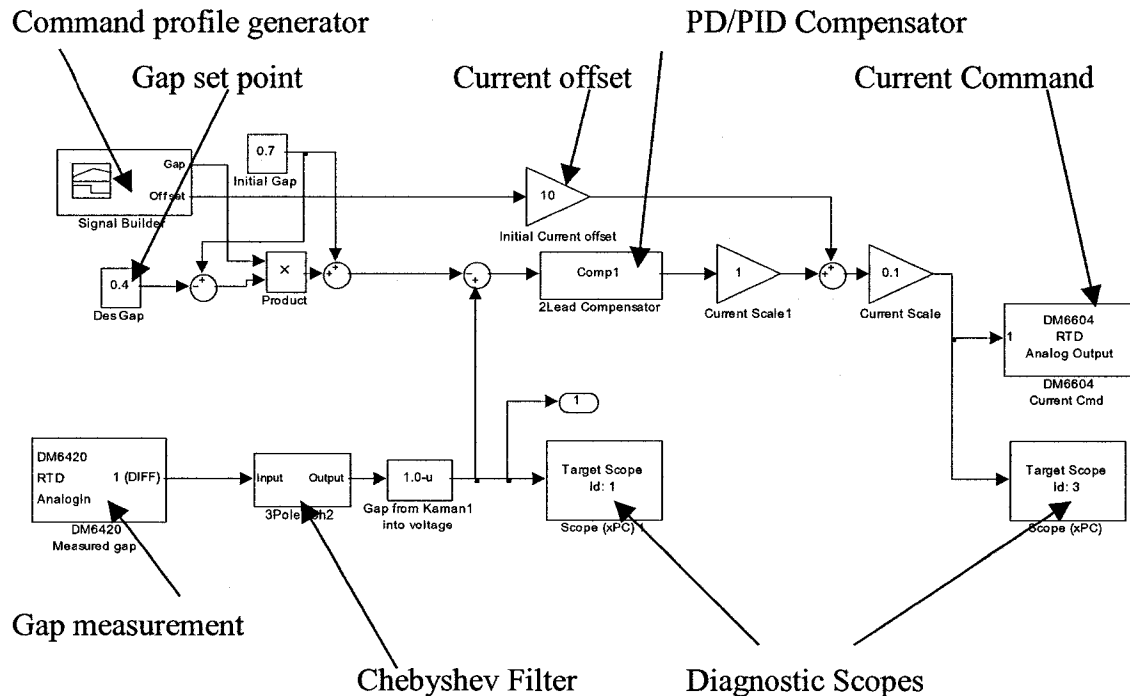
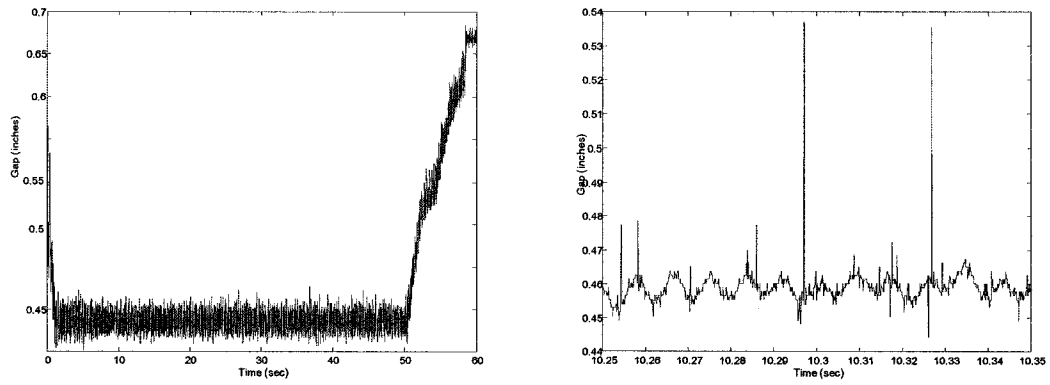


Figure 4.26 Simulink[®] diagram of the gap feedback control law

Obtained gap results (Figure 4.27) were satisfactory; however, after zooming in on the gap history a small fluctuation of around 0.025 [in.] with around 120 [Hz] frequency was noted (Figure 4.27b). It was also observed that current command to the amplifier carried a lot of high frequency noise (see Figure 4.28) and steady oscillation of +/- 15 [Amps] at approximately 120 [Hz]. In Figure 4.28 the best results are shown when a 3 pole 3400 [Hz] Chebyshev digital filter together with 4000 [Hz] analog 8 pole Butterworth filter were utilized in the gap feedback control loop.



a) full time 60 sec. range

b) 1 ms time range

Figure 4.27 Gap responses with PD compensator – pure gap feedback

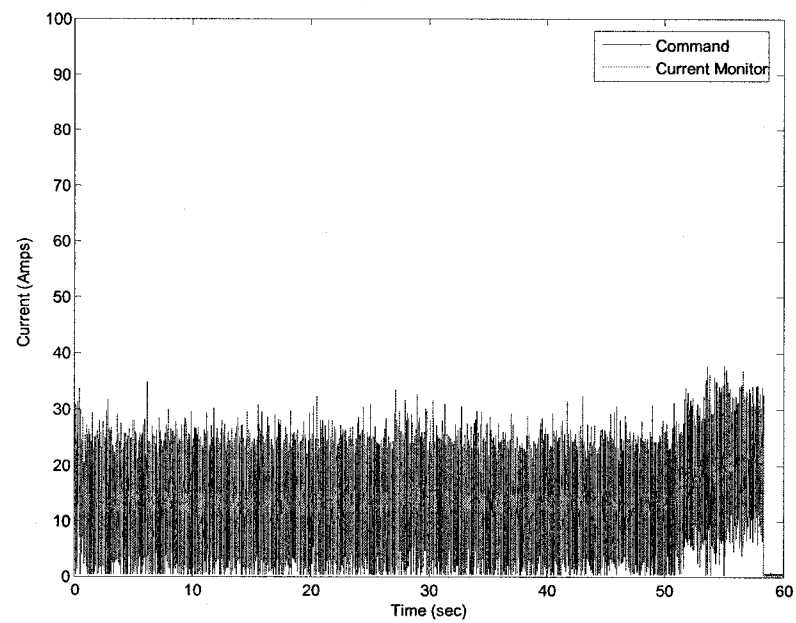


Figure 4.28 Noisy current command signal

4.5.2 PD/PID Compensator based on Gap with Acceleration Feedback

The next test was carried out with the sensor fusion approach described in section 4.2 when acceleration signal together with gap feedback were used. The same PD compensator, which was applied in the previous experiment, was used. The only change was made in the Simulink[®] control scheme in agreement with the analysis introduced in section 4.2 by incorporating a leaky integrator. The new control scheme diagram was uploaded into the PC104 computer as shown in *Figure 4.29*. New features in comparison to a pure gap feedback control law are marked by arrows.

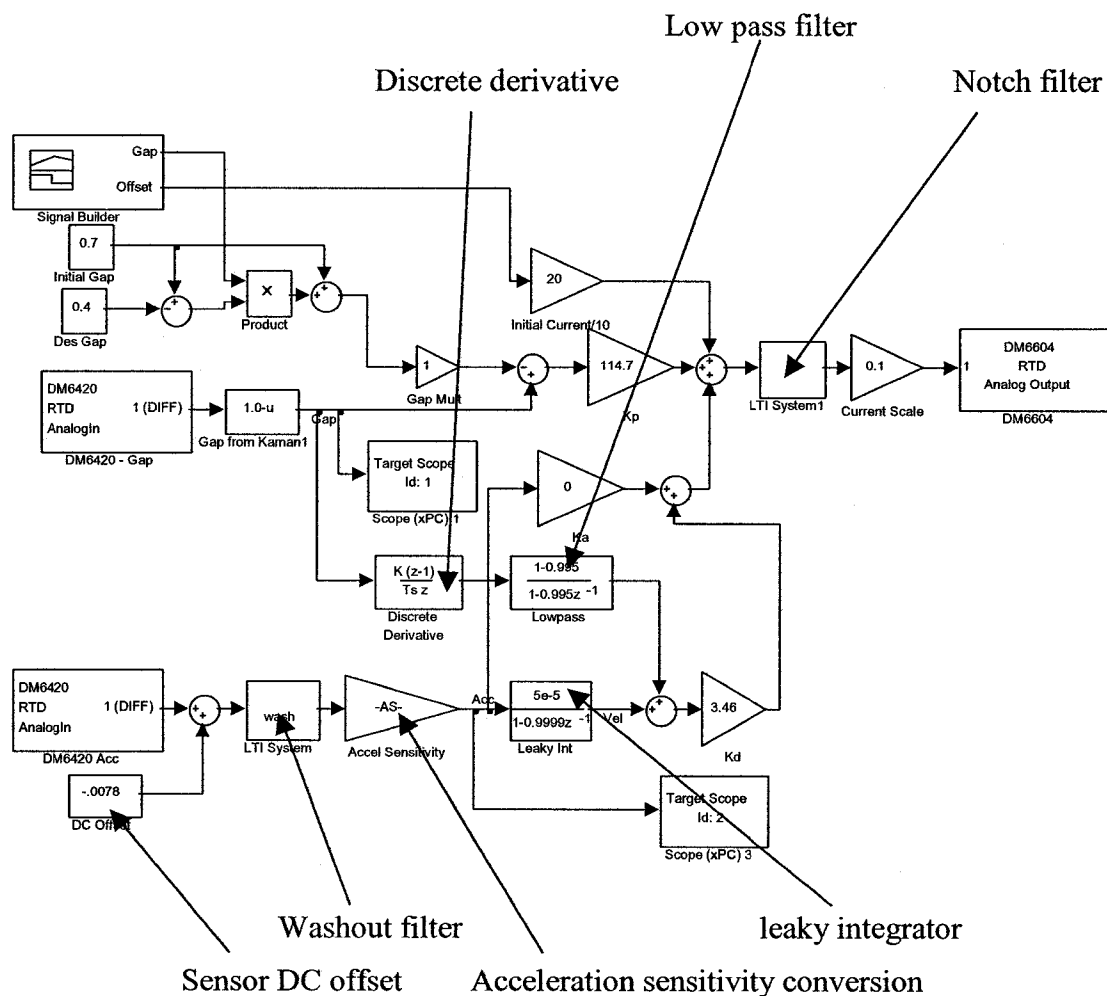


Figure 4.29 Simulink[®] diagram of the mixed gap and acceleration feedback control law

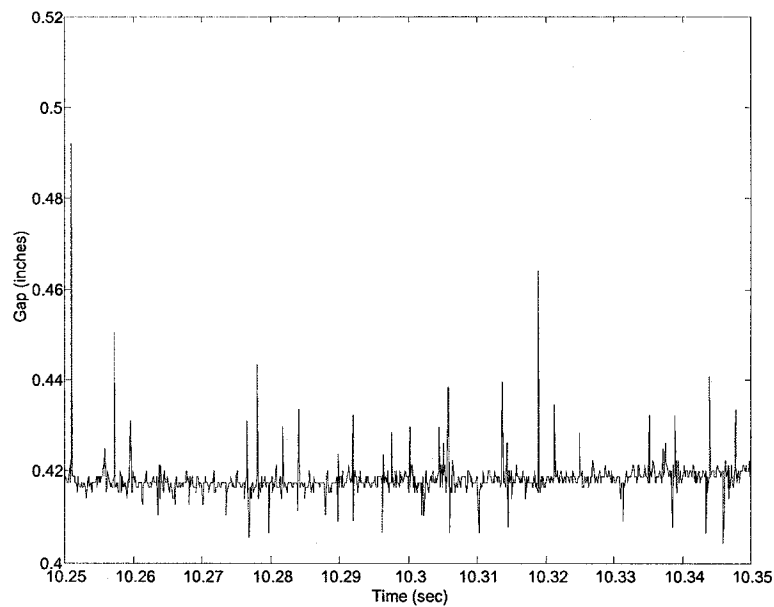


Figure 4.30 Gap response with PD compensator – gap and acceleration feedback in range of 1 ms time range

As can be seen in *Figure 4.30* performance was significantly improved compared to the pure gap feedback case. There is no 120 [Hz] oscillation visible and also the current command signal looks smoother with a lower noise amplitude range. Current signal noise is in the range between 19 and 25 Amps (*Figure 4.31*) versus 0 to 30 Amps (*Figure 4.28*).

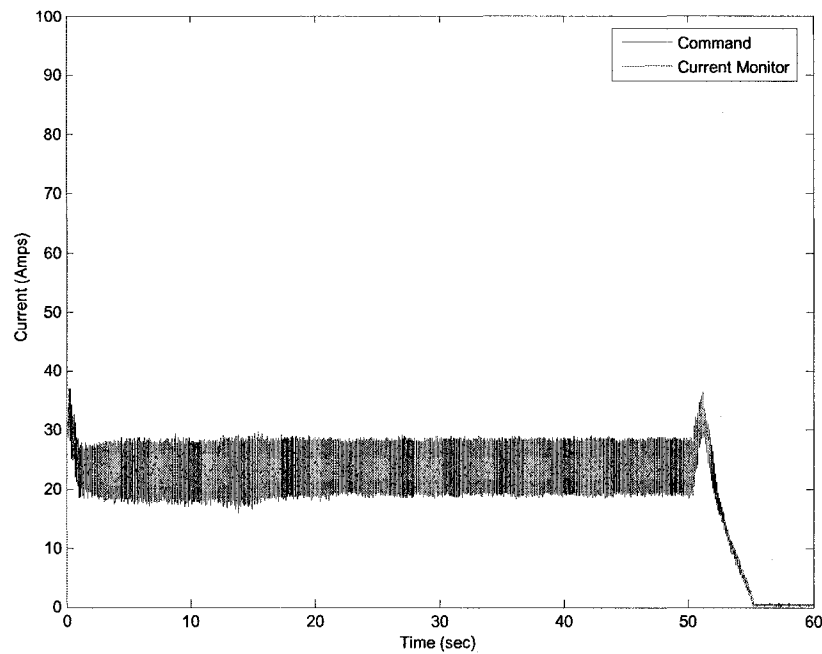


Figure 4.31 Current command signal (gap and acceleration feedback)

After the applied load to Test Rig was increased some issues related to gap response were observed. Gap started to exhibit 0.8 [Hz] variations (Figure 4.32). This behavior was predicted by analysis and shown in the Figure 4.11.

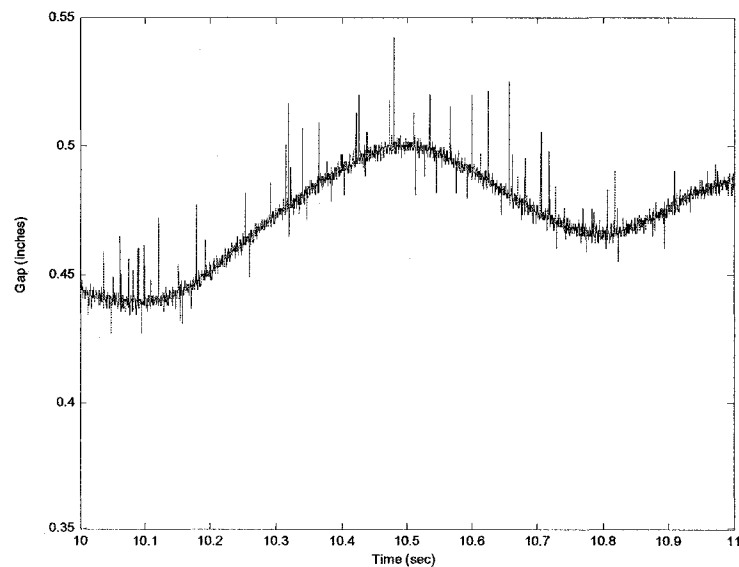


Figure 4.32 0.8 [Hz] fluctuations in gap response

In spite of this, the system remained stable. Thus, the test-rig system with acceleration feedback as an additional source of data coupled with pure gap information provided stable and robust performance.

4.5.2.1 Steady State Error Tests

As was mentioned in 4.1.2.1, when using the PD compensator, steady state error is expected in the test-rig gap response. In *Figure 4.33*, system response without a current offset is illustrated (0.4 [in] gap is commanded). As can be seen 0.17 [in] error occurs, which validates the analytical simulation presented in *Figure 4.9*. It is common to use an integrator to drive down this error. The Test Rig system performs better with an acceleration measurement in parallel to gap sensing thus an integrator was incorporated into this setup. Steady state error was eliminated while the gap remaining in the satisfactory range (see *Figure 4.34*).

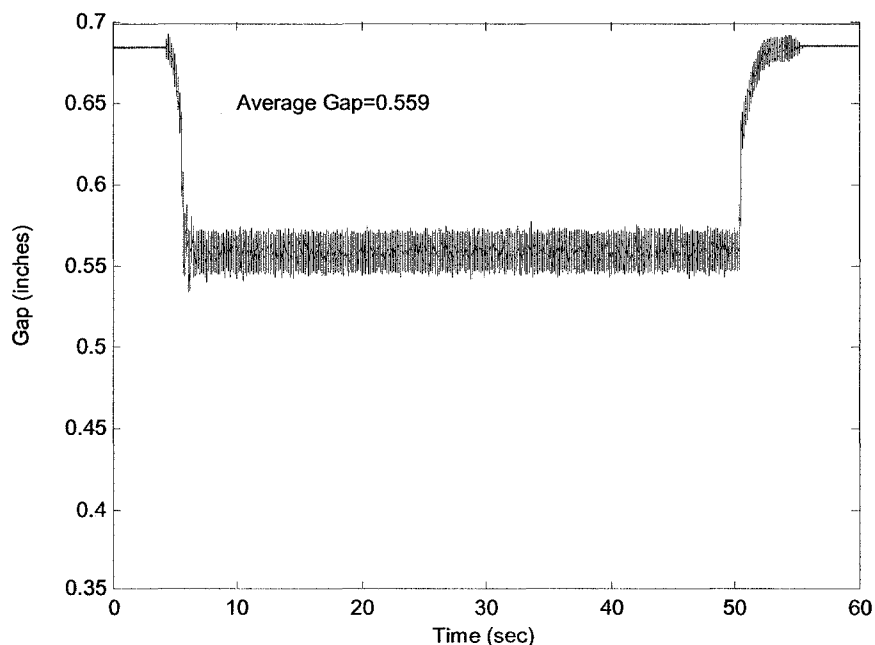


Figure 4.33 Test Rig response without current offset and without integrator

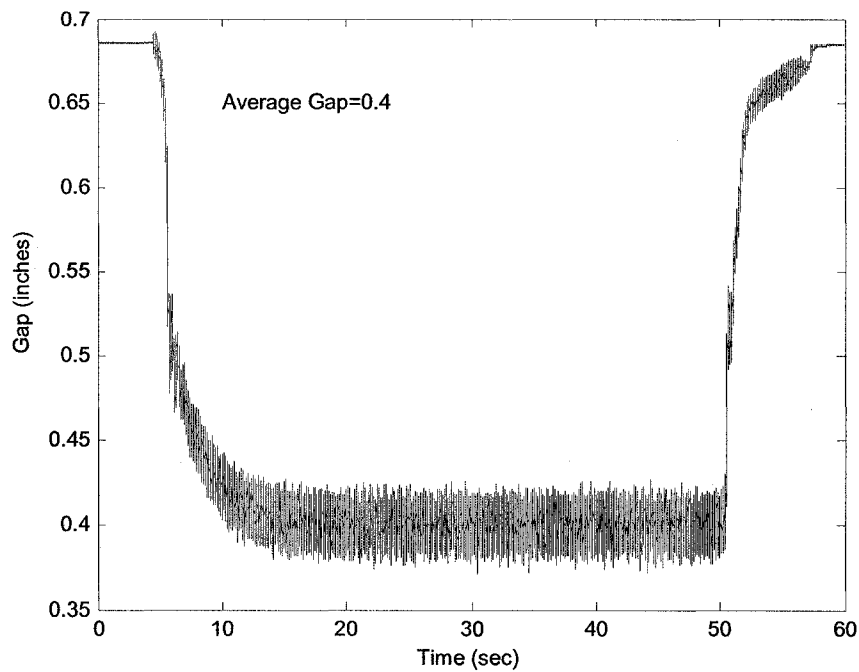


Figure 4.34 Test Rig response with integrator when acceleration feedback is used

A new PID compensator was designed based on root loci ($K_I=60$, $K_P=-188$, $K_D=-2.2$) to find a maximum phase and gain margin.

4.5.3 Compensator with Linearized Calculation (Force Inverse)

The control law developed in section 2.14 was tried on the test-rig setup. As was predicted this compensator worked over a very wide range of controller coefficient values for K_P and K_D . These tests used an m-file to describe the electromagnet force in model inversion computations. A simple form of the force model that does not account for fringing is used (see Figure 4.35).

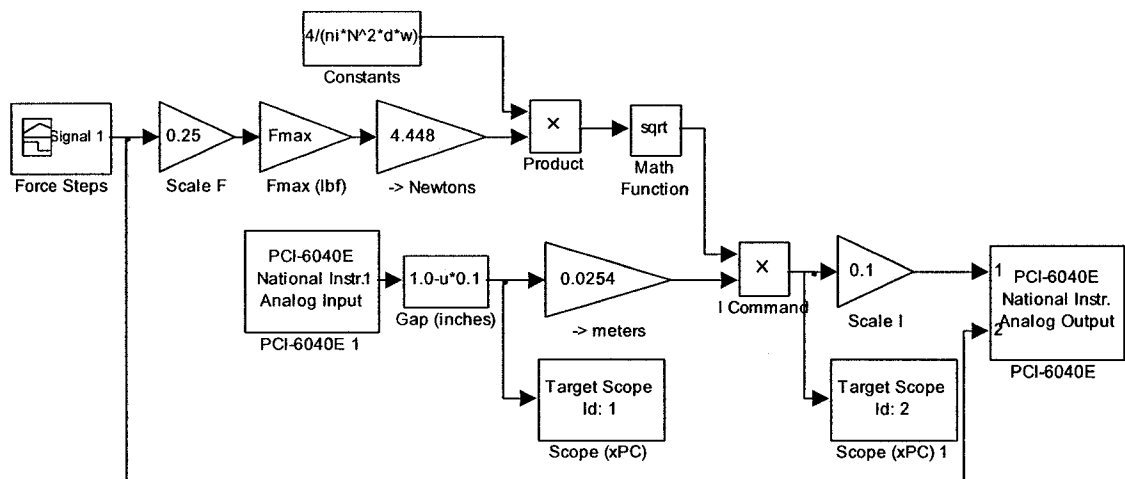


Figure 4.35 Model of the force inverse calculation

Experimental results when inverse force calculation is used are shown in the Figure 4.36 and Figure 4.37.

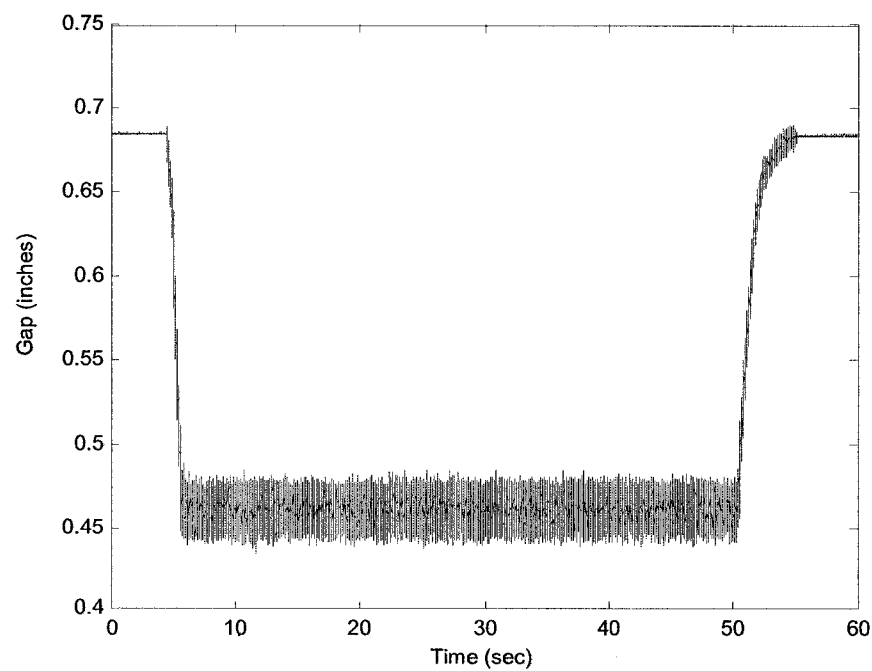


Figure 4.36 Test Rig response with force inversion ($K_P=35000$, $K_D=350$)

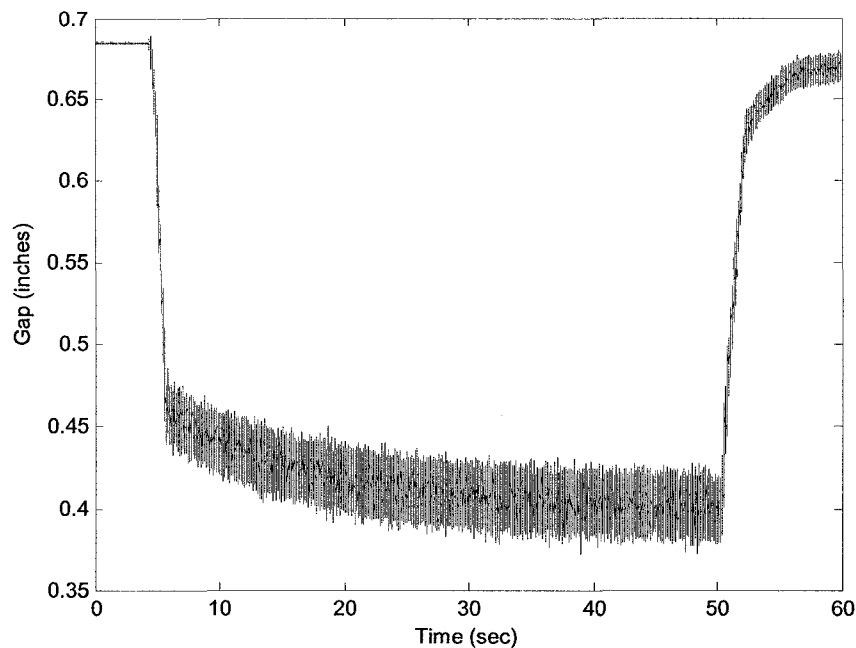


Figure 4.37 Test Rig response with force inversion and integrator $K_I=3000$

It is worth noting when the values of K_P and K_D were varied in range of $\pm 50\%$ the Test Rig Maglev system remained stable. The integrator which eliminated steady state error also did not introduce any undesired behaviors.

4.5.4 Compensator with Flux Feedback

In the last experiment a flux feedback loop was incorporated into the control law. The test-rig characteristics, as shown in section 4.3, resulting from the additional flux loop became linear and easier to stabilize. On the host computer a new Simulink® model was created and applied to the actual plant. In Figure 4.38 new components of the control law with flux feedback are marked by arrows.

Results obtained when flux measurement were utilized are shown in Figures 4.39 4.40. In the first Figure 4.39 gap response with a simple PD controller is presented while in Figure 4.40 gap response with an additional integrator ($K_I=20$) incorporated into control law are shown. Comparing to the previous compensators results this setup provided good performance and robustness. Compensator gains were varied by $\approx 70\%$

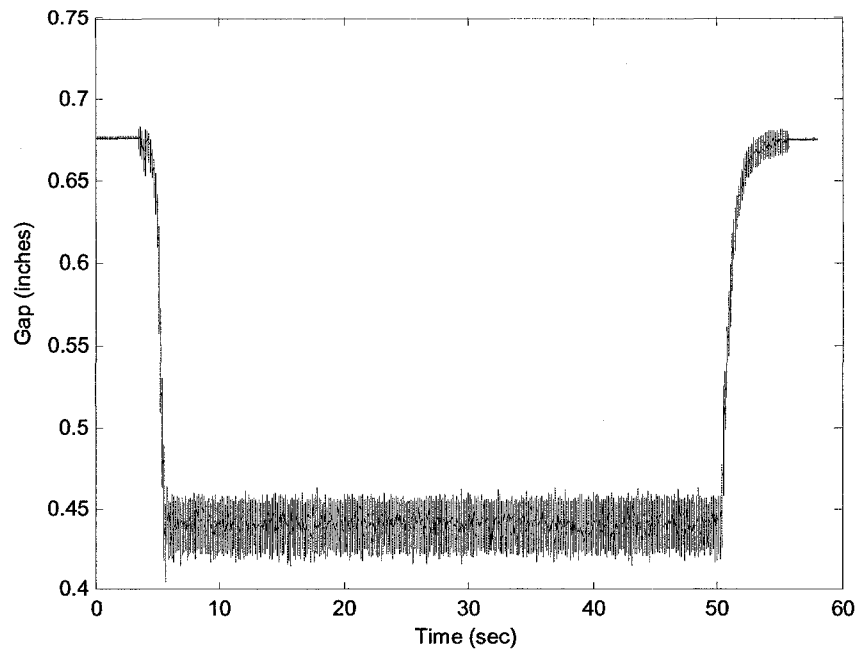


Figure 4.39 Gap response system with PD compensation and flux feedback

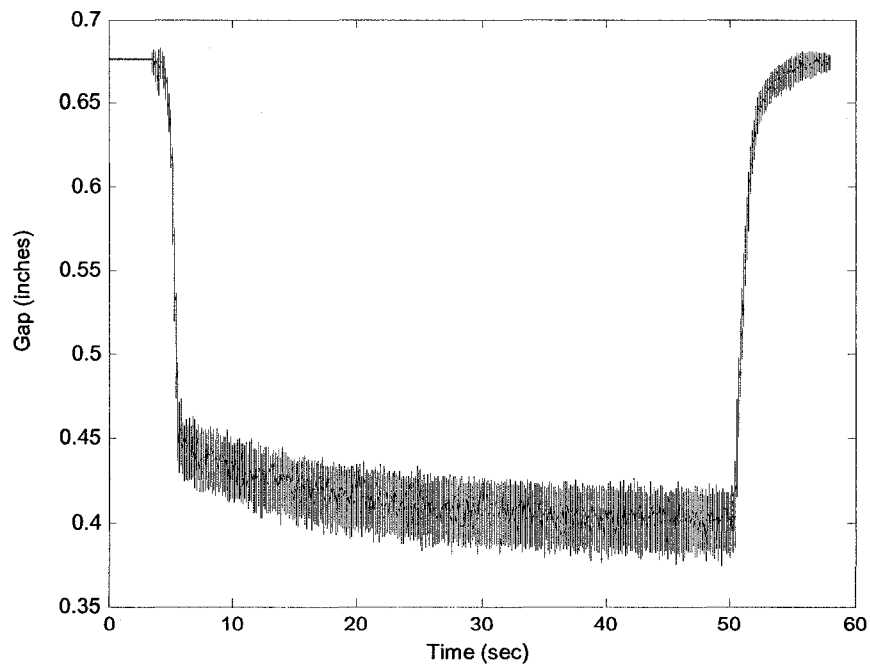


Figure 4.40 Gap response system with PID compensation and flux feedback

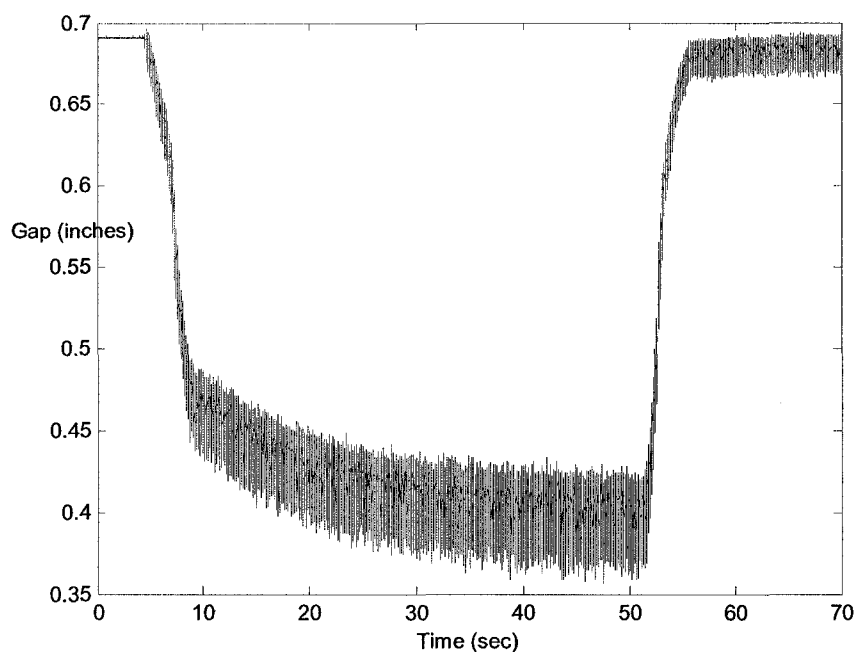


Figure 4.41 Gap response system with PID compensation and flux feedback and additional load (320 lbs)

In the last figure (*Figure 4.41*) a gap response is shown when the additional load is applied to the Test Rig (to simulate passenger loading in the real ODU Maglev vehicle).

4.6 Conclusion

In this chapter compensators were designed and tested on the actual Test Rig Maglev plant. To compare all control laws the following table was created (*Table 4.7*).

Compensation / Model	Linear Models	Non-linear Model	Experiment	Comments
PD/PID	Fast response (0.4 sec.) <i>Figure 4.8</i>	Good tracking <i>Figures 4.9, 4.12</i>	Noisy response <i>Figure 4.27</i>	NOTE 1
PD/PID with mixed Gap and Accelerometer Feedback	NOT TESTED	NOT TESTED	Significant noise rejection <i>Figure 4.30</i>	NOTE 2
PD/PID with Inverse Calculation	Robust response	Robust response	Noise rejection and robust to weights variation <i>Figures 4.36, 4.37</i>	NOTE 3
PD/PID with Flux Feedback Loop	Robust response <i>Figure 4.21</i>	Robust response	Noise rejection and robust to weights variation <i>Figures 4.39, 4.40, 4.41</i>	NOTE 4

Table 4.7 Comparison of tested on actual plant control laws

Note 1: According to analysis the compensator which used just gap measurement should provide stable and reasonable results. In the one-degree-of-freedom experiment pure gap feedback based on the PD compensation needed a current offset or integrator

(PID) to achieve the desired gap, which is a typical for the PD design. For the system without applied load, stable response was obtained; however some gap fluctuation with frequency of 120[Hz] was noted. Current commands (output from compensator) also included unacceptable noise with amplitude in range of ± 15 Amps. The fluctuation was caused by taking the signal derivative which exaggerated noise peaks. This simple control design did not work for different (heavier) Test Rig systems, as a result of the effect of different Maglev pole positions relating to different vehicle mass and linearized coefficient k_z (see equations 2.32 and 2.46).

Note 2: After acceleration measurement was incorporated and merged with the gap feedback, the performance of the Maglev system was improved significantly compared to PD compensator with gap feedback only. The compensator's design (its transfer function) remained the same; analytical simulation was not carried out. In the one-degree-of-freedom experiment the noise in both the command signal and in the gap response were reduced. By avoiding direct derivative calculation inside the compensator, the current command signal noise reduction reached values greater than 100%, compared to the pure gap feedback approach. However, a small fluctuation in gap response was still noted and a stable result with applied additional load was not available.

Note 3: When an inverse force calculation was added to the PD/PID compensator with acceleration feedback the Test Rig system responded much better. Both analytical approaches and experiments agreed and provided very good characteristics. In the gap response there were no visible fluctuations. Further, the same compensator could work with different loads applied to the Test Rig (however with significantly longer settling time), moreover controller gains could be changed by $\pm 50\%$ without any impact on the system stability.

Note 4: Following the idea introduced for force inversion, a compensator with the flux feedback was designed. There are two main advantages of this approach compared to force inverse calculation. First, better system linearization can be obtained. Second, additional data is provided in the control loop. This additional data provided more accurate levitation force evaluation. The PD/PID compensation together with the flux feedback delivered the best performance among all controllers evaluated in this work. Test Rig response was quick with small overshoot for both analytical models and

experiments. Flux feedback provided even greater flexibility and tolerance of uncertainty resistance than as described above for control design with an inverse force calculation. In this case a compensator gains accepted variation within the range of $\pm 70\%$ of their nominal values. After 320 [lbs] load was applied to the Test Rig, the controller with flux feedback achieved the desired gap command, in this case with only slightly longer settling time.

It can be concluded that among control laws presented, the best results were provided with the gap and acceleration fusion feedback, together with the inverse force calculation or flux feedback. Only these approaches were able to significantly suppress the noise in the current command signal and at the same time get very smooth gap tracking. Also it can be said (based on the observation of the *Table 4.7*) that to analytically investigate prospective control design, a very good and detailed non-linear model is required. Switching from the linear to the non-linear plant model can cause lack of integrity with the actual system and furthermore can provide unrealistic results.

The majority of investigated compensators showed at least similar behaviors to these evaluated analytically. Apart from compensator design results for Maglev applications, some interesting observations were shown both analytically and experimentally in this chapter.

First, controllers which can linearize the system provide more robust response. In this regard, an interesting observation (presented in section 2.14) can be related to the reduced expression for inverse force calculation (equation (2.118) vs. (2.119)). It was shown experimentally that it is not necessary to use full levitation force expression to apply inverse calculation and linearize Maglev system. Second, compensators which stabilize the electromagnet pole do not necessary guarantee overall system stability.

Thus, while it is relatively easy to deal with Maglev unstable poles, noise and non-linearities are significant issues for control design. This fact emphasizes that problems during control law design for Maglev systems are mainly caused by three factors:

- external noise entering the control loop,
- non-linear behaviors due to magnetic levitation force,
- derivative calculation inside the compensator.

5. ODU Maglev Vehicle Model

In this chapter a model of the Old Dominion Maglev system is presented. The Old Dominion Maglev system is a single EMS vehicle. It is approximately 45 [ft] long with the capacity to carry 100 passengers. It is intended to cover a 1.2 [mile] route in 3 – 5 minutes. This vehicle uses twelve, 200 [lbs] magnets (*Figure 5.1*), 3 computers and 2 Linear Induction Motors LIM's (*Figure 2.2a*). It was designed to travel at speeds up to 40 [m.p.h] along the 0.6 [mile] long guideway, which is supported by concrete columns 2 feet in diameter and spaced 80-90 [ft] apart. The existing Maglev vehicle is shown in *Figure 5.1a* and *Figure 5.1b*.

The vehicle has two separate sub-frames called bogies in the front and rear (see *Appendix A.3*). Each bogie has six lift magnets. These U-shaped lift magnets are attached to the bogies using aluminum “hockey sticks” (*Figure 5.2a*). The hockey sticks' positions are symmetrical with respect to the centerline of the vehicle. The layout of the coils is shown in the *Figure 5.1c*.

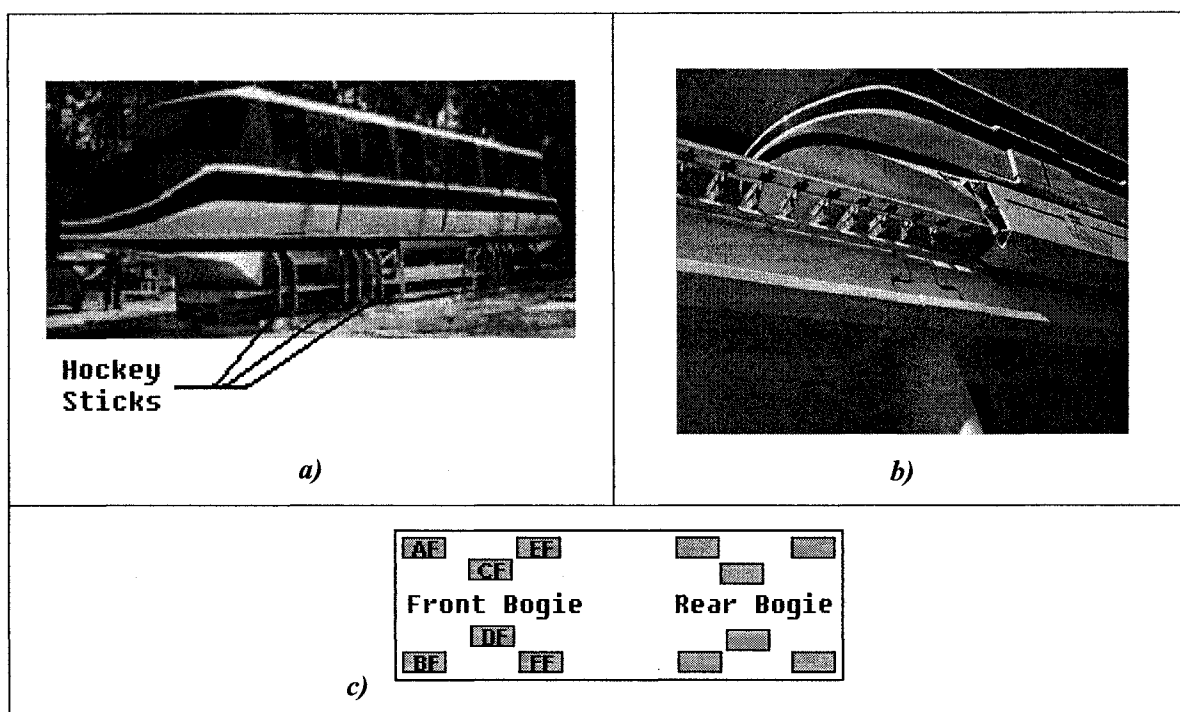


Figure 5.1 ODU Maglev system a) Maglev vehicle, b) Vehicle on the track, c. Layout of the lift magnets

The small difference (0.5 [in.]) in the horizontal position of magnets CF and DF was provided to improve cross guidance stability of the vehicle. It can be calculated [81] that this offset is sufficient to maintain lateral position of the ODU Maglev vehicle at up to 40 [m.ph.] crosswind gust.

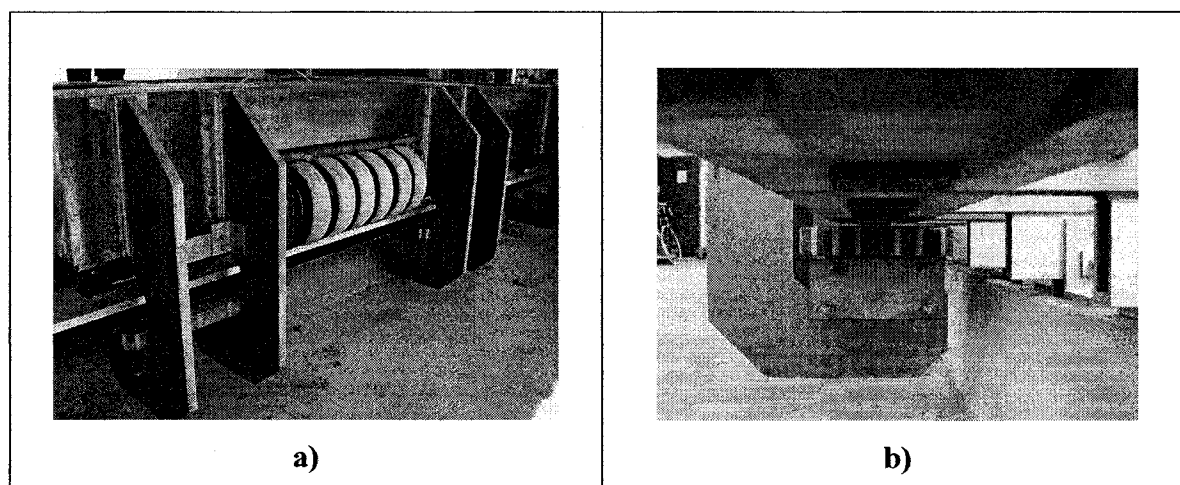


Figure 5.2 Electromagnets mount a) LIM magnet, b) Coil assembly to the hockey stick

Detailed schematics and drawings of the Maglev chassis are attached in *Appendixes A.1-A.3*.

5.1 Control Current Drive Model (CID)

In the section 3.1 a model of the electromagnet with a commercially available current amplifier as used in the test rig was presented. The ODU Maglev vehicle uses custom-made amplifiers referred to as Control Current Drives (CIDs) [82]. The CIDs were designed and fabricated by Williams Consulting Inc. for American Maglev.

The CID is a microprocessor-based device. It is used to drive the magnet coils in either current, or voltage controlled mode. The CIDs drive the magnets via an H-bridge configuration. Two of the phases of the H-bridge (outputs U and V) are utilized by switching MOSFET transistors (arrows in the *Figure 5.3*). The other phase presented in *Figure 5.3* looks like a third circuit loop and can be recognized as a chopper for dynamic braking. This part of the IGBT module is used for safety purposes. The main function of the CID is executed by the PM100CVA100 Intellimod Module, which is controlled by a Motorola DSP56F803BU80 processor.

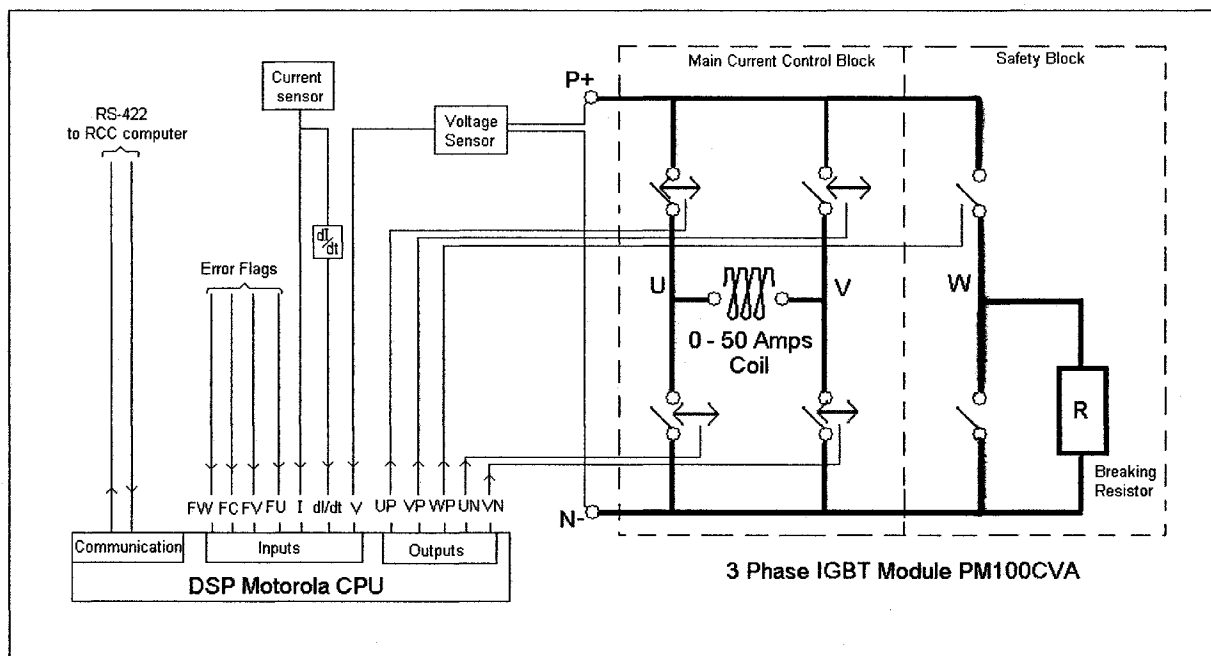


Figure 5.3 Schematic of the CID

According to actual measurements of current and voltage (dual 4 channel 12 bit A/D converters with $1.5 \cdot 10^{-6}$ seconds conversion), the Motorola CPU switches voltage between one of 3 states:

- 1). Turned-on high (+700 [V] on the magnet)

- 2). Turned-on low (-700 [V] on the magnet)
- 3). Off (2 diode drops plus the IR voltage drop of the magnet)

The process is carried out in a $1 \cdot 10^{-4}$ second cycle. There is also $3 \cdot 10^{-6}$ seconds of dead time between each cycle, to avoid a situation in which the UP and VN switches are not open, while simultaneously UN and VP are still closed.

The complete model of the CID is non-linear and computationally cumbersome. For linearization and control design, a simplified CID model was developed. The simplified model (Figure 5.4) exhibits good fidelity to the full model.

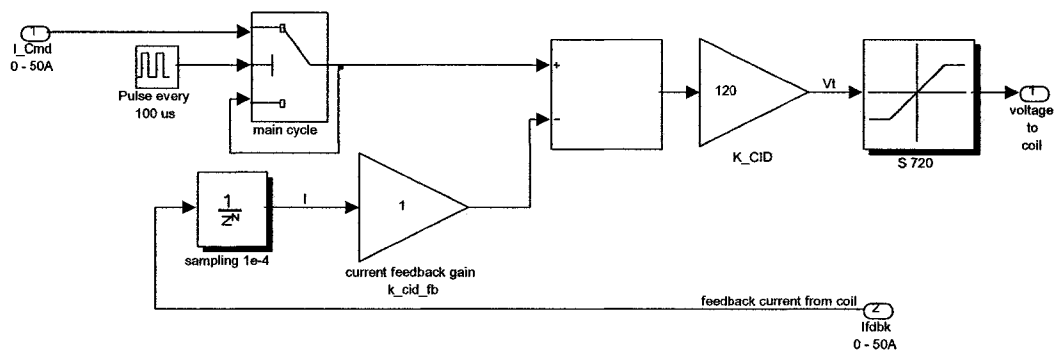


Figure 5.4 Simplified model of CID

The non-linear simulation model shown in the Figure 5.5 was also used.

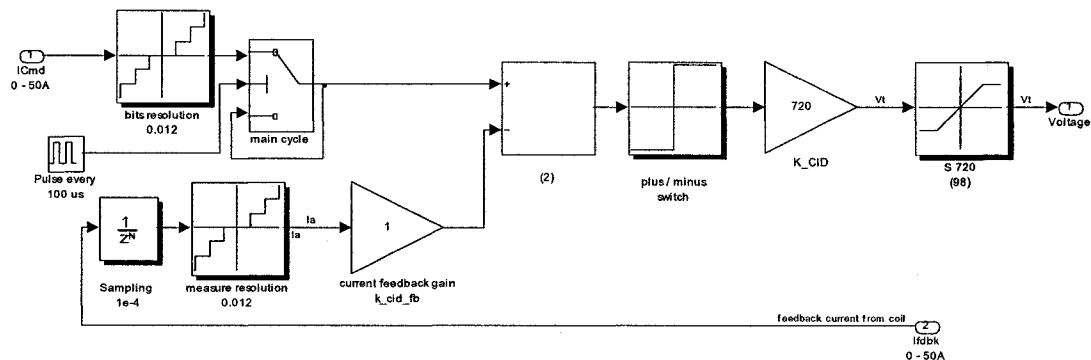


Figure 5.5 Model of CID for non-linear simulation

5.2 Coil Dynamics due to Inductance (CID)

The dynamic behavior of the electromagnet and CID together can be expressed using the same equations used to describe the PWM amplifier (2.27). There are two differences:

- The CID's power supply has a higher voltage source $V_{source}^{CID} = 700$ [V]
- The current feedback gain is $K_{CID} = 120$

The K_{CID} constant was found experimentally in the same manner applied to the PWM.

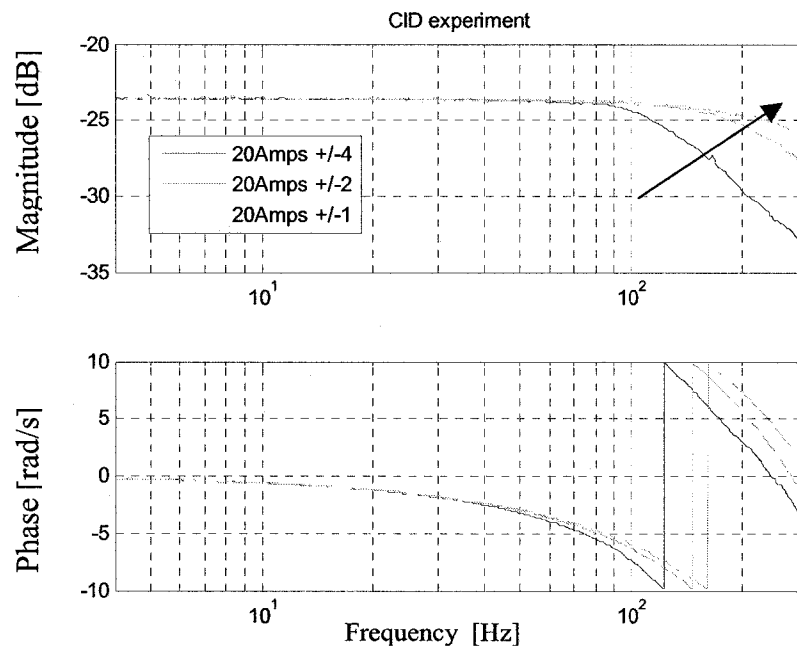


Figure 5.6 CIDs frequency responses obtained from experiment

To get a pole at ~ 100 [Hz] (see figure above), the value of the current gain feedback K_{CID} must equal ~ 120 (265 was determined for amplifier 100A40K). In the Figure 5.5 arrow indicates increasing current amplitude variation.

5.3 Model of the Structural Part of the ODU Maglev System

A schematic representation of the ODU Maglev plant in the x,y,z co-ordinate system is shown in the below *Figure 5.7*

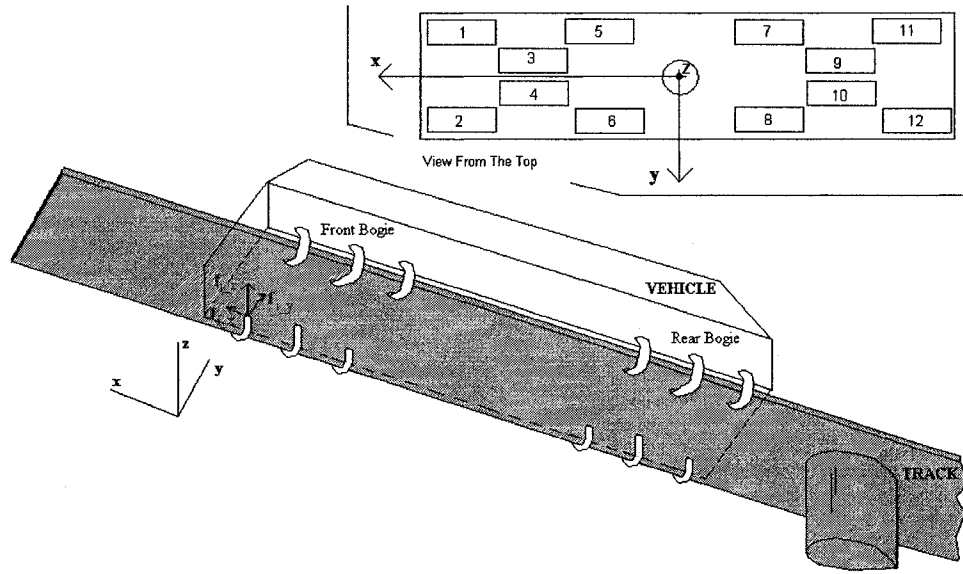


Figure 5.7 Schematic model of the ODU Maglev System

By considering the structural model of the ODU Maglev plant presented in the *Figure 5.7*, the following Equations of Motion (EOM) can be obtained:

$$\begin{aligned}
 M_V \cdot \ddot{\zeta} &= \sum_{i=1}^{N_f} f_i + \begin{bmatrix} 0 \\ 0 \\ m_V \cdot g \end{bmatrix}; \\
 J_V \cdot \ddot{\alpha} &= \sum_{i=1}^{N_f} \lambda_i \cdot f_i; \\
 \ddot{q}_V + D_V \cdot \dot{q}_V + \Lambda_V \cdot q_V &= \Phi_V^T \cdot [f]; \\
 \ddot{q}_T + D_T \cdot \dot{q}_T + \Lambda_T \cdot q_T &= \Phi_T^T \cdot [-f]; \\
 \text{for } i &= 1, \dots, N_f
 \end{aligned} \tag{5.1}$$

The notation used for (5.1) is explained in the *Table 5.1*.

VARIABLE / CONSTANT	DESCRIPTION
$\zeta = \begin{bmatrix} x \\ y \\ z \end{bmatrix}_{3 \times 1}$	Rigid body center of mass displacements (x - longitudinal, y - lateral, z - levitation)
$\alpha = \begin{bmatrix} \phi \\ \theta \\ \psi \end{bmatrix}_{3 \times 1}$	Rigid body rotations (ϕ - roll angle, θ - pitch angle, ψ - yaw angle)
$[q_V]_{nv \times 1}$	Modal coordinates for the Maglev vehicle
$[q_T]_{nt \times 1}$	Modal coordinates for the Maglev track
$f_i = \begin{bmatrix} f_{i_x} \\ f_{i_y} \\ f_{i_z} \end{bmatrix}$	Force vector for i -th actuator (electromagnet)
$f = \begin{bmatrix} f_1 \\ f_2 \\ \vdots \\ \vdots \\ f_{N_f} \end{bmatrix}_{3 \cdot N_f \times 1}$	Force vector for all actuators (electromagnets)

$M_v = \begin{bmatrix} m_v & 0 & 0 \\ 0 & m_v & 0 \\ 0 & 0 & m_v \end{bmatrix}_{3 \times 3}$	Maglev vehicle mass matrix
$J_v = \begin{bmatrix} J_{vxx} & 0 & 0 \\ 0 & J_{vyy} & 0 \\ 0 & 0 & J_{vzz} \end{bmatrix}_{3 \times 3}$	Moment of inertia matrix about center of the mass of the vehicle
$\lambda_i = \begin{bmatrix} 0 & -\lambda_z & \lambda_y \\ \lambda_z & 0 & -\lambda_x \\ -\lambda_y & \lambda_x & 0 \end{bmatrix}_{3 \times 3}$	Skew symmetric position operator matrix for i-th actuator
$R_f = [\lambda_1 \quad \lambda_2 \quad \dots \quad \lambda_{N_f}]_{3 \times 3N_f}$	Skew symmetric position operator matrix for all actuators (electromagnets)
$D_v = 2 \cdot \begin{bmatrix} \zeta_{v1} \cdot \omega_{v1} & 0 & 0 & 0 & 0 \\ 0 & \zeta_{v2} \cdot \omega_{v2} & 0 & 0 & 0 \\ 0 & 0 & \cdot & 0 & 0 \\ 0 & 0 & 0 & \cdot & 0 \\ 0 & 0 & 0 & 0 & \zeta_{vnt} \cdot \omega_{vnt} \end{bmatrix}_{nv \times nv}$	Maglev vehicle damping matrix
$D_T = 2 \cdot \begin{bmatrix} \zeta_{T1} \cdot \omega_{T1} & 0 & 0 & 0 & 0 \\ 0 & \zeta_{T2} \cdot \omega_{T2} & 0 & 0 & 0 \\ 0 & 0 & \cdot & 0 & 0 \\ 0 & 0 & 0 & \cdot & 0 \\ 0 & 0 & 0 & 0 & \zeta_{Tnt} \cdot \omega_{Tnt} \end{bmatrix}_{nt \times nt}$	Maglev track damping matrix

$\Lambda_T = \begin{bmatrix} \omega_{T1}^2 & 0 & 0 & 0 & 0 \\ 0 & \omega_{T2}^2 & 0 & 0 & 0 \\ 0 & 0 & \cdot & 0 & 0 \\ 0 & 0 & 0 & \cdot & 0 \\ 0 & 0 & 0 & 0 & \omega_{Tnt}^2 \end{bmatrix}_{nt \times nt}$	Maglev vehicle stiffness matrix
$\Lambda_V = \begin{bmatrix} \omega_{V1}^2 & 0 & 0 & 0 & 0 \\ 0 & \omega_{V2}^2 & 0 & 0 & 0 \\ 0 & 0 & \cdot & 0 & 0 \\ 0 & 0 & 0 & \cdot & 0 \\ 0 & 0 & 0 & 0 & \omega_{Vnv}^2 \end{bmatrix}_{nv \times nv}$	Maglev track stiffness matrix
$[\Phi_V]_{nv \times 3 \cdot N_f}$	Maglev vehicle modes shape matrix (taken from FE data)
$[\Phi_T]_{nt \times 3 \cdot N_f}$	Maglev track modes shape matrix (taken from FE data)

Table 5.1 Notation table for structural ODU Maglev model

According to *Figure 5.1* and the actual data, it can be seen that:

1. The ODU Maglev system has 12 electromagnets $N_f = 12$;
2. Vehicle mass is in the range of 25000 – 40000 [lbs];
3. Vehicle inertia is (when $m_V = 105$ [lbs]): $J_{Vxx} = 3.951 \cdot 10^7$ [lbs · in²];
 $J_{Vyy} = 4.368 \cdot 10^8$ [lbs · in²]; $J_{Vzz} = 4.295 \cdot 10^8$ [lbs · in²];
4. Damping ratios are assumed to be: $\zeta_{V1} = \zeta_{T1} = 0.025$;
5. By taking the first 9 natural frequencies for both track and vehicle model:
 $nt = nv = 9$;
6. Position of actuators according to *Figure 2.3* can be expressed as:

$$\begin{aligned}
\lambda_1 &= \begin{bmatrix} 0 & 37.31 & -31.82 \\ -37.31 & 0 & -195.75 \\ 31.82 & 195.75 & 0 \end{bmatrix}; \lambda_2 = \begin{bmatrix} 0 & 37.31 & 31.82 \\ -37.31 & 0 & -195.75 \\ -31.82 & 195.75 & 0 \end{bmatrix}; \\
\lambda_3 &= \begin{bmatrix} 0 & 37.31 & -31.82 \\ -37.31 & 0 & -129.25 \\ 31.82 & 129.25 & 0 \end{bmatrix}; \lambda_4 = \begin{bmatrix} 0 & 37.31 & 31.82 \\ -37.31 & 0 & -129.25 \\ -31.82 & 129.25 & 0 \end{bmatrix}; \\
\lambda_5 &= \begin{bmatrix} 0 & 37.31 & -31.82 \\ -37.31 & 0 & -100 \\ 31.82 & 100 & 0 \end{bmatrix}; \lambda_6 = \begin{bmatrix} 0 & 37.31 & 31.82 \\ -37.31 & 0 & -100 \\ -31.82 & 100 & 0 \end{bmatrix}; \\
\lambda_7 &= \begin{bmatrix} 0 & 37.31 & -31.82 \\ -37.31 & 0 & 100 \\ 31.82 & -100 & 0 \end{bmatrix}; \lambda_8 = \begin{bmatrix} 0 & 37.31 & 31.82 \\ -37.31 & 0 & 100 \\ -31.82 & -100 & 0 \end{bmatrix}; \\
\lambda_9 &= \begin{bmatrix} 0 & 37.31 & -31.82 \\ -37.31 & 0 & 129.25 \\ 31.82 & -129.25 & 0 \end{bmatrix}; \lambda_{10} = \begin{bmatrix} 0 & 37.31 & 31.82 \\ -37.31 & 0 & 129.25 \\ -31.82 & -129.25 & 0 \end{bmatrix}; \\
\lambda_{11} &= \begin{bmatrix} 0 & 37.31 & -31.82 \\ -37.31 & 0 & 195.75 \\ 31.82 & -195.75 & 0 \end{bmatrix}; \lambda_{12} = \begin{bmatrix} 0 & 37.31 & 31.82 \\ -37.31 & 0 & 195.75 \\ -31.82 & -195.75 & 0 \end{bmatrix},
\end{aligned}$$

where index $i = 1$ corresponds to magnet AF, index $i = 2$ corresponds to magnet BF, etc. (values are given in inches).

Through the use of a Finite Element model prepared⁴ in Nastran software, the first 9 natural frequencies for the vehicle and track can be obtained (*Table 5.2, Table 5.3*):

⁴ Finite Element Model was created by research team at ODU, Mechanical Engineering Department

Variable name	Freq [Hz]	Description
ω_{y1}	10.13	Rocking sideways in y
ω_{y3}	11.37	Twisting about x
ω_{y3}	12.96	Bending in z 2-node
ω_{y4}	13.50	Bending in z 3-node
ω_{y5}	13.74	Coupled bending with twisting
ω_{y6}	13.79	Coupled bending with twisting
ω_{y7}	15.67	Coupled Modes hard to recognize
ω_{y8}	16.36	Coupled Modes hard to recognize
ω_{y9}	16.88	Coupled Modes hard to recognize

Table 5.2 First nine natural frequencies for Vehicle, obtained from Nastran⁵

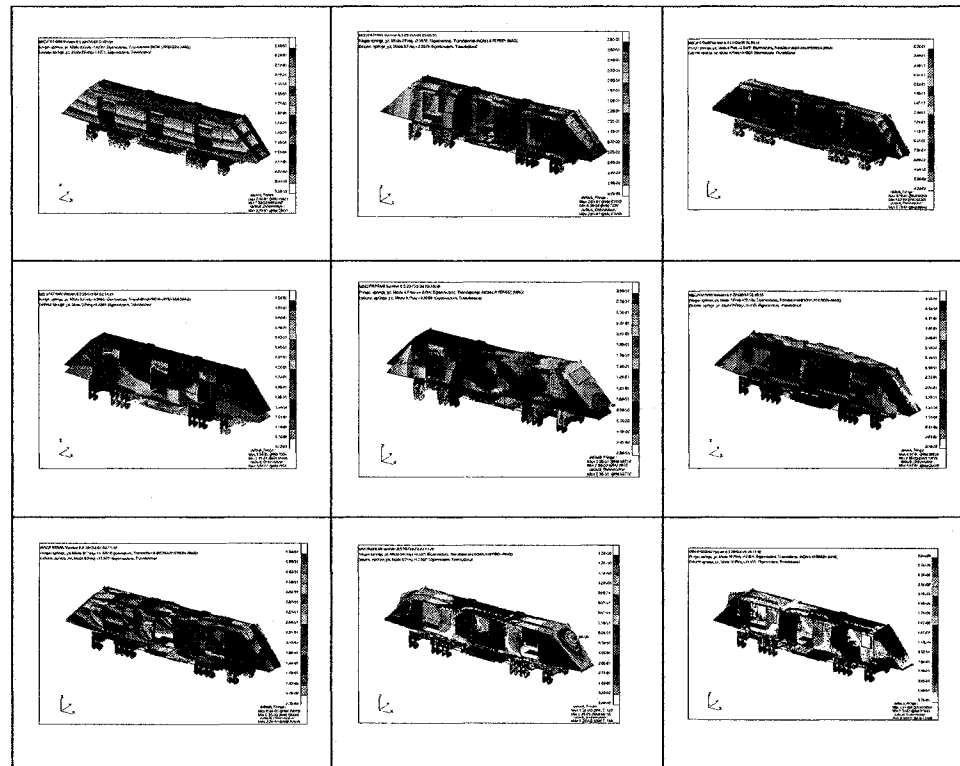


Table 5.3 Visualization of the first 9 natural frequencies for the Maglev vehicle

⁵ First 6 modes were neglected, they are rigid body modes

Variable name	Freq [Hz]	Description
ω_{T1}	2.12	Horizontal bending (y)
ω_{T2}	2.83	Translation (x)
ω_{T3}	2.85	1 st Vertical bending (z)
ω_{T4}	3.05	Rotational about (x)
ω_{T5}	4.34	Rotational about (z)
ω_{T6}	7.44	Horizontal bending (y) + Rot (x)
ω_{T7}	8.84	Rotational about (x)
ω_{T8}	8.86	2 nd Vertical bending
ω_{T9}	13.03	Rotational about (x)

Table 5.4 Track (first nine) natural frequencies obtained from Nastran software

5.4 State Space Format of the Structural Maglev Equations of Motion

The Equations of Motion (5.1) can be transformed to a more convenient state-space format

$$\begin{aligned}\dot{\vec{x}} &= A\vec{x} + B\vec{u} \\ \vec{y} &= C\vec{x} + D\vec{u}\end{aligned}\tag{5.2}$$

Let equations (5.1) denote as follows:

$$\begin{aligned}\ddot{\zeta} &= M_V^{-1} \sum_{i=1}^{N_f} f_i; \\ \ddot{\alpha} &= J_V^{-1} \sum_{i=1}^{N_f} \lambda_i f_i;\end{aligned}\tag{5.3}$$

$$\begin{aligned}\ddot{q}_V &= -\Lambda_V q_V - D_V \dot{q}_V + \Phi_V^T[f]; \\ \ddot{q}_T &= -\Lambda_T q_T - D_T \dot{q}_T + \Phi_T^T[-f];\end{aligned}\tag{5.4}$$

for all above equations index $i = 1, \dots, N_f$

The Equations (5.2) denote rigid body dynamics, while (5.3) represents modal dynamics due to system flexibility. Using state space notation, *equation (5.3)* becomes:

State vector \bar{x} :

$$\begin{aligned} \bar{x}_{48 \times 1} = & \left[\begin{array}{l} x, y, z, \dot{x}, \dot{y}, \dot{z}, \phi, \theta, \psi, \dot{\phi}, \dot{\theta}, \dot{\psi}, q_{1V}, q_{2V}, q_{3V}, q_{4V}, q_{5V}, q_{6V}, q_{7V}, q_{8V}, q_{9V}, \dots \\ \dots \dot{q}_{1V}, \dot{q}_{2V}, \dot{q}_{3V}, \dot{q}_{4V}, \dot{q}_{5V}, \dot{q}_{6V}, \dot{q}_{7V}, \dot{q}_{8V}, \dot{q}_{9V}, \dots \\ \dots q_{1T}, q_{2T}, q_{3T}, q_{4T}, q_{5T}, q_{6T}, q_{7T}, q_{8T}, q_{9T}, \dot{q}_{1T}, \dot{q}_{2T}, \dot{q}_{3T}, \dot{q}_{4T}, \dot{q}_{5T}, \dot{q}_{6T}, \dot{q}_{7T}, \dot{q}_{8T}, \dot{q}_{9T} \end{array} \right]^T \end{aligned} \quad (5.5)$$

Input vector \bar{u} :

$$\bar{u}_{36 \times 1} = [f]^T; \quad (5.6)$$

This vector represents forces acting on the chassis. For further calculation, 24 input forces will be utilized (levitation and lateral).

Output vector \bar{y} :

$$\bar{y}_{3 \times 1} = [x, y, z]^T; \quad (5.7)$$

Thus, the components of equations (5.2) have following forms:

$$A = \begin{bmatrix} A_R & 0 & 0 \\ 0 & A_V & 0 \\ 0 & 0 & A_T \end{bmatrix}_{48 \times 48}; \quad (5.8)$$

where,

$$A_R = \begin{bmatrix} 0_{3 \times 3} & I_{3 \times 3} & 0_{3 \times 3} & 0_{3 \times 3} \\ 0_{3 \times 3} & 0_{3 \times 3} & 0_{3 \times 3} & 0_{3 \times 3} \\ 0_{3 \times 3} & 0_{3 \times 3} & 0_{3 \times 3} & I_{3 \times 3} \\ 0_{3 \times 3} & 0_{3 \times 3} & 0_{3 \times 3} & 0_{3 \times 3} \end{bmatrix}_{6 \times 6}; \quad (5.9)$$

$$A_V = \begin{bmatrix} 0_{9 \times 9} & I_{9 \times 9} \\ -\Lambda_V & -D_V \end{bmatrix}_{18 \times 18}; \quad (5.10)$$

$$A_T = \begin{bmatrix} 0_{9 \times 9} & I_{9 \times 9} \\ -\Lambda_T & -D_T \end{bmatrix}_{18 \times 18}; \quad (5.11)$$

$$B = \begin{bmatrix} 0_{3 \times 36} \\ (M_V^{-1} \cdot I_{3 \times 3})_{3 \times 36} \\ 0_{3 \times 36} \\ (J_V^{-1} \cdot R_f)_{3 \times 36} \\ 0_{3 \times 36} \\ \Phi_{V9 \times 36}^T \\ 0_{9 \times 36} \\ -\Phi_{T9 \times 36}^T \end{bmatrix}_{48 \times 36}; \quad (5.12)$$

$$C = \begin{bmatrix} (I_{3 \times 3})_{36 \times 3} & 0_{36 \times 3} & R_f^T_{36 \times 3} & 0_{36 \times 3} & \Phi_{V36 \times 9} & 0_{36 \times 9} & -\Phi_{T36 \times 9} & 0_{36 \times 9} \end{bmatrix}_{36 \times 48}; \quad (5.13)$$

$$D = [0]_{36 \times 36}; \quad (5.14)$$

where:

$$R_f = \begin{bmatrix} \lambda_1, \lambda_2, \lambda_3, \lambda_4, \lambda_5, \dots, \lambda_{12} \end{bmatrix}_{3 \times 36} \quad (5.15)$$

Note that depending on the position of the Maglev vehicle with respect to the track, the mode shape matrix Φ_f^T in (5.12) and (5.13) will vary.

Transformation from modal coordinates into state space can be accomplished by another modal transformation. In physical coordinates the system equations are expressed as [83]:

$$[M]\{\ddot{x}\} + [C_d]\{\dot{x}\} + [K]\{x\} = \{F\} \quad (5.16)$$

Taking the first nine natural frequencies, the structural coordinates are related to modal coordinates as follows [74]:

$$\{x\}_i = q_i \{\Phi\}_i \quad (5.17)$$

and

$$\sum_i^{NN} \{x\}_i = \{x\} = q_i \{\Phi\}_i = \sum_i^{NN} q_i \{\Phi\}_i = [\Phi]\{q\} \quad (5.18)$$

where NN is the number of modes being considered and is equal (according to Table 5.1) to n_t for track or n_v for the vehicle model. The Φ mode shape matrix in (5.12) and (5.13) is obtained from Nastran (procedure SOL103). Knowing this value it can be written that,

$$\{q\} = [\Phi]^{-1} \{x\} \quad (5.19)$$

Substituting (5.19) into (5.16)

$$[\overline{M}]\{\ddot{q}\} = -[\overline{C}_D]\{\dot{q}\} - [\overline{K}]\{q\} + \overline{F} \quad (5.20)$$

$$\{\ddot{q}\} = -[\overline{M}]^{-1}[\overline{C}_D]\{\dot{q}\} - [\overline{M}]^{-1}[\overline{K}]\{q\} + [\overline{M}]^{-1}[\overline{F}] \quad (5.21)$$

with conditions:

$$[\overline{M}] = [\Phi]^T [M] [\Phi]; \quad (5.22)$$

$$[\overline{C}_D] = [\Phi]^T [C_D] [\Phi] = [D_D]; \quad (5.23)$$

$$[\overline{K}] = [\Phi]^T [K] [\Phi] = [\Lambda]; \quad (5.24)$$

$$[\overline{F}] = [\Phi]^T [F]; \quad (5.25)$$

The mass matrix is normalized. The state space formulation is rewritten:

$$[D_D] = [\overline{M}]^{-1}[\overline{C}_D] \quad (5.26)$$

$$[\Lambda] = [\overline{M}]^{-1}[\overline{K}] \quad (5.27)$$

which provides a final modal set of equations:

$$\{\ddot{q}\} = -[D_D]\{\dot{q}\} - [\Lambda]\{q\} + [\Phi]^T [\overline{F}] \quad (5.28)$$

In (5.18) the mode shape matrix occurs only next to the $[F]$ matrix. Thus, in state space formulation, the B matrix includes $[\Phi]^T$. Also equation (5.19) holds:

$$\{x\} = [\Phi]\{q\} \quad (5.29)$$

which means that the C matrix also contains the mode shape matrix $[\Phi]$.

Based on the information obtained from the modal transformation, a state space model described by (5.8)-(5.13) can be shown using Bode plots. In *Figures 5.8* and *5.9*, Bode plots illustrate the levitation degree-of-freedom (displacement in z direction) only. Numbers from 1 to 12 in the figure legends represent electromagnets' numeration.

It can be noted by observing the characteristics in these figures that the dominant influence on the Maglev system is a track bending mode at $\omega_{T3} = 2.85$ [Hz]. It can also be concluded that different vehicle positions on the track cause the system's transfer function zeros to move. This phenomenon was explored analytically in Chapter 2.

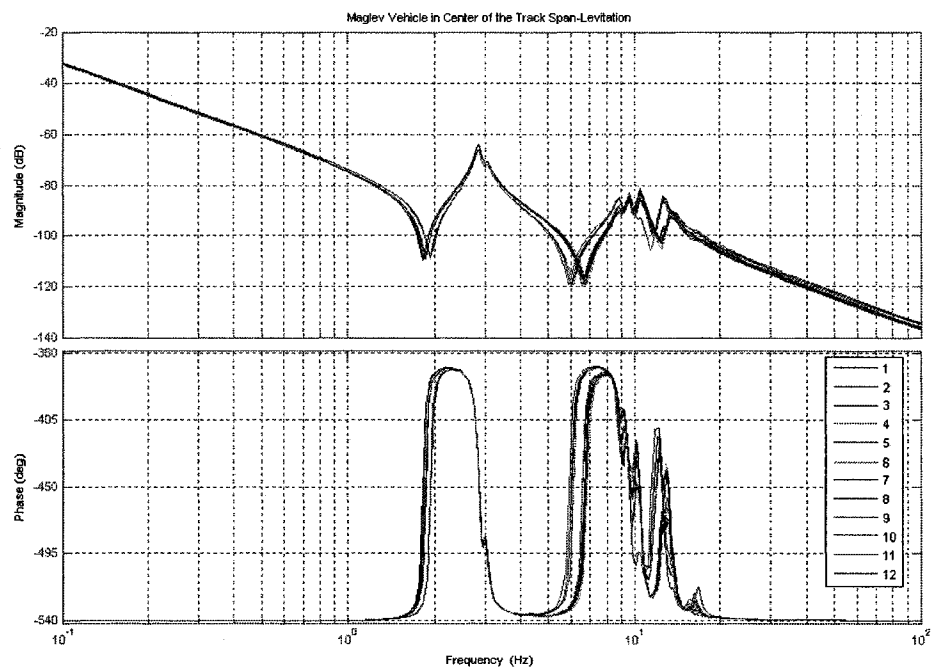


Figure 5.8 Bode plots for levitation DOF - case when vehicle is in the middle of the track span (center between pillars)

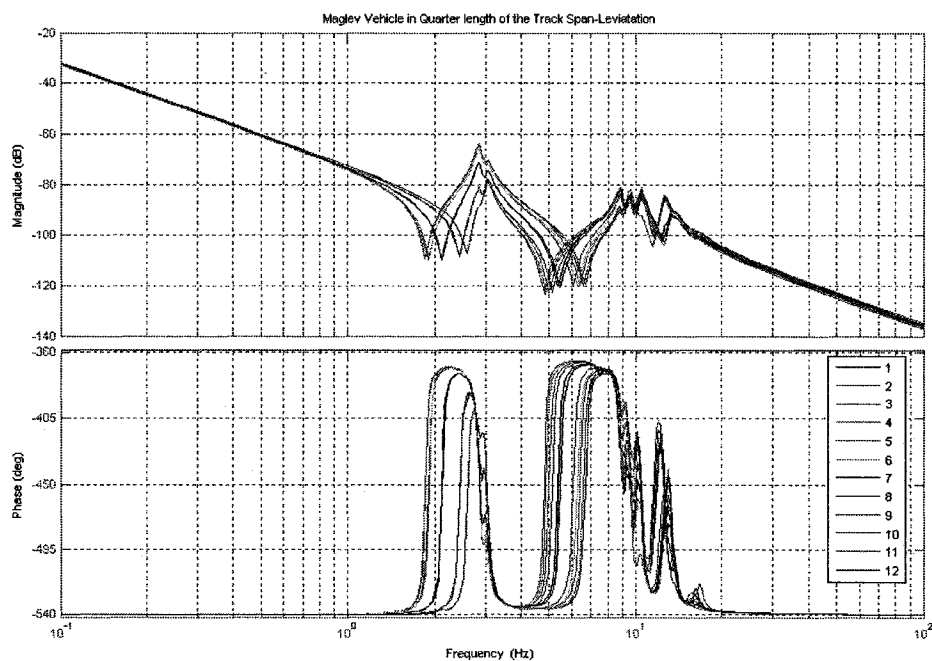


Figure 5.9 Bode plots for levitation DOF - case when vehicle is close to pillar (approximately one quarter length of the track span)

According to these Bode plots, it can be said that the structural part of the Maglev system is stable.

5.5 Complete Equations of Motion for the ODU Maglev System

As it was pointed out above, the model of the Maglev electromagnetic suspended system can be divided into two parts. The complete EOM for the Maglev system are expressed in a form where the electromagnetic and structural parts are combined. The structural dynamics are covered by the state space equations (5.8)-(5.12) derived in section 5.3. The A matrix includes rigid body motions and flexibility modes. The B matrix includes 36 force inputs (alternately lateral and levitation forces and gravity force), and the C matrix produces as an output vector of 36 gaps (also alternately lateral and levitation displacements).

The electromagnetic part of the ODU Maglev system is described by the expressions derived in chapters 3.1 and 3.3, where the inputs are the 12 current commands for the 12 CID devices. Through the coil models (inductance and magnetic force expressions), lateral and levitation forces are obtained. Forces are consistently recognized as inputs into the structural model described in chapter 5.3.

A schematic view of these system equations is shown in *Figure 5.10*.

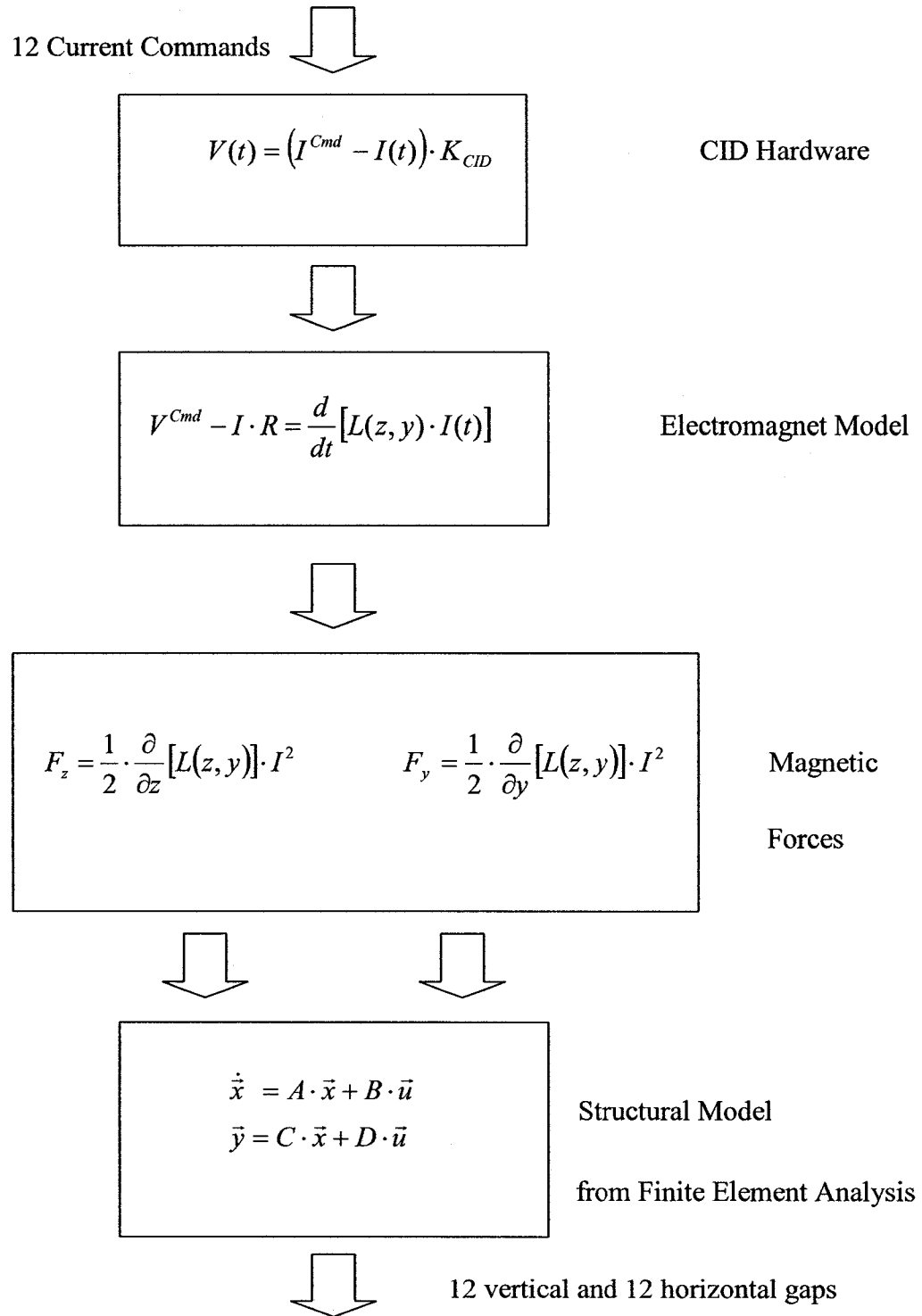


Figure 5.10 Scheme of the complete ODU Maglev model

State-space equations (5.8)-(5.12) describe the structural model only. Now, after accounting for the electromagnets incorporated into the system, equations become:

$$\begin{aligned}\dot{\vec{x}} &= \tilde{A} \cdot \vec{x} + \tilde{B} \cdot \vec{u} \\ \vec{y} &= \tilde{C} \cdot \vec{x} + \tilde{D} \cdot \vec{u}\end{aligned}\quad (5.30)$$

where a new state-space vector is:

$$\begin{aligned}\vec{x}_{60 \times 1} = & \left[\begin{array}{l} x, y, z, \dot{x}, \dot{y}, \dot{z}, \phi, \theta, \psi, \dot{\phi}, \dot{\theta}, \dot{\psi}, q_{1V}, q_{2V}, q_{3V}, q_{4V}, q_{5V}, q_{6V}, q_{7V}, q_{8V}, q_{9V}, \dots \\ \dots \dot{q}_{1V}, \dot{q}_{2V}, \dot{q}_{3V}, \dot{q}_{4V}, \dot{q}_{5V}, \dot{q}_{6V}, \dot{q}_{7V}, \dot{q}_{8V}, \dot{q}_{9V}, \dots \\ \dots q_{1T}, q_{2T}, q_{3T}, q_{4T}, q_{5T}, q_{6T}, q_{7T}, q_{8T}, q_{9T}, \dot{q}_{1T}, \dot{q}_{2T}, \dot{q}_{3T}, \dot{q}_{4T}, \dot{q}_{5T}, \dot{q}_{6T}, \dot{q}_{7T}, \dot{q}_{8T}, \dot{q}_{9T}, \dot{I}_1, \dots \\ \dot{I}_2, \dot{I}_3, \dot{I}_4, \dot{I}_5, \dot{I}_6, \dot{I}_7, \dot{I}_8, \dot{I}_9, \dot{I}_{10}, \dot{I}_{11}, \dot{I}_{12} \end{array} \right]^T\end{aligned}\quad (5.31)$$

Components of matrix \tilde{A} in (5.30) follow:

$$\tilde{A} = \begin{bmatrix} A'_R & 0 & 0 & A_{K_i} \\ 0 & A_V & 0 & A_{B1} \\ 0 & 0 & A_T & A_{B2} \\ 0 & 0 & 0 & A_{CID} \end{bmatrix}_{60 \times 60}; \quad (5.32)$$

where,

$$A'_{K_i} = \begin{bmatrix} 0_{5 \times 12} \\ \{k_i\}_{1 \times 12} \end{bmatrix}_{6 \times 12} + [B]_{6 \times 12(z)}; \quad (5.33)$$

$$A'_{B1} = [B]_{6:24 \times 12(z)}; \quad (5.34)$$

$$A'_{B2} = [B]_{24:42 \times 12(z)}; \quad (5.35)$$

$$A'_R = \begin{bmatrix} 0_{3 \times 3} & I_{3 \times 3} & 0_{3 \times 3} & 0_{3 \times 3} \\ 0_{3 \times 3} & \{k_z\}_{1 \times 1} & 0_{3 \times 2} & 0_{3 \times 3} \\ 0_{3 \times 3} & 0_{3 \times 3} & 0_{3 \times 3} & I_{3 \times 3} \\ 0_{3 \times 3} & 0_{3 \times 3} & 0_{3 \times 3} & 0_{3 \times 3} \end{bmatrix}_{6 \times 6}; \quad (5.36)$$

$$A_V = \begin{bmatrix} 0_{9 \times 9} & I_{9 \times 9} \\ -\Lambda_V & -D_V \end{bmatrix}_{18 \times 18}; \quad (5.37)$$

$$A_T = \begin{bmatrix} 0_{9 \times 9} & I_{9 \times 9} \\ -\Lambda_T & -D_T \end{bmatrix}_{18 \times 18}; \quad (5.38)$$

$$A_{CID} = \begin{bmatrix} \left(-\frac{(K_{CID} + R)}{L} \right) I_{12 \times 12} \end{bmatrix}_{12 \times 12}; \quad (5.39)$$

In equations (5.32), (5.33), (5.34) matrix [B] refers to (5.12), index i.e.: 6:24x12(z) means: rows of matrix [B] from 6 to 24, and 12 columns which are referred to z displacement modes only. Vector \vec{u} in this case represents current values inside the 12 electromagnets. Thus, a new \check{B} matrix has the form:

$$\check{B}_{60 \times 12} = \begin{bmatrix} 0_{48 \times 12} \\ \left(\frac{K_{CID}}{L} \right) I_{12 \times 12} \end{bmatrix}^T \quad (5.40)$$

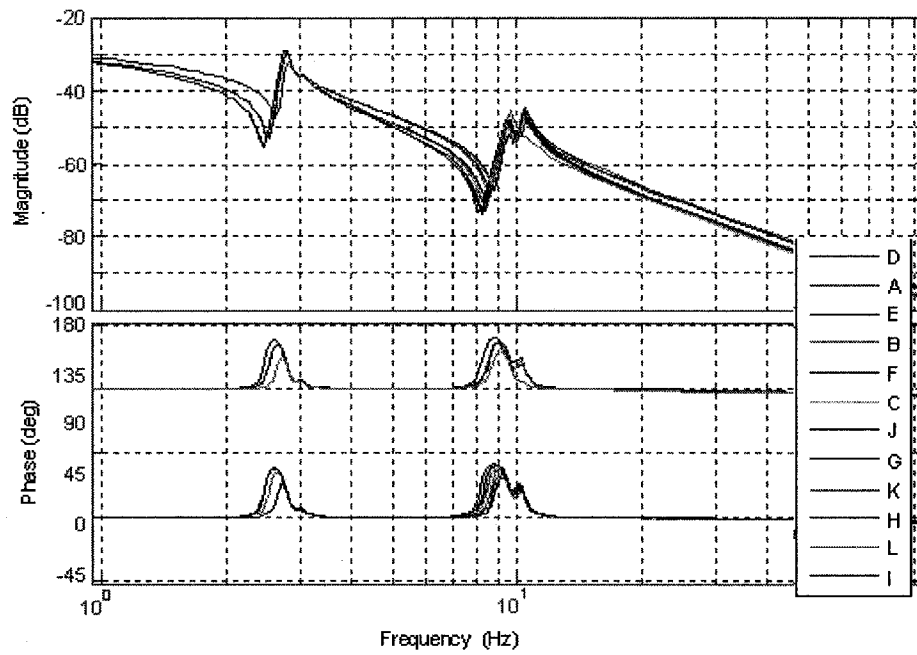
The output vector \vec{y} now represents the 12 gap outputs compared to 36 measurements in the previous model. There are only displacements in the z direction for each magnet.

$$\begin{aligned} \check{C}_{12 \times 60} &= [C_{12 \times 48} \quad 0_{12 \times 12}] = \\ &= \begin{bmatrix} (I_{3 \times 3})_{12 \times 3} & 0_{12 \times 3} & R_f^T_{12 \times 3} & 0_{12 \times 3} & \Phi_{V12 \times 9} & 0_{12 \times 9} & -\Phi_{T12 \times 9} & 0_{12 \times 9} & 0_{12 \times 12} \end{bmatrix} \end{aligned} \quad (5.41)$$

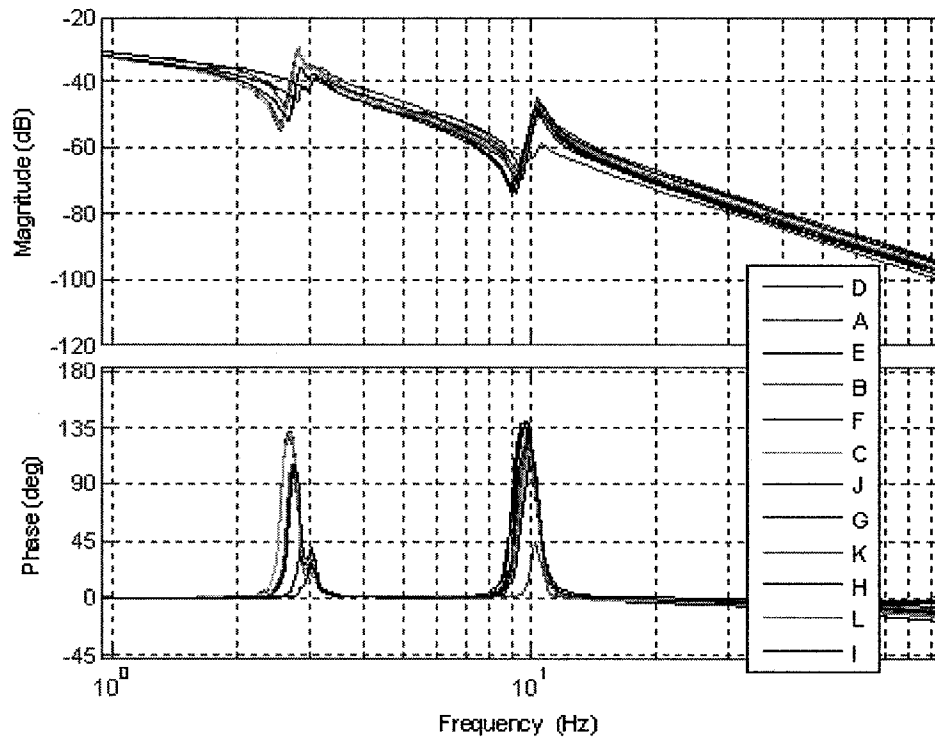
Matrix \check{D} is zero, with dimension 12x12.

$$\check{D} = [0]_{12 \times 12}; \quad (5.42)$$

In the figures below (*Figure 5.11a* and *Figure 5.11b*), Bode plots for the Maglev vehicle a) placed in the center of track span, and b) above the pillar are presented. Because model (5.32)-(5.42) after reduction differs from system (5.8)-(5.12) a new magnet notation was introduced where magnet number 1 according to *Figure 5.7* is now denoted as *A*, magnet number 2 as *B* and so on.



a) Vehicle above concrete pillar



b) Vehicle in the middle of track span

Figure 5.11 Bode plots for the ODU Maglev system

It can be seen that for model with the electromagnets included, the position of the transfer function's zeros still vary with the vehicle's placement on the track. With this exception, many similarities to the test rig Maglev model introduced in Chapter 3 can be noticed. The main form of the transfer function remains the same as was shown for the test rig.

- 1) The input-output relation for each magnet has one unstable pole.
- 2) There are 12 high frequency poles due to current feedback in 12 electromagnets.
- 3) Zero-pole pairs from structural flexibility play the same role as was seen in the test-rig model.

As a result of the above, it was decided to design control laws for the SISO subsystem (similar to the test-rig case) and then apply them to the full ODU Maglev Vehicle. Results of this application are presented in Chapter 6.

5.6 Conclusion

In this chapter a model was developed for the complex, flexible Maglev system at ODU. Results from finite element analysis were used for accurate structural modeling. It was illustrated how the finite element data can be transformed into a set of state-space equations, a very convenient notation for further compensator design. The ODU Maglev systems dynamics appear to be very similar to those of the test-rig discussed in Chapter 3 and 4.

6. ODU Maglev Control

In the previous chapter control laws for a simple version of the Maglev system were introduced. In Chapter 5 model of the multivariable MIMO Maglev system at ODU was developed. In this chapter a control system for this modeled plant is discussed.

Among many similarities between test-rig and ODU Maglev vehicle, there are four differences:

- a) The ODU vehicle has slightly different flexibility characteristics compared to the test rig introduced in Chapter 3.
- b) The ODU vehicle is a MIMO system where there are 12 inputs (currents) and 12 outputs (gaps).
- c) Zeros of the ODU Maglev transfer function change their positions due to different position of the Maglev train on the track.
- d) In the ODU vehicle, custom made CID units are used instead of the PWM amplifiers used for the test-rig system.

Differences in current amplifiers (CID vs. PWM) were already discussed in Chapter 3 and Chapter 5. Also the phenomenon of zero movement for the vehicle placed on the flexible levitated guideway was discussed in chapter 2. Therefore, only the first two factors a), b) will be explored further in this chapter.

6.1 Stability Issues Due to ODU Maglev Structural Flexibility

Since levitation stability is the main issue for this investigation, a compensator for stable levitation control has to be designed which remains robust in the presence of structural flexibility. Assuming collocation between actuators and sensors, a simple proportional and rate controller can be designed, where basic control can be expressed as (4.2) where K_P and K_D denote the proportional and rate gain matrices, not single constants as was the case in Chapter 4. They are assumed to be positive for the structural system stability investigation. By taking under consideration only the flexible poles of the system obtained from finite element analysis, without considering electromagnetics, it is known [84] that when K_P and K_D are symmetric, and $K_P \geq 0$. Then the closed loop system given by equations (5.8) - (5.12) is stable in the sense of Lyapunov [84][85] if $K_D > 0$, and is asymptotically stable if $K_P > 0$. According to this theorem the closed loop system matrix A_{CL} :

$$A_{CL} = A - B \cdot \left(K_P C - \frac{K_D}{K_P} C_R \right) \quad (6.1)$$

where the C_R matrix corresponds to velocity states of the system, is guaranteed to be stable providing that the above conditions are satisfied. From (6.1) the Eigenvalues for closed loop feedback system can be easily calculated. *Figure 6.1* and *Table 6.1* shows the values of the close-loop system are stable as expected.

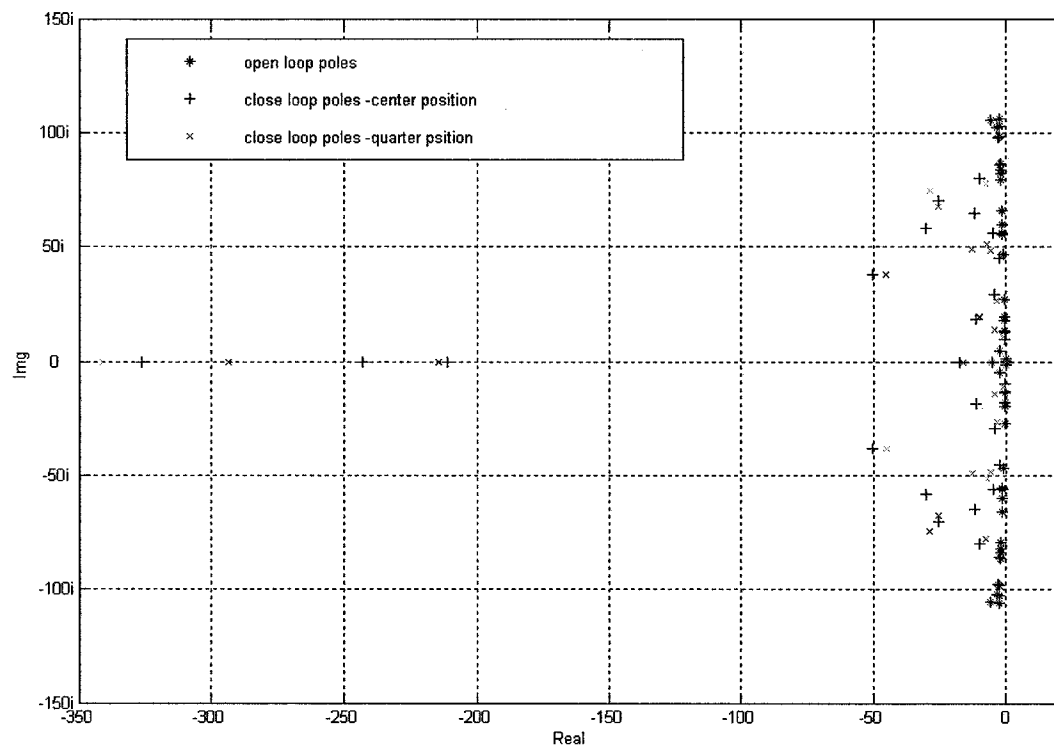


Figure 6.1 Maglev poles before and after closing feedback loop

Open Loop poles	Closed Loop Poles- Center	Closed Loop Poles- Quarter
100x	100x	100x
-0.0205 + 0.8184i	-3.2648	-3.4150
-0.0205 - 0.8184i	-2.4288	-2.9347
-0.0044 + 0.1778i	-2.1112	-2.1429
-0.0044 - 0.1778i	-0.0554 + 1.0551i	-0.0557 + 1.0552i
-0.0048 + 0.1916i	-0.0554 - 1.0551i	-0.0557 - 1.0552i
-0.0048 - 0.1916i	-0.0347 + 1.0217i	-0.0360 + 1.0223i
-0.0117 + 0.4673i	-0.0347 - 1.0217i	-0.0360 - 1.0223i
-0.0117 - 0.4673i	-0.0273 + 0.9805i	-0.0269 + 0.9809i
-0.0139 + 0.5565i	-0.0273 - 0.9805i	-0.0269 - 0.9809i
-0.0139 - 0.5565i	-0.5044 + 0.3778i	-0.2876 + 0.7457i
-0.0150 + 0.5999i	-0.5044 - 0.3778i	-0.2876 - 0.7457i
-0.0150 - 0.5999i	-0.0996 + 0.7986i	-0.0737 + 0.7751i
-0.0199 + 0.7946i	-0.0996 - 0.7986i	-0.0737 - 0.7751i
-0.0199 - 0.7946i	-0.0221 + 0.8580i	-0.0222 + 0.8580i
-0.0209 + 0.8367i	-0.0221 - 0.8580i	-0.0222 - 0.8580i
-0.0209 - 0.8367i	-0.0221 + 0.8579i	-0.0222 + 0.8578i
-0.0246 + 0.9843i	-0.0221 - 0.8579i	-0.0222 - 0.8578i
-0.0246 - 0.9843i	-0.2541 + 0.6989i	-0.2518 + 0.6740i
-0.0265 + 1.0603i	-0.2541 - 0.6989i	-0.2518 - 0.6740i
-0.0265 - 1.0603i	-0.3030 + 0.5802i	-0.4531 + 0.3768i
-0.0164 + 0.6551i	-0.3030 - 0.5802i	-0.4531 - 0.3768i
-0.0164 - 0.6551i	-0.1183 + 0.6466i	-0.1256 + 0.4903i
-0.0217 + 0.8662i	-0.1183 - 0.6466i	-0.1256 - 0.4903i
-0.0217 - 0.8662i	-0.0459 + 0.5585i	-0.0711 + 0.5109i
-0.0216 + 0.8630i	-0.0459 - 0.5585i	-0.0711 - 0.5109i
-0.0216 - 0.8630i	-0.0234 + 0.4476i	-0.0563 + 0.4818i
-0.0257 + 1.0276i	-0.0234 - 0.4476i	-0.0563 - 0.4818i
-0.0257 - 1.0276i	-0.0414 + 0.2909i	-0.0348 + 0.2661i
-0.0033 + 0.1332i	-0.0414 - 0.2909i	-0.0348 - 0.2661i
-0.0033 - 0.1332i	-0.1156 + 0.1807i	-0.0995 + 0.1919i
-0.0045 + 0.1790i	-0.1156 - 0.1807i	-0.0995 - 0.1919i
-0.0045 - 0.1790i	-0.1744	-0.1618
-0.0068 + 0.2726i	-0.0045 + 0.1778i	-0.0046 + 0.1777i
-0.0068 - 0.2726i	-0.0045 - 0.1778i	-0.0046 - 0.1777i
-0.0139 + 0.5553i	-0.0050 + 0.0959i	-0.0428 + 0.1413i
-0.0139 - 0.5553i	-0.0050 - 0.0959i	-0.0428 - 0.1413i
0	-0.0066 + 0.1258i	-0.0087 + 0.1038i
0	-0.0066 - 0.1258i	-0.0087 - 0.1038i
0	-0.0251 + 0.0459i	-0.0220 + 0.0473i
0	-0.0251 - 0.0459i	-0.0220 - 0.0473i
0	-0.0527	-0.0527
0	-0.0529	-0.0530
0	-0.0016 + 0.0140i	-0.0014 + 0.0135i
0	-0.0016 - 0.0140i	-0.0014 - 0.0135i
0	-0.0001 + 0.0029i	-0.0001 + 0.0029i
0	-0.0001 - 0.0029i	-0.0001 - 0.0029i

Table 6.1 Maglev poles for the open- loop and closed- loop cases: center position, and quarter position on guideway span

It can be seen that with this simple control law all the closed-loop poles have negative real parts, indicating stability of the structural system. This means that in spite of the flexible modes the system can be stabilized. However this result does not account for the electromagnetic actuator dynamics associated with magnetic levitation.

6.2 ODU Maglev Vehicle as MIMO System

In Chapter 5 a complex Maglev model was introduced by (5.32)-(5.42) where \tilde{B} and \tilde{C} matrices represent a 12 input 12 output system. In spite of uncoupled CID's and electromagnet models, the system is still coupled by its structural equations. In such a case it is important to decide whether a centralized or decentralized control law should be utilized. This problem was explored in Chapter 2.

In [57] it was proven that if the sensors and actuators are collocated a proper control law solution exists for the decentralized robust system problem if and only if a solution exists to the centralized robust problem. Also in [55] it was shown that the decentralized controller has the property that "spillover problems" associated with unmodeled high-frequency elastic modes could be eliminated. The decentralized approach is very convenient for control design where single pairs of SISO sub-systems can be investigated separately [60].

However, if there is a desire to shape a closed loop transfer function or there is bounded gain limitation, then in such situations decentralized control can provide worse performance compared to the centralized approach [56],[58]. The main reason for this state of affairs is caused by off-diagonal terms in the decentralized system transfer function. To be able to minimize impact of these factors RGA (Relative Gain Array) methods introduced by Bristol [86] are used. The RGA matrix measures interaction for all possible single input-output (SISO) pairings of the considered variables. But even if the perfect values are found for RGA there might be significant one-way interaction in the system which can deteriorate response [87]. Also for larger systems than 3x3 (as is the case in this thesis) variable pairings based on RGA may fail, because the RGA may

be unable to discriminate between several feasible sets, find feasible sets, or simply cannot find any feasible set of variable pairings [55].

The advantage of using a centralized approach was proven only for the systems that were very well modeled and where there was no significant uncertainties existing [57] resulting from nonlinearities or flexibility. Another important issue, which makes the centralized approach undesired in this particular application, is related to the very small operation range for gaps. With very small gaps, it is almost impossible, based on their measurements, to obtain centralized variables (transforming measurements gaps into pitch, roll, yaw angles and rates) see section 2.11.

Because of all of the above it was decided that for the purpose of achieving stable levitation the decentralized approach to design 12 decouple compensators will be used based on sequential design [61][88].

6.3 PD/PID Compensation

Consider the system expressed by (5.32)-(5.42) assuming that the inputs are current commands and the outputs are the gaps between electromagnets and the track. For simplification sensor offset was neglected, thus, the system is considered collocated.

There are 12 transfer functions, which have to be stabilized by feedback control. First, to avoid high order transfer functions for root locus design, the Maglev model was reduced in such way that pole-zero pairs, which nearly cancel each other, were eliminated. This step was necessary to make system easier for further investigation and for future interpretation of results. In the new system only 24 of 60 states are left. Comparison between ODU Maglev systems before and after reduction is shown in the *Figure 6.2*. This comparison validates the reduction assumptions made above.

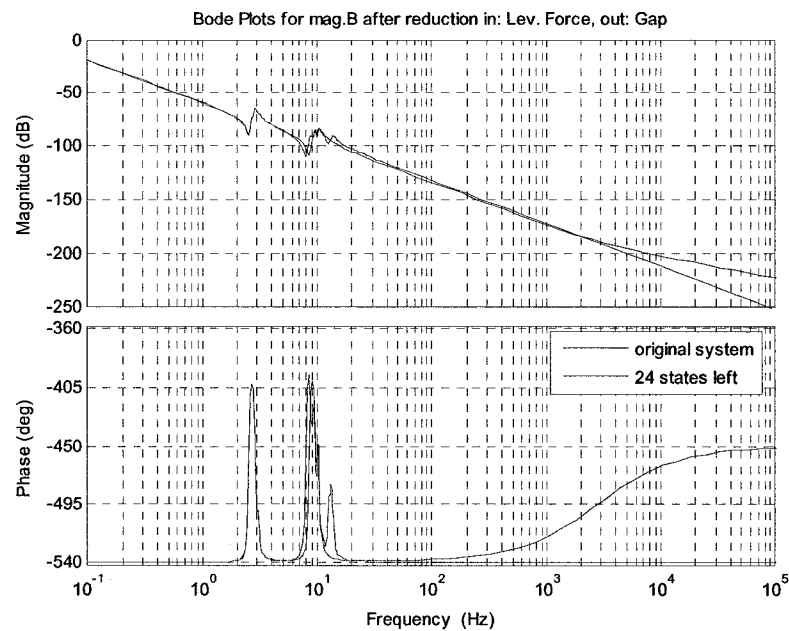


Figure 6.2 Original structural ODU Maglev system and after reduction (example for magnet B only)

The reduced system models for 2 different positions on the guideway are shown in Figures 6.3 and Figure 6.4.

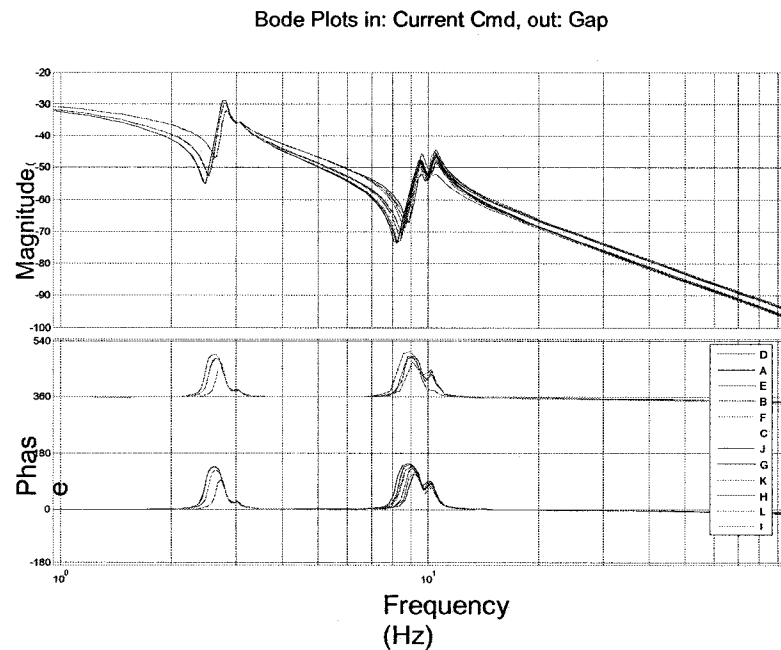


Figure 6.3 Reduced model of the ODU Maglev system (vehicle at center position on the guideway 12 magnets transfer functions)

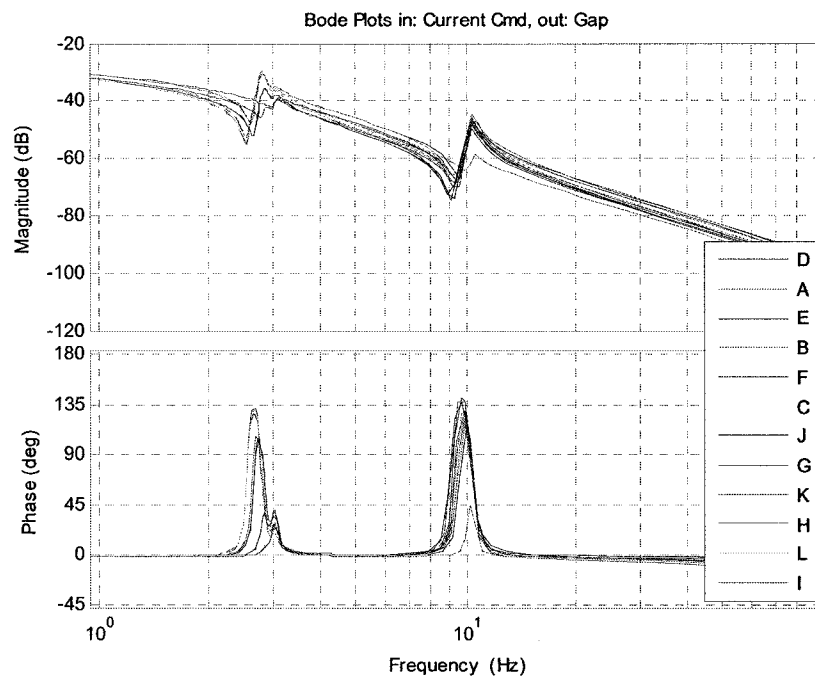


Figure 6.4 Reduced model of the ODU Maglev system (vehicle at quarter position on the guideway12 magnets transfer functions)

By observing the Bode plots above it can be said that the first track zero is shifted from around 8 Hz when the vehicle is in the center of the track length to around 9.5 [Hz] when the vehicle is placed in the quarter length of the guideway. Also some zero movement can be distinguished between zeros for the same cases on *Figure 6.3* and *Figure 6.4*. This small variation is a result of different location of the magnets. The most widely separated magnets, thus having the greatest moment arm, are 391.5 inches apart. The gain value for a given magnet increases when the force moment arm is greater; therefore, the largest transfer functions gains are associated with the most distal magnets (A, C, L, I) see *Figure 6.5*.

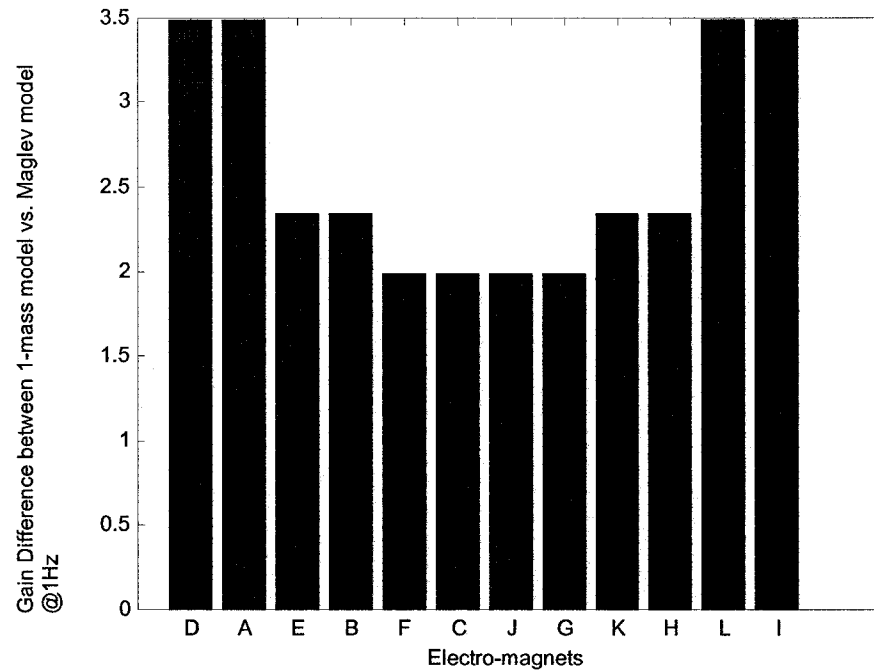


Figure 6.5 Impact of the cross product matrix on the Maglev transfer functions

As can be seen, the cross product matrix [89] has impact even on these magnets which are close to the mass center (~ 2 dB difference). This can be rectified by a centralized control approach. However, it is still possible to design a controller, which would have gain margin higher than 3.5 dB (maximum gain fluctuation seen on the above figure).

Requirements for the prospective compensator are similar to these for the test-rig system. The maximum gain and phase margin has to be achieved while time response has to be at least less than 1 sec. and damping ratio in a reasonable range, higher than 0.7. Because of the system non-linearities the design procedure is performed for two different operational conditions (at gap = 0.7 [in.] and gap = 0.4 [in]). Using a root locus method in an analogous way as was done in Chapter 4 a design process can be carried out.

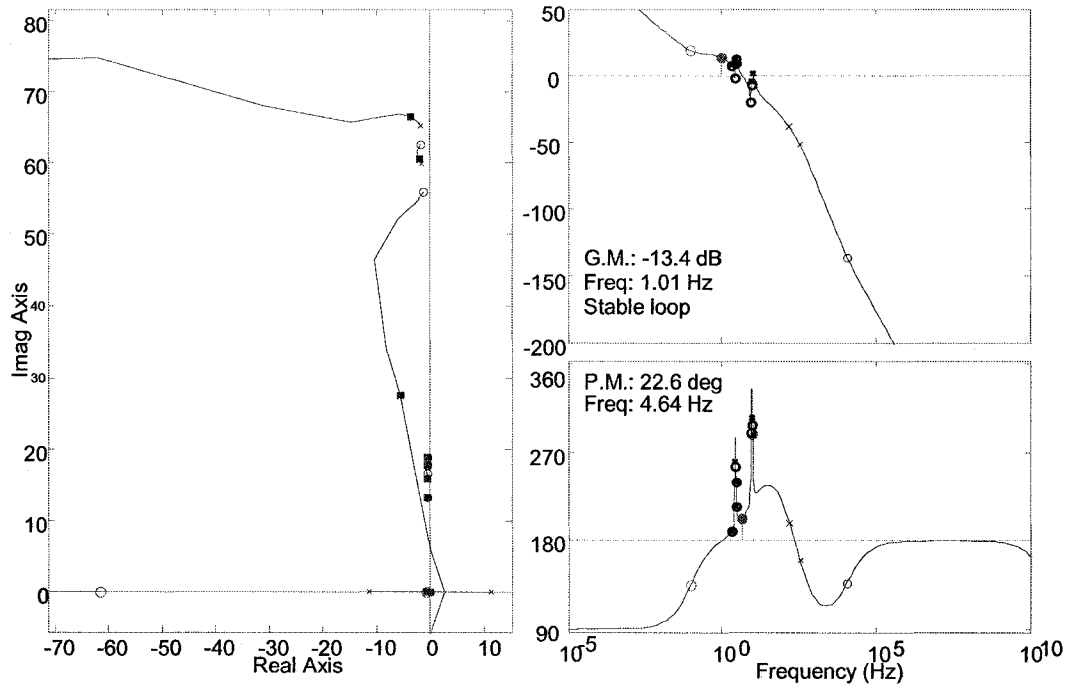


Figure 6.6 Root locus and Bode design (example for magnet A at gap = 0.4 [in])

System single transfer functions still remain in the form introduced in (2.43). Only because mass, inertia and number of modes are changed a gain and number of pole-zero pairs is different in the new transfer functions expressions.

$$G_{i,j}(s) = \frac{-K_{ij} \sum_k (s^2 + s2\zeta_k \omega_k + \omega_k^2)}{(s - p_1)(s + p_2)(s + p_3) \sum_k (s^2 + s2\zeta_k \omega_k + \omega_k^2)} \quad (6.2)$$

Where in equation (6.2), index i and j correspond to particular gap/current relation for magnet ($i=1..12, j=1..12$), index k corresponds to number of flexible modes which are taken under consideration. Thus, it is easy to conclude that the similar design approach for the compensator as was utilized in Chapter 4 can stabilize the system.

On the ODU Maglev vehicle different gap sensors were used compared to the test rig setup. It was equipped with optical sensors with 1 [msec.] delays. Therefore special concern was pointed out about phase margin for prospective compensators with minimum value at least ~ 20 [deg]. Therefore an additional lead part was added to the

previously designed PD control. The proposed compensator's phase margins are listed in the table below and their Bode plots are shown on the *Figure 6.7*.

Proposed Compensators	Magnet A Center case		Magnet A Quarter case	
	Gap = 0.4	Gap = 0.7	Gap = 0.4	Gap = 0.7
	Phase Margin [deg]	Phase Margin [deg]	Phase Margin [deg]	Phase Margin [deg]
1) $\frac{-12223.341(s + 6.251)(s + 1.224)}{s(s + 1000)}$	43	69	44	70
2) $\frac{-2678.4992(s + 61.47)(s + 0.5929)}{s(s + 1000)}$	24	19.7	22	13
3) $\frac{-11118.9808(s + 20.23)}{(s + 1000)}$	44	59	45	16
4) $\frac{-18017.3781(s + 61.47)(s + 0.08814)}{s(s + 1000)}$	18	44	20	52
5) $\frac{-9562.0339(s + 26.41)(s + 0.3866)}{s(s + 1000)}$	47	51	48	37

Table 6.2 Proposed compensators for ODU Maglev train

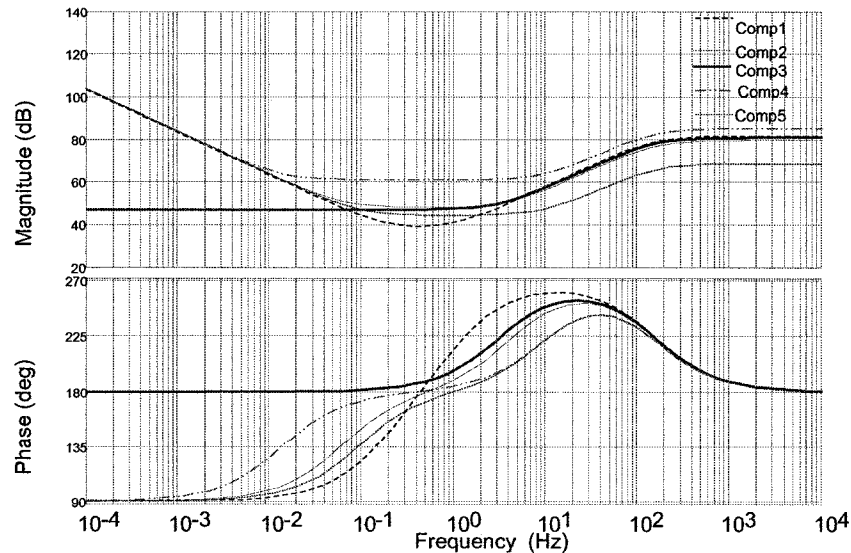


Figure 6.7 Compensators Bode plots

First, after merging all SISO subsystems a linear simulation was carried out. All designed compensators performed differently for step input commands after off-diagonal terms were added into the transfer functions. Of the controllers evaluated, only *Comp1* and *Comp4* provided acceptable response (see *Figure 6.8*). All controllers in the linear simulation based on model (5.20) gave stable response but the size of the overshoot for 2nd, 3rd and 5th were not acceptable and their settling time was too high (~ 6 seconds). Also it can be seen that since it lacks integration, *Comp3* exhibits significant steady state error (*Figure 6.8*).

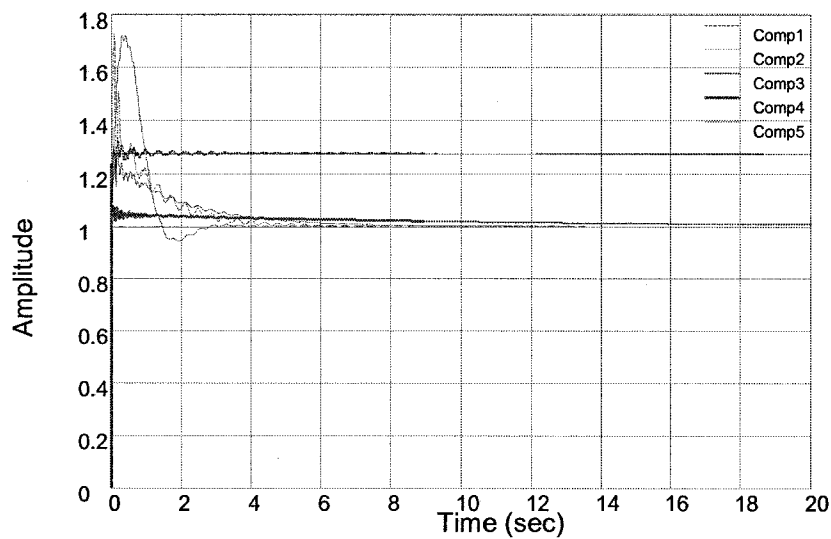


Figure 6.8 Step response of the linear ODU Maglev train (Magnet A)

Based on above results it was decided that for nonlinear simulation only *Comp1* and *Comp4* would be investigated further. The non-linear model of the ODU Maglev was built in Matlab® Simulink® (see *Figure 6.10*). A Simulink® model was prepared based on the equations introduced in Chapter 3 and Chapter 5. Expressions inside CID blocks are covered by (2.22) while the force expressions inside electromagnets model (2.15) and (2.18). the structural system block is based on equation (5.7) - (5.10). The *Comp1* exhibits the best performance (*Figure 6.9*) and this one was used during tests on the actual plant.

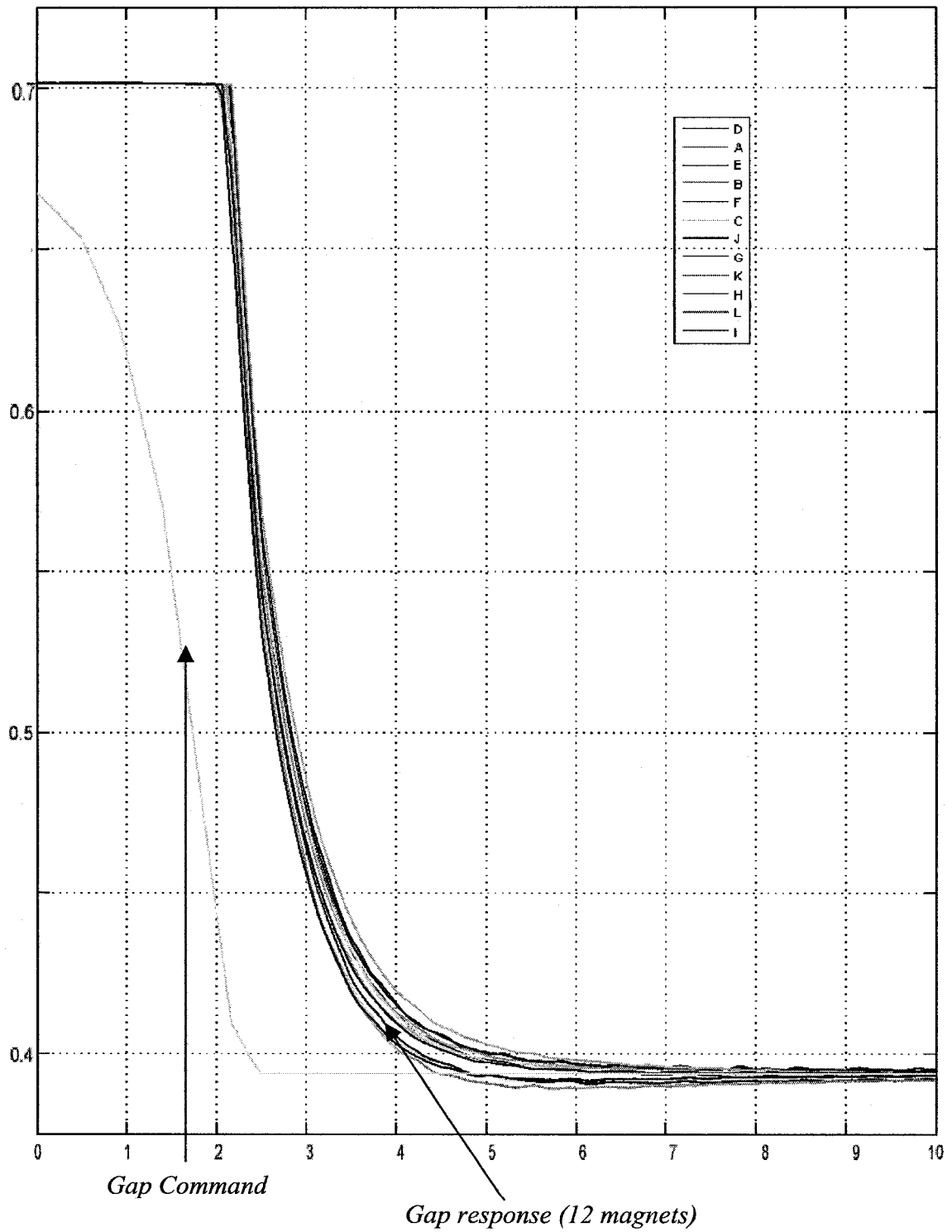


Figure 6.9 Full Maglev model simulation results gap [in.] vs. time [sec.]

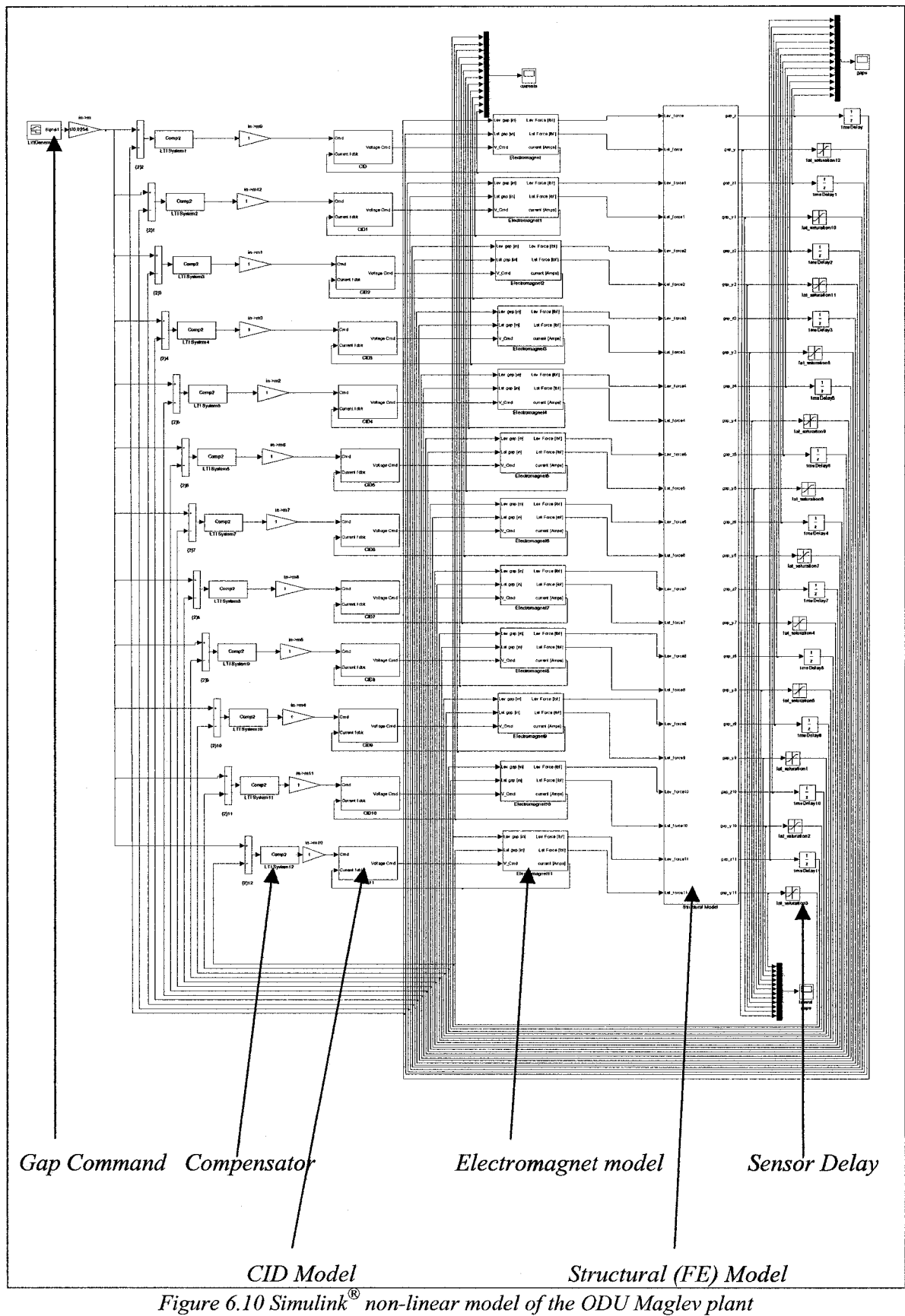


Figure 6.10 Simulink® non-linear model of the ODU Maglev plant

6.3.1 Experiment Results

The compensator designed in the above section 6.3 was validated experimentally. A decentralized approach was utilized using the same control for each magnet. PC104 computers were used to control the magnets and to store data. The vehicle uses one PC104 computer for levitation control of each bogie (6 magnets). In *Figure 6.11* below results for one bogie only are shown. The other end of vehicle was supported on jacks in the position it would be in while levitated. In the figure below some difference in the initial gap values can be seen, this is due to different gap sensor position for each magnet.

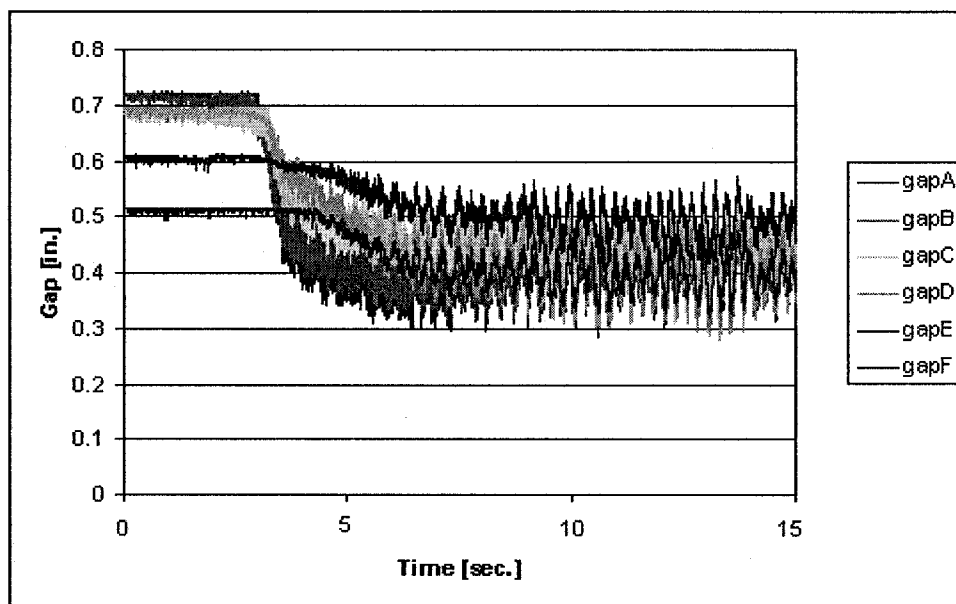


Figure 6.11 Gap response of the actual ODU Maglev vehicle

It can be noted that the system achieved stable levitation but with significant high frequency noise in the gap data. This situation is very similar to the behavior shown in Chapter 4, where the control law for the test-rig was only based on gap feedback⁶. However, because the ODU Maglev vehicle was not equipped with either acceleration or flux sensors, other tests with controllers proposed and suggested in section 4.7 couldn't be carried out.

For ride quality and public use these results are not acceptable. However because of lack of access to the actual ODU Maglev plant only this simple control law was tested.

⁶ This situation is being revised at the time of this writing

Based on analysis carried out in the previous chapters for the test-rig Maglev system one can say that the undesired characteristics which appeared for ODU Maglev vehicle can be resolved by:

- utilizing a control law with inverse force calculation .
- changing damping rate in the control law.
- improving or adjusting digital filters.
- adding anti-aliasing filters.

If there is a possibility to change a hardware setup at ODU Maglev vehicle it would be suggested to:

- add acceleration sensors
- incorporate Hall flux sensors

All these suggestions may significantly improve the gap response and make the system easier for control design (linearization). Keeping in mind similarities showed in this work between the test-rig and the ODU Maglev system, it can be said that robust control laws, which worked well for laboratory 1-degree-of-freedom setup would work better or at least improve performance of the real 12 magnet vehicle.

6.4 Conclusion

In this chapter a control law for the full MIMO Maglev ODU system was designed. According to analytical results supported by experimental data it was shown that Maglev system can be stabilized using a decentralized approach. During tests on the real system, the Maglev vehicle exhibited structural vibration of the track and vehicle. Since the ODU Maglev vehicle was designed to be a low cost project, the approach used to build the track requires a trade-off for a more robust control law. It is necessary to carry out further investigation to tune the compensator due to its poor response in the actual plant. However, the results obtained in this section and compared to the test-rig characteristics pointed the way to achieve better performance.

7. CONCLUSION

In this thesis several different design approaches applicable to low cost Maglev systems were evaluated analytically, and selected methods were tested experimentally. Procedures for modeling Maglev systems, control design, and system implementation were explored. These procedures were carried out for two physical systems, the one-degree-of-freedom Maglev test-rig and the multi-input multi-output ODU Maglev vehicle.

Starting from simple examples, the fundamental and characteristic behaviors particular to magnetic suspension were illustrated. The Maglev plant is inherently unstable as an open-loop system. Feedback control is required for stable operation. It was shown that closed-loop stability can be achieved over a limited range of gains using PD control in a positive feedback loop. Moreover, based on a lumped-parameter model which incorporates structural flexibility, it was shown that this property is retained, providing that collocated actuator and sensor pairs are used. If the system is non-collocated, a flexible Maglev structure with PD compensation can achieve marginal

stability at best. In this case, the stability can be recovered by adding acceleration feedback.

To extend the investigation to flexible systems, finite element structural model data was used to account for existing flexible modes in a Maglev plant. For large flexible structure systems, eigenvectors and eigenvalues obtained from finite element software can be relatively easily converted (using modal transformation) into transfer function form. This transformation was illustrated in details in this dissertation, and it was shown that it is a very convenient tool for flexibility modeling.

With regard to choosing an appropriate control strategy it was shown that for MIMO Maglev systems, a centralized (modal) control approach which is based on gap measurements results in some flexible modes being uncontrollable. This may leave marginally stable modes subject to instability as a result of such influences as discrete-time controller implementation. Thus, the centralized control approach is not recommended for Maglev systems with significant flexibility.

Because of Maglev's inherent instability, lead compensation is required to stabilize the system. It was analytically illustrated that an appropriate way of signal derivation for the PD compensator is necessary to get better system response. Thus, an appropriate combination of the low pass filter, washout filter and leaky integrator is recommended. This assertion was supported by simulation examples and test rig experiments.

When the different control laws were applied to the actual plants, it turned out that noise is the most undesirable factor leading to unacceptable performance. Therefore, methods for applying two filters to the Maglev control loop architecture were presented. First, a digital filter designed to suppress noise in the control signal (compensator output) was shown. Second, an analog filter was incorporated to avoid aliasing. Also, it was mentioned that it is not desirable to use notch filters due to the interactions between the vehicle and the track at several positions along the guideway. A flexible track or guideway implies that the Maglev's transfer function zeros move which can interact with a notch filter and possibly make the overall system less robust or even unstable.

The laboratory test-rig provided an important source of information to evaluate control robustness and to provide guidelines for Maglev compensator design. According

to these results it turned out that in spite of the fact that pure gap feedback based on PD/PID compensation can achieve desired gap, this control design did not retain stability when test-rig load was increased. Acceleration measurements which are merged together with the gap feedback improve Maglev performance significantly by suppressing noise relating to the compensator derivative calculation and made the gap response smoother. Of the compensators tested, only the PD/PID compensator with merged gap and acceleration and either inverse force calculation or flux feedback based on real experiments exhibited acceptable characteristics. In these cases in the gap response there were no visible fluctuations. Moreover, the same compensator could work with different load applied to the test-rig. Both designs (flux feedback and force inverse calculation) incorporate similar idea of linearizing system nonlinearities.

Summarizing above, it can be said that the first main conclusion of this thesis is that designing a control law for a Maglev plant is a trade-off between compensator lead (required for stability) and compensator lag (needed for noise suppression).

As was mentioned above, in this work, some ideas for dealing with the system's non-linearities through the use of either different system models or favorable control laws were presented. Two different control laws including inverse force calculation and flux feedback were designed and tested to linearize Maglev's non-linear characteristics. It was shown that these approaches provide very good results, and make the system more robust when compared to controllers which must work with a *purely* non-linear plant. It was shown that when the inverse force expression is introduced to the compensator design, a simple method for prescribing the levitation force command can be utilized. Through this method (instead of using full force expression), a simpler formula can be incorporated and still guarantee satisfactory results. This new method of linearizing the Maglev system allows one to avoid tangential calculation, reduces computation time and can render a control loop much faster in the working application.

The second main conclusion is that for a low cost Maglev system where robustness is required (due to complexity of this type of plant), project designers must rely and focus more on the alternative control solutions. This means that for low budget magnetically levitated suspension systems, the controller design is even more crucial to

the objectives of achieving a stable and comfortable ride. In this dissertation, this statement has been supported by both analytical and experimental results. Compared with classical Maglev control concepts based on gap measurements only, better characteristics were achieved when:

- 1) the system was linearized using:
 - the addition of flux feedback to the loop, and
 - inverse force calculation,
- 2) additional data is provided to the controller, i.e. acceleration measurements.

This observation leads to a final conclusion. A trade off for not only the control design is required (between noise rejection and stability robustness), but also from a general perspective: a trade off between low cost of construction and how the control is designed.

Future work on the ODU Maglev research project is expected to involve deeper investigation of the comparison between centralized and decentralized control approach, the exploration of more advanced control design, and more tests and experiments to be carried out on the actual magnetically suspended vehicle.

REFERENCES

- [1] Windborne J.F. "EMS Control System Design for Maglev vehicle – a critical system" *Automatica*, vol.29, No.5 p.1345-1349 (1993)
- [2] Friedland Bernard "Control System Design", McGraw Hill, (1986)
- [3] Kuo Benjamin C, Farid Golnaraghi, "Automatic Control Systems", John Wiley & Sons, Inc. 8th Edition (2003)
- [4] Phelan Richard M. "Automatic Control Systems", Cornell University Press, (1977)
- [5] Hitay Ozbay, "Introduction to Feedback Control Theory", CRC Press, (2000)
- [6] Stengel F Robert "Stochastic Optimal Control", JohnWiley and Sons (1986)
- [7] Bender E.K., Paul I.L "Analysis of optimum and preview control of active vehicle suspension", Report for the US Department of Transportation contract C-85-65, Department of Mechaznical Engineering MIT, (IX 1967)
- [8] Muller Peter C., "Design of optimal state-observers and its application to Maglev vehicle suspension control", *Journal of Dynamic Systems Measurement and Control* (1976)
- [9] Namerikawa T., M. Fujita T "Uncertainty structure and μ -synthesis of magnetic suspension system", *IEE Japan* vol.121C, No.6 (2001)
- [10] Barrett G.R., T.G. Clapp "Coprime factorization design of novel Maglev presser foot controller", *Mechatronics* vol.5. no.2/3 pp.279-294, (1995)
- [11] Brein W., G.Leitmann "State feedback for uncertain dynamic systems", *Applied Mathematics and Computation* 22, p.65-87 (1987)
- [12] Zhou Kemin, Doyle John C. "Essential of Robust Control", Prentice-Hall, Inc. ISBN: 0-13-525833-2, (1998)
- [13] Kyong B. Lim and David E. Coxy, "Robust Tracking Control of a Magnetically Suspended Rigid Body", Research project Report at NASA Langley Research Center Hampton, Virginia
- [14] Zi-Jiang Yang, Masayuki Minashima "Robust nonlinear control of a feedback linearizable voltage controlled magnetic levitation system", *IEEE Transaction on Industrial Electronics*, vol.41, no.3, (XI 2001)
- [15] Vidyasagar M. "Nonlinear system Analysis, Prentice-Hall, (1993)
- [16] Kolk W. Richard, Robert A. Lerman "Nonlinear System Dynamic", Van Nostrand Reinhold, New York (1992)

- [17] Krstic Miroslav, Ioannis Kanellakopoulous, Petar Kokotovic "Nonlinear and Adaptive Control Design", John Wiley & Sons, Inc. (1995)
- [18] Feng Zhao, Jeff A. May, Shiou C. Loh "Controller Synthesis and verification for non-linear systems", IEEE Control System Magazine (1998)
- [19] Beheshti, S.M. Nematollahzadeh "Design of active Suspension Control using Singular Perturbation Theory", 15th Triennial World Congress, Barcelona, Spain, (2002)
- [20] Gutierrez H.M. "Sliding mode control of non-linear input system: application to magnetically levitated fast – tool servo", IEEE Transaction on Industrial Electronics, vol.45, no.6, (XII 1998)
- [21] Pam Haley, Don Soloway, Brain Gold "Real-time Adaptive Control Using Neural Generalized Predictive Control" Research project Report at NASA Langley Research Center Hampton, Virginia
- [22] Ching-Yu Tyan, Paul P. Wang, "Neural Fault Diagnosis and Fuzzy Fault Control for a Complex Dynamic System", National Science Foundation Grant No. ECS-9216474 and Electric Research Institute Grant RP8030-3 Report
- [23] Zadeh L. "Fuzzy Sets Information and Control" Vol. 8, p.338 – 353, Journal of Information and Control, vol.8, LA (1965)
- [24] Maxwell James C., "Electricity and Magnetism", vol.1 and 2 reprinted in Dover, Publication (1954)
- [25] Sinha P.K "Electrodynamics suspension: Dynamic and Control", IEEE Control Engineering Series 30 ISBN: 0 86341 063 4, (1986)
- [26] D'Arrigo Aldo, Rufer Alfred "Integrated Electromagnetic levitation and guidance system for the SwissMetro project", Project Report, Swiss Federal Institute of Technology, (1999)
- [27] Tomohiro Seki, "The Development of HSST-100L", 14th International Conference on Magnetically Levitated Systems – Maglev, Bremen, Germany (1995)
- [28] Yoshiho Hikasa, Yutaka Takeuchi "Detail and Experimental Results of Ferromagnetic Levitation system of Japan Air Lines HSST-01/-02 Vehicles", IEEE, vol.vt-29, no.1, (II 1980)
- [29] Zhang Y, S-G.Xu, "Analysis of dynamic Response for HSST Maglev vehicle model", Physica p.341-348 (2000)

- [30] Masaaki Fujino Tkeshi Mizuma, "Total test operation of HSST-100 and planning project in Nagoya", 14th International Conference on Magnetically Levitated Systems (Maglev), Bremen Germany 1995
- [31] Michinori Shida, Eisuke Masada, Jyunpei Baba, Tatsuya Shimogata, "A Hybrid Control Scheme for Electromagnetic Suspensions System HSST", Department of electrical Engineering-Report, University of Tokyo, (2000)
- [32] Meisinger Reinhold "Simulation of Maglev Vehicles Riding Over Single and Double Span Guideways", Mathematic and Computers Simulation XXI pp.197-206, (1979)
- [33] Shtrikman S., Thomas H. "On the Dynamical Stability of the Hovering Magnetic Top", S.Gov, (III 1998)
- [34] Akira Chiba, Masatsuga Takemoto, Ken Shimada, "A Design and Characteristics of Switched Reluctance Type Bearingless Motors", 4th International Symposium on Magnetic Suspension Technology, (V 1998)
- [35] Yohji Okada, Bunshu Nagai, Katsuhiko Karino, "Angular Coordinate Repetitive Control of Magnetic Bearing", 4th International Symposium on Magnetic Suspension Technology, (V 1998)
- [36] Drago Mataka, Motoki Hinada, "A note on the third stage control of the M-V launch vehicle" Japan Aerospace Exploration Agency Project Report ISSN: 1349-1113, Jaxa RR-03-004E, (2004)
- [37] Limbert D.A., H.H. Richardson, D.N. Wormley, "Controlled Dynamic Characteristics of Ferromagnetic Vehicle Suspension Providing Simultaneous Lift and Guidance", Journal of Dynamics Systems, Measurement, and Control, Vol.101 p217, (IX 1976)
- [38] Limbert D.A Dissertation Thesis MIT (1976)
- [39] Brzezina W., J. Langerholc "Lift and side forces on rectangular pole pieces in two dimensions", Journal of applied Physic, vol.45 no.4 (IV 1974)
- [40] Davey Kent, S. "Survey of Maglev Systems Focusing Primarily on Lift ", 5th International Symposium on Magnetic Suspension Technology (2000)
- [41] Haus Hermann A., James R. Melcher, "Electromagnetic Field and Energy", Prentice Hall, (1990)
- [42] Binns K.J., Lawrenson P.J., Trowbridge C.W. "The Analytical and Numerical Solution of Electric and Magnetic Fields", Bookcraft (Bath) Ltd., (1994)

- [43] Grover Fredrick W. "Inductance Calculation", Dover Publication, Inc., New York (1946)
- [44] Thompson Marc T., "Electrodynamic Magnetic Suspension – Models, Scaling Laws, and Experimental Results", IEEE Transactions on Education, vol.43, no.3, (VIII 2000)
- [45] Thompson Marc T. "Inductance Calculation Techniques", Approximations and Handbook Methods, (1999)
- [46] Mei-Yung Chen, Kun-Nam Wu, Li-Chen Fu "Design, implementation and self-tuning adaptive control of Maglev guiding system", Mechatronics vol.10 no.7 p.215-237 (2000)
- [47] Rektorys Karel "Survey of Applicable Mathematics", Kluwer Academic Publishers (1991).
- [48] Shina P.K, A.N. Pechev "Model reference adaptive control of a Maglev system with stable maximum descent criteria", Automatica 35 p.1457-1465 (1999)
- [49] Sinha P.K., G.Pech H.A.Abbassi "Digital Control of an Electromagnetic Suspension System Using the TMS-32020 Signal Processor", Automatica vol.27 no.6 pp.1051-1054 (1991)
- [50] Bania Piotr, "Maglev", Dissertation Thesis, AGH Krakow (1999)
- [51] Zayadine Michel "Etude de Reglage en Position de la Sustentation Magnetique par attraction", Dissertation Thesis, Ecole Polytechnic in Lausanne, (1996)
- [52] Bong Wie, Kuk-Whan Byun "New Generalized Structural Filtering Concept for Active Vibration Control Synthesis", AIAA, Journal of Guidance, vol.12, no.2 p.147-154, (III 1989)
- [53] Robert H. Cannon Jr., Dan E. Rosenthal, "Experiments in Control of Flexible Structures with Non-collocated Sensors and Actuators", AIAA, Journal of Guidance, vol.7, no.5 p.546-553, (V 1989)
- [54] Schmitz Eric "Experiments on the End-Point position Control of a very flexible one-link manipulator", Stanford University, Research Report for NASA Langley Research Center, (VI 1985)
- [55] Johansson Karl Henrik, Anders Rantzer "Decentralized Control of Sequentially Minimum Phase Systems", IEEE Trans. on Automatic Control, vol. 44, p. 10, (XI 1999)
- [56] Schierman John, Schmidt David K, "On the Limitations of Decentralized Control" AIAA Control and Dynamics, 0731-0590 vol.20 no.2 p.384-397 (1997)
- [57] West-Vukovich George S., Edward J.Davison "The Decentralized Control of Large Flexible Space Structures", IEEE. Automatic Control, vol. 29, issue 10, p.866-879, (X 1984)
- [58] Yoshida K., H.Takami, L.Shi, "Decoupled control of levitation and propulsion in underwater LM car ME02", Mathematics and Computers simulation 46 p.239-256 (1998).

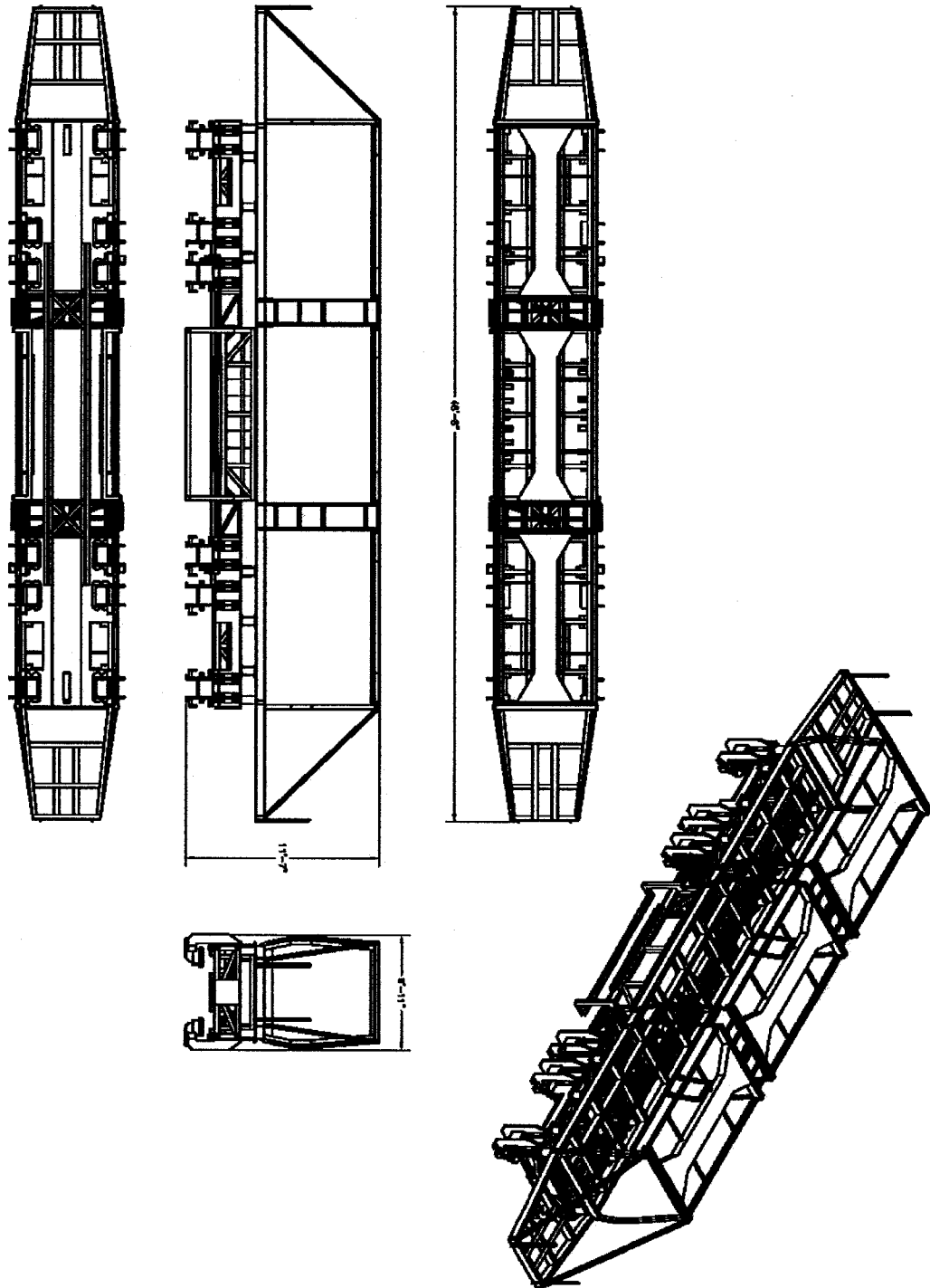
- [59] Xiao Jing Zheng, Jian Jun Wu, You-He Zhou, "Numerical analyses on dynamic control of five-degree-of-freedom maglev vehicle moving on the flexible guideways", *Journal of Sound and Vibration* 235(1), p.43-61, (2000)
- [60] Helen Ryaciotaki-Boussalis Kosmatopoulos E.B., Ioannou, P.A "Centralized, Decentralized and Overlapping Control Techniques for a Large Segmented Telescope", 38th IEEE Control Systems Magazine, (2000)
- [61] Maciejowski J.M "Multivariable Feedback Design", Addison-Wesley, Inc. ISBN: 0-201-18243-2, 5th Edition (1994)
- [62] McLagan Neil Stuart, "Control of an Electromagnetic Vehicle Suspension", Dissertation Thesis, University of Reading (1992)
- [63] Goodall Roger "Dynamic and control requirements for EMS Maglev suspensions", Maglev Conference, Shanghai (X 2004)
- [64] Wilson C. Brian, Panagiotis Tsiotras, Bonnie Heck-Ferri, "Implementation of the generalized complementary Flux constraints for low-loss active magnetic bearings", AIAA Guidance, Navigation and Control Conference and Exhibit, (15 VIII 2005)
- [65] Jung-Chun Wei, Tzong-Jer Yang "Theoretical Calculation of Magnetic Force for Type II Superconductor in a Levitated Magnetic Field", *Chinese Journal of Physics* vol.34 no.6 (XII 1996)
- [66] Seon-Ho Lee, Jong Tea Lim "A unified Estimation for Scheduled Controllers in Non-linear Systems", *IEICE Trans. Fundamentals*, vol.E84-A, no.7, (XII 2001)
- [67] Chao-Ming, Jia-Yush, Min-shin Chen "Adaptive Control of repulsive Maglev suspension systems", *Control Engineering Practice* no.8 pp.1357-1367, (2000)
- [68] Wormley D.N., H.H. Richardson "Transportation vehicle/beam-elevated guideway dynamic interaction", *Journal of Dynamic Systems, Measurement and Control* (1974)
- [69] Snyders J.E., D.N.Wormley "Dynamic interactions between vehicles and elevated, flexible randomly irregular guideways", *Journal of Dynamic Systems, Measurement and Control* (1977)
- [70] Chiu W.S., R.G.Smith, D.N.Wormley, "Influence of Vehicle and Distributed Guideway Parameters on High Speed Vehicle-Guideway Dynamic Interaction", *Journal of Dynamic Systems, Measurement, and Control*, (III 1971)
- [71] Silva Clarence W., David N. Wormley "Automated Transit Guideways: Analysis and Design", Lexington Books ISBN: 0-669-04407-5, (1983)

- [72] Biggers S.B, Wilson J.F. “Dynamic interaction of high speed tracked air cushion vehicles with their guideways – a parametric study”, AIAA/ASME 12th structure, Structural Dynamics and Material Conference, (IV 1971)
- [73] Cai Y., S.S.Chen, D.M.Rote, H.T.Coffey ”Vehicle/guideway interaction for high speed vehicles on the flexible guideway”, Journal of Sound and Vibration 175(2), p.625-646, (1994)
- [74] Clarence W. de Silva “Vibration Fundamentals and Practice”, CRC, 1st Edition, ISBN: 0849318084, (1999)
- [75] Srinivasan, A. “Nonlinear Vibration of Beams and Plates”, Int. J. Non-linear Mechanics, Vol.1, No.3, p.179-191, (1966)
- [76] Pota Hemanshu R., Thomas E. Alberts “Teaching Vibration Analysis using Symbolic Computation Software”, ASME, UMIST, (1996)
- [77] Freuchte Roger D, Robert H. Nelson Thomas A. Radomski,”Power Conditioning Systems for a Magnetically Levitated Test Vehicle”, IEEE Transaction on Vehicular Technology, vol.29, no.1, (II 1981)
- [78] Chi-Tsong Chen, Saunders “Analog and Digital Control System Design”, Collage Publishing (1993)
- [79] Terrell Trevor J. “Introduction to digital filters”, The Macmillan Press Ltd. (1980)
- [80] Hassouneh Munther A., Hsien-Chiarn Lee and Eyad H. Abed “Washout Filters in Feedback Control: Benefits, Limitations and Extensions”, American Control Conference, Boston, Massachusetts, (2004)
- [81] Howell J.P ”Aerodynamic response of Maglev train models to a crosswind gust”, Journal of the Wind Engineering and Industrial Aerodynamics, vol.22 p.205-213 (1986)
- [82] Williams Chip, “Design Specification for the Maglev Levitation Control/Current Driver”, Williams Consulting Co, Manual, (VI 2001)
- [83] Reddy J. N. “An Introduction to the Finite Element Method”, McGraw Hill Series in Mechanical Engineering, (2005)
- [84] Joshi S.M.”Control of Large Flexible Space Structures”, Springfield Verlag, (1989)
- [85] Feng Zhao “Intelligent Simulation in Designing Complex Dynamic Control Systems”, Artificial Intelligent in Industrial Decision Making, Control and Automation, (1995)
- [86] E.H. Bristol “On a new measure of interactions for multivariable process control”, IEEE Trans. Autom. Control, (1966)

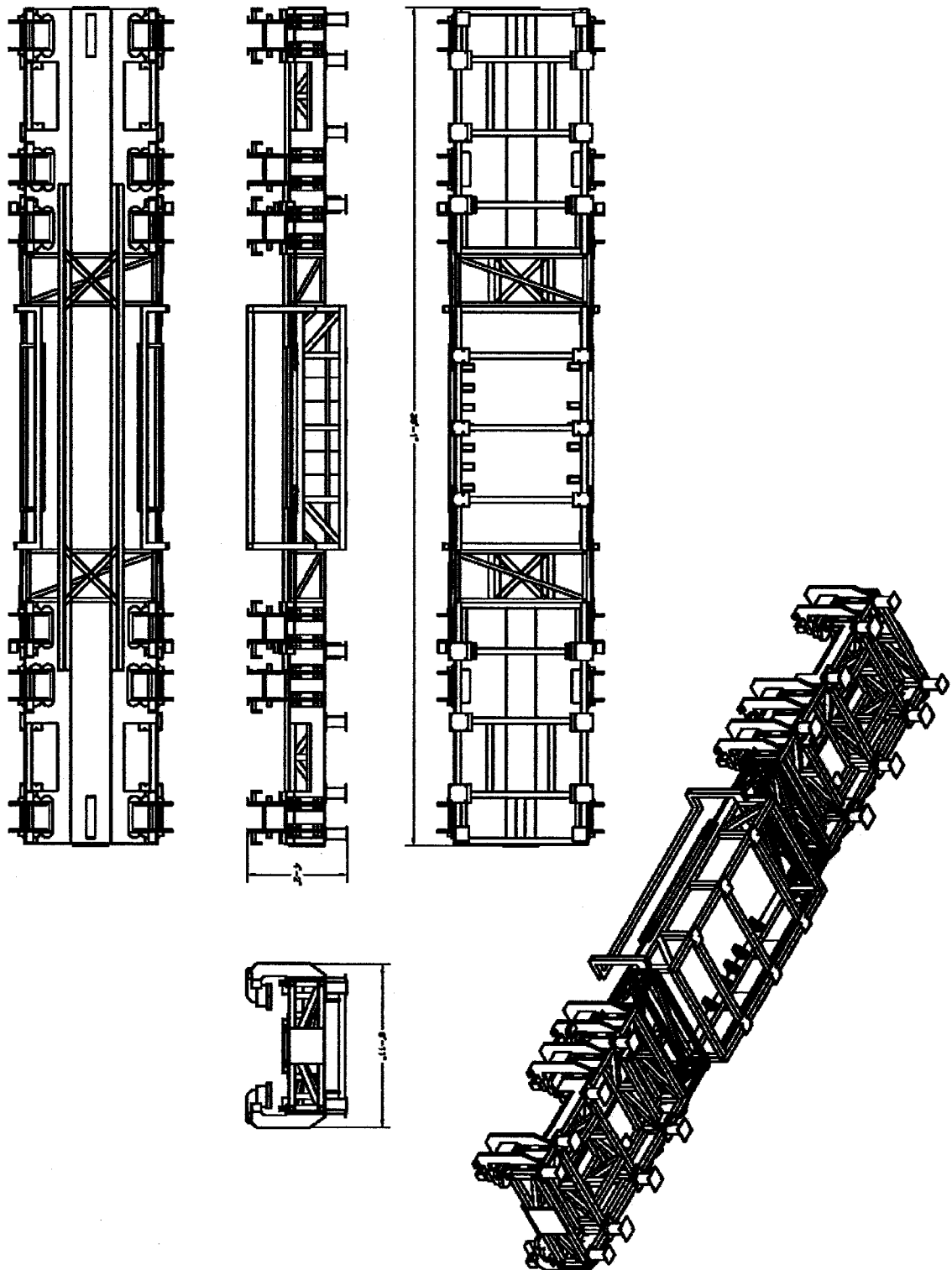
- [87] Haggblom Kurt .E “Limitation and use of the RGA as a controllability measure”, Automation Conference, Helsinki, (V 1995)
- [88] Sinha P.K “Multivariable Control”, Macler Dekker, Inc. (1984)
- [89] Murray R.M, Z. Li and S.S. Sastry “A Mathematical Introduction to Robotic Manipulation”, Springfield-Verlag, (1991)

Internet sources:

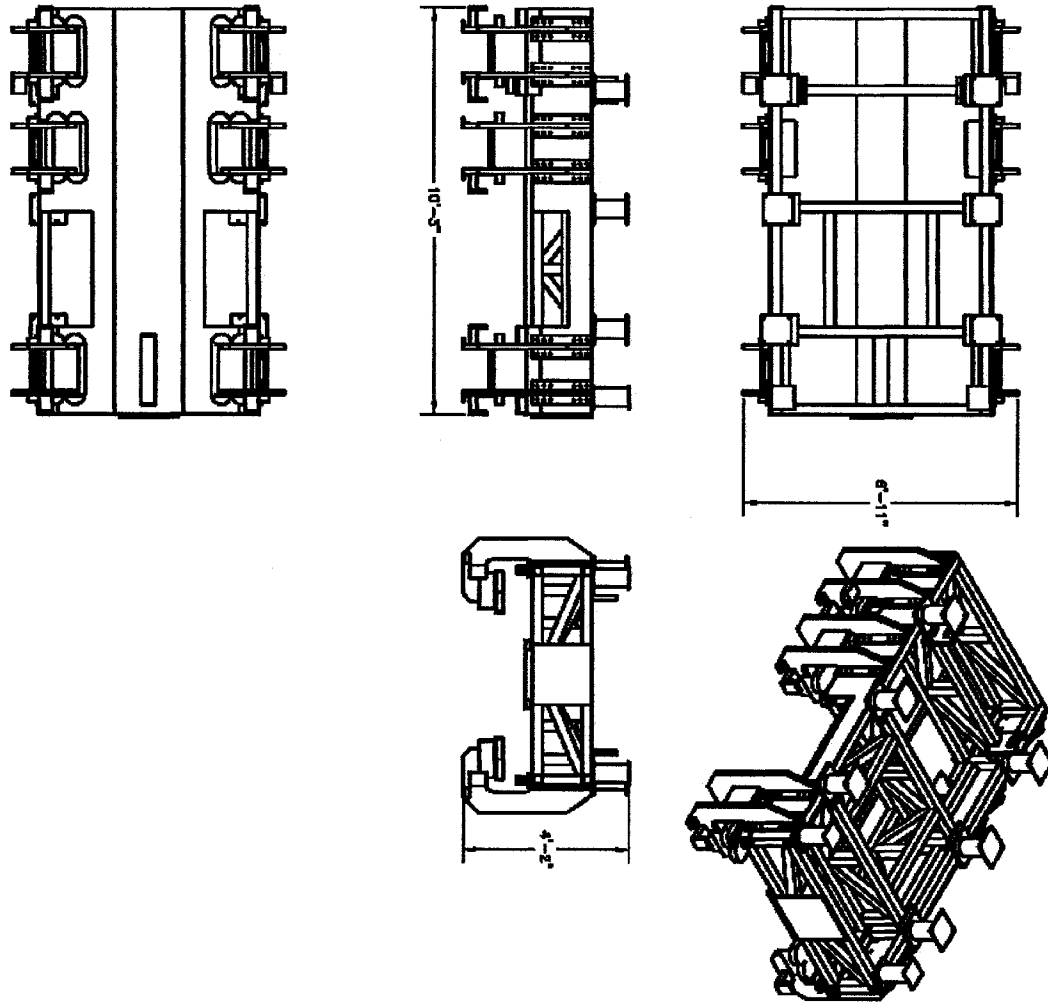
- [1i] <http://www.mathpages.com/home/index.htm>
- [2i] <http://www.maglev.de/>
- [3i] <http://hsst.jp/>
- [4i] <http://www.transrapid-usa.com>
- [5i] <http://mail.american-maglev.com/>
- [6i] <http://www.o-keating.com/hsr/maglev.htm>
- [7i] <http://www.boeing.com/defense-space/space/maglev/>
- [8i] http://www.space.gc.ca/asc/eng/csa_sectors/space_science/microgravity/mvis.asp
- [9i] <http://www.powerlabs.org/emguns.htm>
- [10i] http://www.levitronix.com/Documents/TechnicalPapers/Magnetic_Suspension_Systems_for_Biomedical_Applications.pdf

APPENDIX A.1 – ODU Maglev Vehicle Drawings

APPENDIX A.2 – ODU Maglev Chassis Drawings



APPENDIX A.3 – ODU Maglev Bogie Drawings



GRZEGORZ OLESZCZUK

Kochanowskiego 26 /57
 Płock 09-402
 Poland

Phone: +48 (024) 264-39-41
 Mobile: +48 502 196 115
 E-mail: grzegorz.oleszczuk@honeywell.com

DOB: 3rd of September 1976
 POB: Plock, Poland

AREAS OF EXPERTISE

Control Systems, Processing, Distributed Control Systems, PLC Controllers, Flight Dynamics and Control, Advanced Programming, Process Optimization, Signal Static and Dynamic Process Modeling, Analysis (linear & nonlinear), Composite Materials, Vibrations, Piezoelectric Materials, Robotics, Research and Testing

EDUCATION

May 2002 – August 2006

Old Dominion University, Norfolk, VA (scholarship)

➤ Ph.D. – Department of Aerospace Engineering

Major: Dynamics and Controls

Dissertation title: “Robustness and Control of Magnetically Levitated Transportation Systems”

Oct 1995 – April 2000

Warsaw University of Technology, Warsaw, Poland

➤ M. Sc. Eng – Department of Power and Aeronautical Engineering

Major: Automation and Robotics

Thesis title: “Design of the Advanced Optimization Algorithms in Application of the Distributed Control Systems for Petrochemical Processes”

Related Post-Graduate Ph.D. Coursework*Controls*

- Modern Control Theory
- Applied Digital Signal Processing
- Actuators and Sensors
- Robotics Analysis and Control
- Advanced Control Methodologies
- Flight Dynamic and Control

Multidisciplinary

- Nonlinear Systems

Structural Mechanics (Experimental)

- Experimental Structural Dynamics
- Experimental Modal Analysis

Structural Mechanics

- Structural Vibrations
- Random Vibrations
- Mechanics of Composite Structures

Others Courses and Trainings

ORACLE: SQL Programming
ORACLE: Oracle9i Administrating

Siemens: PLC S7 Controllers, Advanced Programming (STEP7)

Siemens: PLC networks: Design, service and maintenance.

EXPERIENCE

- | | | |
|---------------------------|---|----------------|
| September 2006 – Present | Advanced Process Control Senior Engineer
<i>Honeywell (Process Solutions)</i> <ul style="list-style-type: none"> The Advanced Process Control (APC) operations across Europe, Middle East & Africa (EMEA). Data gathering and process evaluation, controller tuning & instrumentation recommendation development of inferential measurements and multivariable control system design optimization and associated commissioning activities | Warsaw, Poland |
| June 2003 – August 2006 | Research Assistant
<i>Research Foundation (participation in Lockheed Martin project)</i> <ul style="list-style-type: none"> Application and testing/ control strategies for Magnetic Levitation Vehicle | Norfolk, VA |
| June 2002 - May 2003 | Research Assistant
<i>Old Dominion University</i> <ul style="list-style-type: none"> Developing and modeling control strategies for Magnetic Levitation Vehicle (Matlab, C++) Participation in two research projects for Oceana Sensor Technologies Ltd. / control and optimization of internal engine combustion, real time bearing fault diagnosis. Unimation Puma 240 Robot Programming | Norfolk, VA |
| September 2000 - May 2002 | Software Engineer
<i>ORLEN Automatyka Sp.z.o.o</i> <ul style="list-style-type: none"> Voting system for Annual Meetings of Stockholders – design and application (Delphi) Polythene installation, Control system and interlock algorithms for 4MW compressor – design and application (Siemens DR24) Visualization and diagnostic software design on Oil Composed Installation (Visual Basic) Refining chromatograph (Ashland and Marathon software)- calibration and service PLC (s7 and S5 controllers) - service and maintenance. Claus Plant, Visualization and diagnostic software for electrical processes (GE Fanuc controllers and VersaPro software) <p>Other responsibilities:</p> <ul style="list-style-type: none"> PC Computers Hardware and Software – service EMP software (SAP) – service | Plock, Poland. |
| July 1999 – July 2000 | Project Assistant (Master Degree Practical Training)
<i>PKN ORLEN S.A.</i> <ul style="list-style-type: none"> Modeling thermodynamic processes on CDU2 - Crude Distillation Unit (heat exchanger modeling based on DCS ABB MOD 300 systems) Advance control systems design and application (ABB, MOD 300 - APC) | Plock, Poland |
| July 1999 – August 1999 | Project Assistant
<i>Fisher Rosemount, Ltd. (part time)</i> <ul style="list-style-type: none"> Administered quality control procedures in the start-up phase of a DCS project. (Investigate customer needs and application requirements) | Warsaw, Poland |
| March 1999 - June 1999 | Data Base Specialist
<i>Allianz Poland (part time)</i> <ul style="list-style-type: none"> Responsible for existing data base maintenance, streamlining and tuning Coordinated operations between regional branches and IT division | Warsaw, Poland |

May 1998 - April 1999 **Intern** Warsaw, Poland
Westinghouse Poland, Ltd.
 • Participation in DCS Ovation System training

June 1997 – July 1997 **Intern** Warsaw, Poland
Petrochemia Plock (recently PKN ORLEN SA)
 • Modeling thermo-chemical processes on CDU2 (combustion in oil and gas furnace)
 • Advance control system design and application (ABB MOD 300 - TCL)

PUBLICATIONS / CONFERENCE PROCEEDINGS “On the influence of structural flexibility on feedback control system stability for EMS Maglev vehicles” - Thomas. E. Alberts, **Grzegorz Oleszczuk**, The 19th International Conference on Magnetically Levitated Systems and Linear Drives, Dresden September 2006

 “Active Control of Supersonic Nonlinear Panel Flutter Using Piezoelectric Actuation” - Qinqin Li, **Grzegorz Oleszczuk**, Jen-Kuang Huang, and Chuh Mei, 9th ISVR Conference 2006

ACTIVITIES AND MEMBERSHIP

February 1998 – January 2000 Board Member of “*Mazovian Aviation Club*” (*non-profit*)
 Member of Fédération Aéronautique Internationale (*FAI*)

Present Membership of American Institute of Aeronautics and Astronautics (*AIAA*)
 Present Membership of Electrical Electronic and Information Engineering (*EIEE*)

AWARDS ■ Research scholarship at Warsaw University of Technology, February 1999 - June 1999
 ■ Research Assistantship at Old Dominion University, June 2002 - May 2006

OTHER SKILLS Computer Skills:
 • Operating systems: MS Windows, UNIX, Linux
 • Programming: C/C++, Turbo Pascal/Delphi, Fortran, SQL, Step7, TCL
 • Other Tools: Matlab, MathCAD, AutoCAD, Unigraphics, VersaPro, ORACLE
 • Finite Element Method: Ansys
 • Office Software: Word, Excel, PowerPoint
 Language Skills: Polish (native), English (very good), Russian and German (re-familiarization required)

HOBBIES Soaring/piloting airplanes; R/C models, History

REFERENCES*(Alphabetical order)*

Dr. Thomas E. Alberts - Professor, Aerospace Engineering Department, Old Dominion University, Norfolk, VA, e-mail: talberts@odu.edu, ph.: 001 757 683-3736

Dr. Jeremiah F. Creedon, - Project Director, Research Foundation, Norfolk, VA, e-mail: jcreedon@odu.edu, ph.: 001 757 683-3733

Jerzy Klatte - Technician Director, ORLEN Automatyka, Plock, Poland, email: jerzy.klatte@orlen.pl ph.: +48 24 365 -45-69

Andrzej Klimkiewicz - Technician Service Manager, ORLEN Automatyka, Plock, Poland, email: andrzej.klimkiewicz@orlen.pl ph.: +48 24 365 -35-54

Waldemar Nagorko - Advance Process Control Department, PKN ORLEN SA, Plock, Poland, e-mail: waldemar.nagorko@orlen.pl, ph.: +48 24 365 -53-43

Dr. Brett Newman - Professor, Graduate Program Director, Aerospace Engineering Department, Old Dominion University, Norfolk, VA, e-mail: bnewman@odu.edu, ph.: 001 757 683-4913

Dr. Andrzej Teodorczyk - Professor, Graduate Program Director, Warsaw University of Technology, Institute of Heat and Power Engineering, Warsaw, Poland, e-mail: ateod@itc.pw.edu.pl , ph.: +48 22 660-52-26, +48 22 825-02-41